Modulation of endothelial permeability during *ex vivo* lung perfusion

Jenny Gilmour

Thesis submitted in partial fulfilment of the requirements for the degree of Doctor of Philosophy

Translational and Clinical Research Institute

Newcastle University

March 2023

Abstract

Introduction: *Ex vivo* lung perfusion (EVLP) enables donor-lung assessment, but extended periods of perfusion cause lung injury and inflammation. Development of novel perfusate formulations could enable longer and advanced assessment strategies. EVLP also offers the opportunity for therapeutic administration pre-transplantation. S1P-receptor-1 (S1PR1) activation reduces endothelial permeability. It has been shown to reduce oedema formation during ischaemia reperfusion injury (IRI) and has the potential to improve endothelial integrity of marginal donor-lungs. Our aim was to validate a novel perfusate solution and then assess the therapeutic effects of S1PR1 agonist CYM5442 administration on vascular permeability during EVLP of human lungs declined for transplantation.

Methods: RNA-sequencing and gene-set enrichment analysis (GSEA) was carried out on porcine lung biopsies post-EVLP to identify IRI-associated gene sets and validate novel perfusate modified Steen. *In vitro*, trans-endothelial electrical resistance (TEER) of pulmonary endothelial cell monolayers was assessed following treatment with models of IRI (SIN-1 and H_2O_2), CYM5442 or co-treatment. CYM5442 was tested *ex vivo*; human lung pairs were split, before administration of CYM5442 or vehicle to each single lung and 6 hours perfusion. Then permeability to Evan's blue dye and wet/dry ratio was assessed.

Results: Modified Steen showed significant negative enrichment of inflammatory gene-sets compared with Steen, but cold static storage (CSS) and EVLP was still associated with significant positive enrichment. *In vitro*, SIN-1 significantly decreased TEER of human pulmonary endothelial monolayers (p=0.0114), which was rescued by co-treatment with CYM5442 (p=0.0179). During EVLP, CYM5442 significantly reduced bronchoalveolar lavage Evan's blue concentration (p=0.0070) and wet/dry ratio (p=0.0258; N=2).

Conclusion: Despite use of a novel perfusate with anti-inflammatory properties, CSS and EVLP caused activation of inflammatory pathways, reinforcing the need for therapeutic intervention. *In vitro* and *ex vivo* permeability testing identified the potential of CYM5442 to improve barrier integrity. Targeting S1PR1 during EVLP could improve endothelial integrity of unsuitable donor-lungs prior to transplantation.

The impact of COVID-19

The COVID-19 pandemic started during the first year of my PhD project and has had a significant impact on my work.

Firstly, access to the laboratory was limited for over 6 months. When access was finally allowed, it was limited to a certain number of people as per the laboratory size and there were significant restrictions on using facilities at the university, such as flow cytometry and bio-imaging. As this project was almost entirely laboratory based, this hugely delayed *in vitro* and *ex vivo* experiments. This not only limited the extensiveness of our *in vitro* permeability testing, but ultimately meant that we did not fulfil our intended sample size for human EVLPs within the time frame of this submission.

Furthermore, as part of our collaboration with XVIVO Perfusion, this project was intended to analyse biomarkers in samples from a randomised, controlled, multicentre clinical trial; the Non-ischaemic preservation of donor heart in heart transplantation. As this trial was delayed due to COVID-19, this aspect of the work had to be abandoned and instead, RNA-sequencing was performed on samples from a pre-existing study which was intended to validate a novel perfusate. Also, as part of the collaboration, I was scheduled to complete a 3 month secondment with XVIVO in Sweden to take advantage of their established porcine EVLP programme. However, due to COVID-19 impacting the company financially and delaying their ongoing research, these experiments could not be scheduled within the time frame of the study. This led us to attempt to optimise a porcine DCD EVLP model ourselves, which was ultimately unsuccessful, meaning this current study lacked the addition of a large animal model as was initially intended.

Acknowledgements

I would firstly like to thank the Medical Research Council Discovery Medicine North Doctoral Training Partnership (MRC DiMeN DTP), National Institute for Health and Research Blood and Transplant Research Unit (NIHR BTRU) and the Wellcome Trust for funding this work, without which this research would not be possible. I would also like to acknowledge my collaborators XVIVO Perfusion, who provided financial support for RNA-sequencing and Steen Solution.

I would like to give a huge thank you to my supervisors Professor Simi Ali, Professor Andrew Fisher, Professor John Kirby and Annelie Sigvardsson who have continued to provide support and expert guidance throughout the project.

I would like to share my thanks to Annelie Sigvardsson and Emilia Henriksson for carrying out the porcine EVLP experiments and providing samples and physiological parameter data used for chapter 3. I would also like to express my gratitude to my colleagues in the Applied Immunobiology and Transplantation group. In particular, I would like to thank Professor John Dark, Nicholas Chilvers, Chong Yun Pang, Marnie Brown and Lucy Bates for giving up their time to assist on so many lung perfusions, which were often long and out of hours. Specifically, I'd like to acknowledge Nicholas Chilvers for providing his surgical expertise for porcine and human work and also giving up yet more of his time to accept lung offers and organise transport on top of attending perfusions. I'd also like to thank Marnie Brown and Lucy Bates, who's organisational and technical skills enabled perfusions to run smoothly. The perfusion aspect of this project would not be possible without such a great team. I'd also particularly like to thank Chong Yun Pang for always making himself available to provide advice on upcoming experiments and being so helpful in the lab, as well as being a supportive friend throughout my PhD.

I am also very grateful for the external support I received throughout the project; I would like to thank Cockle Park Farm and in particular, Mark Brett and Emma Malcolm without whom, we would not have been able to carry out our porcine lung retrievals. I would also like to thank the Newcastle University Bioinformatics Unit for advice on using the Ingenuity Pathway Analysis (IPA) software.

Finally, I would like to extend my gratitude to the organ donors and their family members for their generous contributions, as well as the specialist nurses who consented for our research.

Table of Contents

Table of Figures

Table of tables

Abbreviations

β-ME	β-mercaptoethanol
A1AT	Alpha-1 antitrypsin
Abl	Abelson Murine Leukaemia Viral Oncogene Homolog 1
AC	Adenylate cyclase
AdhIL-10	Adenoviral interleukin-10
AJ	Adherens junction
Akt	Protein Kinase B (PKB)
ALI	Acute lung injury
AMP	Adenosine monophosphate
AP-1	Activator protein 1
ApoM	Apolipoprotein M
APS	Ammonium persulfate
ARDS	Acute respiratory distress syndrome
ATP	Adenosine triphosphate
BAL	Bronchoalveolar lavage
BCA	Bicinchoninic acid
BH4	Tetrahydrobiopterin (THB)
BPM	Breaths per minute
BSA	Bovine serum albumin
cAMP	Cyclic adenosine monophosphate
CD	Cluster of differentiation
cDNA	Complimentary DNA
CIT	Cold ischaemic time
CLUE	Direct lung ultrasound evaluation
CO	Cardiac output
CPM	Counts per million
CSS	Cold static storage
CT	Computerised tomography
CT	Cycle threshold
Cx	Connexin
CXCL8	C-X-C motif ligand 8
DAMP	Damage-associated molecular pattern
DAPI	Diamidino-2-phenylindole
DBD	Donation after brain death
DCD	Donation after cardiac death
DCFDA	2',7' –dichlorofluorescin diacetate
DEG	Differentially expressed gene
DEPC	Diethyl pyro carbonate
DMSO	Dimethyl sulfoxide
DNA	Deoxyribonucleic acid
EB	Evan's blue
ECD	Extended criteria donor
EDTA	Ethylenediaminetetraacetic acid
EGF	Epidermal growth factor
Em	Emission
eNOS	Endothelial nitric oxide synthase
ERK	Extracellular related kinase

ET	Endotracheal
EV	Extracellular vesicle
EVLP	*Ex vivo* lung perfusion
Ex	Excitation
FBS	Foetal bovine serum
FBXO3	F-box only protein 3
FCS	Foetal calf serum
FDR	False discovery rate
FITC	Fluorescein Isothiocyanate
GJ	Gap junction
GSEA	Gene set enrichment analysis
GTP	Guanosine triphosphate
H&E	Haematoxylin and eosin
HAEC	Human amniotic epithelial cell
HSA	Human serum albumin
HCl	Hydrochloride
HCMEC	Human cardiac microvascular endothelial cell
HIF-1α	Hypoxia inducible factor 1 alpha
HMEC-1	Human dermal microvascular endothelial cell 1
HMGB1	High motility group box 1
HO	Heme oxygenase
HPMEC	Human pulmonary microvascular endothelial cell
HRP	Horseradish peroxidase
HSP90i	Heat shock protein 90 inhibitor
HUVEC	Human umbilical vein endothelial cell
IBW	Ideal body weight
ICAM-1	Intercellular adhesion molecule 1
IFN	Interferon
IFU	Instructions for use
IL	Interleukin
IMP	Inosine monophosphate
iNOS	Inducible nitric oxide synthase
IPA	Ingenuity pathway analysis
IPKB	Ingenuity pathway knowledge base
IRI	Ischaemia reperfusion injury
ISHLT	The international Society for Heart and Lung Transplantation
ITU	Intensive treatment unit
JAM	Junction adhesion molecule
LAP	Left atrial pressure
LAPO2	Left atrial oxygen partial pressure
MAPC	Multipotent adult progenitor cell
MLCK	Myosin light chain kinase
MPO	Myeloperoxidase
MPTP	Mitochondrial permeability transition pore
mRNA	Messenger ribonucleic acid
MSC	Mesenchymal stromal cell
mtNOS	Mitochondrial nitric oxide synthase
NAC	N-acetylcysteine
NaCl	Sodium chloride

NAD+	Nicotinamide adenine dinucleotide
NADPH	Nicotinamide adenine dinucleotide phosphate
NES	Normalised enrichment score
NET	Neutrophil extracellular trap
NFκB	Nuclear factor kappa B
NGS	Next generation sequencing
NO	Nitric oxide
NOS	Nitric oxide Synthase
NOX2	Nicotinamide adenine dinucleotide phosphate oxidase 2
OCT	Optimum cutting temperature
OGG1	8-oxoguanine DNA glycosylase
PA	Pulmonary artery
PAP	Pulmonary artery pressure
PBS	Phosphate buffered saline
PBST	Phosphate buffered saline with tween
PDTC	Pyrrolidine dithiocarbonate
PECAM-1	Platelet and endothelial cell adhesion molecule 1
PFA	Paraformaldehyde
PGD	Primary graft dysfunction
PI3K	Phosphatidylinositol-3 kinase
PIPC	Phosphoinositide phospholipase C
PKC	Protein kinase C
PLC	Phospholipase C
PMN	Polymorphonuclear
PPAR	Peroxisome proliferator-activated receptor
PPMEC	Porcine pulmonary microvascular endothelial cell
PTP	Tyrosine phosphatase
PVDF	Polyvinylidene fluoride
PVR	Pulmonary vascular resistance
RA	Retinoic acid
RBC	Red blood cell
RNS	Reactive nitrogen species
ROCK	Rho-associated protein kinase
ROS	Reactive oxygen species
RT-qPCR	Real time quantitative polymerase chain reaction
RVI	Royal Victoria Infirmary
S1P	Sphingosine-1-phosphate
S1PR	Sphingosine-1-phosphate receptor
SA	Salicylic acid
SD	Standard deviation
SDS	Sodium dodecyl sulfate
SDS-PAGE	Sodium dodecyl-sulfate polyacrylamide gel electrophoresis
SIN-1	3-morpholinosydnonimine
SOD	Superoxide dismutase
SPHK	Sphingosine kinase
SPL	Sphingosine-1-phosphate lyase
SPNS2	Spinster homolog 2
TBHP	Tert-butyl hydroperoxide
TBST	Tris buffered saline with Tween

TEER	Trans-epithelial/Trans-endothelial electrical resistance
TEMED	Tetramethylethylenediamine
THI	Tetrahydroxybutylimidazole
TJ	Tight junction
TLR4	Toll-like receptor 4
TMZ	Trimetazidine
TNF	Tumour necrosis factor
TNF-α	Tumour necrosis factor alpha
TNFR	Tumour necrosis factor receptor
TPM	Transcripts per million
UMI	Unique molecular index
VCAM-1	Vascular cell adhesion molecule 1
VE-cadherin	Vascular endothelial cadherin
VEGF	Vascular endothelial growth factor
VEGFR2	Vascular endothelial growth factor receptor 2
VSMC	Vascular smooth muscle cell
WIT	Warm ischaemic time
WT	Wild type
XPS	XVIVO Perfusion System
XTT	2,3-Bis-(2-Methoxy-4-Nitro-5-Sulfophenyl)-2H
ZO-1	Zona occludens 1

1. Introduction

1.1. Lung transplantation

Respiratory diseases contribute to significant morbidity and mortality worldwide and their prevalence continues to increase. In fact, the incidence of chronic respiratory disease increased by 39.8 % between 1999 and 2017 and is one of the leading causes of deaths globally (GBD Chronic Respiratory Disease Collaborators, 2020). The only viable treatment option for very select patients with end stage respiratory diseases is lung transplantation. During lung transplantation, donor lungs are retrieved from a deceased donor, before transferring to a recipient. In rare cases, lung lobes can also be obtained from live donation and transplanted into recipients.

The first human lung transplantation was performed by Hardy *et al*. in 1963. Following donation after circulatory death (DCD), a single left lung was transplanted into a 58-year old man with left lung bronchial carcinoma. The recipient survived for 18 days before dying from renal failure and infection. Following this, various attempts at lung transplantation were made with no long term success. However, in 1983, the Toronto lung transplant group successfully performed the first single lung transplantation with long term patient survival post-transplant. In fact, the patient went on to live for over 7 years following the procedure (Toronto Lung Transplant Group, 1986). The Toronto group also went on to perform the first successful bilateral lung transplantation in 1986, with the patient demonstrating excellent lung function post-transplant (Patterson *et al*., 1988). These advances were primarily attributable to the combined improvement of immunosuppressive regimens, surgical technique and patient selectivity.

1.1.1. Clinical utilisation of donor lungs today/ the challenges of lung transplantation today

Today, this progress has allowed lung transplantation to become a well-established standard of care. However, success is limited by an inadequate number of donor lungs and low organ utilisation rates. Since 2011, the number of patients on the national active lung transplant list has gradually increased. Furthermore, the number of transplantations carried out annually is insufficient to fulfil organ demand; between 2021-22 there were 267 patients on the waiting list, whilst only 109 lung transplantations were carried out. Whilst this discrepancy is in part due to a low number of potential donor lungs, low utilisation rates only further exacerbate

the problem; utilisation rates from donation after brainstem death (DBD) and DCD in the same year were only 10 % and 4 % respectively (NHS Blood and Transplant, 2022).

Utilisation rates are low for the lung, primarily due to the stringencies of the selection criteria defining an 'ideal' donor. According to the ISHLT, an 'Ideal' donor should be aged under 55 years old, have ABO compatibility, a clear chest radiograph, PaO2 >300 on FiO2 = 1.0, PEEP 5 cm H_2O, tobacco history <20 pack-years, no chest trauma, no aspiration or sepsis, no prior cardiopulmonary surgery, a sputum gram stain showing an absence of organisms and no purulent secretions after bronchoscopy (Orens *et al*., 2003). Lungs retrieved from a donor which does not meet the ISHLT selection criteria are referred to as extended criteria donor (ECD) organs. In addition, although the early examples of human lung transplantation used DCD organs, donation after brainstem dead (DBD) quickly became the preferred donation option (Krutsinger *et al*., 2015). This is due to the capacity to minimise the warm ischaemic time (Sánchez-Cámara *et al*., 2022).

In order to address the discrepancy between the amount of transplants that take place and the number of patients on the waiting list, the use of ECD and/or DCD organs is becoming frequently more routine at transplant centres. However, there is yet to be a consensus reached on the effect of these organs on transplant outcome and mortality. For example, various studies showed comparable post-transplant survival between ECD lungs and standard criteria lungs (Moreno *et al*., 2014, Suh *et al*., 2020, Christie *et al*., 2021) and also between DCD and DBD lungs (Krutsinger *et al*., 2015, Van Raemdonck *et al*., 2019). However, Moreno *et al* also showed that ECD grafts were associated with lower post-transplant oxygenation ratios (Moreno *et al*., 2014) and Smits *et al* concluded that post-transplant survival was significantly reduced in higher risk organs (Smits *et al*., 2011). It has also been suggested that perhaps ECD grafts are not suitable for higher risk recipients (Moreno *et al*., 2014, Suh *et al*., 2020). ECD organs could offer a straightforward solution to improving waiting list mortality, although their potential association with higher degrees of ischaemia reperfusion injury (IRI) means their use is not without risk.

1.2. Lung ischaemia reperfusion injury

IRI is a complex and multifactorial process which is inevitable during lung transplantation. It occurs as a result of the cessation of blood flow to an organ when it is retrieved from a donor and its re-establishment in the recipient. Reperfusion of the lung is paradoxical as although it is vital for regain of function, it also worsens the oxidative stress caused by ischaemia through the reintroduction of oxygen (den Hengst *et al*., 2010). Characteristic pathology of lung IRI is increased endothelial permeability and oedema, increased pulmonary vascular resistance, reduced oxygenation and pulmonary hypertension (Forgie *et al*., 2021). Clinically, it presents as pulmonary infiltrates visualised on a chest x-ray (Ferrari and Andrade, 2015). Ultimately, IRI can lead to primary graft dysfunction (PGD) of the transplanted lung, which is a major cause of post-operative morbidity and mortality (Chen-Yoshikawa, 2021). In fact, PGD currently has an incidence of around 30 % in the lung despite surgical advances (Porteous *et al*., 2015) and accounts for one of the most common causes of early mortality following transplantation (Chambers *et al*., 2019). Furthermore, ECD organs are more prone to IRI, increasing the incidence of PGD (Botha *et al*., 2006).

1.2.1. Anoxia versus ischaemia – a mechanistic distinction

The lung is distinct from other organs in that it has a dual oxygen supply and is not solely reliant on vascular blood flow to the tissue. As well as the delivery of oxygenated blood via the bronchial arteries, the lung receives oxygen from the external environment through alveolar ventilation. Thus, ischaemia of the lung is not always associated with immediate anoxia of the lung parenchyma, as residual oxygen in the alveoli can maintain local tissue oxygenation for some time. This means that adenosine triphosphate (ATP) is not depleted, a distinction from the anoxia-reoxygenation in other organs or in cases where lungs have low alveolar oxygen tension (less than 7 mmHg). Instead, oxidative stress is initiated by a loss of mechanotransduction (de Perrot *et al*., 2003, den Hengst *et al*., 2010).

Loss of flow is detected in a process known as shear sensing by the “mechanosome”, which consists of caveolae, platelet and endothelial cell adhesion molecule 1 (PECAM-1), vascular endothelial growth factor receptor 2 (VEGFR2) and vascular endothelial (VE)-cadherin (Chatterjee and Fisher, 2014, Noel *et al*., 2013, Tzima *et al*., 2005). Conversely, in other organs or lungs with low alveolar oxygen, the mechanisms of IRI are triggered by a switch to anaerobic respiration. However, glycolysis is insufficient to replenish ATP levels, leading to ATP depletion

and IRI initiation (Pike *et al*., 1993). The distinct role of loss of flow during lung IRI has been demonstrated both in situ and *in vitro*; endothelial cells were shown to be the major source of reactive oxygen species (ROS) following stop of flow, despite maintenance of physiological oxygen. These studies demonstrate that loss of flow rapidly generates ROS independently from hypoxia (Chatterjee *et al*., 2006, Zhang *et al*., 2008, Zhang *et al*., 2005a, Wei *et al*., 1999).

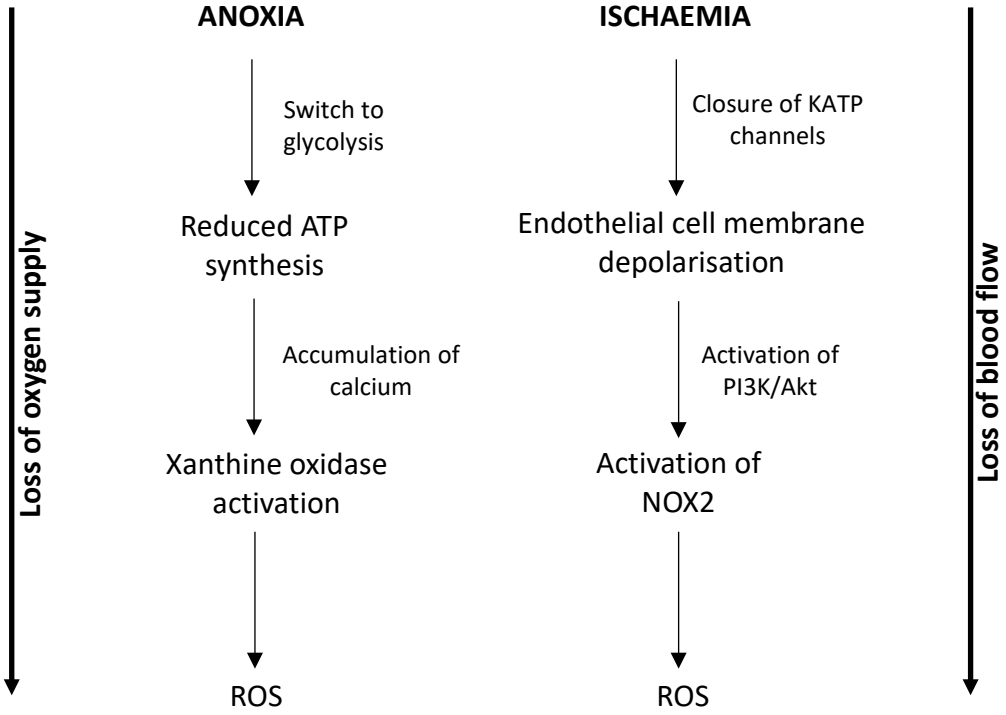

Figure 1.1. Anoxia and ischaemia as distinct pathways for reactive oxygen species release.

Anoxia and ischaemia generate reactive oxygen species (ROS) in different ways. Depletion of oxygen leads cessation of oxidative phosphorylation and switch to glycolysis. This leads to reduced ATP, which ultimately causes ion imbalance and intracellular calcium accumulation. Xanthine dehydrogenase is converted to Xanthine oxidase. In comparison, Ischaemia leads to a closure of ATP-sensitive K^+ channels (KATP) channels, which results in endothelial cell membrane depolarisation, followed by activation of the Phosphoinositide 3-kinase/protein kinase B (PI3K/Akt) complex. This activates NADPH oxidase (NOX2). Ultimately, both xanthine oxidase and NOX2 contribute to ROS release by reducing oxygen to superoxide. Adapted from Chatterjee *et al* (Chatterjee and Fisher, 2014).

1.2.2. Disruption of ionic balance during ischaemia

During anoxic ischaemia, glycolysis leads to H^+ accumulation, resulting in cellular acidification. In order to combat this, the cell excretes H^+ via Na^+/H^+ exchange, bringing in Na+ (Pike *et al*., 1993). Gradual ATP depletion also leads to impairment of the Na^+/K^+ ATPase, ATP-dependent Ca^{2+} reuptake by the endoplasmic reticulum and active Ca^{2+} excretion (Ca^{2+}-ATPase pumps), causing Na^+ and Ca^{2+} accumulation (Wu *et al*., 2018). Even in the absence of anoxia, ischaemia causes a similar influx of calcium ions, although it is postulated that this is via voltage gated T-type Ca^{2+} channel activation (Al-Mehdi *et al*., 2000, Song *et al*., 2001, Wei *et al*., 2004).

Increasing accumulation of cytoplasmic Ca^{2+} causes increased mitochondrial uptake and mitochondrial swelling (Webster, 2012), as well as opening of mitochondria permeability transition pores (MPTPs) (Kalogeris *et al*., 2014). Ca^{2+} accumulation also causes activation of phospholipases and proteases, alteration of the cell shape by causing cytoskeletal contraction and increased endothelial barrier permeability (Ferrari and Andrade, 2015). Proton accumulation results in decreased cellular pH which reduces enzyme function and causes nuclear chromatin clumping. Sodium and calcium ion retention also leads to hyper-osmolarity, resulting in water entry, cell swelling and lysis (Wu *et al*., 2018, Webster, 2012).

1.2.3. Generation of reactive oxygen species

ROS cause oxidative stress through lipid peroxidation and protein and DNA damage and also activate the inflammatory cascade that characterises IRI. There is a vast amount of evidence that ROS are primarily produced in the endothelial cells of the lung immediately following ischaemia (Al-Mehdi *et al*., 1998, Chatterjee *et al*., 2006, Zhang *et al*., 2008, Zhang *et al*., 2005a). Furthermore, the largest increase in ROS can be seen upon the re-introduction of oxygen during perfusion, as this interacts with free radicals, overwhelming the natural antioxidant system (den Hengst *et al*., 2010). Production of oxygen centred free radicals such as the hydroxyl radical ($^{\bullet}OH$), hydrogen peroxide (H_2O_2) and the superoxide radical ($O_2^{\bullet-}$) from the pathways below are of the greatest consequence in IRI (Chatterjee *et al*., 2014).

1.2.3.1. Mitochondrial-dependant generation of ROS – producers and targets of ROS

The cellular event triggering ROS production in hypoxic ischaemia is the depletion of ATP in the mitochondria as this leads to failure of the respiratory chain due to a lack of electron acceptors. This leads to increased electron leak at complexes I and II of the respiratory chain

in particular (den Hengst *et al*., 2010), leading to superoxide and hydrogen peroxide production (Chen *et al*., 2008). Mitochondrial superoxide is also derived from other sources such as glycerol-3-phosphate dehydrogenase, growth factor adaptor Shc ($p66^{Shc}$) and nicotinamide adenine dinucleotide phosphate (NADPH) oxidase 4, but to a far lesser extent than the respiratory chain (Kalogeris *et al*., 2014).

ROS and calcium overload in the mitochondria then contributes to MPTP opening upon the onset of reperfusion. This contributes to further ROS by decreasing mitochondrial membrane potential (Brookes *et al*., 2004) and also leads to increased mitochondrial permeability and rupture of the outer mitochondrial membrane, releasing pro-apoptotic factors such as cytochrome-c into the cytosol (den Hengst *et al*., 2010, Kalogeris *et al*., 2014). This not only means the loss of an important free radical scavenger from the mitochondria, but also results in caspase activation as part of the apoptotic pathway (Borutaite *et al*., 2003).

1.2.3.2. Xanthine oxidase

During hypoxia, cessation of aerobic metabolism means that high energy phosphates such as ATP or adenosine monophosphate (AMP) cannot be utilised. Thus, they are broken down into inosine monophosphate (IMP), which is dephosphorylated to inosine. This can then be degraded to hypoxanthine, which is degraded to xanthine, H_2O_2 and ROS by xanthine oxidase. Xanthine oxidase is formed via a calcium-dependent conversion of xanthine dehydrogenase. This mechanism is specific to the hypoxic lung and does not occur in the absence of hypoxia. Pre-treatment with xanthine oxidase inhibitors caused attenuation of LIRI in an anoxia-reoxygenation rat lung model (Lynch *et al*., 1988) and reduced superoxide generation in an *in vivo* rabbit lung anoxia/reoxygenation model (Kennedy *et al*., 1989). However, during ventilated ischaemia, xanthine oxidase inhibition did not reduce ROS formation. Instead, NADPH oxidase inhibition showed reduced ROS, whilst this had no effect in a model of anoxia/reoxygenation (Al-Mehdi *et al*., 1997a, Zhao *et al*., 1997). Thus it is clear that the two models have distinct pathways for ROS generation.

1.2.3.3. NADPH-dependant generation of superoxide

As discussed in section 1.2.1, in the non-hypoxic ischaemic lung, it is the loss of shear stress which is the most significant in ROS generation. Changes in blood flow due to ischaemia are sensed by the mechanosome, leading to closure of ATP-sensitive K^+ channels in the

endothelial membrane, which are usually maintained in an open state (al-Mehdi *et al*., 1996, Al-Mehdi *et al*., 1997a, Chatterjee *et al*., 2006, Zhang *et al*., 2008, Zhang *et al*., 2005a, al-Mehdi *et al*., 1997b). This causes membrane depolarisation and activation of endothelial Phosphoinositide 3-kinase (PI3K)-protein kinase B (Akt) complex (Chatterjee *et al*., 2012). Following this, NADPH oxidase 2 (NOX2) is activated (den Hengst *et al*., 2010, Chatterjee and Fisher, 2014). NOX2 can then mediate the reduction of oxygen to form H_2O_2 and superoxide anion whilst oxidising NADPH (Eckenhoff *et al*., 1992, Ferrari and Andrade, 2015). Downstream, this leads to activation of transcription factors hypoxia inducible factor 1 subunit alpha (HIF-1α), nuclear factor kappa B (NFκB) and activator protein 1 (AP-1) (Chatterjee and Fisher, 2014). NADPH oxidase in endothelial cells, vascular smooth muscle and macrophages is the primary source of ROS in the non-hypoxic lung (Ovechkin *et al*., 2007). Neutrophils also generate ROS via NOX2 derived mechanisms, which is crucial for the oxidative burst released upon activation (Carbone *et al*., 2019).

1.2.3.4. NOS-dependent generation of ROS

Under normal conditions, nitric oxide is tissue protective and has roles which include regulating vascular tone, reducing leukocyte adherence, scavenging free radicals and maintaining normal vascular permeability (Anaya-Prado *et al*., 2002). Despite its beneficial effects at low concentrations, in excessive amounts it can interact with ROS to form peroxynitrite and reactive nitrogen species (RNS) (Ghafourifar *et al*., 1999, Ovechkin *et al*., 2007). During IRI, calcium influx into the cell and mitochondria can result in the activation of Ca^{2+} dependent isoforms of NO synthase (NOS) such as endothelial NOS (eNOS) and mitochondrial NOS (mtNOS) to overproduce NO (Tozawa *et al*., 1999, Song *et al*., 2001, Manevich *et al*., 2001, Bringold *et al*., 2000). Independently of Ca^{2+}, inducible nitric oxide synthase (iNOS) is also stimulated to produce large concentrations of NO by pro-inflammatory cytokines (Xie *et al*., 1994). As well as NO overproduction, oxidative stress is also derived from eNOS uncoupling as a result of endothelial dysfunction. ROS oxidise tetrahydrobiopterin (BH4), an essential cofactor, leading to eNOS uncoupling. This leads to the production and accumulation of superoxide (Gielis *et al*., 2011, Förstermann and Münzel, 2006).

1.2.3.5. The inflammatory response

Lung IRI results in sterile inflammation (Laubach and Sharma, 2016) as oxidative stress results in activation of the inflammatory cascade. NOX2 activation in endothelial cells results in

activation of various transcription factors such as NFκB and AP-1 and adoption of a pro-inflammatory phenotype. Endothelial cells then increase production of adhesion molecules such as E-selectin, vascular cell adhesion molecule-1 (VCAM-1), intercellular adhesion molecule-1 (ICAM-1) and also release tissue factor and C-X-C motif ligand 8 (CXCL8) (den Hengst *et al*., 2010). Alveolar macrophages are activated via toll like receptor 4 (TLR4) by damage associated molecular patterns (DAMPs) released into the extracellular environment as a result of tissue damage. This leads to stabilisation of transcription factors such as NFκB and release of cytokines such as tumour necrosis factor (TNF)-α, interleukin (IL)-1β, IL-6, IL-2, CXCL-8, IL-9, IL-10, IL-18 and type 1 interferons (de Perrot *et al*., 2003, Laubach and Sharma, 2016). TNF-α also induces CXCL8 production from alveolar type 2 epithelial cells (Laubach and Sharma, 2016). Chemokine release and increased adhesion molecule expression then leads to binding and infiltration of recipient neutrophils upon reperfusion.

1.2.3.6. Neutrophil transmigration

Neutrophils are recruited very quickly to the lung and are found adherent to post-capillary venules within minutes of reperfusion (Rodrigues and Granger, 2010). The blood flow within a vessel pushes the neutrophil towards the vessel wall, where the transmigration sequence is initiated (Gane and Stockley, 2012). In a process termed 'rolling', leukocytes temporarily interact with endothelial cells in low affinity associations mediated by selectins. This allows exposure to chemokines at the interface between the blood and endothelium (Cooper *et al*., 2002). Neutrophil migration is a dynamic process which is reliant on chemokine gradients. Chemokine gradients are formed by chemokine binding of glycosaminoglycans on the surface of endothelial cells, allowing directed movement to the site of injury (Thompson *et al*., 2017). Increasing concentrations of chemo-attractants result in the activation of β_2 integrins on the surface of leukocytes. Integrins facilitate firm adherence of the neutrophil to the endothelium via binding adhesion molecules such as ICAM-1, VCAM-1 and platelet-endothelial cell adhesion molecule-1 (PECAM-1)(Cooper *et al*., 2002). Transmigration can then either be transcellular or paracellular (Gane and Stockley, 2012).

Once they have infiltrated the tissue, neutrophils contribute to tissue damage via various mechanisms. Activated neutrophils undergo degranulation, releasing granules loaded with proteolytic enzymes and ROS in an oxidative burst (Vermeiren *et al*., 2000). In fact, activated neutrophils are suggested to be the main source of superoxide following reperfusion (Duilio

et al., 2001). Neutrophils also form neutrophil extracellular traps (NETs). NETs are generated by a cell death programme termed 'NETosis' and are comprised primarily of a network of extracellular DNA, histones and proteins from neutrophil granules (Sayah *et al*., 2015, Laubach and Sharma, 2016). Disruption of NETs has been shown to mediate protection against PGD by Sayah *et al*, who confirmed their presence during lung IRI (Sayah *et al*., 2015).

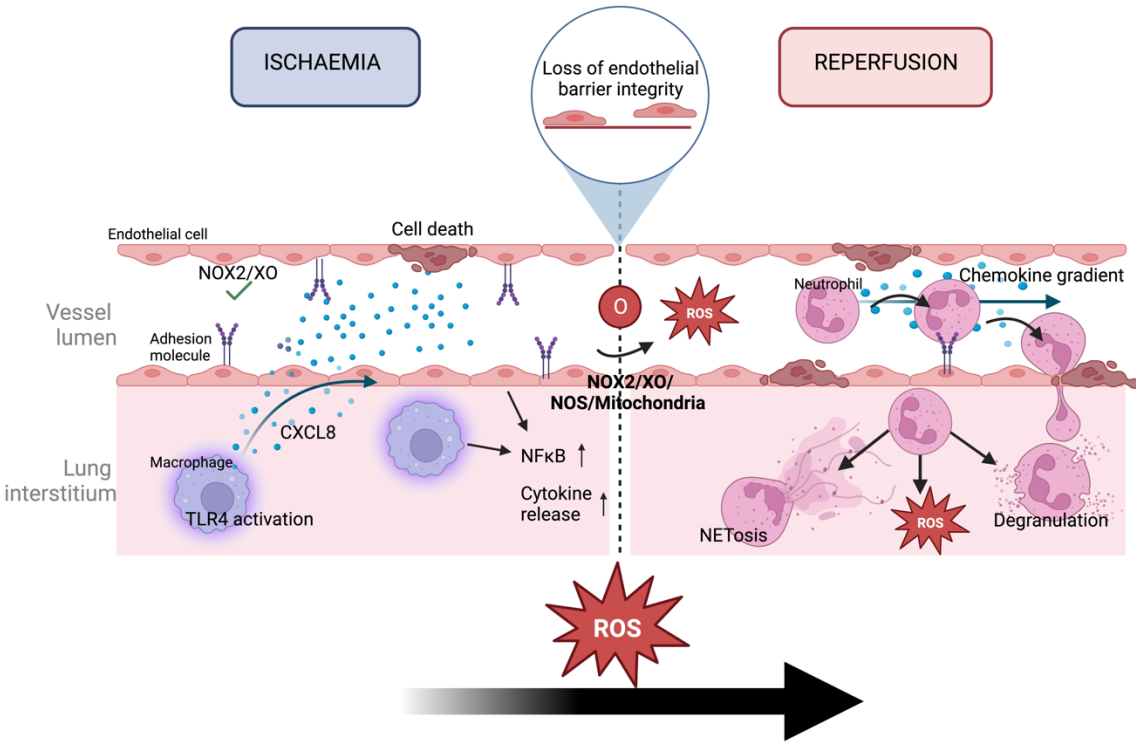

Figure 1.2. Pathophysiology of ischaemia reperfusion injury.

Ischaemia reperfusion injury (IRI) is a dual-phase pathology. During ischaemia, stop of flow leads to activation of NADPH oxidase 2 (NOX2), whilst depletion of oxygen leads to activation of xanthine oxidase (XO). Alveolar macrophages are activated by damage associated molecular pattern (DAMP) interaction with toll-like receptor 4 (TLR4). Transcription factor NFκB is upregulated in endothelial cells and alveolar macrophages, causing increased adhesion molecule expression on endothelium and increased cytokine and chemokine release from endothelial cells and macrophages. Chemokines then form a chemokine gradient by binding to glycosaminoglycans on the endothelial cell surface. Reactive oxygen species (ROS) are formed through NOX2, XO, nitric oxidase synthase (NOS) and through the mitochondria and cause cell death. Upon reperfusion, oxygen is reintroduced to the system, which increases ROS release. Recipient neutrophils follow the chemokine gradient, bind to adhesion molecules on the endothelium and transmigrate through. Neutrophils then cause tissue damage by degranulation and NETosis and also release ROS. As well as cell death, the endothelial cell monolayer is destabilised and endothelial cell permeability is increased. Image created using BioRender.

1.3. The endothelial barrier

1.3.1. Blood vessels and endothelial cells

The endothelial barrier of blood vessels is postulated to be the primary site of ROS production following IRI (Chatterjee and Fisher, 2014).

Blood vessels transport blood with nutrients and oxygen to tissues and also transport waste away (Alkadhim *et al*., 2015). There are three types of blood vessels; arteries, veins and capillaries and their structure depends on their function. Veins and arteries are made up of three layers; the tunica externa, comprised of connective tissue, the tunica media, made up of vascular smooth muscle cells (VSMCs) and elastic fibres and the tunica intima, which consists of an endothelial lining. Capillaries differ in that they are only comprised of a single endothelial layer in order to facilitate diffusion (Ng *et al*., 2018).

Endothelial cells form a monolayer which covers the inner apical surface of both blood and lymphatic vessels (Hernández-Reséndiz *et al*., 2018). They maintain a healthy vascular state by controlling leukocyte adhesion and aggregation of platelets, reducing inflammation and thrombus formation. They also regulate vascular tone through release of vasoactive substances and interaction with vascular smooth muscle cells (Yang *et al*., 2016). One of the main roles of the endothelium is to control vascular permeability; whilst low molecular weight substances can move through the endothelium via passive diffusion, permeability to liquid and proteins is a process which is tightly controlled (Mehta and Malik, 2006, Hellenthal *et al*., 2022).

1.3.2. Endothelial cell junctions and their function

Intercellular junctions control endothelial permeability and leukocyte transmigration (Vestweber *et al*., 2014). Endothelial junctions comprise of tight junctions (TJ), gap junctions (GJ) and adherens junctions (AJ). Whilst both TJs and AJs facilitate cell-cell adhesion, GJs allow cell-cell communication. (Bazzoni and Dejana, 2004).

1.3.2.1. Gap junctions

Transmission electron micrographs first identified GJs as 2-3 nm gaps between cells (SÁEz *et al*., 2003, Benedetti and Emmelot, 1965). GJs are comprised of connexin (Cx) proteins, specifically Cx43, Cx40 and Cx37 in endothelial cells, and these proteins form connexons.

Connexons form a hexagonal pattern and act as intercellular channels to connect the cytoplasm of cells adjacent to each other (Bazzoni and Dejana, 2004). GJs are primarily involved in intercellular communication via passage of small molecules such as ions, nucleotides, amino acids and second messengers through these channels (Simon and Goodenough, 1998, Okamoto and Suzuki, 2017). In this way, endothelial cells can communicate with other endothelial cells, as well as VSMCs, leukocytes and platelets (Okamoto and Suzuki, 2017). For example, myoendothelial GJs are thought to have key roles in blood flow distribution by relaying vasomotor signals between endothelial cells and VSMCs via transmission of Ca^{2+} and small signalling molecules (Schmidt *et al*., 2008). In fact, Cx40 knockout mice were shown to exhibit irregular vasomotion in arterioles and reduced vasodilatory response (Wit *et al*., 2000, Jobs *et al*., 2012), which was mirrored in endothelial cell-specific Cx40 knockout mice (Chadjichristos *et al*., 2010, Meens *et al*., 2015). Aside from their roles in GJs, Cx channels also facilitate the paracrine functions of cells by release of molecules into the extracellular environment (Esseltine and Laird, 2016).

Although primarily involved in intercellular communication, there is also evidence of the involvement of Cxs in regulation of endothelial permeability. It is suggested that Cx43 and Cx40 co-localise with TJ protein zona occludens 1 (ZO-1) and claudin-5. Accordingly, lipopolysaccharide (LPS) treatment of rat pulmonary endothelial cells reduced Cx40 expression and increased permeability. Barrier integrity was restored via overexpression of Cx40 (Nagasawa *et al*., 2006). Kandasamy *et al* showed that endotoxin induced vascular leak was associated with increased Cx43 expression which declined progressively, whilst VE-cadherin showed an inverse trend, showing a relationship between the two (Kandasamy *et al*., 2015). These studies suggest the involvement of Cxs in endothelial permeability modulation via direct relationships with other junction proteins.

1.3.2.2. Tight junctions

Functionally, TJs are essential in establishing the barrier capabilities of endothelial cells and regulate paracellular permeability and cell polarity (Bazzoni and Dejana, 2004). TJs were initially termed zonula occludens when they were first define by electron microscopy in 1963 (Farquhar and Palade, 1963). They are comprised of transmembrane proteins such as occludins, claudins and junctional adhesion molecules (JAMs), which complex with intracellular scaffold proteins cingulin, paracingulin and zona occludens and lipids in the cell

membrane (Lee *et al*., 2008). ZO-1 is perhaps the most extensively studied intracellular TJ protein (Bazzoni and Dejana, 2004).

Although controversial, it is postulated that TJs have a role in maintenance of cell polarity; they act as a fence to prevent the diffusion of lipids and membrane proteins between the apical and basolateral membranes (Tsukita *et al*., 2001). This was discovered very early on, when Pisam *et al* identified that disruption of TJs lead to apical and basolateral membrane protein mixing (Pisam and Ripoche, 1976) and Balda *et al* suggested a role for occludin in this mechanism (Balda *et al*., 1996). TJs also have roles in modulating endothelial integrity; TJ permeability can vary based on the number of tight junction strands and also tissue to tissue, especially as strand number differs depending on tissue type. In fact, trans-epithelial electric resistance (TEER) was found to correlate with the number of TJ strands in different tissues (Tsukita *et al*., 2001). The complexity of the network pattern and TJ number is also something which influences junction permeability. For example, in high pressure arteries, TJs are more complex and at the blood brain barrier, more numerous in order to tightly maintain vessel barrier integrity at these sites (Wallez and Huber, 2008). Koto *et al* suggested a role for TJ protein claudin-5 in maintaining neural vascular integrity. Inhibition of claudin-5 expression *in vitro* lead to reduced TER (Koto *et al*., 2007).

1.3.2.3. Adherens junctions

AJs and their transmembrane component VE-cadherin, are arguably the most important in controlling vascular permeability. VE-cadherin is a type II cadherin and facilitates junction adhesion and intercellular stability and also contributes to TJ mechanical maintenance (Cerutti and Ridley, 2017). Structurally, VE-cadherin connects adjacent cells via its extracellular domain; the cytoplasmic tail is bound to p120-catenin at the juxtamembrane domain, whilst it is bound to β-catenin and pakoglobin at the c terminal domain. β-catenin and pakoglobin then indirectly link VE-cadherin to the actin cytoskeleton via α-catenin. Additionally, TJ protein occludin is linked to AJs by ZO-1 and the actin cytoskeleton (Hellenthal *et al*., 2022).

Studies have suggested the importance of VE-cadherin in maintenance of endothelial integrity. Some of the first evidence used monoclonal antibodies to block VE-cadherin and showed enhanced accumulation of neutrophils (Gotsch *et al*., 1997) and increased vascular permeability in mice *in vivo* (Corada *et al*., 1999). As well as the role of AJs in vascular permeability changes, studies have also shown changes to protein assembly at AJs enable

leukocyte migration; Allport *et al* described a loss of cadherin-catenin complexes at areas where monocytes were migrating (Allport *et al*., 2000).

The importance of AJ and their associated protein VE-cadherin and their roles in modulation of vascular integrity and leukocyte transmigration are clear and disruption of VE-cadherin at AJs is characteristic of various pathologies, such as IRI.

1.3.3. IRI mediated alterations to endothelial junctions and vascular integrity

It is well established that IRI is associated with increased vascular endothelial permeability and vascular leak, leading to pulmonary oedema formation which is characteristic of the pathology in lung transplantation. The earliest study demonstrating this dates back to 1974; Whalen *et al* showed a significant increase in oedema formation following hypoxia/reperfusion of the heart (Whalen *et al*., 1974). Whilst this early study proposed cell swelling as a mechanism causing endothelial hyper-permeability, more recent studies have focused on the changes to endothelial junctions and specifically; the proteins associated. During IRI, changes to intercellular junction proteins leads to a change in endothelial morphology; the actin cytoskeleton is altered and junctions between cells are destabilised, forming small intercellular pores (Ferrari and Andrade, 2015). As well as interruption of cell-cell adhesion interactions, cell-matrix adhesion interactions are disrupted and a detachment from the basal membrane follows. Enhanced permeability then contributes to oedema formation in tissues due to fluid infiltration and cellular infiltration results in increased inflammation, leading to organ function impairment (Rodrigues and Granger, 2010). There are various different ways in which junction proteins are altered during IRI.

1.3.3.1. Adherens and Tight junction protein phosphorylation

During IRI, induction of hypoxia inducible factor in response to hypoxia causes the transactivation of vascular endothelial growth factor (VEGF), which is suggested by various studies to mediate alterations to endothelial permeability and results in the activated endothelial phenotype typical of IRI (Murakami and Simons, 2009). As a result, countless studies have used VEGF treatment to explore the mechanisms behind IRI-mediated junction alterations.

VEGF has been demonstrated to increase vascular permeability via facilitation of junction protein phosphorylation in an Src family kinase dependent manner. This causes subsequent

internalisation and loss at the cell surface. Eliceiri *et al*. showed that mice deficient in Src were protected from VEGF induced increases in vascular permeability (Eliceiri *et al*., 1999). Additionally, blockade of VEGF, VEGFR-2 or Src pharmacologically stabilised endothelial barrier integrity, highlighting their key roles (Weis *et al*., 2004).

Phosphorylation of TJ proteins have been described in response to IRI. For example, Harhaj *et al* demonstrated occludin phosphorylation alongside VEGF-associated permeability increases (Harhaj *et al*., 2006). Specifically, it is suggested that occludin undergoes phosphorylation at Ser490, which leads to subsequent ubiquitination and loss at the cell junction. Muthusamy *et al* also suggested that this was a consequence downstream of VEGFR2 activation via phosphorylation at Tyr1175 (Muthusamy *et al*., 2014).

It is generally accepted that phosphorylation of VE-cadherin is of the greatest consequence in IRI. Wessel *et al*. showed that VEGF stimulation induced strong phosphorylation of Tyr685 in human umbilical vein endothelial cells (HUVECs) and that phosphorylation at this site alone had implications in vascular permeability (Wessel *et al*., 2014). Furthermore, other studies have suggested that Src kinase phosphorylates VE-cadherin exclusively at Tyr685 (Wallez *et al*., 2007). However this is disputed; phosphorylation at Tyr658 and Tyr731 in response to VEGF have been demonstrated (Monaghan-Benson and Burridge, 2009) and shown to disrupt catenin binding by VE-cadherin and disrupt barrier function as a result (Murakami and Simons, 2009, Potter *et al*., 2005). However, reliability of results due to discrepancies in antibody specificity have been raised. Instead, phosphorylation of Tyr731 is suggested to have more of a role in leukocyte extravasation (Wessel *et al*., 2014). Indeed HUVECs with Y658F or Y731F point-mutant VE-cadherin exhibit reduced leukocyte transmigration (Allingham *et al*., 2007). Wessel *et al*. also demonstrated that phosphorylation of Tyr685 was induced, whilst phosphorylation of Tyr731 was constitutive, showing high baseline levels that were only altered by leukocytes (Wessel *et al*., 2014). As well as VEGF/Src-mediated mechanisms, Tonks *et al* described the irreversible inactivation of tyrosine phosphatases (PTPs) during IRI via oxidation of a Cys residue in the active site due to ROS. This prevents reversal of VE-cadherin phosphorylation during IRI, contributing to hyper-permeability (Tonks, 2006).

1.3.3.2. Adherens and tight junction protein expression and localisation

Studies have also utilised *in vitro* and *in vivo* models of IRI to demonstrate changes to expression of junction proteins. Studies universally agree that IRI results in a decrease in

protein expression of TJ and AJ proteins; Wang *et al* showed that in an *in vitro* model of hypoxia/reoxygenation, monolayer permeability to fluorescein isothiocyanate (FITC)-dextran was significantly increased and protein expression of ZO-1 and VE-cadherin were significantly decreased in human cardiac microvascular endothelial cells (HCMECs) (Wang *et al*., 2022a). Other studies have corroborated VE-cadherin and ZO-1 protein downregulation *in vitro* and *in vivo*, alongside increases in permeability to Evan's blue (EB) and/or FITC-dextran (Wang *et al*., 2020a, Wang *et al*., 2021). Literature also describes reductions in protein expression of other molecules in response to IRI, such as claudin-5 (Koto *et al*., 2007, Wang *et al*., 2022a) and occludin (Wang *et al*., 2022a, Antonetti *et al*., 1998).

Other studies have assessed mRNA expression of junction proteins although these results are controversial. Pasten *et al* described an increase in VE-cadherin mRNA in response to kidney IRI in mice (Pasten *et al*., 2021), whilst Wang *et al* contradicted this, describing reduced mRNA expression of ZO-1, occludin, claudin-5 and VE-cadherin *in vitro* (Wang *et al*., 2020b).

As well as changes to mRNA and protein expression, there is a general consensus that IRI facilitates a reduction in junction proteins at the intercellular surface. For example, Ito *et al* described reduced immunofluorescence cell surface staining of VE-cadherin after modelling hepatic IRI *in vitro* and *in vivo* (Ito *et al*., 2018), whilst another study described loss of ZO-1 organisation in arteriolar vessels in a model of retinal IRI (Muthusamy *et al*., 2014). Wang *et al* went further and demonstrated a reduction in localisation of ZO-1, occludin, claudin-5 and VE-cadherin in brain microvascular endothelial cells following a hypoxia/oxygenation model, leading to increased EB and FITC-dextran permeation (Wang *et al*., 2020b).

1.4. Sphingosine-1-phosphate

Endothelial cell integrity is a very dynamic process with various modalities of regulation. One of the main modulators of vascular integrity is sphingosine-1-phosphate (S1P). Sphingosine-1-phosphate (S1P) is a sphingolipid mediator with implications in a vast array of regulatory mechanisms such as trafficking of lymphocytes, vascular tone and endothelial barrier integrity. The function exerted by S1P is largely dependent on interaction with G protein-coupled receptors sphingosine-1-phosphate receptor (S1PR)1-5 extracellularly, although it can also act intracellularly (Książek *et al*., 2015).

1.4.1. Regulation of sphingosine-1-phosphate

S1P is comprised of a polar head group with a sphingoid base backbone and its production is a very dynamic process. Sphingosine is produced via degradation of ceramide and then is phosphorylated by sphingosine kinase (SPHK) 1 or 2 to get S1P. Following synthesis, S1P can then undergo one of three pathways. Firstly, it can be recycled following de-phosphorylation by S1P phosphatases and contribute to ceramide synthesis. Secondly, it can be released into the extra-cellular environment from red blood cells, platelets and endothelial cells, with erythrocytes identified as the major source of S1P (64). Depending on their source, this process is facilitated differently. In endothelial cells, S1P transporter spinster homolog 2 (SPNS2) exports S1P, whilst in platelets, it is exported as a result of platelet activation and is granule-mediated. Meanwhile, export of S1P from red blood cells is not well described. Thirdly, S1P can be irreversibly degraded by S1P lyase (SPL) into ethanolamine phosphate and hexadecenal (Proia and Hla, 2015, Książek *et al*., 2015). SPL is instrumental in maintenance of low tissue levels of S1P and without it, the S1P gradient is disrupted (Schwab *et al*., 2005).

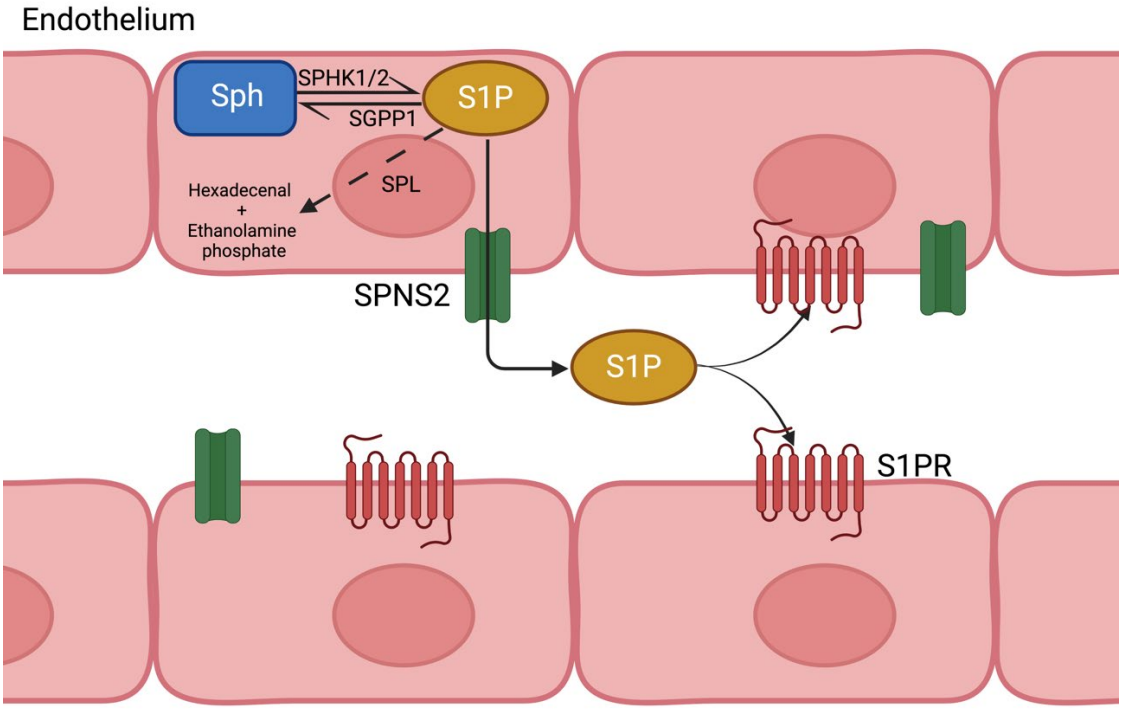

Figure 1.3. The S1P synthesis pathway in endothelium.

Sphingosine (Sph) is phosphorylated to sphingosine-1-phosphate (S1P) via sphingosine kinase (SPHK) 1/2. It can then be recycled back to Sph through de-phosphorylation by S1P phosphatase 1 (SGPP1), irreversibly catabolised by S1P lyase (SPL) or transported out of the cell by transporter spinster homolog 2 (SPNS2). Once in the extracellular environment, it can interact with S1P receptors (S1PRs). Image created using BioRender. Adapted from Spiegel *et al* (Spiegel *et al.*, 2019).

Tissue and circulatory distribution of S1P is a highly regulated process; S1P is maintained at a gradient with circulatory levels high in both blood and lymph at approximately 1 μM and 100 nM respectively, whilst tissue levels remain low (Proia and Hla, 2015). This is vital for the various homeostatic functions of S1P, such as the facilitation of lymphocyte egress from lymphoid organs (Obinata and Hla, 2019, Okazaki *et al*., 2007). Red blood cells and endothelial cells are the primary contributors of plasma S1P, with the latter being of the highest importance and providing around 75 % (Pappu *et al*., 2007).

In plasma, S1P is primarily bound to high-density lipoprotein (HDL) (65%) or albumin (35%). In HDL, S1P is bound to Apolipoprotein M (ApoM). ApoM is an important chaperone of S1P and helps deliver it to receptor S1PR1 (Ruiz *et al*., 2017). In fact, in ApoM deficient mice, vascular leak is increased, indicating reduced barrier enhancing S1PR1 signalling and this is rapidly reversed by supplementation with ApoM/S1P (Christensen *et al*., 2016). The chaperones allow the aqueous solubility of S1P and presentation to receptors (Proia and Hla, 2015)

1.4.2. Sphingosine-1-phosphate receptors

Extracellular S1P has the capacity to interact with a broad range of G-protein coupled receptors, which are termed S1PR1-5. The receptors comprise of seven helices which span the cell membrane, as well as an extracellular N-terminus and intracellular C terminus. S1P binding of the receptors results in receptor activation, followed by recruitment and activation of specific G-proteins (Bryan and Del Poeta, 2018).

The distinct signalling pathways downstream of each receptor, as well as their cellular and tissue distribution largely determines their roles in homeostasis and pathology. S1PR1-3 are ubiquitously expressed, whilst S1PR4 and 5 are found on specific cells (Blaho and Hla, 2014). S1PR1 has long been established as the most abundant S1PR on endothelial cells, whilst S1PR2 and S1PR3 expression is more modest (Ruiz *et al*., 2017, Liu *et al*., 2001). S1P is a potent ligand for S1PRs. Its binding affinity is highest for S1PR1, with an equilibrium dissociation constant (K_d) of 8.1 nM. The K_ds for S1PR2, S1PR3 and S1PR4 have also been described and are 27 nM, 23 nM and 63 nM respectively (Adada *et al*., 2013). Extracellular S1P signalling is also suggested to be influenced by plasma concentrations of S1P; physiologically relevant concentrations preferentially activate S1PR1, whilst high concentrations activate S1PR3 (Shikata *et al*., 2003).

1.4.2.1. S1PR1

S1PR1 was the first receptor to be functionally identified in 1998 by Lee *et al* (Lee *et al*., 1998). S1PR1 is ubiquitously expressed, with particularly high levels seen in blood vessels due to its expression on the endothelium (Regard *et al*., 2008). S1PR1 is essential for vascular maturation and disruption of the EDG1 that encodes it in mice is associated with embryonic lethality (Liu *et al*., 2000). As well as its roles in vascular development, neurogenesis, lymphocyte trafficking and the anti-inflammatory response, S1PR1 is vital for maintenance of vascular barrier integrity (Chun *et al*., 2010).

S1PR1 exclusively couples to G-protein $G_{\alpha i}$. In fact, abolishment of $G\alpha i$-mediated signalling with pertussis toxin treatment causes a 100 % inhibition of S1P mediated TER increases (Garcia *et al*., 2001). This causes activation of PI3K signalling and recruitment of protein kinase Akt, which is phosphorylated and activated. Akt activates small guanosine triphosphate (GTP)ase Rac. Downstream, Rac recruits cortactin, which causes actin polymerisation and cell spreading. Active Akt-1 also phosphorylates serine 1177 on eNOS, which increases NO production and causes inhibition of cellular contractility downstream. Garcia *et al*. also suggested p21-associated Ser/Thr kinase PAK-1 and LIM kinase activation downstream of Rac, which causes the inactivation of actin-severing cofolin (Garcia *et al*., 2001). Li *et al*. later added to this preliminary information, suggesting an important role for phosphoinositide phospholipase C (PIPC) in Akt recruitment to the cell membrane (Li *et al*., 2015). Activation of S1PR1 has also been suggested to cause activation of Phospholipase C (PLC) calcium mobilisation, which in turn contributes to eNOS activation. Inhibition of adenylate cyclase (AC) has also been described, which inhibits production of cyclic AMP (cAMP), decreasing cAMP-dependent protein kinase activity (Okamoto *et al*., 1998).

1.4.2.2. S1PR2 and 3

S1PR2 and 3 both couple to the same G-proteins; $G_{\alpha i}$, $G_{\alpha 12/13}$ and $G_{\alpha q}$ and thus activate similar signalling pathways, although elicit distinct functions.

The role of S1PR2 in regulation of vascular integrity is far less established than S1PR1 and S1PR3, although increased S1PR2 stimulation has been shown to cause stress fibre formation and increased expression is associated with increased dermal microvascular permeability and oedema (Sanchez *et al*., 2007, Du *et al*., 2012). There is also evidence that S1PR2 has important

metabolic functions in the liver and pancreas, with S1PR2 even linked to causing fibrosis in liver cirrhosis. Literature has also described the role of S1PR2 in muscle function, including muscle cell chemotaxis, proliferation, differentiation and contraction, largely attributed to its mediation of calcium influx into cells. This is controversial and depends on the tissue of origin (Adada *et al*., 2013). S1PR2 has also been described to inhibit cell migration; Kimura *et al* showed that S1PR2 inhibitor JTE013 significantly increased neural progenitor migration towards areas of infarction in the brain (Kimura *et al*., 2008), whilst other literature has shown that VSMC migration is inhibited by S1PR2 activation of small GTPase Rho (Takashima *et al*., 2008). S1PR2 has also been linked to diabetic neuropathy in the kidney (Liu *et al*., 2012). Because of its anti-migratory effects, S1PR2 has been reported to have anticancer effects although its positive regulation of cellular proliferation mean that this is controversial (Adada *et al*., 2013).

Various functions for S1PR3 have been described alongside its ability to increase endothelial cell permeability. S1PR3 has also been suggested to have pro-inflammatory functions. For example, it is vital for the induction of inflammatory genes such as IL-1β, IL-6 and TNF-α in macrophages in response to LPS; S1PR3 antagonist TY52156 was shown to suppress this (Heo and Im, 2019). It has also been shown to have roles in endothelial proliferation, migration and tube formation via VEGFR2 activation (Jin *et al*., 2018) and roles in migration of endothelial cells and mesenchymal stem cells (Vézina *et al*., 2018, Li *et al*., 2009). Pathologically, these features help S1PR3 promote cancerous cell migration, invasion and metastasis. Other research has demonstrated the roles of S1PR3 in tissue fibrosis in the lung, heart, muscle and liver, especially in pathologies. Its roles in vascular tone have also been described; similar to S1PR1, S1PR3 can cause vasodilation through activation of eNOS in endothelial cells, but has also been described to cause vasoconstriction in smooth muscle cells via activation of Ca^{2+} and Rho. It has been suggested its effects on vascular tone are determined by its expression in the vasculature and the function of the endothelial cells it is expressed on (Fan *et al*., 2021).

Following activation, S1PR2 and 3 both couple to $G_{\alpha i}$, $G_{\alpha 12/13}$ and $G_{\alpha q}$. Signalling through $G_{\alpha q}$ activates the PLC pathway, which leads to calcium mobilisation and activation of eNOS downstream, modulating vascular tone. It also promotes cell survival via calcium release and activation of protein kinase C (PKC). A downstream target of PKC is NFκB (Adada *et al*., 2013). Signalling through $G_{\alpha 12/13}$ leads to Rho activation. Activation of Rho causes Rho-kinase to inactivate MLC phosphatase. This leads to increased phosphorylation of MLC which leads to

contraction of actin-myosin. Simultaneously, Rho can directly inhibit Rac, limiting barrier enhancement (Li *et al*., 2015).

The roles, function, g-protein coupling and known receptor agonists and antagonists are summarised in Table 1.1. S1PR signalling pathways are summarised in Figure 1.4.

Receptor	G-proteins coupling	Location	Roles	Agonists	Antagonists
S1PR1 (EDG1)	$G_{\alpha i}$	Lymphocytes, neural cells, endothelial cells, atrial myocytes, smooth muscle cells	Lymphocyte egress from lymphoid tissue, migration and function of neural cells, formation and development of cardiovascular and nervous system, expression of anti-inflammatory genes, modulation of endothelial barrier integrity	FTY720, FTY720-P, AUY954, BAF312, SEW-2871, CS-2100, CYM5442, VPC01091, GSK1842799, RP001, Syl948, Amgen 8 (TC-G 1006), Amgen 14 (TC-SP14)	VPC23019, W146, VPC44116, NIBR0213, AD2900,
S1PR2 (EDG5)	$G_{\alpha i}$, $G_{\alpha 12/13}$, $G_{\alpha q}$	Central nervous system, endothelial cells, smooth muscle cells	Hearing and balance, modulation of vascular tone, modulation of endothelial barrier integrity	CYM5520, CYM5478, XAX-126	AB1, JTE-013, AD2900
S1PR3 (EDG3)	$G_{\alpha i}$, $G_{\alpha 12/13}$, $G_{\alpha q}$	Neural cells, endothelial cells, smooth muscle cells	Function and migration of neural cells, modulation of endothelial barrier integrity, vascular tone, inflammation, cell migration	FTY720, FTY720-P, CYM5541, ST-968, ST-1071	CAY10444, TY52156, PCI34051, SPM-354, VPC23019, AD2900, VPC01091
S1PR4 (EDG6)	$G_{\alpha i}$, $G_{\alpha 12/13}$	Lymphocytes	Modulation of dendritic and TH17 cells, vasoconstriction**,** **l**ymphoid tissue expression	FTY720, FTY720-P, ML178, ML248, CYM50260	CYM50358, CYM50374, AD2900
S1PR5 (EDG8)	$G_{\alpha i}$, $G_{\alpha 12/13}$	Central nervous system, oligodendrocytes, natural killer cells	Function of oligodendrocytes, migration of natural killer cells	FTY720, FTY720-P, A-971432	AD2900

Table 1.1. Sphingosine-1-phosphate receptor summary.

Table adapted from Comi *et al* and Fan *et al* (Comi *et al*., 2017, Fan *et al*., 2021).

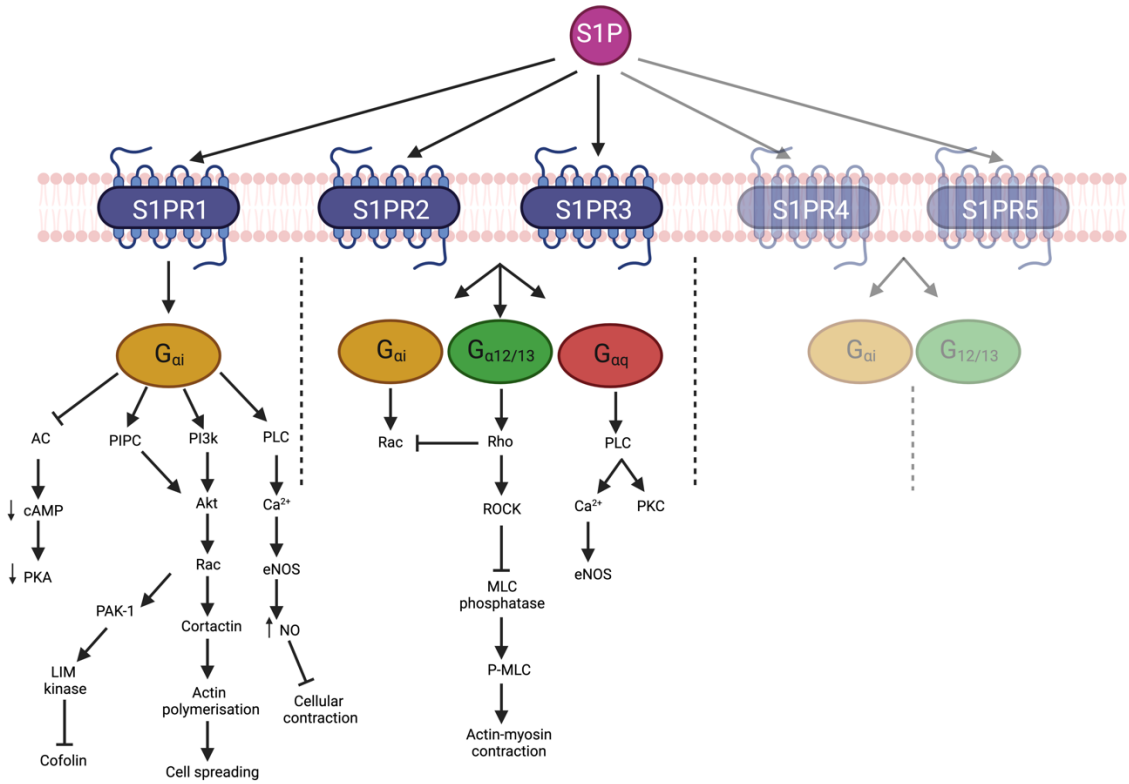

Figure 1.4. S1P receptor signalling which modulates endothelial permeability.

Sphingosine-1-phosphate receptor (S1PR)1, S1PR2 and S1PR3 have roles in modulating endothelial permeability. S1PR4 and S1PR5 do not contribute to endothelial permeability and so are not described. S1PR1 couples with $G_{\alpha}i$, causing phosphatidylinositol-3 kinase (PI3K) activation, recruitment of protein kinase B (Akt) and activation of Rac. Rac mediates cell spreading downstream and inhibition of cofolin, the active severing protein. phosphoinositide phospholipase C (PIPC) activation also contributes to Akt recruitment. Phospholipase C (PLC) is also activated, causing increased nitric oxide (NO) release and inhibition of cellular contraction downstream. Adenylate cyclase (AC) is inhibited, which reduces cyclic adenosine monophosphate (cAMP) and protein kinase A (PKA) activity. S1PR2 and S1PR3 couple to $G_{\alpha i}$, $G_{\alpha 12/13}$ and $G_{\alpha q}$. Downstream from $G_{\alpha 12/13}$, Rho is activated, which directly inhibits barrier enhancing Rac and also causes actin-myosin contraction downstream. Through $G_{\alpha q}$, PLC is also activated, leading to calcium mobilisation and endothelial nitric oxidase synthase (eNOS) activation, as well as activation of protein kinase C (PKC). Image created using BioRender.

1.4.3. Mechanisms behind S1P mediated regulation of the endothelial barrier

To date, various studies have supported the role of S1P in maintaining endothelial integrity at baseline and in response to injury. Garcia *et al* was the first the first to show barrier enhancing effects of S1P supplementation *in vitro*, paving the way for the studies to follow. The study showed dose-dependent increases in TEER across bovine and human pulmonary artery endothelial cells and lung microvascular endothelial cells, suggesting junction stabilisation and tightening. Maximal protection was achieved at a 1 μM concentration of S1P, with higher concentrations associated with barrier dysfunction. S1P also partly reversed thrombin induced endothelial dysfunction (Garcia *et al*., 2001). Accordingly, S1P loss in plasma has been shown to confer an increased vascular permeability at baseline and following inflammatory challenge (Camerer *et al*., 2009).

It has been demonstrated that S1P modulates barrier integrity via signalling through S1PRs to influence cytoskeletal rearrangement and alterations to endothelial junctions.

1.4.3.1. The roles of sphingosine-1-phosphate receptors

The importance of S1PR1 signalling in mediating endothelial barrier protection has been corroborated by various studies. S1PR1 gene deletion/suppression has not only been shown to confer an increase in baseline permeability (Burg *et al*., 2018) but also reduce S1P-mediated barrier enhancement (Garcia *et al*., 2001, Schaphorst *et al*., 2003, Tauseef *et al*., 2008) and confer a reduced capacity of the endothelium to limit permeability in disease models (Tauseef *et al*., 2008, Sammani *et al*., 2010, Burg *et al*., 2018). Furthermore, S1PR1 antagonism attenuated the barrier enhancing effects of S1P and S1PR1 agonist SEW-2871 in the lung (Sammani *et al*., 2010), conferred a higher vulnerability to immune complex mediated inflammation in the lung and the skin (Burg *et al*., 2018), potentiated histamine-induced vascular leak (Lee *et al*., 2009) and reversed S1P mediated (Zhang *et al*., 2010) stabilization of permeability. The fact that antagonists of S1PR2 or S1PR3 did not have any effect and SEW-2871 mediated similar effects on permeability as S1P suggests permeability increases are mediated solely by interaction with S1PR1 (Zhang *et al*., 2010).

The opposite is true for S1PR2 and 3; knock out of S1PR2 and silencing of S1PR3 in LPS-exposed mice significantly reduced protein accumulation in bronchoalveolar lavage (BAL) fluid

compared to wild type and non-silenced mice, confirming that S1PR2 and S1PR3 are necessary for barrier disruption (Sammani *et al*., 2010).

1.4.3.2. Changes to the endothelial cytoskeleton

The cell cytoskeleton consists of actin microfilaments, microtubules and intermediate filaments which control cellular shape and signal transduction between adjacent cells. Cytochalasin B and latrunculin B which disrupt actin polymerisation, have been shown to inhibit the barrier enhancing effects of S1P, suggesting a crucial role for actin assembly in maintaining vascular permeability (Garcia *et al*., 2001). Furthermore, the importance of cytoskeletal proteins cortactin and myosin light chain kinase (MLCK), which associate with actin, have also been described. In fact, translocation of cortactin and MLCK to cell peripheries in response to S1P has been demonstrated. At these sites, cortactin stimulates actin polymerisation and rearrangement, whilst MLCK phosphorylates myosin light chain (MLC) to enable actin-myosin interaction. Cortactin deletion has been shown to attenuate barrier enhancement (Dudek *et al*., 2004).

The role of other proteins, such as the small GTPases Rac and Rho have also been recognised in S1P-mediated cytoskeletal changes. Rho activated by S1PR2 and 3 leads to barrier disruption and promotes formation of stress fibres; activation of RhoA has been associated with cellular contraction and rounding in HUVECS (Vouret-Craviari *et al*., 2002). Furthermore, activation of Rho has been shown to cause F-actin disorganisation (Li *et al*., 2015). In contrast, Rac, which is activated by S1PR1 promotes adherens junction assembly and cytoskeletal rearrangement and inhibition of Rac leads to increased endothelial permeability (Wójciak-Stothard *et al*., 2001). Whilst GTPase activation is dependent on S1PR expression, it is also depends on S1P concentration; physiologically relevant concentrations of S1P facilitates Rac activation via S1PR1, whilst higher concentrations result in RhoA mediated signalling via S1PR2/3 (Shikata *et al*., 2003).

1.4.3.3. Changes to endothelial junctions

As well as regulating the cell cytoskeleton, S1P modifies stabilisation of intercellular TJs and AJs, primarily via modulation of junction proteins. S1P induces VE-cadherin and β-catenin enrichment at intercellular junctions, enhancing assembly of AJs (Lee *et al*., 1999). This was suggested to be dependent on S1PR1 signalling as S1PR1 interruption reduced expression of

VE-cadherin (Lee *et al*., 1999, Lee *et al*., 1998). Gaengel *et al* also showed that S1PR1 actually regulated VEGF-induced VEGFR2 signalling, as VEGF-induced VE-cadherin internalisation was attenuated by S1PR1 agonism (Gaengel *et al*., 2012). As well as affecting AJ protein localisation, loss of S1PR1 correlated with increased phosphorylation of tyrosine residues on VE-cadherin, which promoted junctional destabilization (Jung *et al*., 2012). Indeed, Scotti *et al* showed that S1P treatment reduced VE-cadherin phosphorylation (Scotti *et al*., 2016).

S1P has also been shown to modulate tight junctions; *in vitro* S1P stimulation resulted in enhanced barrier integrity via increased formation of tight junctions and specifically, increased translocation of TJ protein ZO-1 at junctional structures. Notably, barrier enhancement was attenuated by siRNA mediated downregulation of ZO-1 (Lee *et al*., 2006). Conversely, activation of Rho through S1PR2/3 has been shown to cause disassembly of ZO-1, leading to TJ destabilisation (Li *et al*., 2015).

1.5. Sphingosine-1-phosphate and pathology

1.5.1. Sphingosine-1-phosphate and ischaemia reperfusion injury

As previously mentioned, IRI is characterised by fluid and cellular infiltration into effected tissues, which arises due endothelial permeability. To date, various studies have assessed the therapeutic potential of S1P to protect against endothelial hyper-permeability during renal, cardiac, hepatic and neural IRI.

1.5.1.1. Heart

Following myocardial infarction, plasma levels of S1P are significantly reduced, which contributes to myocardial injury (Knapp *et al*., 2009). Accordingly, Morel *et al*. explored the potential benefits of modulating circulating S1P levels in a mouse model of myocardial infarction. *Apom-Tg* mice were generated to have increased levels of serum S1P and did so by approximately 296%. These mice had smaller infarct areas and reduced serum troponin compared to both *wild type (WT)* mice and *Apom* $^{-/-}$ mice with reduced serum S1P levels, indicating reduced cardiac injury and cardiomyocyte death. Neutrophil infiltration was also reduced. The group showed similar results *ex vivo;* exogenous S1P in perfusion buffer was

administered at the onset of EVP and the infarct area was reduced when compared to control groups (Morel *et al*., 2016).

It has also been demonstrated that SPL activity in the heart increases in response to ischaemia and contributes to damage by depleting pools of S1P. SPL knockout resulted in increased levels of S1P, which reduced infarct size and improved recovery following IR. Similar results were seen following inhibition of SPL with tetrahydroxybutylimidazole (THI) (Bandhuvula *et al*., 2011).

1.5.1.2. Liver

S1P supplementation prior to hepatic IRI in mice was shown to attenuate endothelial dysfunction and reduced leukocyte invasion indicated by reduced cluster of differentiation (CD)44 staining. Systemic inflammation and kidney injury were also attenuated (Lee *et al*., 2011).

Other studies have assessed the effects of FTY720 in the liver. FTY720 is an agonist for S1PR 1, 3, 4 and 5, although it has been suggested to preferentially activate S1PR1. S1PR1 antagonism partially reversed S1P or FTY720-mediated protection from murine hepatic IRI, demonstrating the importance of S1PR1 in hepatic protection (Lee *et al*., 2011). Furthermore, Ito *et al*. used S1PR1 agonist SEW-2871 during *in vitro* and *in vivo* models of hepatic IRI. Cell death was reduced *in vivo* and *in vitro*, agonist administration reduced inflammatory cell accumulation, pro-inflammatory profile and adhesion molecule expression (Ito *et al*., 2018).

Because of the clearly damaging effects of S1PR3 activation, research has explored the potential benefits of S1PR3 antagonism in the liver. In mice, S1PR3 antagonist CAY10444 attenuated hyperglycaemia-related liver IRI and reversed hyperglycaemia-modulated M1/M2 polarisation, reducing M1 macrophages in liver tissue (Hu *et al*., 2019). This suggests therapeutic mechanisms beyond just barrier repair.

1.5.1.3. Kidney

The role of S1PR1 in maintaining endothelial barrier integrity during kidney IRI has been elucidated. S1PR1 antagonism partially reversed S1P or FTY720-mediated protection from murine renal IRI (Awad *et al*., 2006). Similarly, S1PR1 deletion exacerbated murine kidney IRI, whilst overexpression suppressed endothelial activation and upregulation of adhesion

molecules (Perry *et al*., 2016). In particular, endothelial specific S1PR1 deletion or chronic S1PR1 blockade worsened renal and hepatic injury, neutrophil accumulation, inflammation and vascular permeability following ischaemic kidney injury.

Due to its roles in barrier disruption, studies have turned to S1PR2 blockade during IR to mitigate injury. In a model of renal IRI, S1PR2 antagonism dose dependently protected against injury as shown by reduced plasma creatinine, reduced tubular damage and reduced necrosis. SiRNA interference with S1PR2 and S1PR2 knockout showed similar findings. Accordingly, S1PR2 activation worsened renal injury, which was attenuated via blockade of Rho or Rho-associated protein kinase (ROCK). The study also went on to suggest that protection was in part mediated via mechanisms involving S1PR1 activation (Park *et al*., 2012).

1.5.1.4. Brain

S1PR3 has been shown to confer barrier disruptive effects in neural IRI. Unsurprisingly, inhibition of S1PR3 immediately after reperfusion with CAY10444 mitigated infarction, neurodegeneration and neurological deficit. Similar to the kidney, S1PR3 modulated the activation of microglia and M1 polarisation (Gaire *et al*., 2018).

Hasegawa *et al* administered FTY720 or S1PR1 agonist SEW-2871 immediately following transient middle cerebral artery occlusion and reperfusion. FTY720 significantly reduced infarct volume and improved neurological score compared to control, which was mirrored by SEW-2871. When agonists were administered in combination with an S1PR antagonist VPC23019, neuroprotection was abolished. FTY720 treatment also lead to maintenance of phospho-Akt and phospho-extracellular signal related kinase (ERK), suggestive of potential mechanisms for protection (Hasegawa *et al*., 2010).

1.5.2. Sphingosine-1-phosphate in lung pathology

The importance of S1P in mediating barrier protection from inflammatory lung diseases has been widely demonstrated. In mice, with reduced S1P levels due to SPHK1 knockout, lungs showed increased EB-albumin extravasation and increased lung wet-dry weight ratio in response to thrombin, indicating a predisposition to endothelial dysfunction (Tauseef *et al*., 2008). Therefore, various studies have assessed the effect of targeting the S1P axis during models of acute lung injury and specifically, IRI.

1.5.2.1. Acute lung injury

Acute lung injury (ALI) is characterised by acute inflammation which leads to endothelial and epithelial disruption. It can be caused by disorders such as pneumonia, pancreatitis, sepsis and IRI and its pathology has been modelled extensively (Johnson and Matthay, 2010). Furthermore, the therapeutic potential of S1P and its receptors has been investigated within the context of ALI.

Peng *et al* demonstrated that S1P and FTY720 significantly reduced permeability and pulmonary oedema following LPS exposure in the mouse (Peng *et al*., 2004), whilst McVerry *et al*. showed similar results in both a rodent model of pure ventilator-induced lung injury and canine-model of LPS-induced, ventilator associated ALI; S1P attenuated oedema and reduced oxygen impairment (McVerry *et al*., 2004). S1P and FTY720 have also both been shown to mediate barrier protection, reduce polymorphonuclear leukocyte (PMN) infiltration and reduce lung injury following induction of acute necrotizing pancreatitis (Liu *et al*., 2008). However, therapeutic effects in ALI have been shown to be concentration dependent; in a model of ventilator-induced lung injury in mice, low doses of FTY720 (0.1 mg/kg) reduced lung permeability, whilst treatment with 2 mg/kg increased permeability and caused apoptosis (Müller *et al*., 2011).

The importance of S1PR1 and its therapeutic potential is not something that has been widely explored in the lung. However, Sammani *et al*. evaluated the effects of increasing concentrations and administration routes of S1P and S1PR1 agonist SEW-2871 in a murine model of LPS-induced injury. In lungs not exposed to LPS, the intra-tracheal administration of 0.5 mg/kg S1P disrupted barrier function and administration of 2 mg/kg was lethal. Although SEW-2871 administration was not lethal, it too exhibited alveolar-capillary barrier disruption at higher concentrations. This disruption was not seen following intravenous administration and in fact, both S1P and SEW-2871 caused reductions in BAL protein accumulation, elucidating the benefits of directly targeting the endothelium via intravenous administration. In LPS challenged lungs, intra-tracheal administration of S1P (0.001-0.1 mg/kg) or SEW-2871 (0.1-0.3 mg/kg) reduced lung oedema and inflammation dose-dependently. Similarly, intravenous administration of S1P (0.3 mg/kg) or SEW-2871 (0.1-0.3 mg/kg) decreased BAL protein and histologic scores, indicating reduced leak and inflammation in a dose-dependent manner (Sammani *et al*., 2010). This study not only emphasises the therapeutic potential of

directly targeting S1PR1 during ALI, but also encourages consideration for the therapeutic administration route and concentration.

Sun *et al* investigated the role of S1PR3 during ALI. *In vitro*, in human lung vascular endothelial cells, exposure to barrier disrupting LPS and thrombin caused S1PR3 nitration and shedding of S1PR3 containing microparticles which reduced TEER. Increased permeability was attenuated by siRNA targeting S1PR3. This is suggestive that during inflammatory lung states, S1PR3 is shed into the circulation and contributes to lung injury. In fact, elevated levels of S1PR3 in the plasma of mice with ALI and humans with severe sepsis-induced ALI was associated with increased mortality (Sun *et al*., 2012). S1PR2 and S1PR3 are also increased in the inflamed mouse paw (Roviezzo *et al*., 2011).

1.5.2.2. Lung ischaemia reperfusion injury

Of particular interest is work exploring the therapeutic potential of S1P and related analogues in the context of LIRI and lung transplantation. In a rat model of transplantation, administration of S1P prior to reperfusion attenuated I/R injury; wet to dry mass ratios and EB extravasation were reduced. BALF neutrophil accumulation and inflammatory profile was also reduced, accompanied by fewer apoptotic endothelial cells (Okazaki *et al*., 2007). As previously mentioned, Stone *et al.* also demonstrated barrier enhancement in a murine model of lung ischaemia reperfusion injury by both FTY720 and a selective S1PR1 agonist and S1PR3 antagonist (VPC01091). Treatment groups exhibited improved lung function, decreased vascular leak, a reduced pro-inflammatory cytokine profile in BALF and attenuation of neutrophil accumulation in the lung. The VPC01091 pre-treated group showed similar results as the non-selective S1PR agonist pre-treated group and an S1PR1 antagonist reversed the protective effects of VPC01091. This emphasises that protection from LIRI is S1PR1-mediated (Stone *et al*., 2015). Although the literature on S1P and lung IRI is not extensive, these studies alone provide a good basis to hypothesise that modulation of the S1P axis could significantly attenuate the associated pathology.

1.6. *Ex vivo* lung perfusion

Ex vivo lung perfusion (EVLP) is a technique which was developed to allow objective assessment and potential reconditioning of ECD lungs that were deemed not immediately suitable for clinical use. The technique has the potential to improve donor lung utilisation and hence reduce waiting list mortality. EVLP allows the restoration of ventilation and circulation to allow assessment in physiologically relevant conditions, enabling visualisation of how the organ would function within a recipient (Pan *et al*., 2018). One of the first successful uses of EVLP in human lung transplantation was carried out by Steen *et al* in 2001. Following from success with animal work, the group used EVLP to assess lungs from a non-heart-beating donor and then transplanted the right lung into a 54-year-old woman who remained healthy for at least 5 months (Steen *et al*., 2001). The group later also carried out the first human transplantation of a non-acceptable donor lung after reconditioning using EVLP (Steen *et al*., 2007). This was some of the first evidence of the potential of EVLP in not only lung assessment, but also in restoring the suitability of ECD lungs.

These early studies and EVLP today were made possible due to development of an optimised perfusate solution. Steen solution is a buffered solution which contains human serum albumin to maintain a physiologically relevant colloid osmotic pressure (Levitt and Levitt, 2016) and Dextran 40 to reduce endothelial-leucocyte interactions (Termeer *et al*., 1998). This supports organ viability during EVLP and Steen has been shown to maintain stable lung function for up to twelve hours during normothermic EVLP (Cypel *et al*., 2008, Cypel *et al*., 2009). Steen solution was critical in providing the accessibility of EVLP to lung transplant programmes worldwide.

1.6.1. Clinical trials

To date, various clinical trials have taken place to assess whether transplantation after use of EVLP has any detrimental effect on transplant outcome. Although pre-clinical animal models have suggested that EVLP is superior to cold static storage (CSS) for the preservation of donor lungs, clinical trials haven't quite replicated these results. Cypel *et al* described improved lung oxygenation and less oedema formation following porcine lung transplantation (Cypel *et al*., 2009), whilst Wang *et al* showed similar findings during a rat EVLP model (Wang *et al*., 2022b). Although clinical trials using standard criteria organs did show a reduction in PGD incidence in the EVLP group compared to CSS, survival between groups was comparable. At the very least,

this demonstrated the non-inferiority of EVLP versus CSS prior to transplantation (Slama *et al*., 2017, Warnecke *et al*., 2018). Trials have since progressed to the inclusion of ECD organs and demonstrated the safety and feasibility of transplanting ECD lungs assessed using EVLP. The NOVEL, HELP and EVLP-MI clinical trials all showed comparable PGD3 incidence at 72 hours and survival between ECD lungs assessed with EVLP compared to standard cold storage lungs (Valenza *et al*., 2014, Cypel *et al*., 2011, Sanchez *et al*., 2022). However, another trial, the DEVELOP-UK study described higher intensive treatment unit (ITU) admittance and reduced oxygenation (Valenza *et al*., 2014), as well as longer ITU stays and higher rates of early PGD3 (Fisher *et al*., 2016) in EVLP groups.

Not only have clinical trials confirmed the safety of using ECD organs evaluated with EVLP for transplantation, but they have also illustrated the potential for improving donor lung allocation at transplant centres; Valenza *et al* showed an improvement in donor lung allocation by 20% (Valenza *et al*., 2014), whilst the EXPAND trial were able to transplant 87 % of ECD lungs included in the study, achieving good short term outcomes (Loor *et al*., 2019). Thus, EVLP has the potential to reduce discard of lungs which function well despite falling short of selection criteria.

1.6.2. Inflammatory cytokine accumulation during EVLP and development of optimal perfusate solutions for lung assessment

Despite the feasibility and efficacy of using EVLP to assess ECD organs and improve lung utilisation, it is well established that pro-inflammatory cytokines and chemokines accumulate over time of perfusion and can lead to lung injury over extended periods. For example, Andreasson *et al* reported the increase of IL-1β and TNF-α over time and even showed that levels were predictive of post-transplant survival, whilst another study similarly showed an increase in TNF-α and CXCL8 as little as 2 hours after the start of perfusion (Kakishita *et al*., 2010, Andreasson *et al*., 2017), despite both of these studies perfusing with Steen solution. Adrian *et al*. also described increased IL-6 and IL-10 during perfusion with afferent blood (Adrian *et al*., 2006). As a result, prolonged periods of EVLP eventually induce lung injury, with Erasmus *et al*. describing an increase in pulmonary artery and ventilation pressure after 6 hours EVLP (Erasmus *et al*., 2006).

Therefore, various studies have explored the potential benefits of formulating novel perfusate solutions which could limit injury during assessment. For example, Eren *et al* explored the

benefits of perfusate supplemented with polymeric human serum albumin compared with normal human serum albumin and described a reduction in oedema formation during EVLP (Eren *et al*., 2023). Another study assessed the effects of perfusing with modified Custodiol-N, which was formulated based on a pre-existing HTK solution, but with the addition of iron chelators LK614 and desferoxamine. This novel perfusate showed superiority compared to Steen solution, resulting in improvements in oxygenation capacity, which remained stable over 4 hours of perfusion (Olbertz *et al*., 2020).

Development of a novel perfusate solution which limited inflammation and lung injury over long periods of perfusion could revolutionise perfusion technology, allowing assessment over many hours or even days, as well as advanced therapeutic strategies for reconditioning of marginal organs.

1.6.3. *Ex vivo* lung perfusion as a therapeutic platform to target ischaemia reperfusion injury

As well as development of perfusate solutions to maintain stable lung function during extended assessment, studies have also explored therapeutic administration during EVLP to recondition organs prior to transplantation. Use of an *ex vivo* platform allows organ modulation away from potential off target systemic effects in the donor/recipient and could be used to reduce IRI. The magnitude of studies utilising EVLP as a therapeutic platform has increased exponentially in the last few years (Griffiths *et al*., 2020). These have ranged from repurposing clinically available pharmaceuticals, to targeting the innate immune system and oxidative stress which drives the pathologic processes characteristic of IRI.

Immunosuppressant drugs are widely used to treat autoimmune and inflammatory conditions. Accordingly, studies have demonstrated the therapeutic potential of steroid administration during EVLP through improved lung function as a result of reduced tissue inflammation and oedema during EVLP (Martens *et al*., 2016). Similarly, use of immunosuppressant Cyclosporin A was protective via mediation of mitochondrial protection and DAMP suppression (Haam *et al*., 2020). Other studies have repurposed drugs used to treat other conditions, such as angina (Cosgun *et al*., 2017) and emphysema (Lin *et al*., 2018).

Other researchers have specifically focused on targeting the innate immune system to reduce the sterile inflammation that is so prominent during IRI. As previously discussed, the transcription factor NFκB is activated very early on in IRI and facilitates the expression of pro-

inflammatory cytokines (den Hengst *et al*., 2010). Thus, studies have explored the effects of suppressing NFκB signalling during EVLP and demonstrated reduced pro-inflammatory cytokine gene transcription and release, which ultimately improved lung function and vascular permeability during EVLP (Francioli *et al*., 2017, Weathington *et al*., 2018). Studies have also explored gene therapies to increase anti-inflammatory IL-10 (Machuca *et al*., 2017) and further downstream, phagocyte depletion has also yielded promising therapeutic results (Yamanashi *et al*., 2022).

Whilst addition of therapeutics into the perfusate is an obvious choice during EVLP, other studies have assessed the effects of inhaled therapeutics during perfusion. For example, administration of a nebulised antioxidant precursor significantly reduced neutrophil activation in BAL post-EVLP and reduced NFκB p50 in tissue following transplantation (Yamada *et al*., 2017). Haam *et al* demonstrated the therapeutic potential of inhaled hydrogen gas, which translated to increased compliance and lowered peak airway pressure during EVLP and post-transplant, with increased tissue expression of antioxidant and anti-inflammatory genes (Haam *et al*., 2018). The barrier enhancing effects of bronchodilator β_2-adrenergic agonist inhalation during EVLP has also been shown (Hijiya *et al*., 2017). Whilst the above therapeutics were all tested in animal models, Hartwig *et al* showed the protective effect of inhaled and dissolved NO in a human randomised multicentre blinded pilot study. Ultimately, treatment allowed longer EVLP times due to improving the health of the perfused lung (Hartwig *et al*., 2022).

Research has also turned to use of cellular therapy during EVLP. Mesenchymal stromal cells (MSCs) and multipotent adult progenitor cells (MAPCs) are bone marrow derived and have known anti-inflammatory and immunomodulatory properties via release of paracrine factors (Martens *et al*., 2017). Thus they are an excellent candidate for application to EVLP. In line with this, both MAPCs and MSCs have been shown to reduce neutrophils and pro-inflammatory cytokines in BAL fluid (Martens *et al*., 2017) and reduce tissue expression of IL-18 and interferon (IFN)-γ and increase anti-inflammatory IL-4 (Nakajima *et al*., 2019) respectively. Stone *et al* suggested that the therapeutic paracrine effects of MSCs are predominantly due to extracellular vesicle (EV) release (Stone *et al*., 2017). As such, Lonati *et al* described beneficial effects on the endothelium as a result of MSC-derived EV delivery during EVLP. The study suggested protection was mediated via modulation of hyaluronan and increased delivery to lung tissue (Lonati *et al*., 2019).

Specific targeting of the oxidative stress that occurs during IRI has also proven to be effective during EVLP. Studies have shown the protective effects of inhibition of c-abl (Magruder *et al*., 2018), direct intracellular ROS removal (Ehrsam *et al*., 2022) and direct administration of antioxidant enzymes (Kim *et al*., 2021) during EVLP and shown reduced IRI progression as a result. Meanwhile, the work of Arni *et al* has focused on processes further upstream by suppressing KATP channel closure, which is the initial trigger of ROS generation following loss of shear stress in the lung. Mitochondrial KATP channel opener diazoxide lowered PVR and increased weight loss, presumably via prevention of mitochondrial membrane depolarisation and ROS generation (Arni *et al*., 2021).

Table 1.2 summarises the studies assessing the effects of administering therapeutics during EVLP in the last 6 years. The potential to improve lung quality prior to transplantation is abundantly clear.

Therapy type	Therapeutic name	Mode of action	Model type	Results
Re-purposed	Methylprednisolone	Anti-inflammatory steroid	Porcine DCD EVLP	↑ compliance and ↓ wet-to-dry ratio, CT density, perfusate pro-inflammatory cytokines (Martens *et al*., 2016)
	Cyclosporin A	Calcineurin inhibitor	Rat EVLP transplant model	↑ P/F ratio, lung compliance, mitochondrial quality and ↓ PVR, perfusate pH and lactate, pro-inflammatory cytokine mRNA and DAMP release (EVLP). ↑ P/F ratio and ↓ cellular and oedema influx and pro-inflammatory cytokine mRNA expression post-transplant (transplant) (Haam *et al*., 2020)
	TMZ	Inhibits free fatty acid β-oxidation, increasing ATP	Porcine EVLP transplant model	↓ lipid peroxidation and neutrophil activation,↑ oxygenation (EVLP and transplantation) (Cosgun *et al*., 2017)
	A1AT	Anti-inflammatory properties	Porcine EVLP (long CIT)	↓ PAP, PVR, airway pressure, oedema formation, apoptosis and iL-1α and CXCL8 levels in perfusate and ↑ compliance (Lin *et al*., 2018)
Targeting innate immunity	PDTC	Inhibition of NFκB	Rat EVLP (long WIT)	↓ oedema, BAL protein accumulation, PVR and pro-inflammatory cytokines in BALF and ↑ compliance (Francioli *et al*., 2017)
	BC1215 small molecule	Suppresses NFκB signalling via blockade of FBXO3	Human EVLP (ARDS model)	↑ oxygenation and ↓ pro-inflammatory cytokines protein in BALF and gene transcription in tissue (Weathington *et al*., 2018)
	Clodronate liposome	Depletion of mononuclear phagocytes	Rat EVLP	↓ cells in lung tissue and PVR (EVLP) and oedema (transplant) and ↑compliance (EVLP) and oxygenation (transplant) (Yamanashi *et al*., 2022)
	Synthetic derivative of melanocortin	Melanocortin system modulation	Rat EVLP (marginal lungs)	↓ ATP depletion, pro-inflammatory cytokine release, leukocytes and perfusate lactate and ↑compliance (Lonati *et al*., 2021)
Gases	Nebulised NAC	Precursor of glutathione (free radical scavenger)	Porcine EVLP transplant model	↑ glutathione in RBCs; ↓ BAL neutrophil activation (EVLP) and NFκB p50 in tissue (transplant) (Yamada *et al*., 2017)
	Hydrogen gas	Anti-oxidative and anti-inflammatory properties	Porcine DCD EVLP transplant model	↓ peak airway pressure (EVLP and transplant) and lung injury, apoptosis, oedema and tissue IL-6 (transplant). ↑ compliance (EVLP) and tissue expression of SOD1, HO-1 and IL-10, (transplant) (Haam *et al*., 2018)
	Nitric oxide (dissolved in perfusate or inhaled)	Vasodilatory, anti-inflammatory, anti-apoptotic	Randomised multicentre blinded pilot study	Allowed longer EVLP times, ↑ $LAPO_2$ and ↓ oedema (Hartwig *et al*., 2022)
	β_2-adrenergic agonist	Bronchodilator, increases cAMP in tissue = barrier enhancement	Canine DCD EVLP transplant model	↑ oxygenation, compliance and ↓ PVR and tissue ATP depletion (transplantation) (Hijiya *et al*., 2017)

Cell therapy	MAPCs	Anti-inflammatory paracrine action	Porcine EVLP	↓ neutrophils and pro-inflammatory cytokines in BALF(Martens *et al*., 2017)
	MSCs	Hepatocyte growth factor related mechanisms	Porcine EVLP transplant model (long CIT)	↓ IL-18 and IFN-γ tissue expression (EVLP) and oedema and apoptosis (transplant) and ↑ IL-4 tissue expression (EVLP) (Nakajima *et al*., 2019)
	MSCs MSC EVs	EV paracrine secretions or internalisation	Murine DCD EVLP	↑ compliance and ↓ PAP, neutrophil infiltration lung injury and oedema. Comparable as above (Stone *et al*., 2017)
	MSC EVs	Modulation of hyaluronan and increased delivery to lung tissue	Rat EVLP	↓ PVR and ↑ perfusate NO metabolites, ATP levels and anti-inflammatory and antioxidant genes (Lonati *et al*., 2019)
Targeting oxidative stress	Imatinib	Reduces ROS via inhibition of c-abl	Rabbit EVLP (long CIT)	↓ double strand breaks, mitochondrial ROS, PAP, airway pressures, oedema and neutrophil influx in BAL and ↑ oxygenation and ventilation (Magruder *et al*., 2018)
	NAD+	Removal of ROS within the cell	Rat EVLP	↓ PAP, tissue MPO, perfusate IL-12 and IL-18 and IL-1α and IL-1β in BAL and ↑ oxygenation and perfusate IL-10 (Ehrsam *et al*., 2022)
	Pegylated catalase	Antioxidant enzyme	Rat EVLP	↓ lactate dehydrogenase, hyaluronic acid and endothelin-1 in tissue and apoptosis (Kim *et al*., 2021)
	Diazoxide	Mitochondrial KATP channel opener	Rat DCD EVLP	↓Reduced PVR and weight gain (Arni *et al*., 2021)
Gene therapy	Adenoviral human IL-10	Increased expression of anti-inflammatory IL-10	Porcine EVLP transplant model	↑ gas exchange and ↓ histologic inflammation score, systemic pro-inflammatory cytokines and lymphocytes capacity to produce IFN-γ (transplant) (Machuca *et al*., 2017)
Other	Recombinant human MG53 protein	Senses redox changes, initiates cell membrane repair	Porcine EVLP	↓ porcine lung injury by preservation of lung architecture, perfusate IL-6 and oedema (Whitson *et al*., 2021)
	HSP90i	Inhibits heat shock protein 90	Porcine DCD EVLP	↓ lung weight gain, oedema, perfusate lactate, PVR and PAP and ↑ dynamic compliance (Nasir *et al*., 2020)
	Fusion protein construct targeting OGG1	Enhances mitochondrial DNA repair	Rat DCD EVLP	↑ fraction of mitochondrial DNA and ↓ vascular filtration coefficients, wet/dry ratio and reduced mitochondrial DNA DAMPs in perfusate (Tan *et al*., 2020)

Table 1.2. Summary of therapeutic applications to EVLP in the last 6 years.

Abbreviations: Trimetazidine (TMZ), α_1-Anti-trypsin (A1AT), Pyrrolidine dithiocarbamate (PDTC), N-acetylcysteine (NAC), Multipotent adult progenitor cell (MAPC), Mesenchymal stromal cell (MSC), Extracellular vesicle (EV), Nicotinamide Adenine Dinucleotide (NAD+), Heat shock protein 90 inhibitor (HSP90i), 8-oxoguanine DNA glycosylase (OGG1), F-box only protein 3 (FBXO3), Acute respiratory distress syndrome (ARDS), Cyclic adenosine monophosphate (cAMP), Cold ischaemic time (CIT), Warm ischaemic time (WIT), Computerised tomography (CT), Arterial partial pressure of oxygen divided by the inspired oxygen concentration (P/F), Pulmonary vascular resistance (PVR), Pulmonary artery pressure (PAP), Bronchoalveolar lavage fluid (BALF), Red blood cell (RBC), superoxide dismutase (SOD)-1, Heme oxygenase (HO)-1, Left atrial oxygen partial pressure ($LAPO_2$), Myeloperoxidase (MPO).

1.6.4. Sphingosine-1-phosphate and *ex vivo* lung perfusion

Many studies have assessed endothelial integrity as an outcome of their administered treatment during EVLP, for example wet/dry ratio, lung weight gain or protein concentration in BALF. However, to date, only one study has directly targeted IRI-mediated endothelial permeability via modulation of the S1P axis during EVLP. Mehaffey *et al* assessed the effect of directly targeting endothelial integrity via SPHK2 inhibition during murine EVLP. As well as its role in S1P production, SPHK2 is postulated to have a role in clearing S1P from the circulation. The study used a murine model of DCD and showed that during EVLP, circulating S1P was increased via supplementation with S1P and an SPHK2 inhibitor in combination. This resulted in increased lung compliance and reduced vascular permeability to EB dye compared to Steen™ solution alone and Steen™ supplemented with only S1P (Mehaffey *et al*., 2018).

Directly targeting endothelial permeability during EVLP via manipulation of S1P signalling could have therapeutic potential. Use of an *ex vivo* platform for S1P treatment could reduce potential off target effects that S1P could exhibit systemically as a result of ubiquitous S1PR expression. This study is evidence that targeting S1P signalling during EVLP could reduce IRI prior to transplantation; the next steps would be to progress to application of S1P and associated analogues to the human EVLP.

1.7. Hypothesis

The hypothesis of this study is that targeting inflammatory processes during EVLP could improve lung assessment and recondition marginal organs; 1) novel perfusate solution 'modified Steen' will perform better than clinically used Steen solution during lung assessment, and 2) therapeutic targeting of S1PR1 signalling via CYM5442 during EVLP of human donor lungs declined for transplant will reduce endothelial permeability, thereby improving potential graft function.

1.8. Aims and objectives

Steen solution has been in clinical use for lung assessment for almost 20 years since its development in 2001. There has since been limited work to develop novel perfusate solutions which would allow more stable and longer term organ assessment.

Studies have verified the role of S1PR1 in facilitating endothelial barrier protection during injury models, including lung IRI. However, only one study has investigated the effects of modulating the S1P axis during murine EVLP and this has not yet been studied in human EVLP.

The overriding aim of this project was to validate a novel perfusate for lung assessment and also to investigate the therapeutic potential of modulating endothelial S1PR signalling using a human *ex vivo* platform.

Three specific aims were established for this project; these form the focus of each of the results chapters:

- Carry out transcriptomic and subsequent pathway analysis on post-EVLP tissue samples to validate novel perfusate solution "modified Steen", as well as to identify pathways associated with IRI which could be targeted for therapeutic intervention
- Establish an *in vitro* model of lung IRI in primary endothelial cells as a context for therapeutic testing
- Measure the effects of S1PR1 agonist on endothelial permeability both *in vitro* and *ex vivo* during IRI.

2. Materials and Methods

2.1. Cell culture

Safety procedures were performed according to Newcastle University's Safety Policy and relevant COSHH and BIOCOSHH forms were read and signed prior to use of any chemical or biological reagents. All cell culture work was performed inside a Class II microbiological safety cabinet with aseptic technique. All cells were grown in a humidified atmosphere at 37 °C and 5% CO_2 in polystyrene 75 cm^3 tissue culture flasks (Greiner, Austria) until reaching at least 80% confluence.

2.1.1. Cell types

2.1.1.1. Human Microvascular Endothelial Cells

Immortalised human dermal microvascular endothelial cells (HMEC-1; ATCC® CRL-3243™) are endothelial cells isolated from human foreskins and transfected with a PBR-322-based plasmid encoding SV40 large Tumour antigen. As a cell-line, HMEC-1 cells can be maintained to a higher passage than primary cells and so were used for initial optimisation experiments prior to progression to primary endothelial cells. HMEC-1 were cultured in complete MCDB 131 medium (Gibco) containing 10% foetal bovine serum (FBS, Labtech), 2 mM L-glutamine (Sigma), 100 units Penicillin/0.1 mg streptomycin/mL (Sigma Aldrich), 10 ng/mL Epidermal Growth Factor (EGF; ThermoFisher) and 1 μg/mL Hydrocortisone (Sigma Aldrich).

2.1.1.2. Human Pulmonary Microvascular Endothelial Cells

Human pulmonary microvascular endothelial cells (HPMEC; Promocell) are primary endothelial cells isolated from the lung of a single human donor. HPMEC were cultured in Endothelial Growth Medium MV2 (Promocell) with one vial of supplement mix added. Complete media contained 5% foetal calf serum (FCS), 5 ng/mL epidermal growth factor (recombinant human), 10 ng/mL basic fibroblast growth factor (recombinant human), 20 ng/mL insulin-like growth factor (long R3 IGF), 0.5 ng/mL vascular endothelial growth factor 165 (recombinant human), 1 μg/mL ascorbic acid and 0.2 μg/mL hydrocortisone.

2.1.1.3. Porcine Pulmonary Microvascular Endothelial Cells

Porcine pulmonary microvascular endothelial cells (PPMEC; Cell Biologics) are primary endothelial cells isolated from porcine lung tissue without large blood vessels. PPMEC were cultured in Complete Endothelial Cell Medium (CellBiologics) with supplement kit added. Complete media contained 2 % FBS, 0.01 mL/mL Antibiotic-Antimycotic, 1 μL/mL VEGF, 1 μL/mL EGF and 2 mM L-glutamine.

2.1.2. Cryopreservation

Cell lines were resuspended in 1 mL freeze mix, which was comprised of 1 part FBS and 1 part cell suspension in media with a final concentration of 10 % Dimethyl Sulfoxide (DMSO) (Sigma Aldrich) in cryovials. Primary cells were resuspended in 0.5 mL Cryo-SFM (Promocell) in cryovials. Cryovials were then placed into a CoolCell™ LX cell freezing container (Corning) at -80 °C to cool at a rate of -1 °C /min. Cells were then stored long term in liquid nitrogen.

When required, cells were resurrected by thawing in a water bath at 37 °C for two minutes before addition to 10 mL of pre-warmed media in a T75 tissue culture flask. Cells were incubated for 24 hours before replacing with fresh media.

2.1.3. Cell maintenance and subculture

In between subculture, media on primary cells was aspirated and replaced with warmed fresh media every 2 days. For cell lines, media was not generally replenished between subculture.

Once cells were at least 80% confluent, media was aspirated from the flask and discarded. Flasks were then washed with 5 mL 1X sterile phosphate-buffered saline (PBS; pH 7.4; Sigma). This was discarded and replaced by 5 mL pre-warmed 1X trypsin-ethylenediaminetetraacetic acid (EDTA; Sigma) for cell lines or 5 mL room temperature Accutase® (BioLegend) for primary cells and flasks were incubated at 37 °C for 3-5 minutes. Cells were then fully detached by gentle tapping. The cell suspension was removed and added to a falcon tube, with an equal amount of pre-warmed media for trypsin neutralisation. HMEC-1 were spun at 300 g for 5 minutes, whilst HPMEC and PPMEC were spun at 220 g for 3 minutes and 120 g for 5 minutes respectively, before pouring off the supernatant and re-suspending the cell pellet in 1-2 mL of pre-warmed media.

2.1.4. Cell counting

If a particular seeding density was required for setting up an experiment, cells were counted using a haemocytometer. Following resuspension in 1-2 mL media, 10 μL of the cell suspension was combined with 10 μL trypan blue (Sigma Aldrich) and added to a chamber of a Neubauer haemocytometer. Trypan blue is a charged dye that does not enter cells unless the membrane is compromised. Viable cells were counted in each of the four squares and then cells per mL was calculated using the below calculation:

$$\left(\left(\frac{\sum Viable\ cells\ in\ 4\ squares}{4}\right)\times 2\right)\times 10^4$$

2.1.5. Cell treatment

Unless otherwise stated, HMEC-1 were treated in 1 % FBS containing media and primary cells HPMEC and PPMEC in serum free media. Serum starvation is described if used prior to treatment.

2.1.6. Viability

2.1.6.1. Trypan blue exclusion

Viability was assessed by taking a 10 μL sample of the cell suspension and combining it with 10 μL trypan blue dye (Thermofisher). 10 μL of the sample was pipetted onto a chamber of a haemocytometer and percentage viability was assessed as below.

$$\Sigma Live\ cells\ per\ mL\ = \left(\left(\frac{\sum Non-blue\ cells\ in\ 4\ squares}{4}\right)\times 2\right)\times 10^4$$

$$\Sigma Dead\ cells\ per\ mL\ = \left(\left(\frac{\sum Blue\ cells\ in\ 4\ squares}{4}\right)\times 2\right)\times 10^4$$

$$\%\boldsymbol{VIABILITY} = \left(\frac{(\sum \boldsymbol{Live\ cells})}{(\sum \boldsymbol{Live\ cells} + \sum \boldsymbol{Dead\ cells})}\right)\times \mathbf{100}$$

2.1.6.2. XTT Cell Proliferation Assay

An 2,3-Bis-(2-Methoxy-4-Nitro-5-Sulfophenyl)-2H (XTT) cell proliferation assay (Roche) was used to assess cell viability in response to various treatments throughout this study. The XTT assay uses a tetrazolium-based compound which converts from a water-soluble compound to an orange coloured formazan product in the presence of actively respiring cells. The colorimetric output can then be quantified using a plate reader and be used to assess the viability in comparison to a control group.

In order to perform an XTT assay for one 96-well microplate, 5 mL XTT labelling reagent was combined with 0.1 mL electron coupling reagent to form the XTT labelling mixture immediately prior to use.

Appropriate cell numbers were seeded onto 96-well plates and allowed to adhere overnight. The next day, cells were treated as desired and then wells were washed with 200 µL PBS before addition of 200 µL treatments in media. Corresponding media alone was added to untreated control wells. Following treatment for the desired time period, treatment was removed and wells washed again with PBS. Then this was replaced with 100 µL 1% FBS containing media for HMEC-1 or serum free media for primary cells with 50 µL XTT labelling mixture. Absorbance readings were measured 24 hours later at 450 nm and 650 nm using a spectrophotometer (Biotek Synergy™). 650 nm values were subtracted from 450 nm values before presenting data as percentage viability relative to untreated.

2.2. Assessment of cell monolayer permeability

2.2.1. Trans-endothelial electrical resistance

Primary endothelial cells were grown on 24-well 0.4 μm translucent transwells (Sarstedt) until confluent. Cells were then treated as desired, before measuring trans-endothelial electrical resistance (TEER) at sequential time points. A transwell with no cells was included as an empty control. Resistance was measured using MILLICELL® ERS probes (Millipore) as shown in Figure 2.1. TEER was calculated by subtracting blank transwell readings and then multiplying this by the transwell surface area.

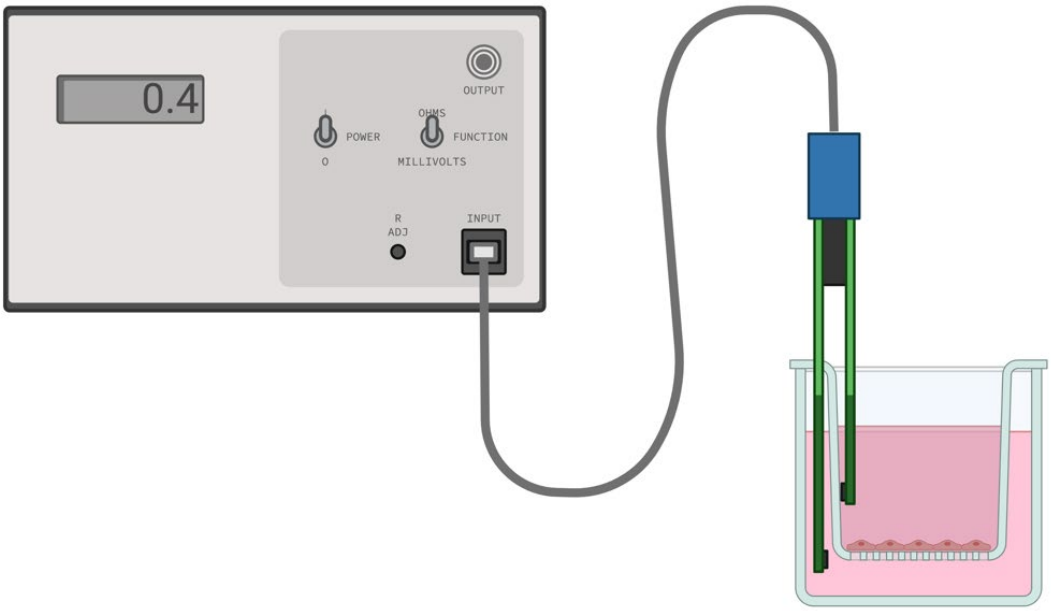

Figure 2.1. Measurement of trans-endothelial electrical resistance.

Trans-endothelial electrical resistance (TEER) of HPMEC and PPMEC monolayers was measured in response to treatment within this study using MILLICELL® ERS probes. Image created using BioRender.

2.2.2. FITC-dextran permeability assays

Cell were grown on transwells until confluent as in 2.2.1. Monolayers were then pre-treated as desired, before removing treatment and replacing with 200 µL fluorescein isothiocyanate (FITC)-dextran (Sigma, mol WT 70000) at 0.5 mg/mL into the top of the transwell, with 600 µL phenol red and serum free media below. Then 50 µL samples were taken from the bottom of each well at 5, 15, 30, 45 and 60 minutes and added to a black clear bottom 96-well plate (Corning) in duplicates. Media alone was used for blanks. Fluorescence was then measured using a TECAN Spark® plate reader (TECAN; Excitation (Ex): 490 nm, Emission (Em): 520 nm) and blanks subtracted from each value. Workflow is described in Figure 2.2.

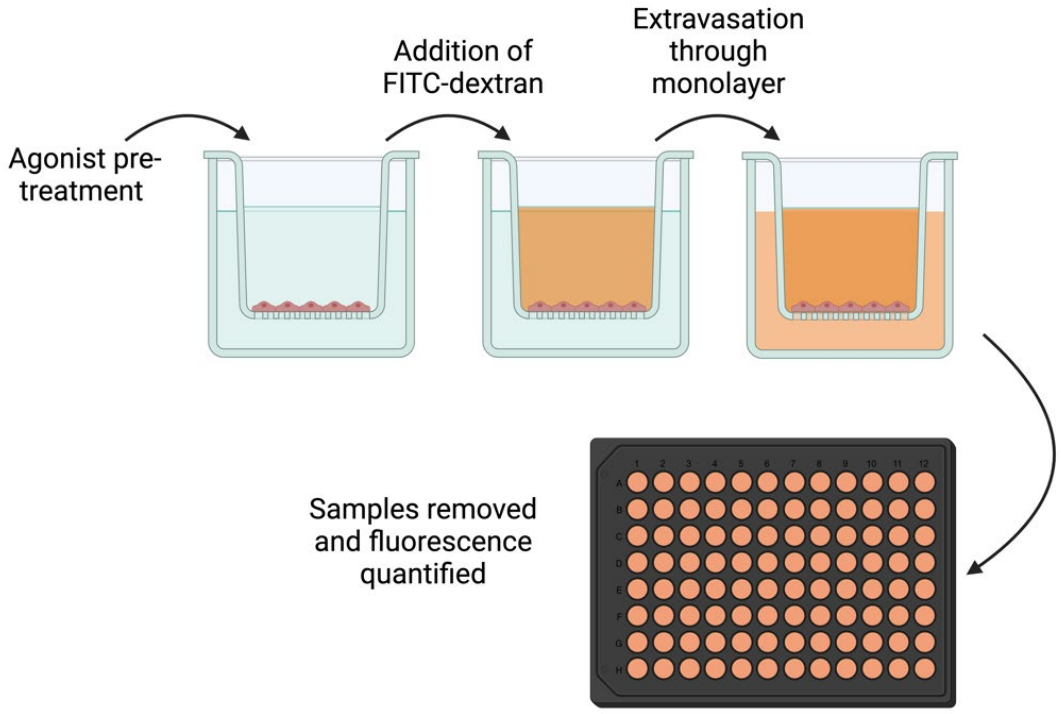

Figure 2.2. FITC-dextran permeability assay workflow.

Confluent endothelial cell monolayers on 0.4 µm transwells were pre-treated as desired in phenol red and serum free media. Then treatment was removed and replaced with 200 µL 0.5 mg/mL fluorescein isothiocyanate (FITC)-dextran in the top of the transwell, with 600 µL fresh media in the bottom. FITC- dextran was allowed to extravasate through the endothelial monolayers, with 50 µL samples removed from below the transwell at sequential time points. Fluorescence was quantified using a plate reader. Image created using BioRender.

2.3. Reconstitution of ligands

2.3.1. CYM5442 hydrochloride

CYM5442 hydrochloride (Tocris) is soluble in water up to a concentration of 10 mM. As a solid, it can be stored for up to 6 months at -20 °C, but once in solution, can only be stored for up to 1 month. 0.5 mg of CYM5442 was reconstituted in 110 µL H_2O to a final concentration of 10 mM, before storing in 10 µL aliquots at -20 °C for up to 1 month. After 1 month, fresh aliquots were made up. Aliquots were diluted in serum free media to the desired concentration immediately prior to cell treatment.

2.3.2. FTY720 Phosphate

FTY720 Phosphate (FTY720P; Cayman chemical) is soluble in chloroform up to a concentration of 0.5 mg/mL and stable for up to 2 years when stored at -20 °C in a sealed glass vial. Chloroform was purged of dissolved gas using a sonicator for 15 minutes, before reconstitution of FTY720P via injection with the purged chloroform in an anaerobic chamber. This was stored at -20 °C. When needed, solution was removed using a needle and syringe; the cap was never removed from the glass vial so as to prevent gas dissolving. This was diluted in serum free media to the desired concentration immediately prior to cell treatment.

2.3.3. SIN-1 chloride

SIN-1 chloride (Tocris) is soluble in H_2O up to a concentration of 100 mM. As a solid, it can be stored for up to 6 months at 4 °C. However, due to the mechanism of action in which SIN-1 generates free radicals, it was only reconstituted immediately prior to use and used on the same day. 1 mg SIN-1 chloride was reconstituted in 50 µL H_2O and diluted in serum free media to the desired concentration immediately prior to cell treatment.

2.4. Gene expression analysis

2.4.1. RNA extraction

For both cells and tissues, mRNA was extracted using the RNeasy Mini Kit (QIAGEN)

2.4.1.1. RNA extraction from cells

Prior to RNA extraction, 10 μL of β-mercaptoethanol (β-ME) was added per 1 mL of lysis (RLT) buffer and 4 volumes of 96-100% ethanol was added per 1 volume of wash buffer RPE.

Following desired treatment, media was aspirated from cells and wells were washed with PBS, before lysis with 350 μL RLT buffer. Wells were scraped with a cell scraper and then each 350 μL sample was added to a QIASHREDDER (QIAGEN) and centrifuged for 1 minute at 17,000 g for further homogenisation. An equal volume of 70 % ethanol was added to flow through, before addition to an RNeasy spin column in a 2 mL collection tube and centrifuging at 8000 g for 15 seconds. Flow through was discarded. 700 μL of wash buffer RW1 was then added to the RNeasy spin column, spun at 8000 g for 15 seconds and again flow through was discarded. 500 μL of wash buffer RPE was then added, followed by another 8000 g 15 second centrifugation and discarding flow through. A further 500 μL of RPE was then added, followed by a centrifugation for 2 minutes at 8000 g. The spin column was then placed in a new collection tube and the tube was spun at 17,000 g for 1 minute to dry the membrane. For RNA elution, spin columns were added to a 1.5 mL collection tube and then 30 μL of RNase free water was pipetted directly onto the membrane. Tubes were spun at 8000 g for 1 minute and eluted RNA was kept on ice. The Nanodrop® One Microvolume UV-Vis Spectrophotometer (Thermofisher Scientific) was used for quantification of RNA purity (O.D.260nm/O.D.280nm) and concentration (ng/μL) using 1 μL of RNA after blanking with 1 μL RNase-free water. RNA was then used immediately to synthesise complementary DNA (cDNA) or stored at -80 °C until ready for use.

2.4.1.2. RNA extraction from tissues

Tissues used for RNA extraction were stored in RNA later at -80 °C. Following thawing, 20-30 mg tissue was weighed out per sample and added to a round bottom 2 mL microcentrifuge tube. Tubes were kept on ice at all times. 350 μL QIAzol (QIAGEN) and one 5 mm stainless steel bead (QIAGEN) was added to each tube, before homogenisation at 20 Hz for 2 minutes

each side using the TissueLyser (QIAGEN). In order to separate RNA from DNA and protein, 140 μL chloroform was added to each tube, followed by a vigorous shake for 15 second. Tubes were then left at room temp for 3 minutes, before centrifugation at 12,000 g at 4 °C for 15 minutes. The upper aqueous phase was removed, added to a QIAshredder and spun at 17,000 g for 3 minutes. 1 volume of ethanol was added to the lysate, thoroughly mixed and added to an RNeasy spin column within a 2 mL collection tube, followed by centrifugation at 8000 g for 15 seconds. Flow through was discarded. 350 μL RW1 was added to the RNeasy column and spun at 8000 g for 15 second, before discarding flow through. Following this, an on column DNA digestion was performed using the RNase-free DNase kit (QIAGEN). 10 μL DNase I stock solution was added to 70 μL buffer RDD per sample, before addition of the solution directly onto the RNeasy column membrane. This was incubated at room temperature for 15 minutes. After this, membranes were washed once with RW1 and twice with RPE, before drying the membrane, eluting the RNA and quantifying as in section 2.4.1.1.

2.4.2. cDNA synthesis

In order to synthesise cDNA, the Tetro cDNA Synthesis kit (Bioline) was used. Per reaction, 400-1000 ng of total RNA was diluted in diethyl pyrocarbonate (DEPC)-treated water to a volume of 12 μL. Each tube was made up according to Table 2.1 as per manufacturer's instructions.

Component	**Volume (μL)**
RNA diluted with DEPC treated water	12
5X reverse transcription buffer	4
Oligo (dT)	1
Reverse transcriptase	1
DNTPs	1
RNase inhibitor	1
Final volume	**20 μL**

Table 2.1. Components added per tube for cDNA synthesis.

Tubes were then added to a T100 Thermal Cycler (Biorad) for a 45 °C incubation for 30 minutes, followed by an 85 °C incubation for 5 minutes. cDNA was then either used immediately for qPCR or stored at -80 °C for later use.

2.4.3. RT-qPCR

Table 2.2 shows the Taqman™ Gene expression assays which were used for real time quantitative polymerase chain reaction (RT-qPCR). Components in Table 2.3 were added to each well of a qPCR 96-well plate as per manufacturer's protocol.

Gene target	Gene Expression Assay	Species	Supplier
HPRT1	Taqman™ Hs02800695_m1	Human	Thermofisher
RPLP0	Taqman™ Hs00420895_gH	Human	Thermofisher
VEGFA	Taqman™ Hs00900055_m1	Human	Thermofisher
S1PR1	Taqman™ Hs00173499_m1	Human	Thermofisher
S1PR3	Taqman™ Hs01019574_m1	Human	Thermofisher
SGPL1	Taqman™ Hs00393705_m1	Human	Thermofisher
SPHK2	Taqman™ Hs02800695_m1	Human	Thermofisher
CXCL8	Taqman™ Hs00174103_m1	Human	Thermofisher
HIF1A	Taqman™ Hs00153153_m1	Human	Thermofisher
ICAM1	Taqman™ Hs00164932_m1	Human	Thermofisher
ACTB	Taqman™ Ss03376563_uH	Porcine	Thermofisher
IL6	Taqman™ Ss03384604_u1	Porcine	Thermofisher
TNFAIP3	Taqman™ Ss04954198_m1	Porcine	Thermofisher
FES	Taqman™ Ss06884012_g1	Porcine	Thermofisher
NDUFB1	Taqman™ Ss06912465_s1	Porcine	Thermofisher
PRDX4	Taqman™ Ss06879099_m1	Porcine	Thermofisher
CDH5	Taqman™ Ss03378336_u1	Porcine	Thermofisher
S1PR1	Custom - AR2XA6A	Porcine	Thermofisher

Table 2.2. Taqman™ gene expression assays used for qPCR.

Component	Volume (μL)
Taqman™ gene expression master mix	10
RNase free water	7
cDNA	2
Taqman™ Assay	1
Total volume	**20**

Table 2.3. Components added per PCR reaction.

Each cDNA sample was plated in triplicate. RNA and RNase free water were used as negative controls to rule out extraneous nucleic acid contamination. Plates were sealed with an optical adhesive film, vortexed briefly to mix and then centrifuged in a plate centrifuge to collect contents at the bottom of each well. qPCR was carried out using the Step One Plus Real-time PCR system with Step One Software V2.3. A comparative CT ($\Delta\Delta$CT) quantification was selected, as well as a 2 hour run time. Table 2.4 demonstrates the run method used. The mean cycle threshold (C_t) value was calculated for each amplification curve then each sample was normalised against a housekeeping gene to calculate ΔC_t values. Data was then presented as fold change ($2^{-\Delta\Delta C_t}$) relative to the control group.

Step	Cycles	Temperature (°C)	Duration
UNG incubation	Hold	50 °C	2 minutes
Polymerase activation	Hold	95 °C	10 minutes
Denature	40	95 °C	15 seconds
Anneal/extend		60 °C	60 seconds

Table 2.4. Description of the run for qPCR.

2.5. Protein expression analysis

2.5.1. Western blot

2.5.1.1. Cell lysis

Following cell treatment, wells of a 6-well plate were aspirated and washed with 1 mL ice cold PBS. This was removed before addition of 50 μL RIPA buffer per well which was made up according to Table 2.5. Wells were scraped with a syringe plunger before collection of lysate into a microcentrifuge tube. Tubes were agitated on a roller at 4 °C for 20 minutes and then centrifuged at 12000 RPM for 20 minutes at 4 °C. Supernatants were removed and added to a new tube before storage at -20 °C or used straight away.

Component	**Final concentration**
Sodium chloride (NaCl)	150 mM
Triton X-100	1 %
Sodium deoxycholate	0.5 %
Sodium dodecyl sulfate (SDS)	0.1 %
Tris-hydrochloride (HCl)	50 mM
Halt™ Protease and Phosphatase Inhibitor Cocktail (100X)	1X (added immediately prior to use)

Table 2.5. RIPA Buffer components.

2.5.1.2. BCA Assay

The Pierce Bicinchoninic acid (BCA) kit (Thermofisher Scientific) was used to calculate protein concentration of cell lysates. Bovine serum albumin (BSA) was serially diluted between 2-0.125 mg/mL with PBS. PBS alone was used as the 0 mg/mL concentration/blank. 10 μL per well of standards and lysates were plated in duplicate on 96-well plates, before addition of 200 μL Working Reagent per well. Working Reagent was made up immediately prior to use by combining Reagent A with Reagent B at a ratio of 50:1. Plates were then sealed and incubated at 37 °C for 30 minutes, before cooling to room temperature and reading with a microplate reader set to 562 nm. Following blank subtraction from all values, a standard curve was constructed and used to calculate unknown sample concentrations.

2.5.1.3. SDS-PAGE

To make a sodium dodecyl-sulfate polyacrylamide gel electrophoresis (SDS-PAGE) gel, glass plates with a distance between them of 1.5 mm were sandwiched together separated by spacers into a casting frame. This was clamped into a casting stand, making sure that the bottom edges of the plates were flush against the grey pad of the casting stand. 12 % separating gel was made by mixing components as detailed in Table 2.6 before pouring in between the glass plates and leaving sufficient space at the top for the stacking gel. Isopropanol was added to the top of the gel to ensure level setting. The gel was left to set at room temperature for approximately 20 minutes, before making 5 % stacking gel as in Table 2.6. Isopropanol was discarded and stacking gel was poured to the top of the glass plates, before insertion of an appropriate comb. This was allowed to set for around 20 minutes at room temperature.

12 % separating gel	
diH_2O	6.5 mL
30 % bis-acrylamide	8.0 mL
Separating gel buffer (100 mL diH_2O, 19.8 g Tris Base, 0.4 g SDS) pH 8.8	5.0 mL
10 % SDS	200 μL
10 % Ammonium persulfate (APS)	200 μL
Tetramethylethylenediamine (TEMED)	20 μL
5 % stacking gel	
diH_2O	4.1 mL
30 % bis-acrylamide	1.0 mL
Separating gel buffer (100 mL diH_2O, 6.6 g Tris Base, 0.4 g SDS) pH 6.8	0.75 mL
10 % SDS	60 μL
10 % Ammonium persulfate (APS)	60 μL
Tetramethylethylenediamine (TEMED)	6 μL

Table 2.6. Components used to make separating and stacking gel.

2.5.1.4. Sample preparation, loading and running the gel

Following protein concentration quantification with a BCA assay, 40 μg of protein per sample was made up with 4X Laemmli sample buffer (Bio-Rad) with 10% β-ME. Samples were then boiled for 10 minutes at 95 °C and loaded into separate wells of the gel alongside one well containing 6 μL PageRuler™ Prestained Protein Ladder (10 to 180 kDa; Themofisher Scientific). The gel was run at 120 V until the dye front reached a desired point on the gel. The gel was run in running buffer diluted 1:5 with dH_2O (15.1 g Tris base, 72 g Glycine, 5 g SDS and dH_2O up to 1 L, pH 7.4).

2.5.1.5. Transfer

The protein from the gel was transferred onto a mini format, 0.2 μm polyvinylidene fluoride (PVDF) membrane using a Trans-Blot Turbo™ transfer pack and the Trans-Blot Turbo Transfer system (Bio-Rad).

2.5.1.6. Immunoblotting and visualisation

Immediately after transfer, membranes were blocked with either 5 % BSA or 5 % milk in 0.1 % Tris buffered saline with tween (TBST). Then the appropriate antibody at desired dilution was added into the block and incubated overnight at 4 °C on a rocker. This was followed by a 3 x 10 minute wash (0.1 % TBST). Then a horse radish peroxidase (HRP)-conjugated secondary antibody at appropriate dilution in the corresponding block was added and incubated for 1 hour at room temperature on a rocker, before another 3 x 10 minute wash. An appropriate chemiluminescent substrate was added for appropriate time, before visualising using the Li-Cor Odessy Fc (Li-Cor). Densitometry analysis was carried out using Image Studio™ and P-ERK/ERK ratio was quantified. Details specific to each antibody are included in Table 2.7. When re-probing, membranes were stripped for 5 minutes in Restore™ PLUS Western Blot Stripping Buffer (Thermofisher Scientific) before a 2 x 5 minutes wash with 0.1 % TBST and procession to the blocking stage.

Primary antibody	Primary dilution	Block	Secondary antibody	Secondary dilution	Substrate
Rabbit anti-Phospho-ERK1/ERK2 (Thr185, Tyr187) Polyclonal IgG (cat. 44-680G, lot. 2066360; Thermofisher Scientific)	1:1000	5 % BSA in 0.1 % TBST	Goat anti-rabbit IgG HRP-conjugated Polyclonal (cat. A6514, lot. SLBV9141; Sigma Aldrich)	1:5000	Pico Super Signal West (cat. 34580; Thermofisher Scientific)
Mouse anti-ERK1/ERK2 Monoclonal IgG1, kappa (cat. 13-6200, clone. ERK-7D8; Invitrogen)	1:500	5 % Milk in 0.1 % TBST	Goat anti-mouse IgG HRP-conjugated Polyclonal (cat. A3673, lot. 07K6004; Sigma Aldrich)	1:2000	Pico Super Signal West (cat. 34580; Thermofisher Scientific)
Mouse anti-α-tubulin Monoclonal (cat. T-5168, clone. B-5-1-2; Sigma Aldrich)	1:5000	5 % BSA in 0.1 % TBST	Goat anti-mouse IgG HRP-conjugated Polyclonal (cat. A3673, lot. 07K6004; Sigma Aldrich)	1:10,000	Pierce ECL substrate (cat. 32209; Thermofisher Scientific)

Table 2.7. Antibodies used for western blot.

2.5.2. ELISA

To calculate cytokine concentration in perfusates, DuoSet® ELISA kits (R&D Systems) were used as detailed in Table 2.8.

Cytokine detected	Species	Catalogue number
TNF-α	Porcine	DY690B
IL-6	Porcine	DY686
CXCL8	Human	DY208-05
IL1-β	Human	DY201

Table 2.8. R&D Systems DuoSet® ELISA kits used to quantify cytokine concentration in perfusates.

Wash buffer, reagent diluent, block buffer and stop solution were all made up according to each kit instructions. Capture antibody, detection antibody and standard were reconstituted according to the protocol.

Kit reagents were diluted to working concentrations only immediately prior to use. Reconstituted capture antibody was diluted with PBS to the working concentration specified in the kit. Reconstituted detection antibody and Streptavidin-HRP were diluted to working concentrations with Reagent diluent as specified. The standard was serially diluted with reagent diluent to construct a seven-point standard curve according to kit protocol. Substrate solution was made using a 1:1 mixture of colour reagent A with colour reagent B (cat. DY999; R&D Systems).

Briefly, 96-well plates were coated with 100 μL capture antibody, sealed with a plate sealer and stored at 4°C overnight. The next day, wells were aspirated and this was followed by 3x washes with 300 μL wash buffer per well. Wells were then blocked with 300 μL reagent diluent/block buffer, depending on kit protocol, for 1 hour. The aspiration/wash step was then repeated, followed by addition of 100 μL per well of standards and samples in triplicate. Reagent diluent alone was used as a blank. This was sealed with an adhesive strip and incubated at room temperature for 2 hours. The aspiration/ wash step was repeated before addition of 100 μL detection antibody, sealing with an adhesive strip and incubation for 2 hours at room temperature. This was followed by another aspiration/wash. Then 100 μL of

streptavidin-HRP was added per well, sealed and incubated for 20 minutes at room temperature away from direct light. This was followed by another aspiration/wash step, before adding 100 μL Substrate solution to each well and incubating at room temperature away from direct light until sufficiently developed. Then 50μL stop solution was added to each well, before determining the optical density of each well using a microplate reader set to 450 nm. Blank readings were subtracted from values and a standard curve was used to calculate sample concentrations.

2.5.3. Staining

2.5.3.1. Haematoxylin & Eosin staining

2.5.3.1.1. Tissue

Immediately following collection, tissue was fixed in 10 % neutral buffered formalin (CellPath) for 48 hours at room temperature, before replacing formalin with PBS and storage at 4 °C. Tissue was then embedded in paraffin and cut into 4 μm sections.

Sections were dewaxed in xylene for 5 mins, before putting into fresh xylene for a further 5 mins. Then slides were rehydrated in a series of alcohols (100-50 % ethanol) for 3 mins each, before putting in running water for 3 mins. Following dewaxing and rehydration, slides were counterstained using Meyer's Haematoxylin (Sigma Aldrich) and washed in running tap water. Sections were then blued in alkalotic tap water for 5 mins, before a further wash in running tap water. Slides were added to Eosin (Sigma Aldrich) for 80 seconds and washed in running tap water again. Sections were dehydrated in a series of alcohols (50-100 % ethanol) for 3 mins each, before adding to xylene for 5 mins and then fresh xylene for a further 5 mins. Slides were then mounted using DPX and a cover slip.

Full section images were obtained using the AxioScan 7 at a 10 x magnification and visualised using QuPath.

2.5.3.2. Immunofluorescence staining

2.5.3.2.1. Cells

Cells grown on chamber slides or transwells were washed with PBS and fixed with 4 % paraformaldehyde (PFA) for 10-15 mins. If permeabilising, cells were washed with PBS with

gentle agitation for 5 mins before addition of 0.1 % Triton X-100 for 15 mins. Then wells were washed with 0.05 % phosphate buffered saline with tween (PBST) for 3x5 mins with gentle agitation, before blocking for 1 hour at room temperature as indicated in Table 9. Wells were then incubated with primary antibody diluted in PBS or PBS alone for no primary wells at 4 °C overnight, before another 3x5 min wash with PBST. Cells were then incubated with secondary antibody diluted in PBS for 1 hour at room temperature, before a final 3x5 min wash with PBST. Mounting media with diamidino-2-phenylindole (DAPI) was added, before covering with a coverslip and storage in the dark at 4 °C until needed. Sections were visualised using the Zeiss Axioimager and Zen Pro Software. Antibody dilutions and conditions used for each cell type are detailed in Table 2.9.

Cell type	Permeabilised	Primary antibody	Primary dilution	Block	Secondary antibody	Secondary dilution
HMEC-1 HPMEC	No	Goat anti-human VE-cadherin Polyclonal IgG (cat. AF938, lot. EFR0220021; R&D Systems)	1:500	10 % chicken serum in PBS	Alexa Fluor 488 chicken anti-goat Polyclonal IgG (cat. A21467; ThermoFisher Scientific)	1:100
PPMEC	Yes	Rabbit anti-VE-cadherin Monoclonal (cat. 2500, clone.D87F2; Cell Signaling Technology)	1:100	10 % goat serum in PBS	Alexa Fluor 488 goat anti-rabbit Polyclonal IgG (cat. AB150077; Abcam)	1:200

Table 2.9. Antibodies and conditions used for Immunofluorescence staining of cells.

2.5.3.2.2. Tissue

Tissues were formalin fixed, paraffin embedded and dewaxed in xylene as described in section 2.4.4.1.2. Slides were then rehydrated in graded alcohols (100-50% ethanol) for 5 mins each, before putting in deionised water for 5 mins. Slides were then submerged in 1 L Tris-EDTA buffer (1.21 g Tris Base, 0.37 g EDTA, 0.5 mL Tween 20, 1 L diH_2O, pH 9) in a pressure cooker set to high for 3 mins, before removing and placing immediately in PBS. Then sections were blocked at room temperature for 1 hour as indicated in Table 10, before an overnight incubation with primary antibody diluted in PBS at 4 °C. For no primary sections, PBS alone was added. The next day, slides were washed 3x5 mins in PBS with 0.05 % Tween 20 with gentle agitation. Then sections were incubated in the dark with secondary antibody diluted in PBS for 1 hour at room temperature, before washing with 0.05 % PBST 2x5 mins with gentle agitation. Subsequently, stained sections were incubated with 0.1 % Sudan Black in 70 % ethanol for 20 mins with gentle agitation to minimise tissue auto-fluorescence. This was followed by a 2x5 min wash with 0.05 % PBST with gentle agitation, before adding mounting media with DAPI (Vectashield) and covering with a coverslip. Slides were then stored in the dark at 4 °C until needed for imaging. Sections were visualised using the Zeiss Axioimager and Zen Pro Software.

Antibodies and conditions used for each tissue type are detailed in Table 2.10.

Tissue/cell type stained	**Primary antibody**	**Primary dilution**	**Block**	**Secondary antibody**	**Secondary dilution**
Porcine	Rabbit anti-VE-cadherin Monoclonal (cat. 2500, clone.D87F2; Cell Signaling Technology)	1:50	10 % goat serum in PBS	Alexa Fluor 488 goat anti-rabbit Polyclonal IgG (cat. AB150077, Abcam)	1:100

Table 2.10. Antibodies and conditions used for immunofluorescence staining of tissue.

2.6. Statistical analysis

Statistical analysis was performed using GraphPad Prism. When required, normality was assessed using a Shapiro-Wilk test. Error bars represent the standard deviation (SD) of the mean, unless otherwise stated and statistical tests are described for each experiment individually. Statistical significance is depicted as follows:

*<0.05

**<0.01

***<0.001

****<0.0001

3. Validation of a novel anti-inflammatory perfusate solution to improve lung assessment

3.1. Introduction

Ischaemia reperfusion injury (IRI) is a significant issue impacting the success of lung transplantation. It is initiated following loss of oxygenated blood flow to the organ, leading to oxidative stress, sterile inflammation, immune cell activation and fluid accumulation, which can ultimately impair lung allograft function and lead to primary graft dysfunction (PGD). Lung transplantation is also limited by a shortfall of available donor lungs and low utilisation rates of these organs as a result of stringent selection criteria (NHS Blood and Transplant, 2022, Ojo *et al*., 2004). Therefore, the use of extended criteria donor (ECD) lungs has become increasingly more frequent, although these organs have been associated with worse outcomes (Mulligan *et al*., 2016) and increased risk of PGD (Botha *et al*., 2006). Whilst ECD lungs may fail to meet selection criteria, they may function well enough to be transplanted. *Ex vivo* lung perfusion (EVLP) provides a platform that allows these lungs to be objectively assessed in order to determine their suitability for transplantation. It also offers the opportunity to administer therapeutics to improve their quality prior to transplantation and protect against subsequent IRI.

Professor Stig Steen and colleagues performed the first human lung transplant following assessment of the donor lung using EVLP (Steen *et al*., 2001) and the group was instrumental in development of Steen solution, which is used clinically as the standard of care perfusate today. Steen is a buffered, low potassium solution, with high dextran and human serum albumin (HSA) content. Dextran 40 in the solution limits endothelial-leukocyte interactions (Termeer *et al*., 1998), whilst HSA maintains a physiologically relevant colloid osmotic pressure (Levitt and Levitt, 2016), reducing lung damage. In fact, Steen solution has been shown to maintain stable lung function for as long as twelve hours (Cypel *et al*., 2008, Cypel *et al*., 2009).

Despite the success of EVLP in recent clinical trials, some degree of IRI is inevitable during reperfusion of the organ during EVLP. Indeed, it has been demonstrated that pro-inflammatory cytokines in both tissue and perfusate increase over the duration of EVLP (Andreasson *et al*., 2017, Kakishita *et al*., 2010) and EVLP for prolonged periods results in lung injury (Erasmus *et al*., 2006, Brandes *et al*., 2002). As the pathophysiological events of IRI

become increasingly well characterised, research has turned to the continuous development of perfusion technology with the aim to improve the conversion of ECD organs to transplantable organs. Studies have focused on reducing the oxidative stress that occurs during reperfusion by development of perfusion solutions with anti-oxidative properties. For example, Olbertz *et al* described the benefits of perfusing lungs with modified Custodiol-N, which contains iron chelators and desferoxamine; these lungs exhibited superior oxygenation capacity compared to lungs perfused with Steen (Olbertz *et al*., 2020).

This has led to development of a new organ perfusate solution by XVIVO Perfusion, Sweden, which is referred to as "modified" Steen within this chapter. Modified Steen has been formulated with the addition of acetal salicylic acid (SA) and retinoic acid (RA) to standard Steen, which have known anti-oxidative and anti-inflammatory properties. Therefore, it could offer the potential to limit organ damage during reperfusion, improving organ assessment and allowing longer and more advanced therapeutic testing.

As well as its undeniable uses for organ assessment and as a therapeutic platform, EVLP offers a unique opportunity to model IRI and gain mechanistic insights into the processes that occur. Therefore, in this chapter, porcine EVLP was used to examine the effectiveness of perfusing with modified Steen compared with standard Steen, and to define gene and protein expression changes that occur during IRI. In this chapter, these two aims were addressed by:

- Recording physiological parameters during EVLP to assess donor lung function
- Using RNA-sequencing to identify genes and pathways in tissues that change during EVLP and to define any differences between standard Steen and modified Steen
- Assessing protein release into perfusate during perfusion
- Looking at gene expression in venous and arterial tissue following EVLP

3.2. Materials and methods

3.2.1. Animals

The study used Swedish domestic pigs of either sex with weights ranging between 30-70 kilograms. The European Directive 2010/63/EU as amended by Regulation (EU) 2019/1010 "On the protection of animals used for scientific purposes" and the Swedish Board of Agriculture's regulations and general guidelines for experimental animals SJVFS2019:9 L150 were complied with during this study. Animal care complied with the European Convention for the production of vertebrate animals for experimental and other scientific purposes. Ethical approval was granted (M174-15 & 15906/2020) and the FDA guidance Utilizing Animal Studies to Evaluate Organ Preservation Devices (May 8, 2019) was complied with throughout the study.

3.2.2. Porcine EVLP model

The porcine EVLPs and sample collection were carried out by collaborators XVIVO Perfusion in Sweden, before shipping over the samples to Newcastle University for analysis.

Pigs were randomised among 3 study groups; Fresh (N=4), Steen (N=5) or modified Steen (N=5). An intramuscular injection of ketamine 20 mg/kg bodyweight, 100 mg xylazine and 0.5 mg atropine was used to anaesthetise pigs. Pigs were also injected with 4 μg/kg fentanyl or 0.4 mg/kg midazolam before thoracotomy was performed. Euthanasia was performed via ventricular fibrillation following sternotomy. Donor lungs were retrieved following standard procurement guidelines and as previously described for porcine models (Steen *et al*., 1994). The Fresh group underwent no intervention following retrieval. The Steen and modified Steen group underwent flushing with 3 L cold Perfadex plus, followed by 24 hours cold static storage (CSS) in Perfadex plus at 4-8 °C to model marginal donor lungs in a clinical setting, before undergoing EVLP.

EVLP was carried out for 4 hours using the XVIVO Perfusion System (XPS) with a minimal intervention strategy. The XPS was set up and primed according to the manufacturer's instructions for use (IFU) with 2 L of either original Steen or modified Steen. The first hour of EVLP was run according to the Toronto protocol as detailed in the XPS IFU and was used as a warm up phase. Following this, the perfusate was exchanged with fresh bottles of the Steen or modified Steen as appropriate. A pressure-controlled system was adopted immediately

following solution exchange, which aimed to maintain a physiological pulmonary artery pressure (PAP) of 13-15 mmHg and left atrial pressure (LAP) of 3-5 mmHg by adjustment of flow. Physiological parameters pulmonary vascular resistance (PVR), flow, PAP, LAP, LA temperature, peak airway pressure, tidal volume, dynamic compliance, and static compliance were recorded automatically throughout EVLP by the XPS system. For the last hour, the heater-cooler was set to 15°C to cool the system as per clinical practice for transplantation.

Workflow and sampling is presented diagrammatically in Figure 3.1. Composition of the perfusate solutions is detailed in Table 3.1.

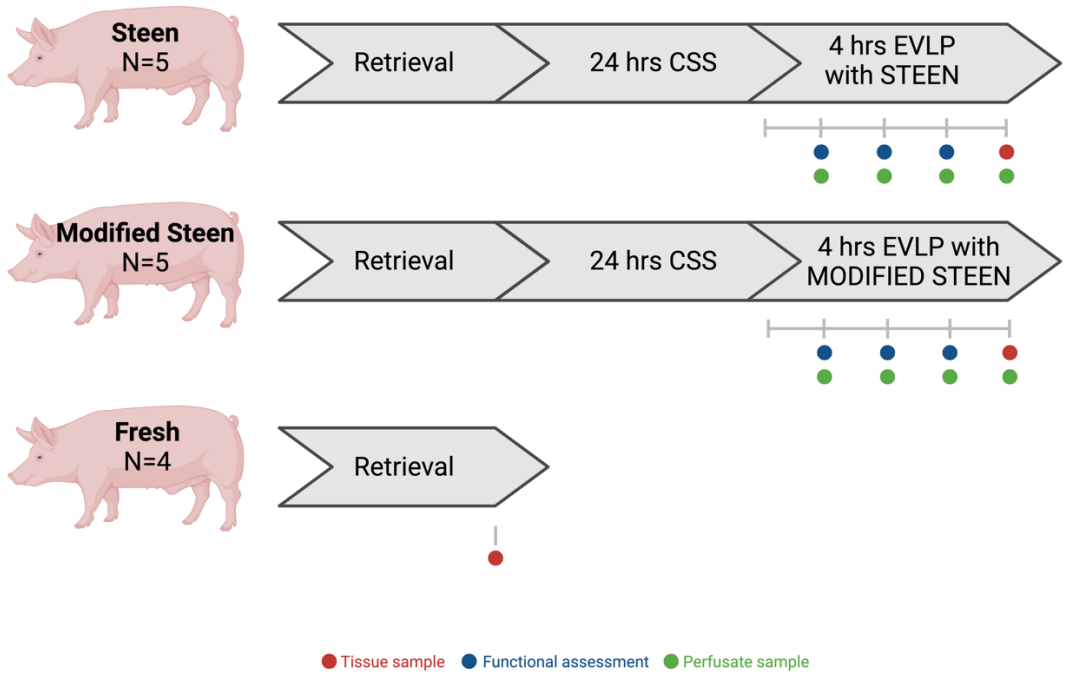

Figure 3.1. Summary of workflow and sampling.

Porcine lungs were retrieved, before random allocation to treatment groups (Fresh, N=4; Steen, N=5; modified Steen, N=5). For the Fresh group, left lower lobe biopsies were taken immediately during retrieval and used as a baseline control. Lungs allocated to the Steen and modified Steen groups underwent 24 hours cold static storage (CSS) in Perfadex® plus before 4 hours *ex vivo* lung perfusion (EVLP) with Steen or modified Steen respectively and right lower lobe biopsies were taken post-EVLP. Functional parameters were recorded during EVLP and sequential perfusate samples were collected.

Component (g/L)	Modified STEEN	Standard STEEN
NaCl	4.44	5.03
D-glucose Monohydrate	1.19	1.98
KCl	0.34	0.34
NaH_2PO_4	0.17	0.19
$CaCl_2$	0.22	0.22
$MgCl_2$	0.24	0.24
Tris	0.24	-
$NaHCO_3$	1.26	1.26
Arginine	0.26	-
HSA (25%)	70	70
Dextran 40	5	5
Dextran 1	0.5	-
$C_9H_8O_4$ (Acetylsalicylic Acid)	0.1	-
$C_{20}H_{28}O_2$ (Retinoic acid)	0.0005	-
$C_{22}H_{30}O_5$ (Methylprednisolone)	0.0035	Added during EVLP*

Table 3.1. Composition of standard Steen and modified Steen.

For EVLP, perfusate was supplemented with 5 mL (25 mg/mL) Imipenem/Cilastatin and 1 mL (5000 IU) heparin. Steen also received 2 mL (50 mg/mL) Solu-Cortef (hydrocortisone). *standard Steen was also supplemented with 0.33 g/L methylprednisolone during EVLP in line with XVIVO's standard protocol, however as modified Steen already contains low amounts of methylprednisolone within its formulation, no more was added.

3.2.3. Gene expression analysis from tissue

Tissue biopsies were collected from the lower lobe of right lungs post-EVLP for Steen and modified Steen groups and the lower lobe of left lungs during retrieval for the Fresh group and stored in RNA later at -80 °C for subsequent mRNA quantification via qPCR and transcriptomics analysis via RNA-seq.

3.2.3.1. RT-qPCR from tissue samples

Lung parenchymal tissue and venous and arterial tissue samples were collected immediately following EVLP. Samples were stored in RNA later at -80 °C until ready for use. Prior to use, tissue samples were thawed on ice, before weighing out 20-30 mg for RNA extraction. Then RNA extraction protocol as detailed in 2.4.1.2 was carried out. Following RNA extraction, cDNA synthesis was carried out as per section 2.4.2. Then qPCR was performed as detailed in section 2.4.3 using Taqman™ gene expression assays to quantify expression of *TNFAIP3, IL6, NDUFB1, PRDX4* and *FES* in lower lobe lung tissue and *S1PR1* and *CDH5* in vein and artery tissue. C_t values were normalised against the β-actin gene *ACTB* and then fold changes were calculated relative to Fresh samples taken during retrieval.

3.2.3.2. 3" RNA-sequencing

Tissue biopsies were sent to QIAGEN for RNA-sequencing.

3.2.3.2.1. Library preparation and sequencing

Library preparation was done using the QIAseq UPX 3' Transcriptome kit. In short, 10 ng of purified RNA was converted into cDNA next generation sequencing (NGS) libraries, during which each cell was tagged with a unique ID and each RNA molecule with a unique molecular index (UMI). After this, cDNA was amplified to ensure sufficient cDNA enrichment for library preparation, before fragmentation, end repair and A-addition. Following adaptor ligation, universal PCR was carried out, during which indices were added. The library was then quality controlled by capillary electrophoresis. Depending on quality and concentration, libraries were pooled in equimolar ratios. The library pool was quantified using qPCR, before sequencing on a NextSeq®500 sequencing instrument according to manufacturer protocol with 100bp read length for read 1 and 27bp for read 2. Then raw data was demultiplexed and FASTQ files generated for each pool using the bcl2fastq Conversion Software (Illumina® Inc.).

3.2.3.2.2. Read demultiplexing, mapping and quantification of gene expression

The "Demultiplex QIAseq UPX 3' reads" tool of the CLC Genomics Workbench 20.0.4 was used for demultiplexing of raw sequencing reads according to sample indices. Processing of demultiplexed sequencing reads was carried out using "The Quantify QIAseq UPX 3' workflow" with default settings.

In short, the reads are annotated with their UMI and then trimmed for poly(A) and adapter sequences, minimum reads length (15 nucleotides), read quality, and ambiguous nucleotides (maximum of 2). They are then deduplicated using their UMI. Reads are grouped into UMI groups when they (1) start at the same position based on the end of the read to which the UMI is ligated (i.e., Read2 for paired data), (2) are from the same strand, and (3) have identical UMIs. Groups that contain only one read (singletons) are merged into non-singleton groups if the singleton's UMI can be converted to a UMI of a non-singleton group by introducing an SNP (the biggest group is chosen). The reads were then mapped to the Pig genome Sscrofa11.1 and annotated using the ENSEMBL Sscrofa11.1.99 annotation.

DESeq2 was used to calculate differential expression and carry out unsupervised analysis. Genes were considered significantly differentially expressed if the FDR<0.01.

Prior to GSEA and IPA, porcine Ensembl gene IDS were converted to human orthologs using bioDBnet : dbOrtho.

3.2.3.2.3. Gene set enrichment analysis

Broad Institute's Gene set enrichment analysis (GSEA) can be used to determine whether an *a priori* defined gene set is significantly different between an experimental and a control group. The software ranks genes into a ranked gene list based on their signal-to-noise ratio for a given comparison of two groups. It then calculates an enrichment score based on the position if its gene members in the ranked gene list. For example, gene sets comprised of genes which primarily feature towards the top of the ranked gene list will be positively enriched and a gene set comprising of genes towards the bottom of the ranked gene list will be negatively enriched. The software also computes a P value by assessing how often the enrichment score is greater than the enrichment score for random permutations and then calculates a normalised enrichment score (NES) by division of the enrichment score from the actual ranking by the mean of the random permutations. A false discovery rate (FDR) can then be calculated by comparing the distribution if NES's from many gene sets and provides the probability that a finding is a false positive. In this way, GSEA allows identification of gene sets which are either significantly positively or significantly negatively overrepresented and may be associated with a particular phenotype.

Transcripts per million (TPM) for each gene for each sample was used as the expression data set. Then the Hallmark gene set collection (50 gene sets) from the Molecular Signatures Database version 7.2 (MSigDB; https://www.gsea-msigdb.org/gsea/msigdb/index.jsp; h.all.v7.2.symbols.gmt) was used with the Human_ENSEMBL_Gene_ID_MSigDB.v7.2.chip chip annotation file. The number of permutations was set to 1000 and permutations type set to 'gene set'. Pathways with an FDR p value <0.05 were considered significant.

3.2.3.2.4. Ingenuity pathway analysis

Qiagen's Ingenuity Pathway analysis (IPA) software goes further than GSEA in that it not only identifies pathways which are overrepresented, but also predicts the activation or inhibition state of a pathway. This is calculated based on the data set's correlation with the activated state of a pathway within the Ingenuity pathway knowledge base (IPKB). The software provides a z-score, with a positive z-score denoting pathway activation and a negative z-score denoting pathway inhibition. P values are reflective of the likelihood that the overlap between genes in the user dataset and a given canonical pathway is due to chance and are calculated using Fischer's exact test.

Expression data for each comparison between two groups was entered into the software, in which the ensemble gene ID, $\log_2$ fold change and FDR for each gene was provided. Then a core analysis was carried out for each, with the 'user data set' used as the reference set and thresholds set at an FDR P value of <0.05 and $\log_2$ fold change of ≥ 1 or ≤ -1. Several core analyses could then be compared using a comparative analysis.

3.2.4. Protein expression analysis in perfusate

10 mL perfusate samples were collected hourly from the venous line during EVLP. 2 mL was used for monitoring of blood gas. The remainder was centrifuged at 2000 xg for 10 min before storing the supernatant at -80 °C until needed.

3.2.4.1. ELISA

For TNF-α and IL-6 protein quantification from perfusates, Porcine Duoset® ELISA kits (Dy690B and DY686 respectively; R&D Systems) were used. ELISAs were performed according to manufacturer instructions as detailed in sections 2.5.2.

3.3. Results

3.3.1. Physiological parameters during porcine EVLP with Steen or Modified Steen

In order to assess lung function during perfusion with either standard Steen or modified Steen, PVR, flow, dynamic compliance and peak airway pressure were recorded over time. Overall, lungs perfused with modified Steen exhibited a significantly reduced PVR compared to lungs perfused with Steen (Figure 3.2A). Modified Steen also allowed lungs to be perfused at significantly higher flow rates, whilst maintaining a physiological pulmonary artery pressure (Figure 3.2B). Whilst not significant, lungs perfused with modified Steen seemed to exhibit marginally improved dynamic compliance and lower peak airway pressure during the course of EVLP as shown in Figure 3.2 C and D respectively.

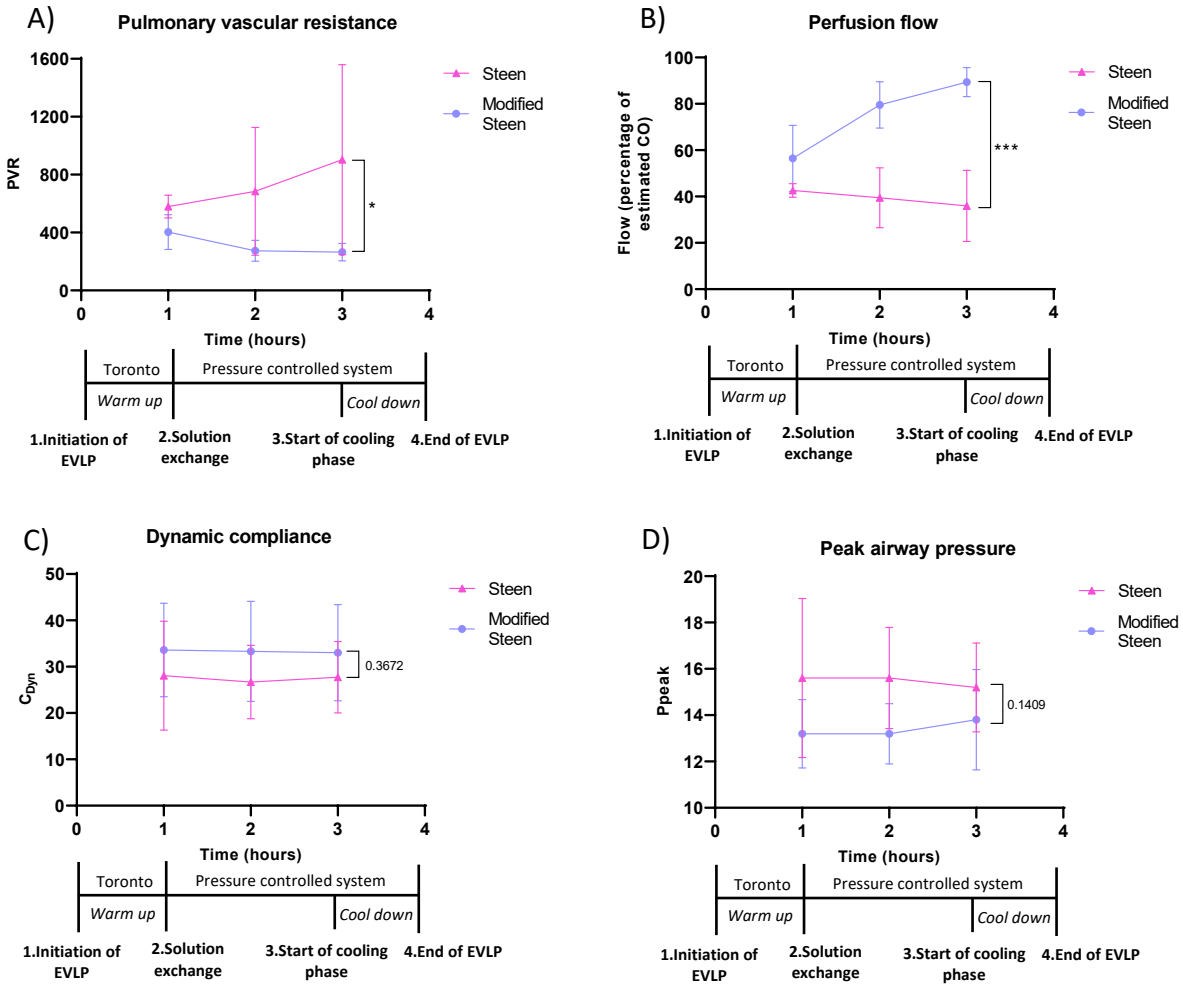

Figure 3.2.Physiological parameters recorded during EVLP.

A) Pulmonary vascular resistance (PVR), **B)** Flow as a percentage of estimated cardiac output (CO), **C)** Dynamic compliance and **D)** Peak airway pressure for lungs perfused with Steen or modified Steen was measured during the course of EVLP, excluding the 1 hour warm up and 1 hour cooling period. N=5 per group. Mean is presented with standard deviation. A two-way repeated measures ANOVA was used to calculate statistical significance between modified Steen and Steen overall. *p<0.05, **p<0.01, ***p<0.001, ****p<0.0001.

3.3.2. RNA-sequencing analysis of biopsy samples taken from Fresh lungs and post-EVLP

RNA-sequencing was performed on post-EVLP and Fresh lung biopsies. As well as directly comparing modified Steen with standard Steen samples, post-EVLP samples were also compared with Fresh samples taken during retrieval. This not only allowed an indirect means of comparing modified Steen with standard Steen, but also allowed exploration of gene expression profiles and pathway analysis during IRI.

3.3.2.1. Unsupervised analysis

An unsupervised analysis was performed. PCA was used to reduce the dimension of the large data set and to explore sample clusters arising naturally based on the expression profile. The variance was calculated agnostic to the pre-defined groups. Data points were projected onto the 2D plane so that they spread out in two directions which explain the most variance. Hierarchical clustering groups similar objects into clusters based on the genes with the highest variance across samples. Both PCA (Figure 3.3A) and hierarchical clustering (Figure 3.3B) did not reveal distinct clustering of Steen versus modified Steen. Instead, there was a clear separation between Fresh lungs and lungs that had underwent EVLP.

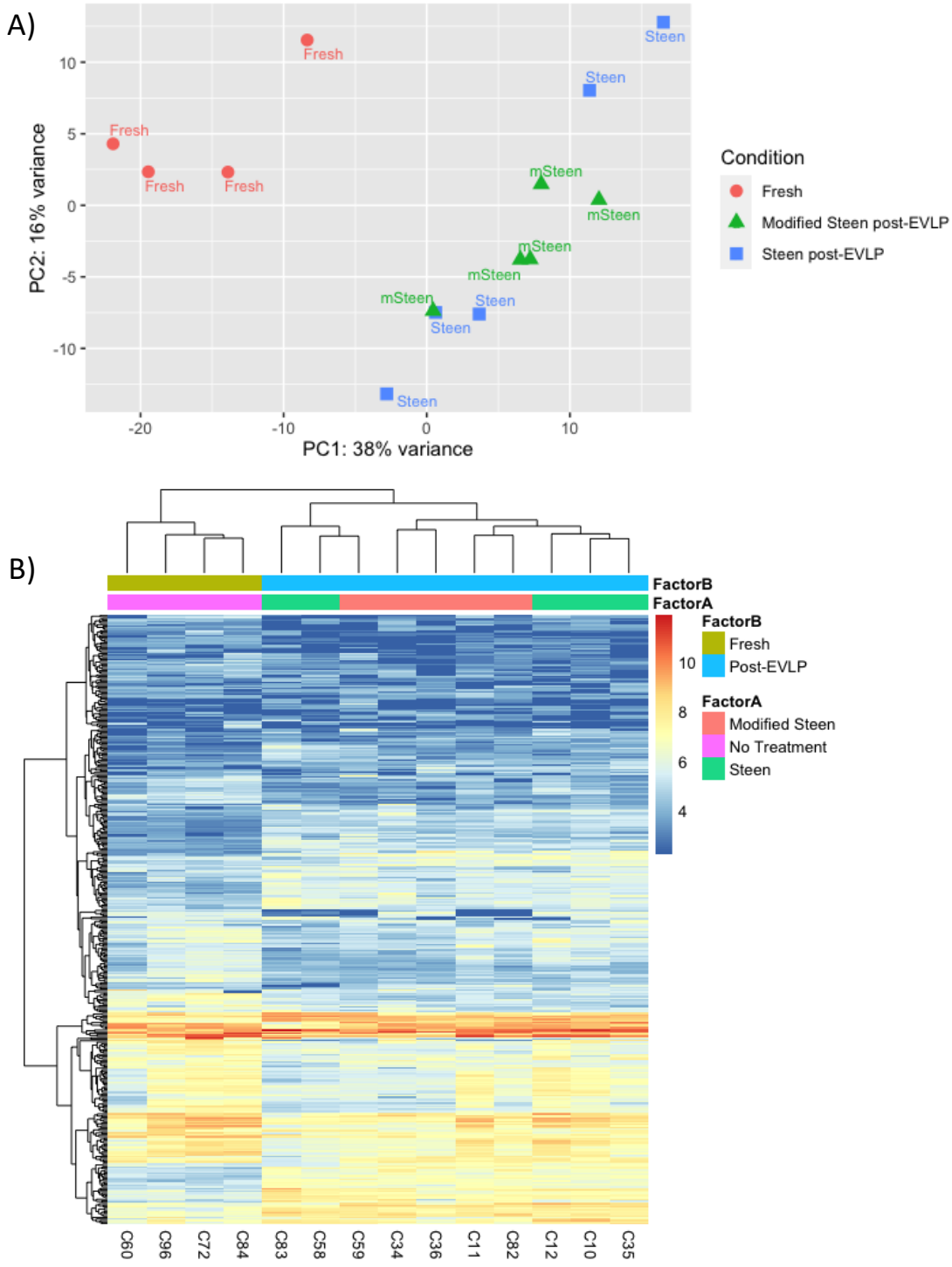

Figure 3.3. Unsupervised analysis of RNA-sequencing data.

A variance stabilizing transformation was applied to raw counts prior to PCA and hierarchal clustering. **A)** PCA plot of sample clusters arising naturally based on the expression profile. **B)** Hierarchal clustering using the top 400 genes with the highest variance across all samples. Each row represents one gene and each column represents one sample. The colour represents the difference of the count value to the row mean. Fresh, N=4; Steen, N=5; Modified Steen (mSteen), N=5.

3.3.2.2. Volcano plots

Comparison of modified Steen post-EVLP with standard Steen post-EVLP showed that only one gene was significantly differentially expressed (Figure 3.4A). Lungs perfused with modified Steen showed significant upregulation of CYP26B1 (log2FC=3.87, adjusted P=0.01), which is crucial for regulation of retinoic acid levels in the body (Stoney *et al*., 2016).

Compared with Fresh samples, standard Steen post-EVLP samples had 436 differentially expressed genes (DEGs), including several immune genes such as *BIRC3, TNFAIP3, SERPINE1, GADD45A, DDX21* and *ICAM1* among the most significant (Figure 3.4B). Modified Steen post-EVLP samples similarly showed significant upregulation of various immune-related genes such as *GADD45A, TNFRSF12A, STX11 and DEPP1*, but notably showed a smaller number of DEGs compared to Fresh than standard Steen (391 DEGS, Figure 3.4C). Among the genes upregulated in Fresh samples compared to either standard Steen or modified Steen post-EVLP samples were *MEIS1, CDH11, NR2F2, CITED2* and *ID1*, all of which have been shown to be responsive to hypoxia.

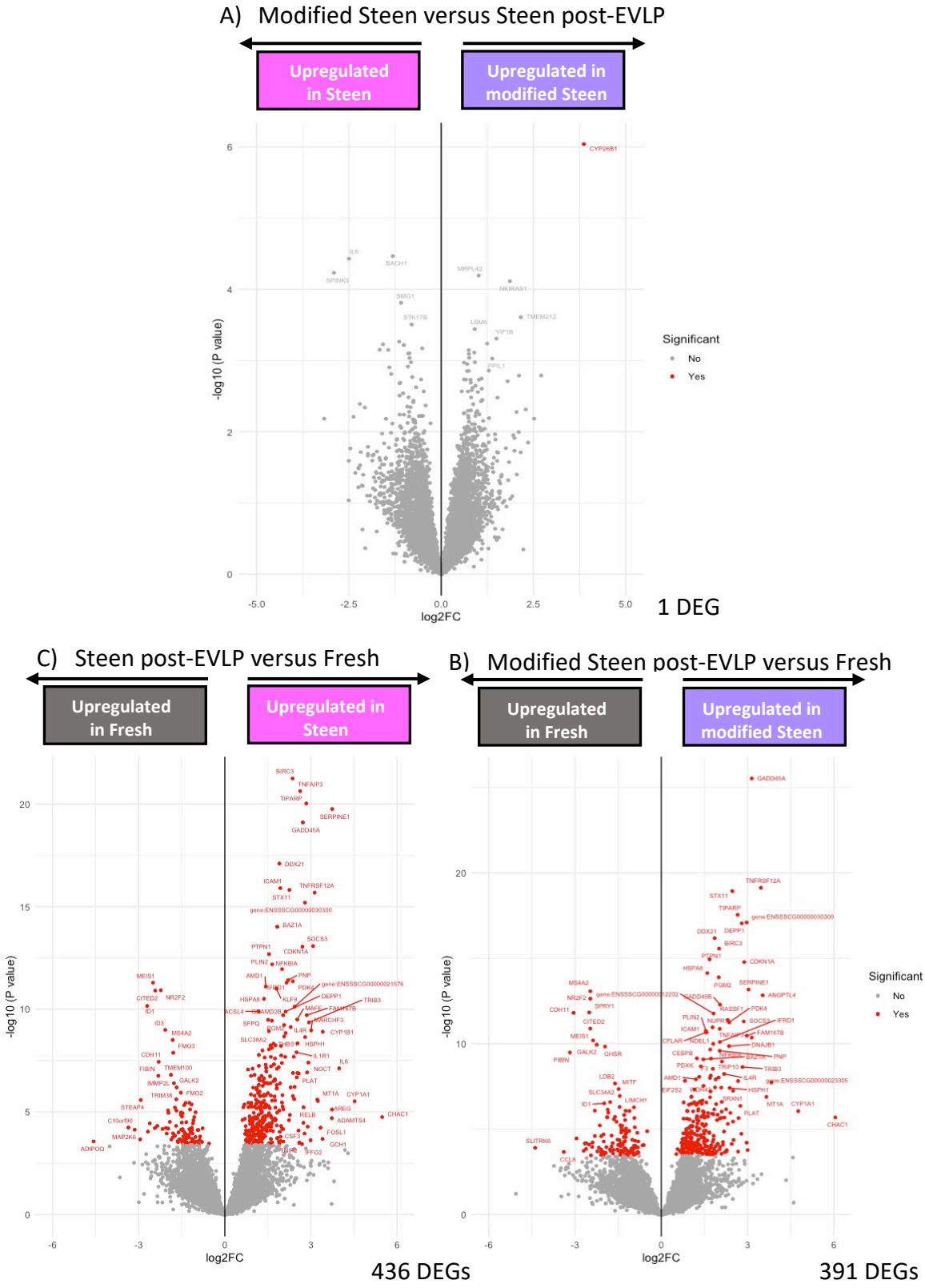

Figure 3.4. Gene expression data from RNA-sequencing.

Volcano plots showing differentially expressed genes (DEGs) when comparing **A)** modified Steen vs Steen post-EVLP, **B)** Steen post-EVLP against Fresh and **C)** modified Steen post-EVLP against Fresh. Genes were considered significantly differentially expressed if $p<0.05$ and adjusted $p<0.01$ and are depicted in red. Log2 fold change was plotted against the inverse of the log10 p value. N=4 (Fresh), N=5 (Steen), N=5 (modified Steen).

3.3.2.3. Gene set enrichment analysis of post-EVLP versus Fresh

GSEA was carried out to identify differential enrichment of gene sets between groups. GSEA calculates a normalised enrichment score for each gene set for a given comparison. A positive enrichment score means that the genes in a pathway are primarily expressed to a higher extent in the experimental versus control group, whilst a negative enrichment score means that the genes in a pathway are generally downregulated in the experimental group compared with the control group.

Comparison of Steen post-EVLP with Fresh samples showed significant positive enrichment of 27 gene sets, whilst modified Steen had fewer, with only 21 gene sets significantly positively enriched when compared with Fresh. Whilst 1 pathway was significantly negatively enriched in Steen post-EVLP versus Fresh, modified Steen showed a total of 3 significantly negatively enriched pathways (Figure 3.5Ai-ii). Whether lungs were perfused with Steen or modified Steen, post-EVLP samples showed enrichment of various inflammatory pathways such as TNF-α signalling via NFκB, Inflammatory response, Apoptosis, IL6 JAK STAT3 signalling, Epithelial to mesenchymal transition and Hypoxia compared with Fresh. It is notable however, that these inflammatory pathways were enriched to a lesser extent in modified Steen post-EVLP compared to Fresh (Figure 3.5B).

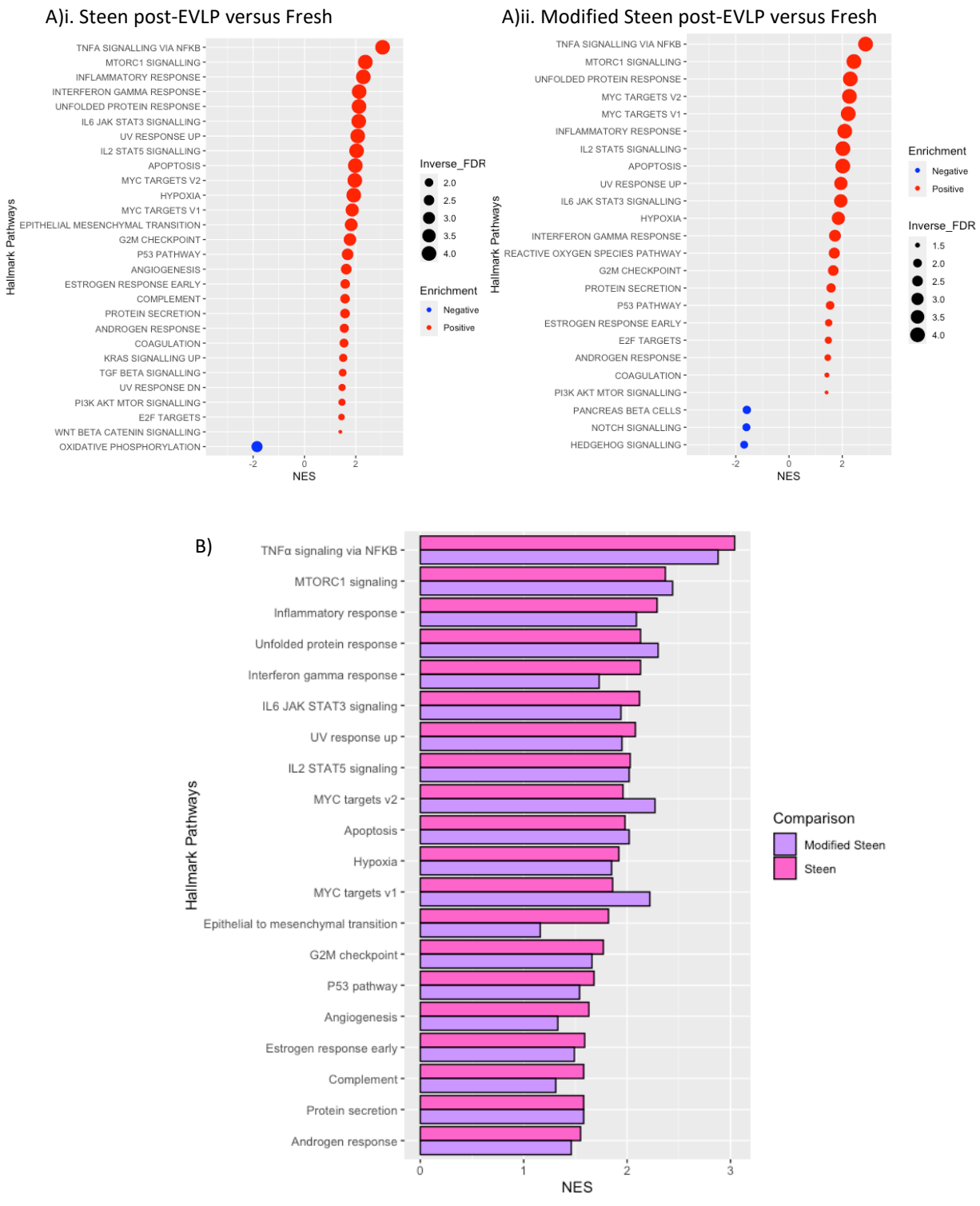

Figure 3.5. Gene set enrichment analysis of RNA-seq data from post-EVLP samples compared to Fresh.

Graphs depict pathways which were significantly positively (red) or negatively (blue) enriched in **Ai)** lungs perfused with Steen compared to Fresh lungs and **Aii)** lungs perfused with modified Steen compared to Fresh lungs. Pathways shown had an FDR p value of <0.05. The graph shows NES along the X-axis and the size of each point corresponds to the inverse of the FDR p value. **B)** Comparison of normalised enrichment scores (NES) between Steen post-EVLP compared with Fresh (pink) and modified Steen post-EVLP compared with Fresh (purple). Depicted are the top 20 pathways for Steen vs Fresh. The graph shows NES along the X axis and hallmark pathways along the Y axis. Depicted are pathways which had an FDR p value of <0.05 between at least one of the comparisons. N=4 (Fresh), N=5 (Steen), N=5 (modified Steen).

3.3.2.4. Gene set enrichment analysis of modified Steen versus Steen post-EVLP samples

Direct comparison of post-EVLP samples identified 2 significantly positively enriched pathways and 12 significantly negatively enriched pathways in modified Steen compared to standard Steen (Figure 3.6). The top two significant negatively enriched pathways in modified Steen were the Epithelial Mesenchymal Transition (NES=-1.90, FDR=0.003) and the TNF-α signalling via NFκB (NES=-1.85, FDR=0.004) pathways. The top two most significantly positively enriched pathways were the oxidative phosphorylation (NES=2.48, FDR 0.000) and reactive oxygen species (NES=1.53, FDR=0.037) pathways.

Figure 3.6. Gene set enrichment analysis of RNA-sequencing data from Modified Steen compared with Steen.

Graph depicting pathways which were significantly positively (red) or negatively (blue) enriched in lungs perfused with modified Steen when compared to lungs perfused with Steen. Pathways shown had an FDR p value of <0.05. The graph shows normalised enrichment score (NES) along the X-axis and the size of each point corresponds to the inverse of the FDR p value. N=5 (Steen), N=5 (modified Steen).

Figure 3.7 explores the epithelial to mesenchymal transition and the TNF-α signalling via NFκB pathways in more detail. Enrichment plots of the epithelial to mesenchymal transition pathway (Figure 3.7Ai) and the TNF-α signalling via NFκB pathway (Figure 3.7Bi) show negative correlation with the modified Steen phenotype.

For heatmaps, z scores were calculated using normalised TPM counts. Z score gives an indication of how much the count for that sample varies from the mean for a given gene. Positive z scores indicate an increased expression compared to the mean and negative z scores indicate reduced expression. The top 50 leading edge genes for the top 2 significantly negatively enriched pathways are depicted in Figure 3.7Aii and 3.7Bii and include various inflammatory genes such as *TNFAIP3, IL6, IL1A*, various cadherin genes eg. *CDH11* and *CDH6,* chemokine genes such as *CXCL8* and *CXCL12* and endothelial adhesion molecule genes, such as *ICAM1*. Generally, z scores for modified Steen samples appeared lower than z scores for Steen samples.

Figure 3.8Ai and 3.8Bi show positive correlation of the Oxidative phosphorylation and Reactive oxygen species pathways with the modified Steen phenotype respectively. As depicted in heatmaps in Figures 3.8Aii and 3.8Bii, the leading edge genes in these pathways were generally antioxidant genes such as *PRDX3, PRDX4, GPX3, SOD1* and *HMOX2*. Also involved in the core enrichment were genes such as *NDUFB1, NDUFS2* and *NDUFB4* (all of which encode different subunits of the mitochondrial respiratory chain complex NADH dehydrogenase), and tyrosine kinase gene *FES* (which has roles in cell spreading and regulation of the actin cytoskeleton). Generally, z scores for modified Steen samples appeared higher than z scores for Steen samples.

A) i.

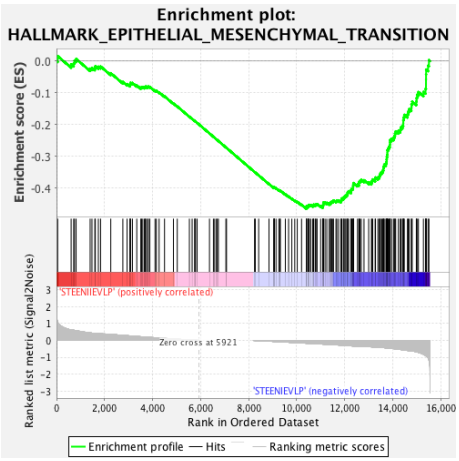

ii. Epithelial to mesenchymal transition

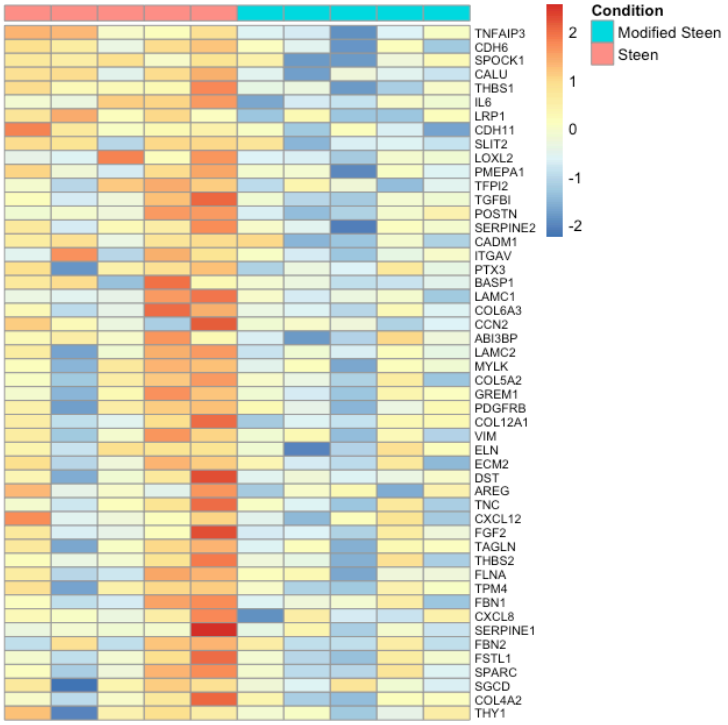

B) i.

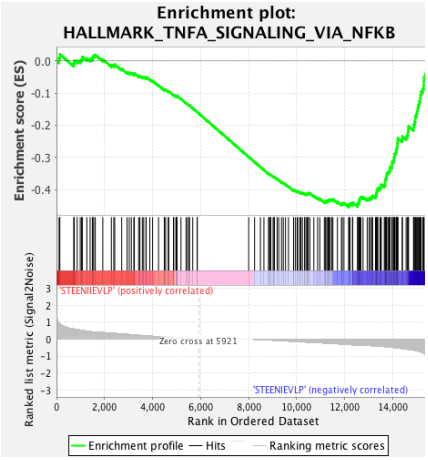

ii. TNF-α signaling via NFκB

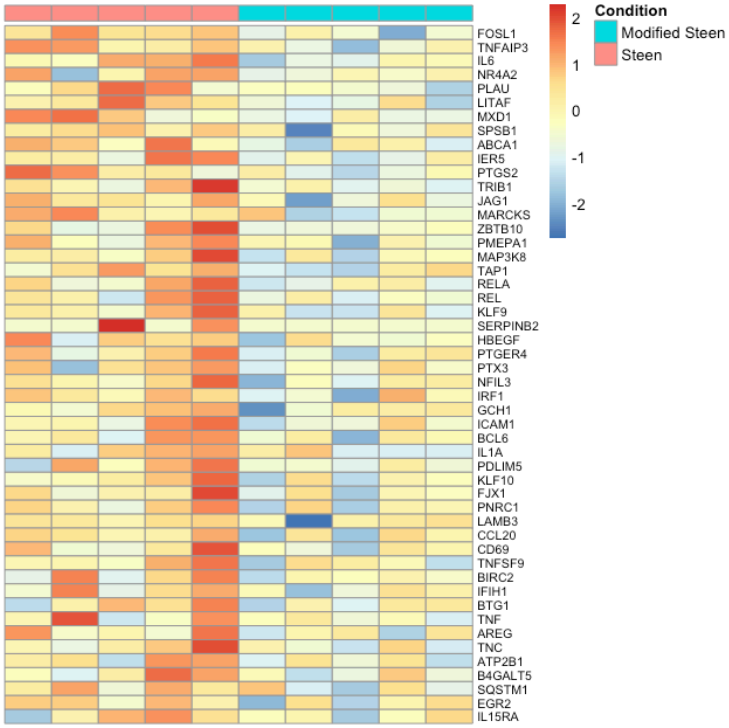

Figure 3.7. Top negatively significantly enriched pathways in modified Steen versus Steen.

The top two pathways with the lowest enrichment scores in modified Steen vs Steen were examined in more detail. Depicted are enrichment plots of the **Ai)** Epithelial to mesenchymal transition pathway and **Bi)** TNF-α signalling via NFκB pathway. Enrichment plots show correlation of the pathway with a particular phenotype. 'STEENIIEVLP' = modified Steen and 'STEENIEVLP" = Steen. Also shown are heatmaps of the top 50 leading edge genes involved in the core enrichment of the hallmark **Aii)** Epithelial to mesenchymal transition and **Bii)** TNF-α signalling via NFκB pathways. Depicted are z scores of each sample for each gene. Red= Positive z scores. Blue= Negative z score.

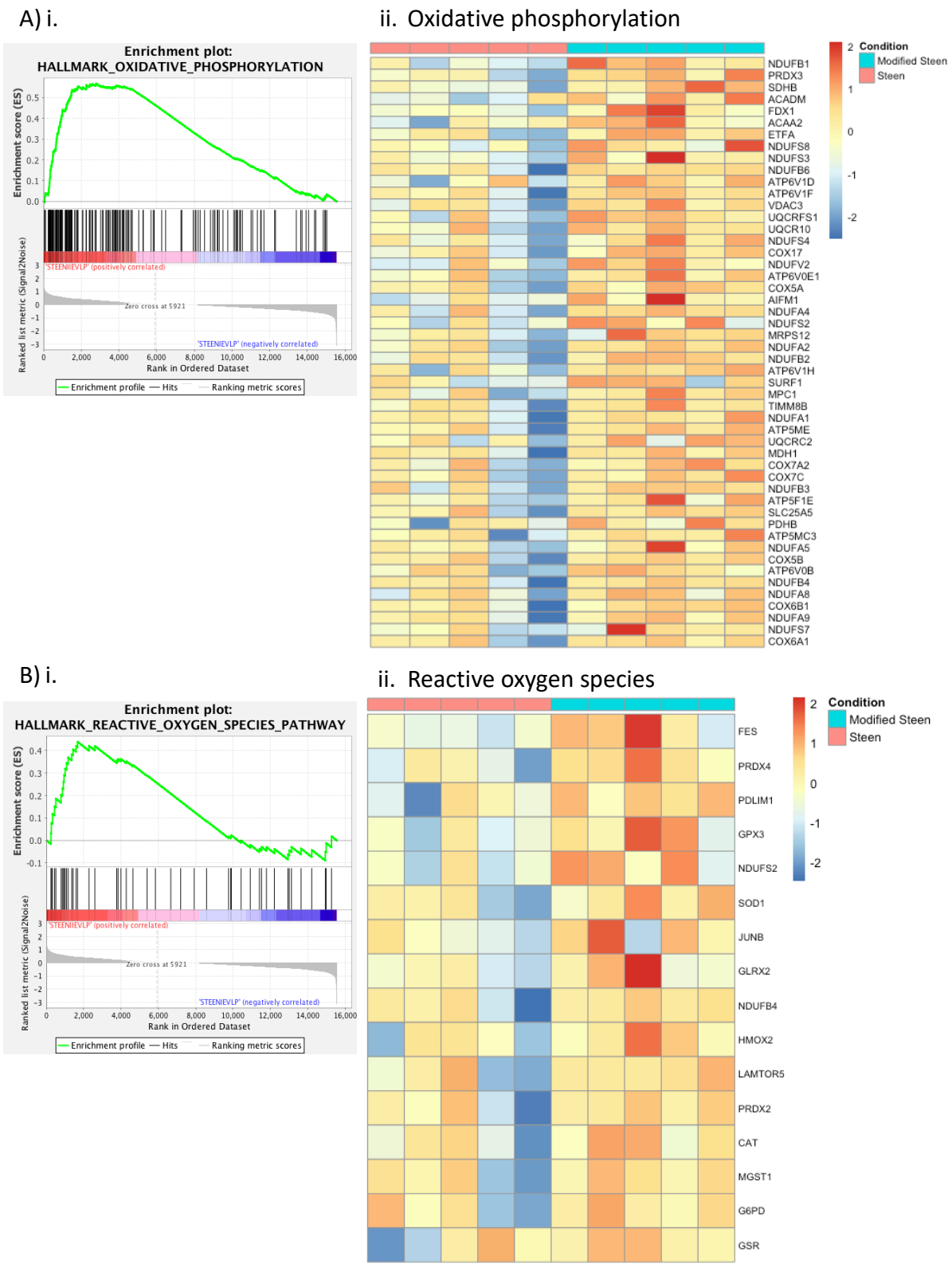

Figure 3.8. Top positively significantly enriched pathways in modified Steen versus Steen.

The top two pathways with the highest enrichment scores in modified Steen vs Steen were examined in more detail. Depicted are enrichment plots of the **Ai)** Oxidative phosphorylation and **Bi)** Reactive oxygen species pathways. Enrichment plots show correlation of the pathway with a particular phenotype. 'STEENIIEVLP' = modified Steen and 'STEENIEVLP" = Steen. Also shown are heatmaps of the top 50 leading edge genes involved in the core enrichment of the hallmark **Aii)** Oxidative phosphorylation and **Bii)** Reactive oxygen species pathways. Depicted are z scores of each sample for each gene. Red= Positive z scores. Blue= Negative z score.

3.3.2.5. Ingenuity pathway analysis

As well as GSEA, IPA was carried out. IPA data goes even further than GSEA by not only identifying pathways that are enriched, but suggesting whether these are activated or inhibited by calculating a z-score unique to IPA. When modified Steen post-EVLP versus standard Steen post-EVLP dataset was entered into the software, only one gene met the cut offs applied to the core analyses and therefore, a direct comparison was not made between the two. Instead, a core analysis was carried out for standard Steen post-EVLP versus Fresh and modified Steen post-EVLP versus Fresh and these were compared.

Our analysis revealed a highly significant overlap of genes with 160 pathways for standard Steen post-EVLP vs Fresh and 164 pathways for modified Steen post-EVLP versus Fresh as depicted ($p<0.05$). Figure 3.9Ai and 9Bi show the top 20 most significantly enriched pathways for standard Steen post-EVLP versus Fresh and modified Steen post-EVLP versus Fresh respectively. Despite using a different pathways database to GSEA, IPA showed similar findings in that the pathways identified had roles in driving or resolving inflammation, oxidative stress and cancer signalling. For standard Steen versus Fresh, IL-10 signalling (p=5.62341325e-8) and Tumour necrosis factor receptor (TNFR)1 signalling (p=4.16869383e-7) were the two most significantly enriched pathways, whilst for modified Steen versus Fresh, TNFR2 signalling (p=1.14815362e-8) and IL-10 signalling (p=2.51188643e-8) were the two most significant.

As previously discussed, IPA provides a z-score which informs the user of the activation status of the enriched pathway. Figure 3.9Aii and 9Bii depict the top 20 most significant pathways ordered by z score for standard Steen post-EVLP versus Fresh and modified Steen post-EVLP versus Fresh respectively. Comparison of standard Steen post-EVLP with Fresh identified inflammatory pathways such as the Tumour microenvironment pathway (z-score =3.9, p=0.0000062) and the IL-6 signalling pathway (z-score =3.153, p=0.0000069) and cellular stress pathways such as the unfolded protein response pathway (z-score =3.162, p=0.000017) among the top 3 most activated pathways. These pathways were not the top pathways for modified Steen post-EVLP versus Fresh; Dendritic cell maturation (z-score =3.207, p=0.0017), Type I diabetes mellitus signalling (z-score =2.887, p=0.000021) and high motility group box 1 (HMGB1) signalling (z-score =2.714, p=0.00042) had the highest z-scores, whilst endothelial nitric oxide (eNOS) signalling (z-score =-2.53, p=0.0028) and peroxisome proliferator-activated receptor (PPAR) signalling (z-score =-2.53, p=0.00028) were inhibited.

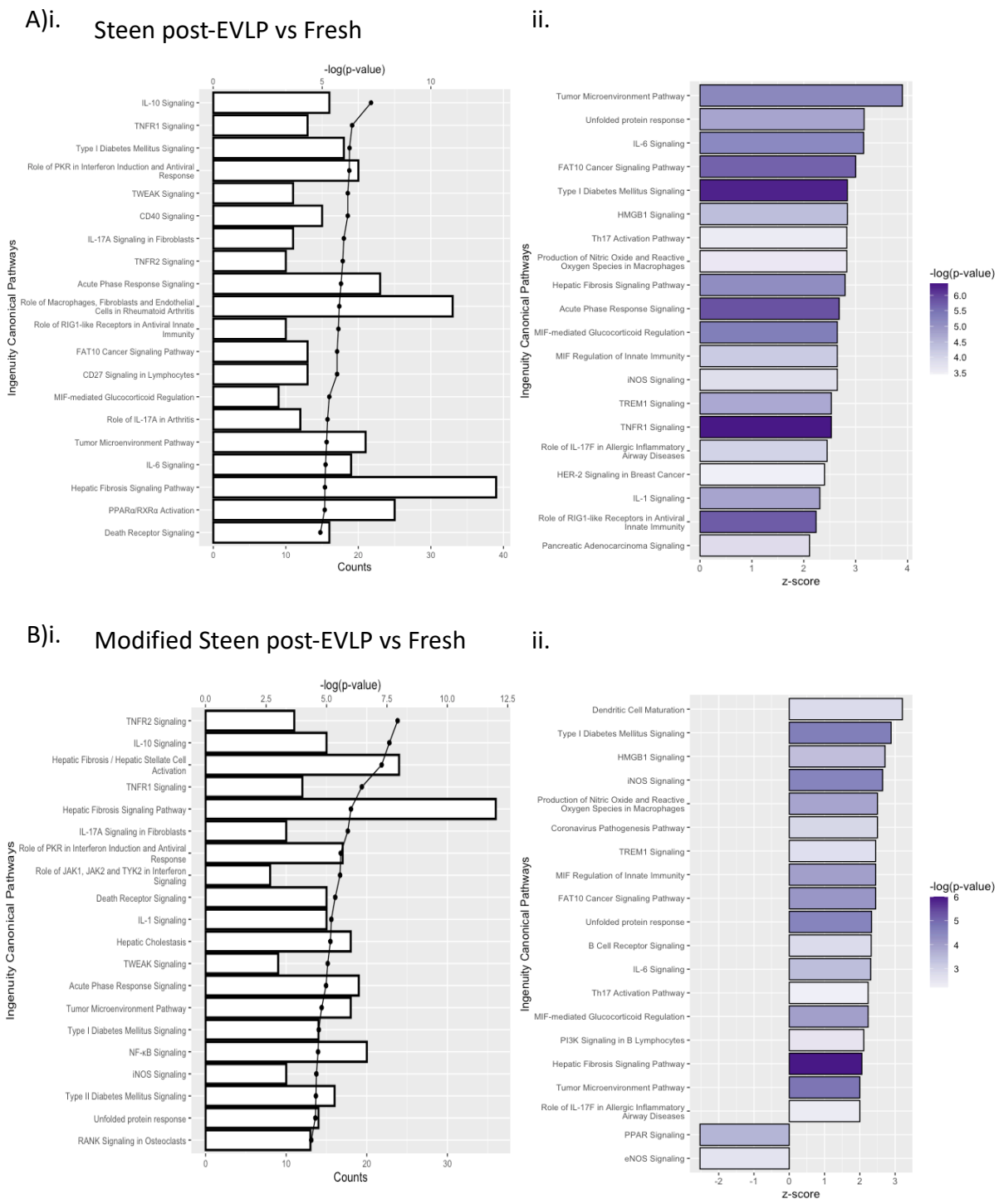

Figure 3.9. Ingenuity pathway analysis.

Gene thresholds for IPA were set as a fold change ratio of ≥ 1 or ≤ -1 and an FDR q value <0.05. Depicted is IPA for **A)** Steen post-EVLP samples versus Fresh samples and **B)** Modified Steen post-EVLP samples versus Fresh samples. **i)** The top 20 most significant pathways irrespective of z-score. Bottom x = gene count, top x = inverse log p value, y = Ingenuity canonical pathways. Bars refer to gene count whilst the line graph refers to inverse log p value. **ii)** The 20 most significant pathways with z-scores ≥ 2 or ≤ -2 are depicted. x = z-score and y = ingenuity canonical pathways. Bars are coloured according to inverse of the log P value. N=4 (Fresh), N=5 (Steen), N=5 (modified Steen). P values were calculated as part of the core analysis using Fischer's exact test.

A comparative analysis was then performed, which allowed comparison between the core analysis of standard Steen post-EVLP versus Fresh and the core analysis of modified Steen post-EVLP versus Fresh. A comparison of the z scores for significant pathways identified is depicted in Figure 3.10A. Pathways showing the most difference between the core analyses were the Tumour microenvironment pathway (z-score: 3.9 vs 2), IL-6 signalling, (z-score: 3.15 vs 2.31) TNFR1 signalling (z-score: 2.53 vs 1.67) and Acute Phase response signalling (z-score: 2.68 vs 1.5), all of which were activated to a lesser extent in modified Steen versus Fresh than standard Steen versus Fresh.

Figure 3.10Bi-iv show each top pathway with a breakdown of the genes involved in the overlap and the log2FC when comparing each post-EVLP group to Fresh. Commonly depicted across all of the top four pathways are various inflammatory genes such as *IL6, TNFAIP3,* NFκB transcription factor complex genes and NFκB inhibitor genes. These genes had higher fold change values compared to Fresh in standard Steen samples than modified Steen.

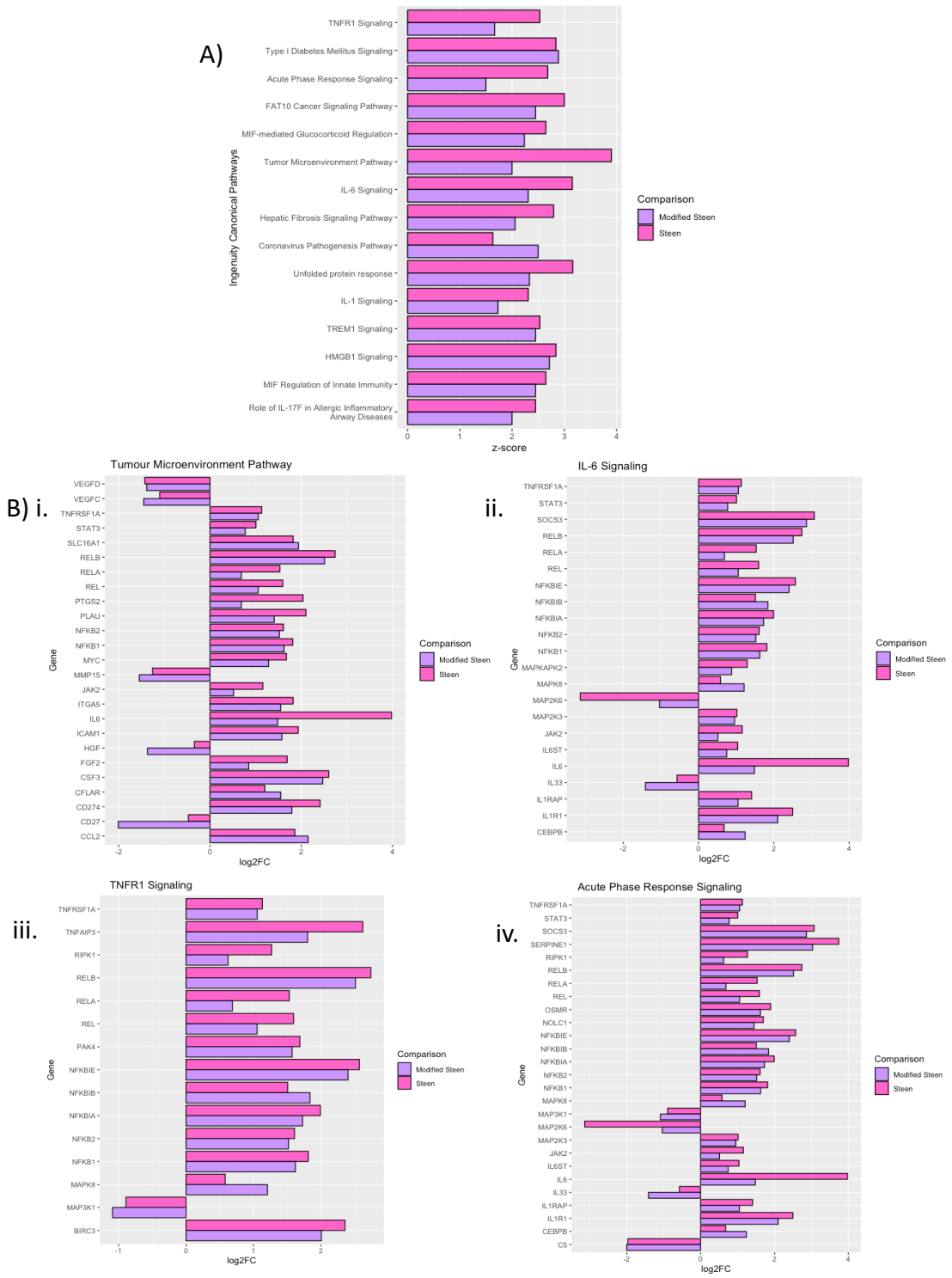

Figure 3.10. IPA comparative analysis.

A comparative analysis within IPA allows you to directly compare z scores of multiple core analyses**. A)** Comparison of z-scores between Steen post-EVLP vs. Fresh (pink) and modified Steen post-EVLP vs. Fresh (purple). Shown are the 20 most significant pathways for Steen versus Fresh with a z-score of ≥ 2 or ≤ -2 for at least one of the comparisons to Fresh. x = z-score and y = ingenuity canonical pathways. **B)** Fold change values were then compared between Steen post-EVLP vs. Fresh (pink) and modified Steen post-EVLP vs. Fresh (purple) in **Bi)** the Tumour Microenvironment Pathway, **Bii)** IL-6 signalling pathway, **Biii)** TNFR1 Signalling Pathway and **Biv)** the Acute Phase response pathway. Pathways selected were four of the most significant with the greatest difference between comparisons. The graphs show log2 fold change along the x axis and genes along the y axis. N=4 (Fresh), N=5 (Steen), N=5 (modified Steen). P values were calculated as part of the core analysis using Fischer's exact test.

3.3.3. Validation of top genes identified in gene expression and pathway analysis

As genes which played a significant role in pathways identified in both GSEA and IPA, *IL6* and *TNFAIP3* were validated using qPCR. *IL6* is a well-known pro-inflammatory cytokine gene and *TNFAIP3* is a gene which is induced in response to TNF-α signalling in endothelial cells (Das *et al*., 2018).

As shown in Figure 3.3A, RNA-sequencing data showed no significant difference between gene expression of *TNFAIP3* or *IL6* when directly comparing modified Steen and standard Steen post-EVLP.

However, there was a significant increase in *TNFAIP3* expression compared to Fresh for standard Steen post-EVLP (Figure 3.3B; log2FC=2.62, adjusted p=1.30E-17) and modified Steen post-EVLP (Figure 3.3C; log2FC=1.80, adjusted p=3.27E-08), albeit to a greater extent for standard Steen. Much like *TNFAIP3, IL6* showed a significant increase when comparing standard Steen post-EVLP to Fresh (Figure 3.3B; log2FC=3.98, adjusted p=1.13E-05), whilst expression in modified Steen samples was not significantly different to Fresh (Figure 3.3C). Accordingly, counts per million (CPM) values from RNA-sequencing for *IL6* (Figure 3.11Ai) and *TNFAIP3* (Figure 3.11Bi) showed that standard Steen post-EVLP samples had increased expression, whilst Fresh and modified Steen post-EVLP samples had comparably much lower counts. qPCR data confirmed this; standard Steen samples had significantly higher expression of both *IL6* (Figure 3.11Aii) and *TNFAIP3* (Figure 3.11Bii) compared to Fresh, whilst modified Steen samples were not significantly different to Fresh.

As leading edge genes in pathways positively enriched in modified Steen versus standard Steen post-EVLP, an attempt was also made to validate *NDUFB1, PRDX4* and *FES* using qPCR.

Although RNA-sequencing revealed no significant difference in fold change of gene expression of *NDUFB1, PRDX4* and *FES* between modified Steen and standard Steen post-EVLP (Figure 3.3A), visualisation of CPM values did suggest a trend of higher counts in modified Steen (Figure 3.12Ai, 3.12Bi and 3.12Ci). This directly contrasts with the trend depicted in qPCR data, which suggested expression of these genes was lower in modified Steen than standard Steen (Figure 3.12Aii, 3.12Bii and 3.12Cii). In fact, for *NDUFB1*, modified Steen had significantly lower expression than Fresh, whilst standard Steen was comparable (Figure 3.12Aii). Due to an inability to validate these genes, they were not carried forward for further study.

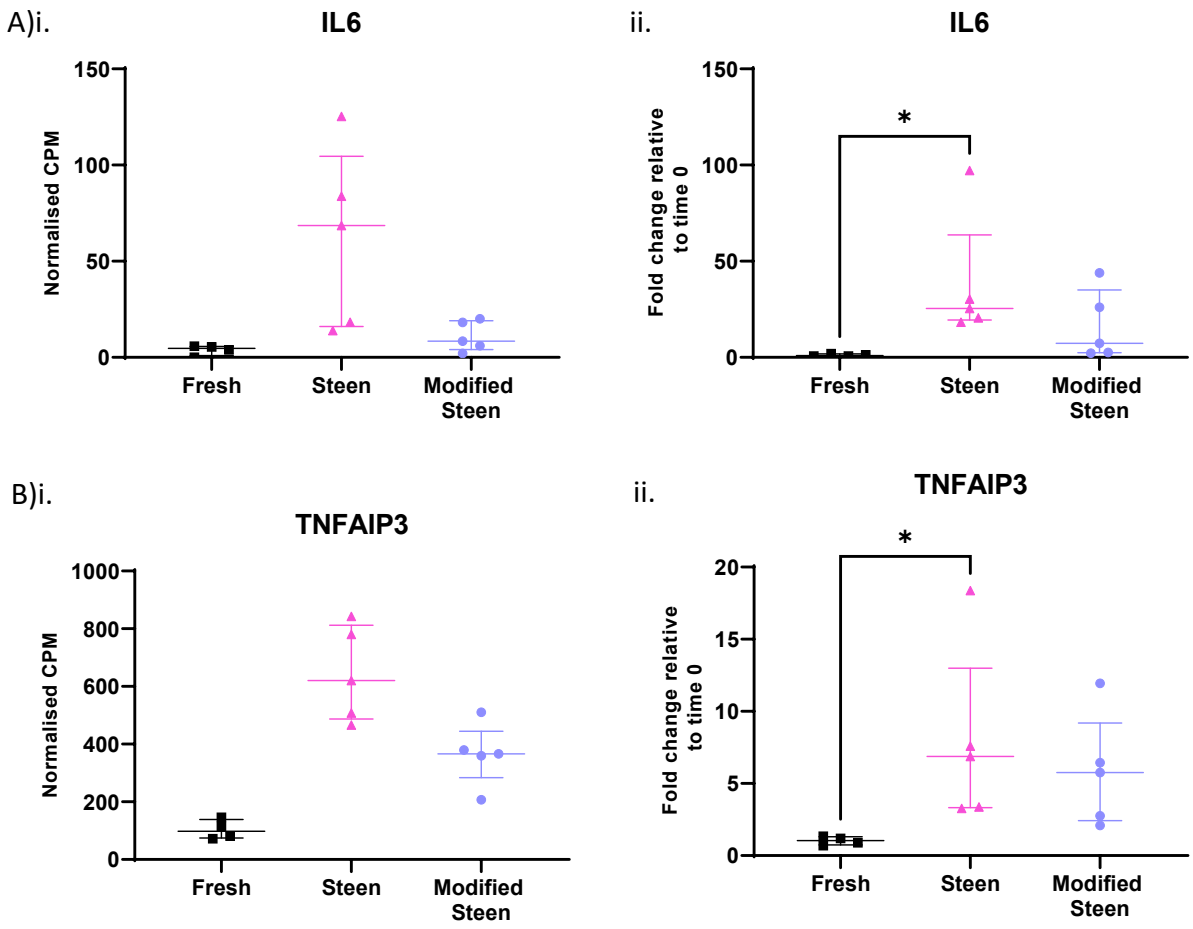

Figure 3.11. Genes which were successfully validated from 3" RNA-sequencing analysis and GSEA.

i) Depicted is normalised counts per million (CPM) values from RNA-sequencing and **ii)** qPCR gene expression data for **A)** *IL6*, **B)** *TNFAIP3*, which are top leading edge genes that appeared in the most significantly positively and negatively enriched pathways in modified Steen vs Steen from GSEA. For qPCR data, gene expression is depicted as relative to Fresh. N=4 (Fresh), N=5 (Steen), N=5 (modified Steen). To calculate statistical significance for RT-qPCR a non-parametric one-way ANOVA was used. Median is presented with interquartile range. *p<0.05.

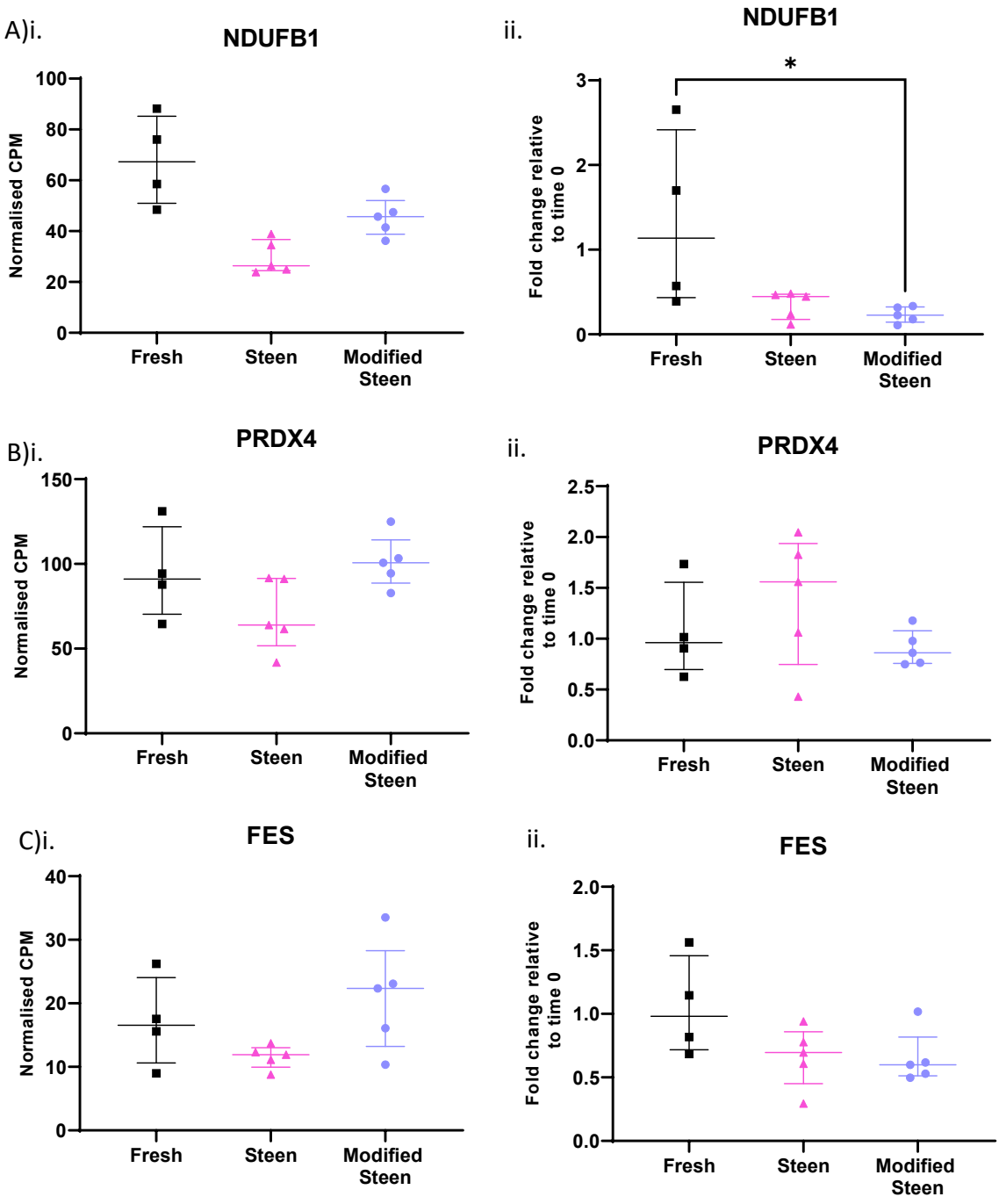

Figure 3.12. Genes which were not successfully validated from 3" RNA-sequencing analysis and GSEA.

i) Depicted is normalised counts per million (CPM) values from RNA-sequencing and **ii)** qPCR gene expression data for **A)** *NDUFB1*, **B)** *PRDX4* and **C)** *FES* which are top leading edge genes that appeared in the most significantly positively and negatively enriched pathways in Modified Steen vs Steen from GSEA. For qPCR data, gene expression is depicted as relative to Fresh. N=4 (Fresh), N=5 (Steen), N=5 (modified Steen). To calculate statistical significance for RT-qPCR a non-parametric one-way ANOVA was used. Median is presented with interquartile range. *p<0.05.

3.3.4. Protein release during perfusion

ELISA was used to quantify IL-6 (Figure 3.13) and TNF-α (Figure 3.14) protein levels in perfusates from lungs perfused with standard Steen or modified Steen. Immediately following solution exchange, cytokine levels of both TNF-α and IL6 were relatively negligible in both groups. Whilst not significant, modified Steen samples showed a trend towards lower levels of both IL-6 and TNF-α compared to standard Steen (Figure 3.13A and 3.14B respectively). Interestingly, levels of IL-6 and TNF-α at 4 hours were significantly higher than the 1 hour start time in standard Steen samples (Figure 3.13Bi and 3.14Bi), whilst modified Steen showed no significant increase over time (Figure 3.13Bii and 3.14Bii).

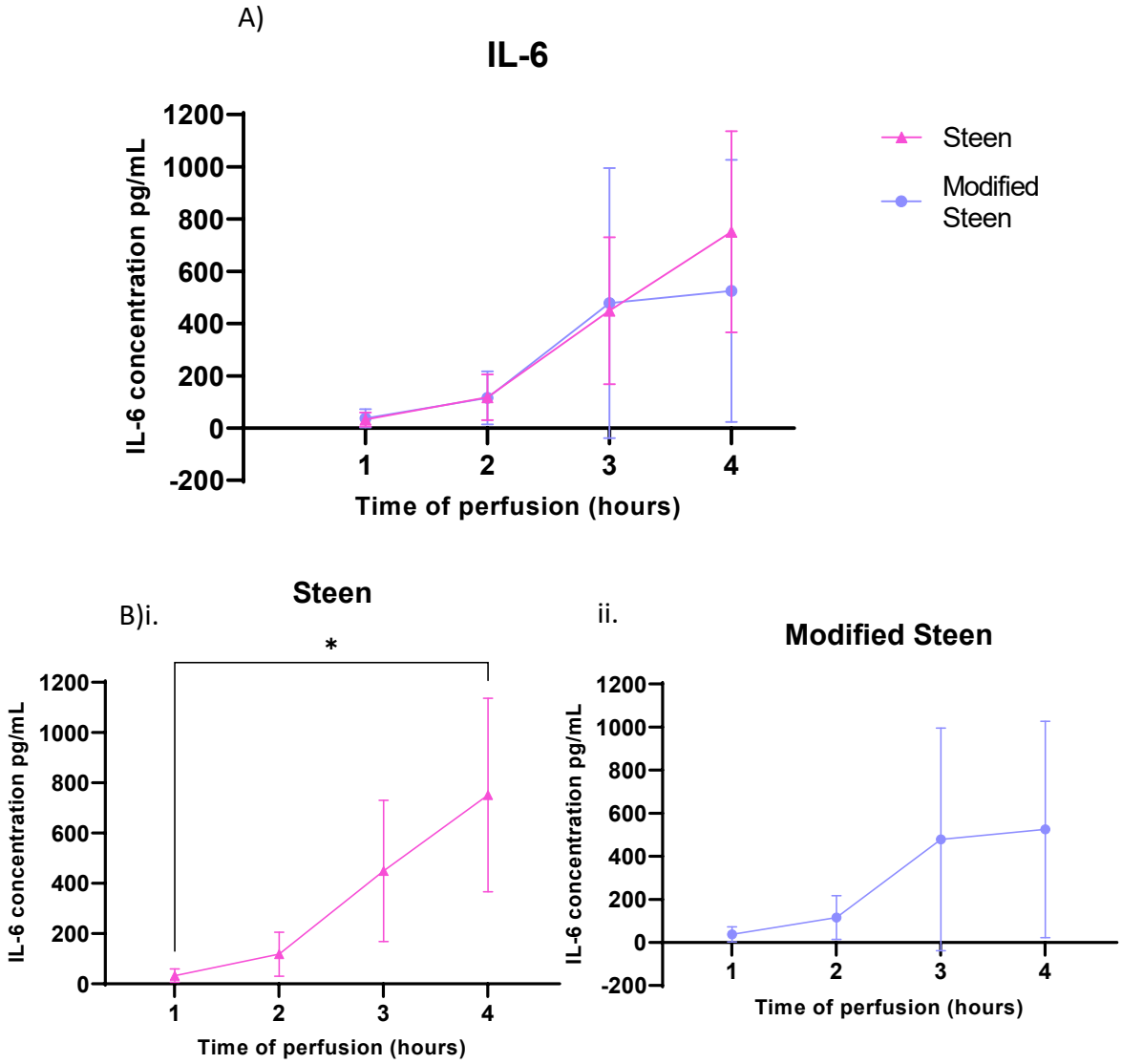

Figure 3.13. IL-6 release during EVLP.

Protein levels of IL-6 in perfusate from lungs perfused with Steen or modified Steen were measured using ELISA and compared. **A)** IL-6 levels in perfusate measured in pg/mL over time during perfusion with Steen or modified Steen. Perfusate samples were taken hourly immediately following the solution exchange after the first hour of heating. A two-way mixed effects ANOVA was used to calculate statistical significance between modified Steen and Steen overall. **B)** IL-6 levels in perfusate measured in pg/mL over time during perfusion with **i)** Steen or **ii)** Modified Steen. To determine statistical significance over time, a one-way mixed effects ANOVA with multiple comparisons test was used. Instead of using repeated measures, we analysed the data instead by fitting a mixed model as implemented in GraphPad Prism 8.0 to accommodate for missing values due to a missing perfusate sample (EVLP2 modified Steen, time point 3 hours). This mixed model uses a compound symmetry covariance matrix and is fit using Restricted Maximum Likelihood (REML). In the absence of missing values, this method gives the same P values and multiple comparisons tests as repeated measures ANOVA. In the presence of missing values (missing completely at random), the results can be interpreted like repeated measures ANOVA. N=5 per group (except missing value). Mean is presented with standard deviation. *p<0.05

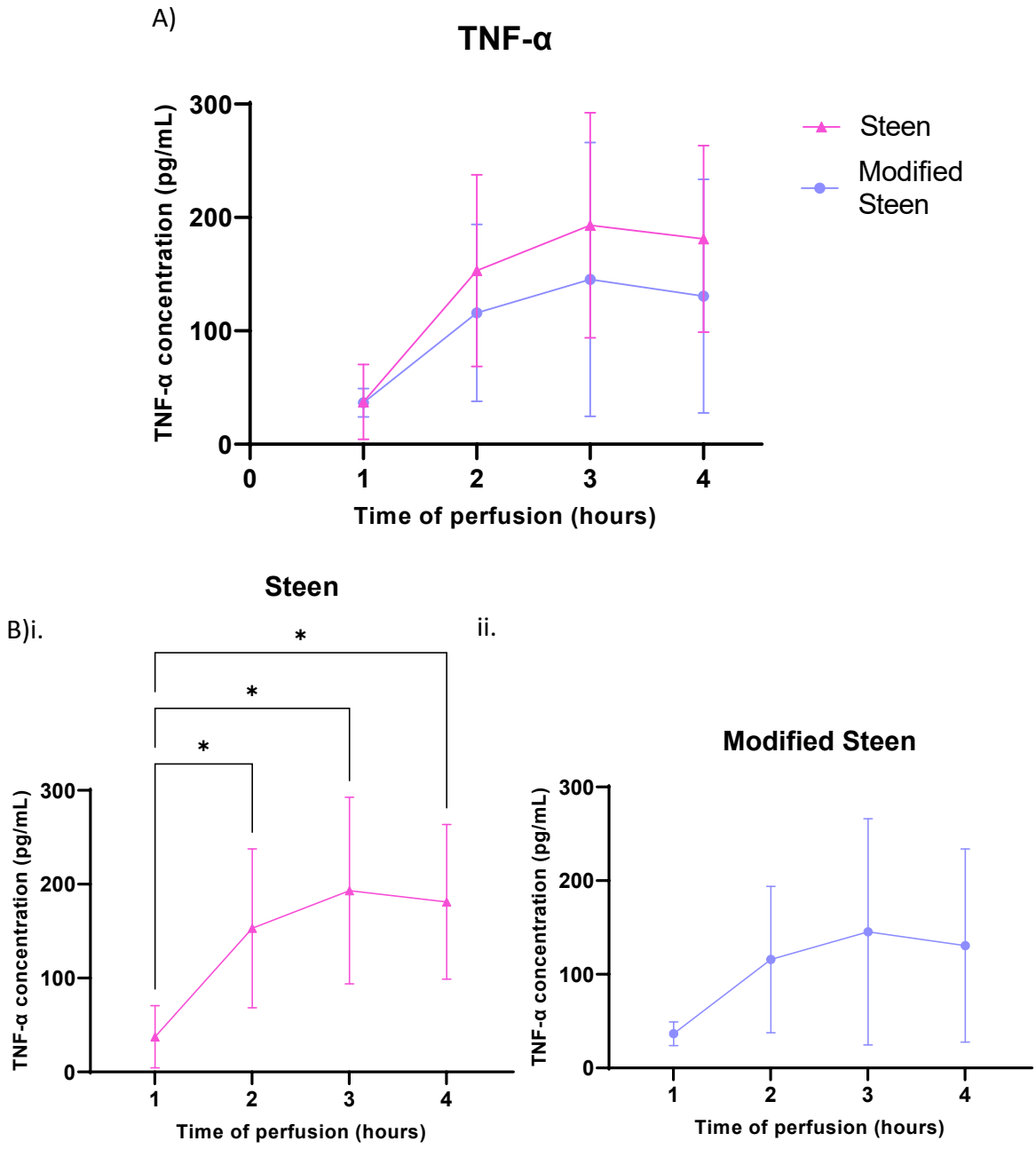

Figure 3.14. TNF-α release during EVLP

Protein levels of TNF-α in perfusate from lungs perfused with Steen or modified Steen were measured using ELISA and compared. **A)** TNF-α levels in perfusate measured in pg/mL over time during perfusion with Steen or modified Steen. Perfusate samples were taken hourly immediately following the solution exchange after the first hour of heating. A two-way mixed effects ANOVA was used to calculate statistical significance between modified Steen and Steen overall. **B)** TNF-α levels in perfusate measured in pg/mL over time during perfusion with **i)** Steen or **ii)** Modified Steen. To determine statistical significance over time, a one-way mixed effects ANOVA with multiple comparisons test was used. Instead of using repeated measures, we analysed the data instead by fitting a mixed model as implemented in GraphPad Prism 8.0 to accommodate for missing values due to a missing perfusate sample (EVLP2 modified Steen, time point 3 hours). This mixed model uses a compound symmetry covariance matrix and is fit using Restricted Maximum Likelihood (REML). In the absence of missing values, this method gives the same P values and multiple comparisons tests as repeated measures ANOVA. In the presence of missing values (missing completely at random), the results can be interpreted like repeated measures ANOVA. N=5 per group (except missing value). Mean is presented with standard deviation. *p<0.05

3.3.5. Artery and vein gene expression during perfusion

Due to the significance of sphingosine-1-phosphate-receptor 1 (S1PR1) and vascular endothelial (VE)-cadherin in vascular integrity, the impact of standard Steen and modified Steen on the genes encoding their expression was assessed in vein and artery samples collected following EVLP. qPCR was used to assess gene expression of *S1PR1* and *CDH5*. Whilst no significant difference between any of the groups was identified, there was a trend towards increased expression of vein *S1PR1* (Figure 3.15Ai) and *CDH5* (Figure 3.15Aii) and artery *S1PR1* (Figure 3.15Bi) and *CDH5* (Figure 3.15Bii) in samples following perfusion with modified Steen compared to Fresh and standard Steen samples. Compared to Fresh samples, standard Steen post-EVLP samples showed comparable vein *S1PR1* expression (Figure 3.15Ai), with a trend towards a slight increase in artery *S1PR1* expression (Figure 3.15Bi). Vein *CDH5* expression seemed slightly higher than Fresh (Figure 3.15Aii), whilst artery *CDH5* expression tended to be slightly lower (Figure 3.15Bii).

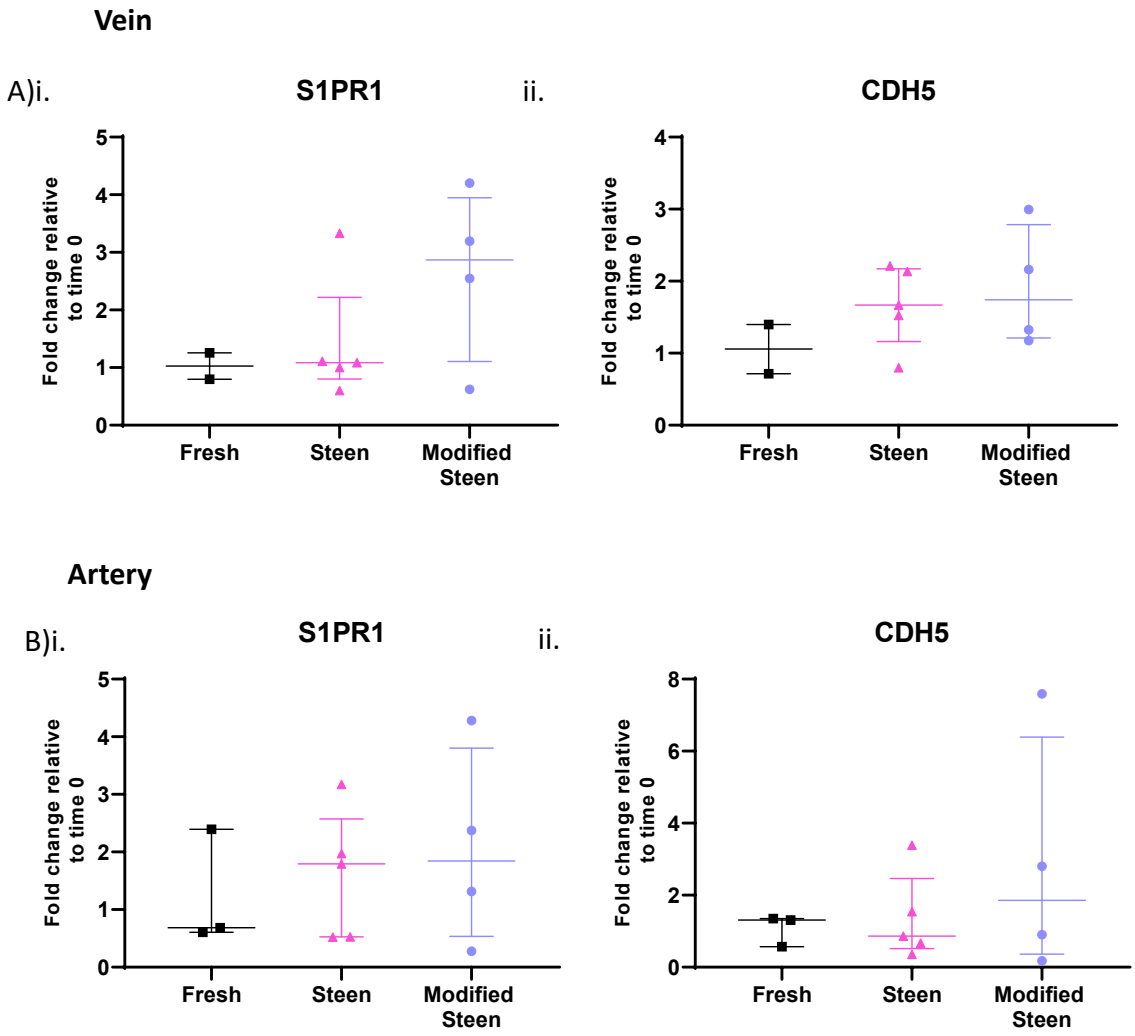

Figure 3.15. *S1PR1* and *CDH5* gene expression in artery and vein.

A) qPCR was used to calculate gene expression of **i)** *S1PR1* and **ii)** *CDH5* in vein samples collected post-EVLP. N=2 (Fresh), N=5 (Steen post-EVLP), N=4 (modified Steen post-EVLP). **B)** qPCR was used to calculate gene expression of **i)** S1PR1 and **ii)** CDH5 in artery samples collected post-EVLP. N=3 (Fresh), N=5 (Steen), N=4 (modified Steen). Samples numbers are based on samples that were collected and sent over by XVIVO. Gene expression is depicted as relative to Fresh. To calculate statistical significance for RT-qPCR a non-parametric one-way ANOVA was used. Median is presented with interquartile range. *p<0.05.

3.4. Discussion

EVLP has the potential to improve the utilisation of ECD lungs by assessing and identifying those with good function and reconditioning the non-transplantable through the application of appropriate therapeutics. This could increase the number of lung transplantations that take place annually and improve waiting list mortality. Due to the potential of EVLP, limiting damaging oxidative and inflammatory processes during reperfusion is vital to improve evaluation and to allow longer and more advanced therapeutic strategies. This chapter aimed to assess the effectiveness of a new perfusate solution identified as modified Steen compared to standard Steen in limiting lung injury during porcine EVLP. Post-EVLP samples were also compared to Fresh samples taken during retrieval in order to better understand the pathways and processes that occur during IRI.

Unsupervised analysis in Figure 3.3 revealed no distinct clustering of modified Steen and standard Steen, but rather showed a separation between Fresh samples and post-EVLP. Volcano plots also revealed that 436 and 391 genes were differentially expressed in standard Steen and modified Steen post-EVLP versus Fresh respectively. Amongst the DEGs were various genes involved in acute inflammation. This was somewhat unsurprising due to the pro-inflammatory nature of IRI, especially as our model had a long CIT. Indeed, it has been widely shown that cytokine gene expression in lung tissue is increased following cold ischaemia (Kaneda *et al*., 2005) and EVLP (Lonati *et al*., 2018, van Zanden *et al*., 2021, Ferdinand *et al*., 2022) and that local inflammatory responses increase with CIT duration and significantly after reperfusion (Iskender *et al*., 2018).

GSEA revealed that the top significantly positively enriched pathway for both standard Steen and modified Steen post-EVLP versus Fresh was TNF-α signalling via NFκB. TNF-α is key in initiating the inflammatory cascade during IRI. In fact, it has been suggested to be one of the most important mediators for complete lung IRI development (Krishnadasan *et al*., 2003, Eppinger *et al*., 1997) and Naidu *et al* demonstrated that it is released by alveolar macrophages as early as 15 minutes after reperfusion (Naidu *et al*., 2004). Furthermore, blockade of TNF-α signalling with an antibody almost halved lung vascular injury (Krishnadasan *et al*., 2003). Thus, our GSEA data corroborates these studies by identifying TNF-α signalling as the most significant in post-EVLP samples compared with Fresh.

Comparison of standard Steen and modified Steen post-EVLP with Fresh using IPA showed similar findings to GSEA in terms of pathway enrichment; TNFR1 and 2 signalling were significantly enriched in post-EVLP samples. TNFR1 and 2 are the key receptors that TNF-α signals through. Additionally, IPA allows prediction of the activation state of enriched pathways. Specifically, inflammatory and oxidative pathways were identified to be activated in post-EVLP samples, with the Tumour microenvironment pathway, unfolded protein response, IL-6 signalling and production of nitric oxide and reactive oxygen species in macrophages all being activated in post-EVLP samples in line with the characteristic pathology of IRI.

As well as underpinning the mechanisms behind IRI, comparing the extent of change of post-EVLP samples from Fresh samples was helpful to validate the effectiveness of modified Steen. Modified Steen post-EVLP had fewer DEGs and significantly enriched inflammatory and oxidative stress related gene sets than standard Steen post-EVLP when both were compared to Fresh samples. Indirectly comparing the two with GSEA and IPA also showed reduced normalised enrichment scores and reduced activation of the inflammatory pathways that were identified.

When directly comparing modified Steen and standard Steen post-EVLP samples, only one gene was found to be significantly differentially expressed; *CYP26B1* was upregulated in modified Steen perfused lungs. This is probably due to the fact that *CYP26B1* is involved in the metabolism of RA (Stoney *et al*., 2016), which is one of the novel components of modified Steen. RA has well established immunomodulatory functions (Orfanos and Bauer, 1983, Brinckerhoff *et al*., 1983, Fumarulo *et al*., 1991) and has been successfully used to treat inflammatory disorders such as lupus nephritis (Kinoshita *et al*., 2003), psoriasis (Ward *et al*., 1983) and arthritis (Nozaki *et al*., 2006). Additionally, modified Steen contains SA, which exerts its anti-inflammatory properties primarily through inhibition of NFκB (Kopp and Ghosh, 1994, Yin *et al*., 1998, Bayón *et al*., 1999). RA has also been shown to modulate the toll-like receptor 4 (TLR4)/NF-κB signalling pathway, causing downregulation of NOS2 and TNF-α (Rafa *et al*., 2017).

In light of this, it is unsurprising that TNF-α signalling via NFκB was one of the most significantly negatively enriched pathways in modified Steen following GSEA. This could indicate that the limitation of lung injury achieved via perfusion with modified Steen is

primarily exerted through inhibition of key transcription factor NFκB, which is usually initiated very early on in IRI. Indeed, alongside TNF-α, NFκB is one of the most important mediators of IRI (Eppinger *et al*., 1997, Krishnadasan *et al*., 2003) and its blockade during EVLP has been shown to mediate protection from reperfusion injury (Francioli *et al*., 2017, Weathington *et al*., 2018). Blockade of NFκB is protective as it inhibits the activation of pro-inflammatory cytokines downstream, reducing inflammatory injury and cell death.

Accordingly, the comparative analysis performed using IPA identified reduced activation of inflammatory pathways in modified Steen post-EVLP versus Fresh compared to standard Steen post-EVLP versus Fresh. Whilst the genes involved in these pathways were primarily genes involved in driving inflammation such as pro-inflammatory cytokine genes *IL6* and *TNFAIP3*, which is induced in response to TNF-α signalling, what was most notable was the involvement of NFκB transcription factor complex genes and NFκB inhibitor genes in these pathways. These genes generally had higher fold changes from Fresh in standard Steen post-EVLP compared to modified Steen post-EVLP, again suggesting a role for NFκB in the protection mediated by modified Steen.

Furthermore, in support of IPA and GSEA findings, qPCR analysis identified that gene expression of *IL6* and *TNFAIP3* was comparable between Fresh and modified Steen post-EVLP, whilst standard Steen tissue showed significantly increased expression compared with Fresh. Correspondingly, we also found that protein levels of IL-6 and TNF-α in perfusate significantly increased over time with standard Steen, whilst modified Steen did not. Typically, EVLP is associated with an accumulation of inflammatory cytokines over time due to the closed nature of the circuit; indeed several papers have shown increases in IL-6 (van Zanden *et al*., 2021, Machuca *et al*., 2015) and TNF-α (Kakishita *et al*., 2010, Andreasson *et al*., 2017) release over time. However, by inhibiting the crucial transcription factor NF-κB, modified Steen seemed to ameliorate this inflammatory expression, release and accumulation.

SA has also been shown to inhibit iNOS in macrophages (Aeberhard *et al*., 1995, Kepka-Lenhart *et al*., 1996, Ryu *et al*., 2000). Furthermore, the anti-oxidative effects of both SA (Randjelovic *et al*., 2012, Sagone and Husney, 1987, Dragomir *et al*., 2004, Halliwell and Gutteridge, 1990) and RA (Siddikuzzaman and Grace, 2013, Liu *et al*., 2020) via scavenging of free radicals, are also well defined. This was somewhat reflected in the IPA data, which showed that production of nitric oxide and reactive oxygen species in macrophages pathways was activated to a lesser

extent in modified Steen post-EVLP versus Fresh than standard Steen post-EVLP versus Fresh. Reductions in oxidative stress also contribute to a reduced inflammatory profile downstream.

Generally papers have shown that higher perfusate levels of pro-inflammatory cytokines are associated with higher PVR values (Kosaka *et al*., 2022) and lungs allowing higher flows had lower gene expression of pro-inflammatory cytokines(van Zanden *et al*., 2021). Indeed, lungs perfused with modified Steen exhibited a significantly lower PVR throughout the course of EVLP and could also maintain physiological PAP despite perfusion at over double the flow rate of standard Steen. Not only does this indicate that modified Steen facilitated better function during EVLP, but also has implications post-transplantation; research has described the negative correlation of PVR during EVLP assessment and post-transplant outcome (Spratt *et al*., 2018, Okamoto *et al*., 2016). This indicates that modified Steen perfused lungs may also function better if transplanted. The fact that lungs perfused with modified Steen were able to tolerate near physiological flow rates has multiple implications. Firstly, it could predict an increased likelihood of functionality at 100 % cardiac output following transplant into a recipient. Secondly, assessment of lungs at near physiological flow is arguably more reflective out how the organ will perform in a recipient. Whilst higher flow rates may be more reflective of physiology, the low PVR achieved in lungs perfused with modified Steen could also allow lower flow rates to be used during EVLP, due to the low resistance in the vasculature. Furthermore, significant oedema is associated with high PVR (Hillyard *et al*., 1991). Therefore, low PVR could limit oedema formation during assessment, which is a significant barrier to the success of EVLP. Therefore, modified Steen could facilitate improvement and development of evaluation techniques.

qPCR analysis of *S1PR1* and *CDH5* expression in artery and vein samples revealed no significant difference, potentially suggesting that modified Steen does not directly affect vascular integrity, although protein expression and cell surface localisation would be necessary to confirm this exactly.

Our data suggest that modified Steen is a superior perfusate solution to the current commercially available standard Steen and comparatively improves lung function by reducing inflammatory injury. Gene expression data suggests that this seems to be primarily mediated through NF-κB inhibition during EVLP, although there could also be a role for the free radical scavenging effects of SA and RA. Modified Steen could therefore improve ECD lung evaluation

prior to transplantation by limiting lung injury during EVLP, facilitating more stable assessment and allowing the potential for longer and more advanced therapeutic administration. Testing using human organs and larger sample sizes would be required to confirm this before eventually moving to a clinical assessment in lung transplant recipient. This chapter also reinforces the potential and also perhaps the need for therapeutic intervention during EVLP by showing upregulation of inflammatory gene sets, even despite use of a novel perfusate with anti-oxidative and anti-inflammatory properties.

4. Optimisation of an *in vitro* ischaemia reperfusion injury model for therapeutic testing

4.1. Introduction

Endothelial cells line the intima of blood vessels in the body and act as a semi-permeable barrier, modulating passage of fluid, proteins and cells into tissue. The endothelium responds to signals in the blood and interacting cells to dynamically alter vascular permeability at basal conditions and also during pathology. Ischaemia reperfusion injury (IRI) induces the release of reactive oxygen species (ROS) and angiogenic factors such as thrombin, bradykinin, histamine and vascular endothelial growth factor (VEGF), which ultimately results in endothelial hyper-permeability. This leads to fluid and inflammatory cell accumulation in tissues which can impair organ function following transplantation (Mehta and Malik, 2006).

IRI instigates changes to the actin cytoskeleton, causing cellular contraction which results in intercellular gap formation. For example, thrombin binding to its receptor causes Ca^{2+} influx which activates myosin light chain kinase (MLCK) via interaction with calmodulin, leading to phosphorylation of myosin light chains (MLCs) and cellular contraction (Dudek and Garcia, 2001). IRI also results in alterations to inter-endothelial junctions and the proteins which stabilise them, which contributes to permeability increases. VEGF has been shown to cause phosphorylation of junction proteins via Src family kinases, which ultimately causes their loss at the cell surface. Phosphorylation of tight junction protein occludin has been described (Harhaj *et al*., 2006, Muthusamy *et al*., 2014), as well as adherens junction protein vascular endothelial (VE)-cadherin (Wessel *et al*., 2014, Wallez and Huber, 2008, Monaghan-Benson and Burridge, 2009, Murakami and Simons, 2009). Loss of junction protein ZO-1, VE-cadherin, claudin-5 and occludin localisation at the cell surface have also been described in response to IRI (Wang *et al*., 2022a, Wang *et al*., 2020b, Wang *et al*., 2021, Koto *et al*., 2007, Antonetti *et al*., 1998).

During basal and inflammatory states, signalling of lipid mediator sphingosine-1-phosphate (S1P) modulates endothelial integrity via activation of G-protein coupled receptors S1P receptor (S1PR) 1 and 3. The former has been shown to activate small GTPase Rac which causes actin polymerisation and cell spreading, as well as adherens junction assembly (Wójciak-Stothard *et al*., 2001). S1PR1 signalling has also been shown to reduce VE-cadherin

phosphorylation and internalisation and also increase enrichment of VE-cadherin and β-catenin at intercellular junctions (Lee *et al*., 1999, Gaengel *et al*., 2012, Jung *et al*., 2012, Scotti *et al*., 2016). In contrast, S1PR3 causes activation of GTPase Rho, which causes inactivation of MLC phosphatase and increased phosphorylation of MLC downstream. This ultimately leads to actin-myosin contraction and cell rounding, as well as actin disorganisation. Rho also directly antagonises the barrier enhancing effects of Rac (Li *et al*., 2015, Vouret-Craviari *et al*., 2002). Studies have thus focused on therapeutic targeting and modulation of S1P receptors during inflammatory conditions such as lung IRI (Stone *et al*., 2015). Following its intracellular synthesis, S1P is released, recycled or irreversibly catabolised by S1P lyase (SPL) (Proia and Hla, 2015). Similarly, sphingosine kinase 2 (SPHK2) has been suggested to have a role in clearance of extracellular S1P from the circulation (Mehaffey *et al*., 2018). Because of their roles in regulating the levels of S1P in the blood, literature has also explored the effects of inhibition of both SPL and SPHK2 and have described therapeutic benefits during IRI (Bandhuvula *et al*., 2011, Mehaffey *et al*., 2018).

The pathology of IRI is initiated by the release of ROS and reactive nitrogen species (RNS), which overwhelm the natural antioxidant system (Taverne *et al*., 2013). ROS are released early on following lung ischaemia and can, in turn, react with nitric oxide (NO) to produce RNS (den Hengst *et al*., 2010). Paradoxically, reestablishment of blood flow only worsens oxidative and nitrosative stress through enhancing oxygen availability (Ferrari and Andrade, 2015). ROS and RNS cause oxidation of nucleic acids, proteins and lipids (Santiago *et al*., 2013) and can contribute to the lipid peroxidation of cell and organelle membranes, mitochondrial damage, protein posttranslational modification, cellular signalling changes and cell death though apoptosis and necrosis (Pacher *et al*., 2007). They also provoke inflammatory responses by activating alveolar macrophages to release pro-inflammatory cytokines during ischaemia and contributing to neutrophil activation following reperfusion in the recipient (den Hengst *et al*., 2010). Because of their roles in IRI, studies have used reactive species to model the pathologic processes that occur (Chua *et al*., 1998, Platt *et al*., 2005). In particular, studies have used peroxynitrite donor, 3-morpholinosydnonimine (SIN-1) to model nitrosative stress. SIN-1 releases nitric oxide and superoxide, which interact to form peroxynitrite, a potent RNS (Bonilla *et al*., 2013). Similarly, studies use hydrogen peroxide (H_2O_2) treatment to model oxidative stress, due to its implications in tissue damage during IRI and capacity to generate the highly reactive superoxide radical (Ransy *et al*., 2020, Bae *et al*., 2016).

It is suggested that endothelial cells are the primary site of ROS release during IRI (Chatterjee and Fisher, 2004, Chatterjee and Fisher, 2014), and accordingly, we sought to model the pathology in an endothelial cell line via treatment with ROS/RNS in order to:

- Explore the gene expression profiles of S1PR1, S1PR3, SPL and SPHK2 to gain insight into their potential roles in pathology and uncover mechanisms which drive the disease process
- Identify an optimal model of IRI in an endothelial cell line and directly modulate the permeability of primary endothelial cell monolayers ahead of therapeutic testing.

4.2. Methods

4.2.1. Immunofluorescence staining of VE-cadherin

Prior to staining, HMEC-1, HPMEC or PPMEC were seeded at a density of 50,000 cells per well onto chamber slides (Falcon) and incubated for 48 hours in a humidified atmosphere at 37 °C. An extra well was included for no primary antibody controls. For characterisation experiments, cells were left untreated. For quantification of VE-cadherin localisation, complete media was removed, wells were washed with 200 μL PBS and then treated with 100 μM H_2O_2 or 1 mM SIN-1 for 0.5, 1, 2, 3 or 4 hours or left untreated. Then the treatment was removed and cells were washed, fixed and stained as described in section 2.5.3.2.1. 3 representative images were taken per treatment using the Zeiss AxioImager.

For quantification, Image J was used to calculate the mean fluorescence intensity per pixel of entire images. The average of the mean fluorescence intensity per pixel of the three images was then calculated. This was then plotted as raw values and as relative to untreated.

4.2.2. Cell viability

4.2.2.1. Trypan blue exclusion

200,000 HMEC-1 were seeded per well onto 6-well plates in duplicates, before incubation for 24 hours in a humidified atmosphere at 37 °C. The next day, complete media was removed and the wells were washed with 1 mL PBS. This was replaced with 2 mL 1 % FBS containing media before incubation in a hypoxic incubator at 1 % O_2 for 2, 6 or 24 hours. A time-matched control was included for each and incubated at 21 % O_2. Immediately after incubation, media was collected from each well and put into a 15 mL falcon. Wells were washed with PBS, which was also collected and put into the corresponding falcon. Then HMEC-1 were detached by incubating with 2 mL pre-warmed 1X trypsin-EDTA (Sigma) for 5 mins. This was removed and put into the corresponding falcon, before addition of an equal volume of complete media for trypsin neutralisation. HMEC-1 were then spun at 300 g for 5 minutes, before pouring off the supernatant and re-suspending in 500 μL media. Then viability for each well was calculated as in section 2.1.6.1. The average percentage for each duplicate was plotted.

4.2.2.2. XTT viability assay

To assess viability in response to SIN-1 and H_2O_2, an XTT viability assay was used. 10,000 HMEC-1, HPMEC or PPMEC were seeded in triplicates onto 96-well plates, before incubation at 37 °C overnight. The next day, HMEC-1 were treated with 50, 100, 200 or 300 μM H_2O_2 for 0.5, 1, 2 or 3 hours or 1, 3 or 5 mM SIN-1 for 2, 3, 4, 6, or 8 hours or were left untreated. For HPMEC or PPMEC, cells were treated with 50, 100 or 200 μM H_2O_2 or 0.5, 1 or 2 mM SIN-1 for 3 hours or left untreated. Then the XTT assay was carried out as described in section 2.1.6.2.

4.2.3. RT- qPCR

For hypoxia and hypoxia/reoxygenation experiments, 200,000 HMEC-1 per well were seeded in triplicates onto 6-well plates and incubated overnight at 37 °C. The next day, media was removed and wells were washed with 1 mL PBS before replacing with 2 mL 1 % FBS containing media. Then cells were incubated at 1 % O_2 for 2, 6 or 24 hours with a matching normoxia control (21 % O_2) or for hypoxia reoxygenation experiments, for 24 hours at 1 % O_2 followed by 6 hours normoxia with a matching normoxia control.

For SIN-1 and H_2O_2 experiments, 200,000 HMEC-1 were seeded in duplicates and incubated overnight, before washing wells with 1 mL PBS. For time course experiments, HMEC-1 were treated with 100 μM H_2O_2 for 0.5, 1, 2 or 3 hours or 1 mM SIN-1 for 0, 2, 3, 4, 6 or 8 hours or left untreated. For assessment of S1P-related genes, HMEC-1 were treated with 100 μM H_2O_2 for 3 hours or 1 mM SIN-1 for 2 hours or left untreated.

Following treatment, wells were washed with 1 mL PBS and RNA was extracted as per section 2.4.1.1. Following this, cDNA was synthesised as in 2.4.2 and RT-qPCR was carried out as detailed in 2.4.3; C_t values were normalised against *HPRT1* and then fold changes were calculated relative to untreated controls.

4.2.4. DCFDA Cellular ROS assay

In order to validate SIN-1 and H_2O_2 models, the cellular ROS released by HMEC-1 in response to treatment was quantified. A 2',7' –dichlorofluorescin diacetate (DCFDA) cellular ROS kit was used (Abcam). DCFDA is a cell permeant fluorogenic dye which is deacetylated by cellular esterases and later oxidised in the presence of ROS to 2', 7'-dichlorofluorescein (DCF). DCF is

highly fluorescent and is detected by fluorescence spectroscopy at Ex: 485 nm, Em: 535 nm. Tert-butyl hydroperoxide (TBHP) is a positive control treatment supplied with the kit.

As cells were being treated for longer time points up to 8 hours, it was first determined whether the treatments could be carried out in media containing phenol red, rather than the supplement buffer supplied with the kit. 25,000 HMEC-1 per well were seeded in triplicates onto 96-well plates and incubated overnight. The next day, wells were washed with 100 μL PBS, before staining with 100 μL 25 μM DCFDA in media for 45 min at 37 °C and washing again with 100 μL PBS. Then cells were treated with 50, 100, 150 or 200 μM TBHP for 4 hours in either 1 % FBS containing media or supplement buffer supplied with the kit. The plate was then read at Ex: 485 nm, Em: 535 nm. Wells containing supplement buffer/ media alone were subtracted as background.

Figure 4.1 shows a comparison of fluorescence intensity for cells treated with TBHP in supplement buffer or media. As the trend depicted is comparable between the two, it was decided that treatments could be carried out in media going forward.

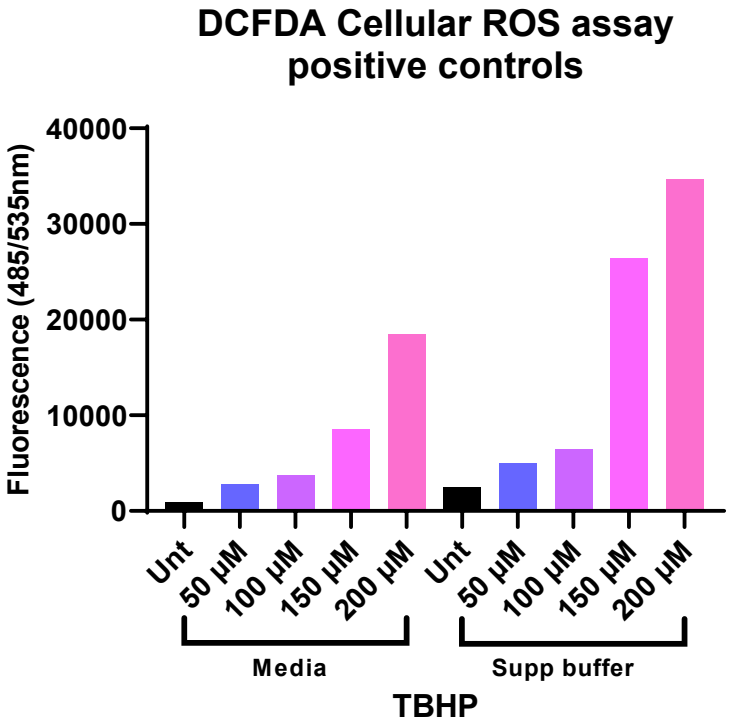

Figure 4.1. Optimisation of DCFDA Cellular ROS assay.

Cells were stained with 2',7' –dichlorofluorescin diacetate (DCFDA) before treating with increasing concentrations of Tert-butyl hydroperoxide (TBHP) in either media or supplement buffer supplied with the kit. Depicted is fluorescence of cells as quantified using a plate reader. N=1.

For H_2O_2 and SIN-1 experiments, HMEC-1 were seeded, incubated, washed and stained as described. Cells were then treated with 100 μM H_2O_2 for 0.5, 1, 2, 3 or 4 hours or 1 mM SIN-1 for 0.5, 1, 2, 3, 4, 6 or 8 hours with a matching untreated control. Positive control wells were treated with 50, 100, 150 or 200 μM TBHP for 4 hours. The plate was read at Ex: 485 nm, Em: 535 nm and wells containing media alone were subtracted as background.

4.2.5. Trans-endothelial electrical resistance

4.2.5.1. Optimisation of monolayer formation

Prior to measurement of trans-endothelial electrical resistance (TEER), the time it took for a confluent monolayer to form for HPMEC and PPMEC was optimised. 150,000 HPMEC/PPMEC were seeded onto 24-well 0.4 μm translucent transwells (Sarstedt) with 300 μL complete media in the top of the transwell and 700 μL media below. A transwell with no cells was included as an empty control. Transwells were left to incubate at 37 °C and media was replenished every 48 hours. Resistance was measured every day using MILLICELL® ERS probes (Millipore) and TEER calculated as described in section 2.2.1. Then data was plotted relative to day 1.

Figure 4.2 shows relative TEER for HPMEC and PPMEC. A significant increase in TEER from day 1 was seen on day 3 and day 5 for HPMEC and PPMEC respectively and were used for growing monolayers in subsequent experiments.

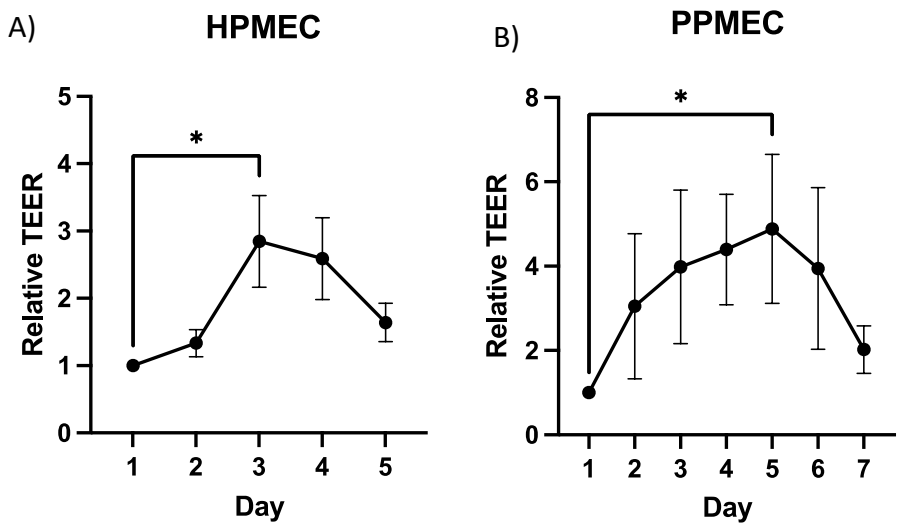

Figure 4.2. Optimisation of primary cell monolayers on transwells.

Monolayers of **A)** HPMEC and **B)** PPMEC were grown on 0.4 μm transwells and the resistance was measured each day. TEER was calculated by subtracting blank transwell readings and multiplying by the transwell surface area. Then values were presented as relative to day 1. N=3. Mean is presented with standard deviation. Statistical significance was determined using a one-way ANOVA with multiple comparisons. *p<0.05, **p<0.01, ***p<0.001, ****p<0.0001.

4.2.5.2. Monolayer permeability in response to treatment

As previously described in section 4.2.5.1, 150,000 HPMEC or PPMEC were seeded onto 0.4 μm transwells and grown for 3 or 5 days respectively. An empty transwell was included as a control. Media was replenished every 48 hours. Once monolayers were confluent, media was removed and transwells were washed with PBS before placing into a new 24-well plate. Then 300 μL serum free media was pipetted into the top of the transwell with 700 μL pipetted below. Cells underwent 1 hr serum starvation, before resistance was measured with the electrodes pre-treatment. Then media was removed and cells were treated with 100 μM H_2O_2 or 2 mM SIN-1 for HPMEC or 200 μM H_2O_2 or 0.5 mM SIN-1 for PPMEC or left untreated. The resistance was measured at 0.5, 1, 2, 3, 4, 5 and 6 hours following treatment. TEER was calculated as described in section 2.2.1 and was presented as relative to pre-treatment values for every transwell.

4.3. Results

4.3.1. Endothelial cell characterisation

As an immortalised cell-line, HMEC-1 cells can be maintained to a higher passage number than primary cells and so were used for initial optimisation experiments prior to progression to primary cells HPMEC and PPMEC. Immunofluorescence staining of VE-cadherin was used to characterise endothelial cell lines and primary cells prior to use in functional assays. VE-cadherin is a junction protein which is expressed exclusively by endothelial cells (Hendrix *et al*., 2001). As shown in Figure 4.3-4.5, VE-cadherin was expressed primarily at cell-cell contacts by HMEC-1, HPMEC and PPMEC respectively, whilst no primary (NP) samples were negative. Extracellular staining of HPMEC (Figure 4.4) and PPMEC (Figure 4.5) is more regular than HMEC-1 (Figure 4.3) due to their contact inhibition and ability to form a monolayer.

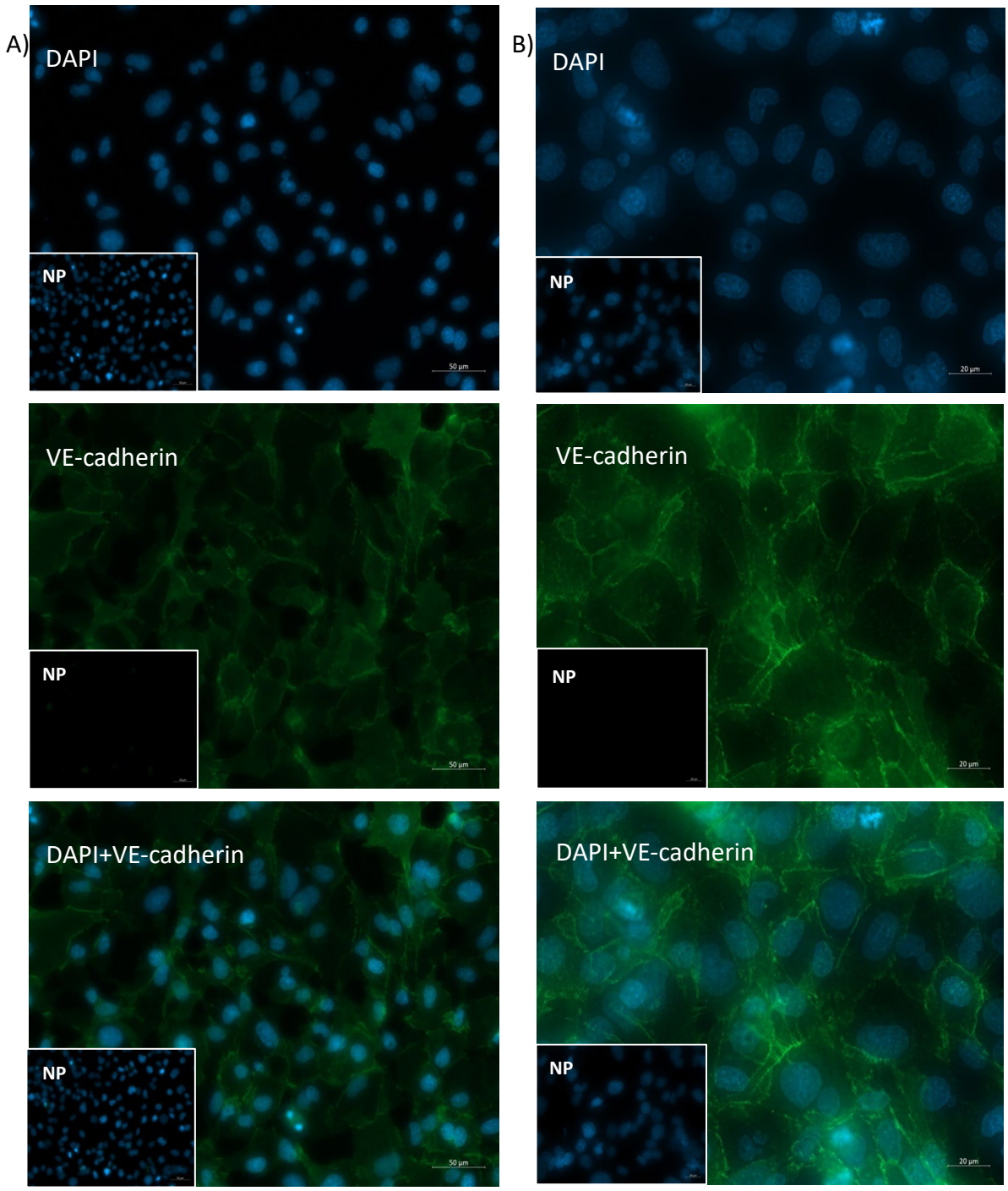

Figure 4.3. Characterisation of HMEC-1.

Immunofluorescence staining of VE-cadherin was used for endothelial characterization prior to experiments. **A)** Images at a 20x magnification. Scale: 50 µm. **B)** Images at a 40x magnification. Scale: 20 µm. Green=VE-cadherin. Blue=DAPI. A no primary (NP) control was included. 3 images were taken for each well. Representative of N=3.

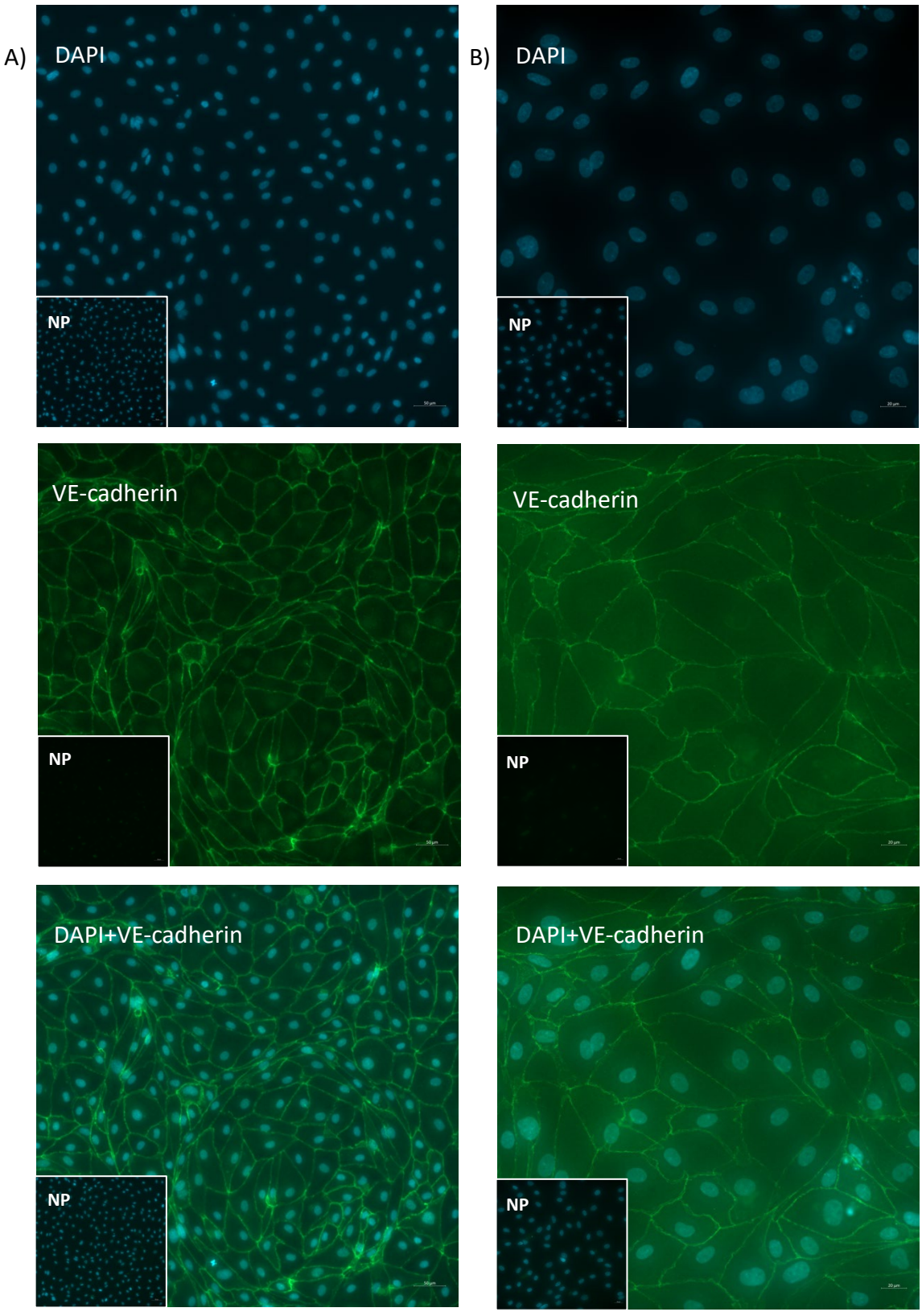

Figure 4.4. Characterisation of HPMEC.

Immunofluorescence staining of VE-cadherin was used for endothelial characterization prior to experiments. **A)** Images at a 20x magnification. Scale: 50 µm. **B)** Images at a 40x magnification. Scale: 20 µm. Green=VE-cadherin. Blue=DAPI. A no primary (NP) control was included. 3 images were taken for each well. Representative of N=2.

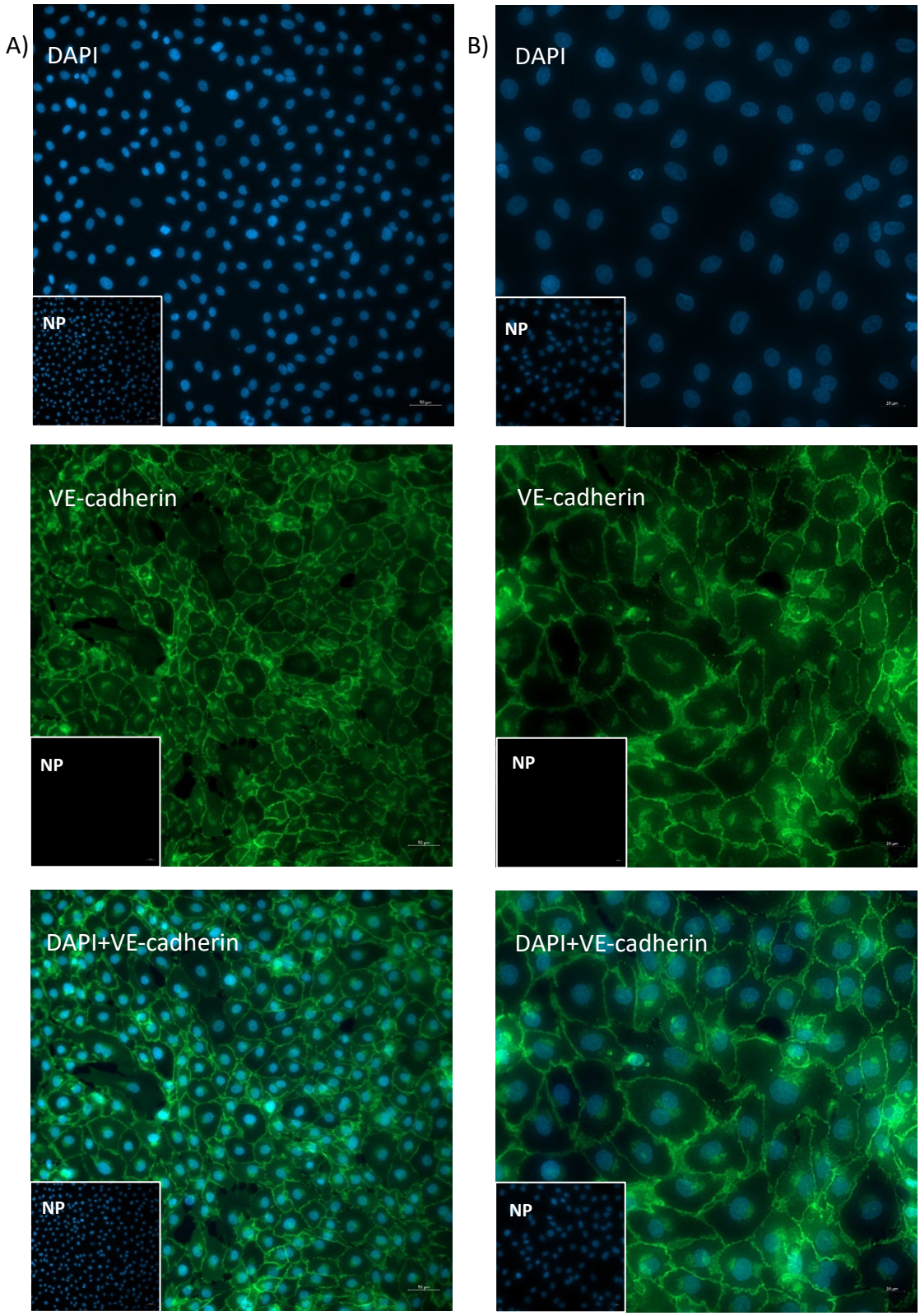

Figure 4.5. Characterisation of PPMEC.

Immunofluorescence staining of VE-cadherin was used for endothelial characterization prior to experiments. **A)** Images at a 20x magnification. Scale: 50 µm. **B)** Images at a 40x magnification. Scale: 20 µm. Green=VE-cadherin. Blue=DAPI. A no primary (NP) control was included. 3 images were taken for each well. Representative of N=2.

4.3.2. Hypoxic incubation to model IRI in HMEC-1

Loss of blood flow is associated with tissue hypoxia in other organs or lungs with low alveolar oxygen levels. Therefore, a hypoxic incubator was used to expose HMEC-1 to 1 % oxygen for increasing time periods to mimic IRI and explore gene expression changes which may influence pathology.

4.3.2.1. Cell death in response to hypoxia

Figure 4.6 showed that 1 % oxygen for up to 24 hours had no significant effect on HMEC-1 viability, although there was a trend towards a lower number of live cells at 24 hours compared to the corresponding untreated.

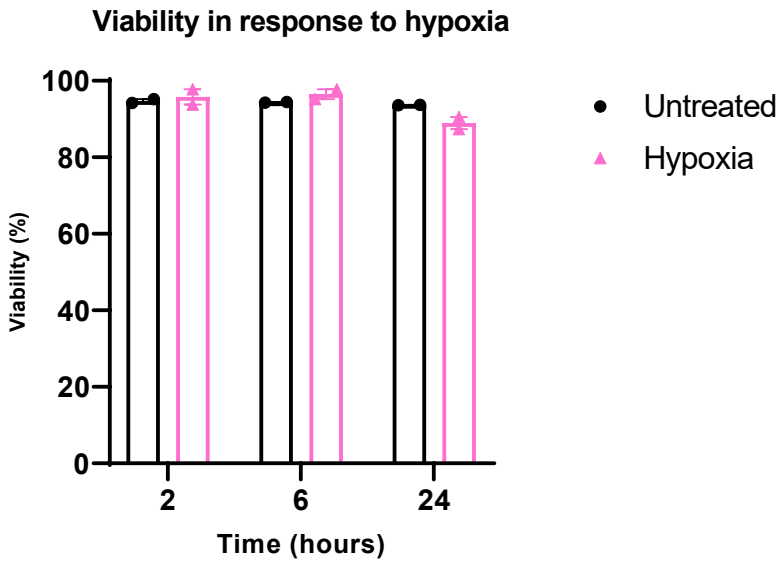

Figure 4.6. HMEC-1 viability in response to hypoxia.

Trypan blue exclusion was used to assess viability changes in response to hypoxia over time. Viability is presented as number of live cells as a percentage of total cells. Each time point of hypoxia had a time matched untreated control. N=2. Mean is presented with standard deviation. A two-way ANOVA with multiple comparisons was used to calculate statistical significance. *p<0.05, **p<0.01, ***p<0.001, ****p<0.0001.

VEGF is trans-activated during IRI and is a key mediator of endothelial hyper-permeability during the pathology. Therefore, gene expression was assessed in response to hypoxia. Gene expression of *VEGFA* increased with hypoxia, peaking at 6 hours, albeit non-significantly (Figure 4.7A). In endothelial cells, HIF-1α protein is stabilised during hypoxia. However, this study found that gene expression of *HIF1A* was reduced over time, which reached significance by 24 hours as shown in Figure 4.7B. CXCL8 is a key chemokine which is released by alveolar macrophages, alveolar type 2 epithelial cells and endothelial cells during IRI. Despite this, data showed that gene expression of *CXCL8* was reduced in HMEC-1 during hypoxia, which was significant at 2 hours (Figure 4.7C).

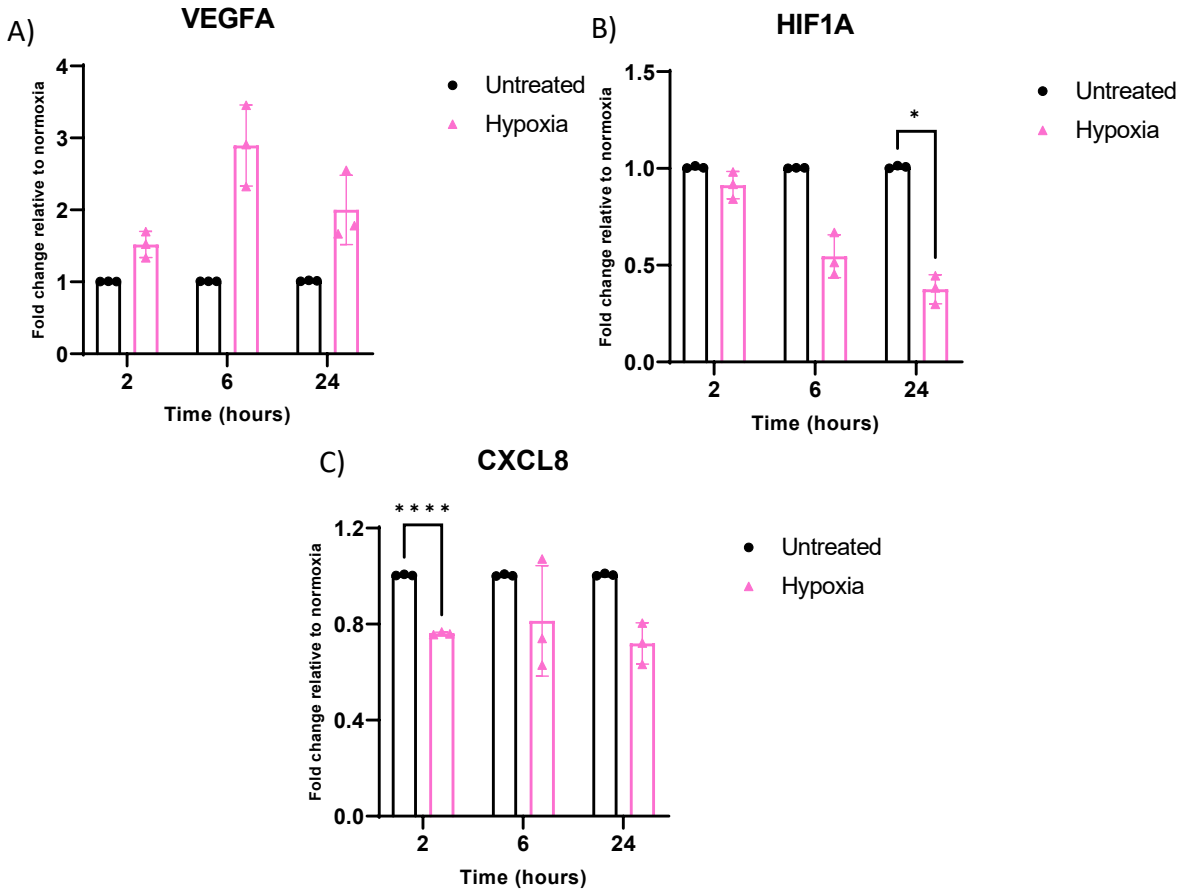

Figure 4.7. Gene expression of IRI-related genes in response to hypoxia in HMEC-1.

RT-qPCR was used to quantify gene expression of **A)** *VEGFA*, **B)** *HIF1A* and **C)** *CXCL8*. Gene expression is depicted as relative to the time matched untreated control for each time point. N=3. Mean is presented with standard deviation. A two-way ANOVA with multiple comparisons was used to calculate statistical significance. *p<0.05, **p<0.01, ***p<0.001, ****p<0.0001.

4.3.2.3. Changes to S1P-related genes in response to hypoxia and hypoxia/reoxygenation

Due to their roles in modulating endothelial permeability, expression of genes encoding S1PR1 and S1PR3 were assessed in response to hypoxia, whilst *SGPL1* and *SPHK2* were assessed due to the role of SPL and SPHK2 in modulating circulating S1P levels.

Gene expression of *S1PR1* and *S1PR3* was decreased by 24 hours, with *S1PR1* showing a significant difference (Figure 4.8A-B). *SGPL1* and *SPHK2* also showed a similar decrease by 24 hours, with only SPHK2 showing significance (Figure 4.8C-D).

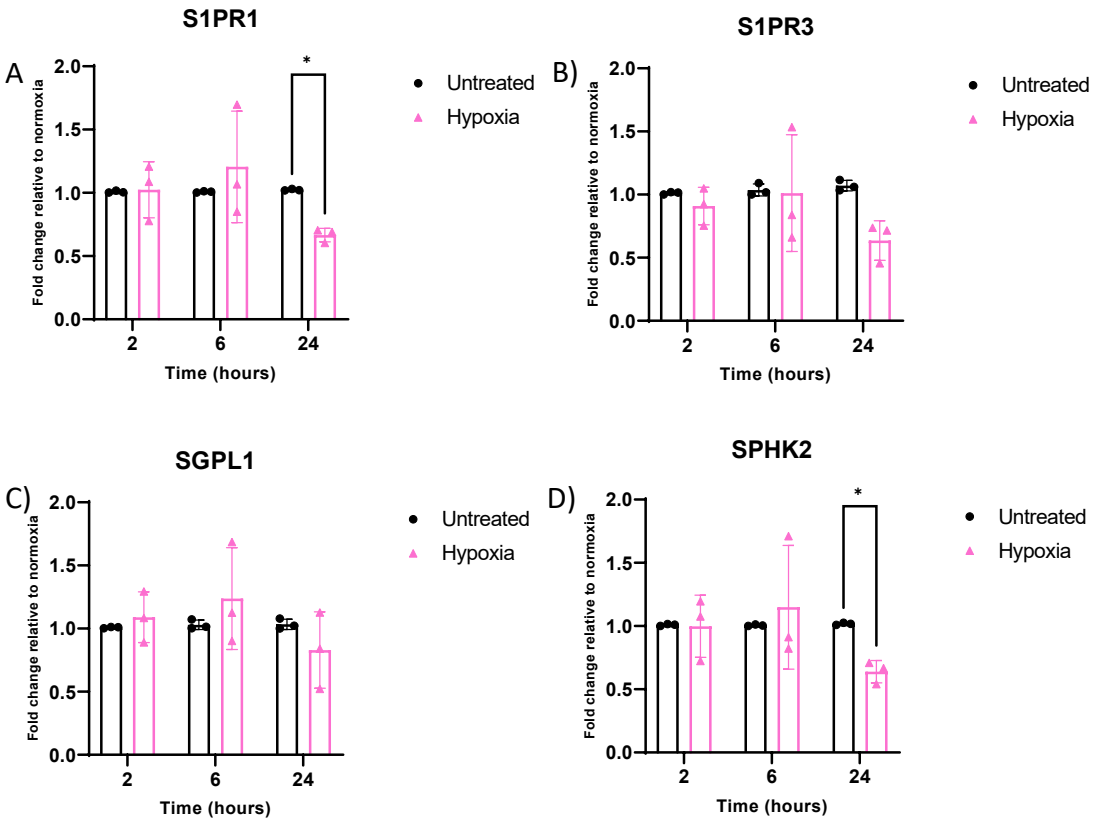

Figure 4.8. Gene expression of S1P-related genes in response to hypoxia in HMEC-1.

RT-qPCR was used to quantify gene expression of **A)** *S1PR1*, **B)** *S1PR3,* **C)** *SGPL1* and **D)** *SPHK2*. Gene expression is depicted as relative to the time matched untreated control for each time point. N=3. Mean is presented with standard deviation. A two-way ANOVA with multiple comparisons was used to calculate statistical significance. *p<0.05, **p<0.01, ***p<0.001, ****p<0.0001.

In order to more accurately mimic the dual phase pathology of IRI, HMEC-1 were exposed to hypoxia for 24 hours, followed by a period of reoxygenation at 21 % oxygen for 6 hours. Compared to untreated, *S1PR1, S1PR3* and *SGPL1* were all significantly decreased following hypoxia and reoxygenation (Figure 4.9A, B and C respectively). In fact, fold change was relatively halved. *SPHK2* also showed a non-significant reduction in Figure 4.9D.

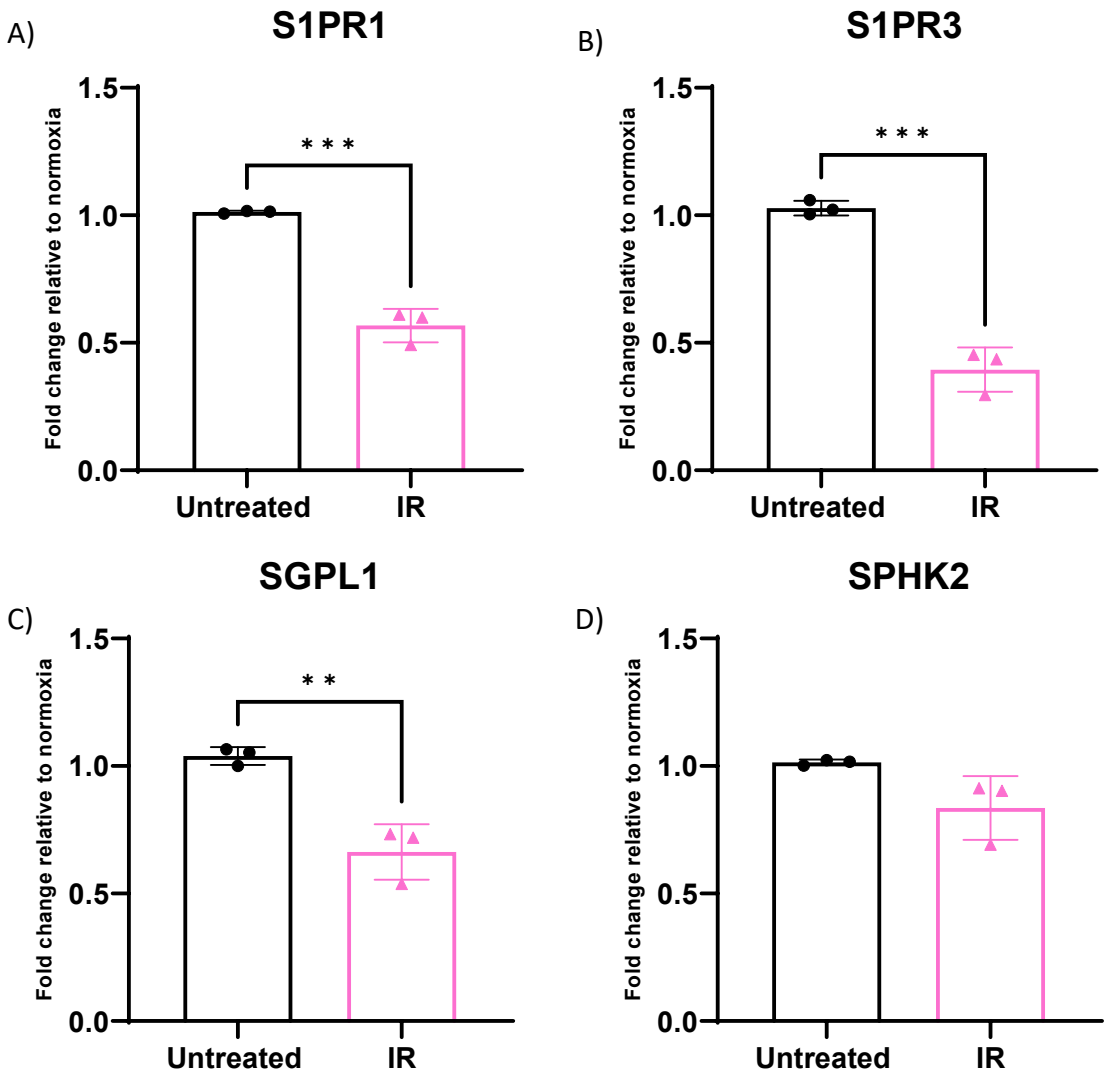

Figure 4.9.Gene expression of S1P-related genes in response to hypoxia/reperfusion in HMEC-1.

RT-qPCR was used to quantify gene expression of **A)** *S1PR1*, **B)** *S1PR3*, **C)** *SGPL1* and **D)** *SPHK2* following 24 hours hypoxia +6 hours reperfusion. IR= ischaemia reperfusion. Gene expression is depicted as relative to untreated. N=3. Mean is presented with standard deviation. An unpaired t test was used to calculate statistical significance. *p<0.05, **p<0.01, ***p<0.001, ****p<0.0001.

4.3.3. ROS and RNS treatment to model IRI in HMEC-1

As the lung primarily undergoes non-hypoxic ischaemia due to alveolar oxygen maintaining tissue oxygenation for some time, it was decided that treating the cells with ROS and RNS at physiological oxygen levels was a better model for lung IRI than hypoxic incubation.

SIN-1 simultaneously generates nitric oxide and superoxide and is a source of peroxynitrite anion, which is also generated during IRI (Hogg *et al*., 1992). Meanwhile H_2O_2 is an example of the type of ROS that is prevalent during IRI and arguably one of the most important in driving injury (Bae *et al*., 2016).

The aim was to eventually narrow treatments down to an optimal concentration and time point range which could be applied to primary cells and was sufficient to alter permeability, but not significantly affect cell viability. Initial dose and time point ranges for H_2O_2 and SIN-1 were chosen based on existing literature (Wilson and Keenan, 2003, Igarashi *et al*., 2007, Zhang *et al*., 2005b, Ashki *et al*., 2014).

When treated with increasing concentrations of H_2O_2, HMEC-1 viability was not significantly different from untreated up to 100 μM and was relatively stable over time. However, concentrations higher than this started to visibly impact viability, with 200 μM significantly reducing viability at 30 minutes and 300 μM at 30 minutes to 2 hours (Figure 4.10A). Therefore, 100 μM was carried forward. For SIN-1, 3 and 5 mM significantly reduced viability at all time points and this seemed to worsen over time. 1 mM significantly reduced viability at earlier time points, but this was not significant at 8 hours (Figure 4.10B). As a physiologically relevant concentration which induced the least cell death, this concentration was carried forward.

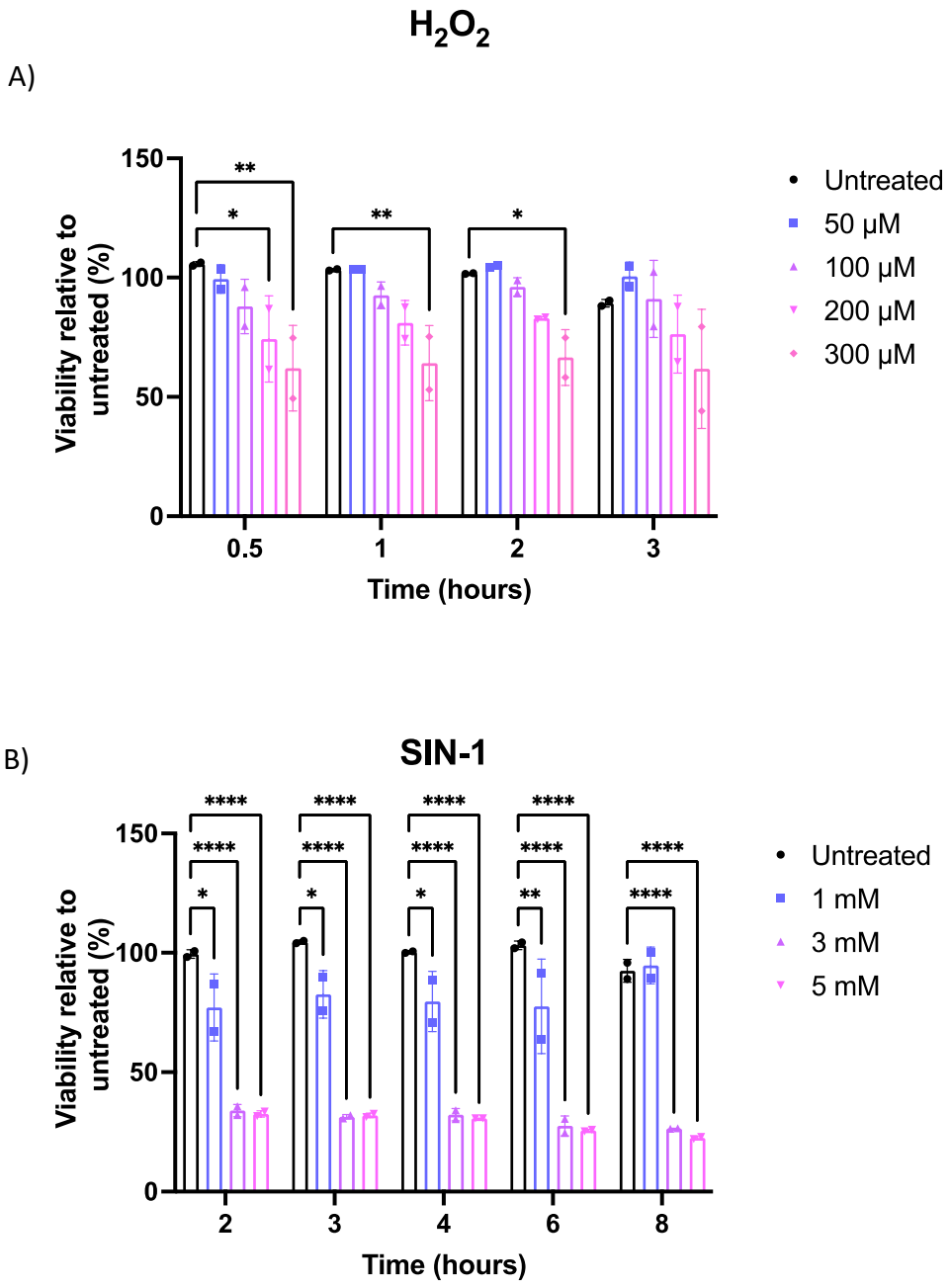

Figure 4.10. HMEC-1 viability in response to H_2O_2 and SIN-1.

An XTT assay was used to assess viability changes in response to **A)** H_2O_2 and **B)** SIN-1 treatment over a range of concentrations at various time points. Viability is presented as a percentage relative to the untreated at each time point. N=2. Mean is presented with standard deviation. A two-way ANOVA with multiple comparisons was used to calculate statistical significance from untreated at every time point. *p<0.05, **p<0.01, ***p<0.001, ****p<0.0001.

To confirm that treatments were influencing ROS release in HMEC-1, a DCFDA cellular ROS assay was used. In response to H_2O_2, ROS was increased across all time points compared to a matching time control and was significant after incubation for all but 2 hours. ROS release due to H_2O_2 treatment was comparable to the lowest positive control of 50 μM TBHP (Figure 4.11A). Figure 4.11B showed that SIN-1 treatment caused considerably higher cellular ROS release than all positive controls at all time points. All time points were significantly increased in comparison to their matched untreated control. As there was no significant increase between time points from 4 hours to 8 hours, later time points of 6 and 8 hours were not be carried forward.

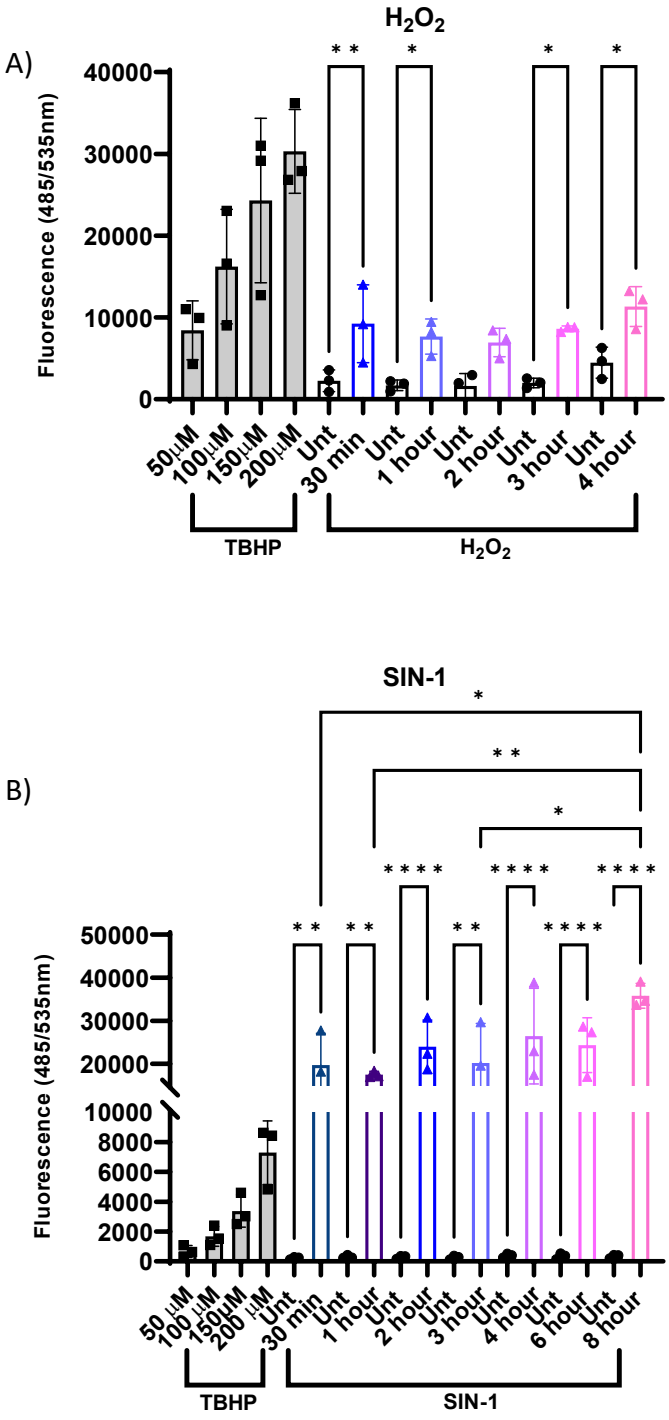

Figure 4.11. Intracellular ROS release in HMEC-1 in response to H_2O_2 and SIN-1.

A DCFDA cellular ROS assay was used to determine intracellular ROS levels in response to increasing time points of treatment with **A)** H_2O_2 (100 µM) and **B)** SIN-1 (1 mM). Each treatment had a time matched untreated control. Cells treated with TBHP were used as positive controls. N=3. Mean is presented with standard deviation. Statistical significance was determined using a one-way ANOVA with multiple comparisons. *p<0.05, **p<0.01, ***p<0.001, ****p<0.0001.

4.3.3.1. Effect of H_2O_2 and SIN-1 on cell surface VE-cadherin localisation

As previous reports have shown destabilisation and loss of VE-cadherin at intercellular junctions during IRI, cell surface VE-cadherin expression was quantified in response to H_2O_2 and SIN-1. Prior to staining, cells were not permeabilised and were stained with an antibody raised against the extracellular domain of VE-cadherin so that only VE-cadherin at the cell surface was visualised for quantification. Equal cell seeding densities were also used to ensure that cell number did not influence fluorescent intensity per pixel of each image.

Figure 4.12A-B and 4.13A-B showed that VE-cadherin staining was isolated to the cell membrane and there was no staining of the no primary antibody control. Figure 4.12A-B depicts 10x and 20x magnification images respectively, showing extracellular VE-cadherin staining in response to increasing time points of 100 μM H_2O_2 treatment. Quantification of mean fluorescence intensity revealed that most reduction was seen following 3 hours of treatment, although this was not significant (Figure 4.12C). Figure 4.13A-B shows 10x and 20x magnification images respectively, of extracellular VE-cadherin staining in response to increasing time points of 1 mM SIN-1 treatment. 2 and 3 hours of 1 mM SIN-1 treatment showed the most reduction in comparison to untreated, although this was not significant (Figure 4.13C). Therefore 3 hours H_2O_2 treatment and 2 hours SIN-1 treatment were carried forward to look at S1P related gene expression.

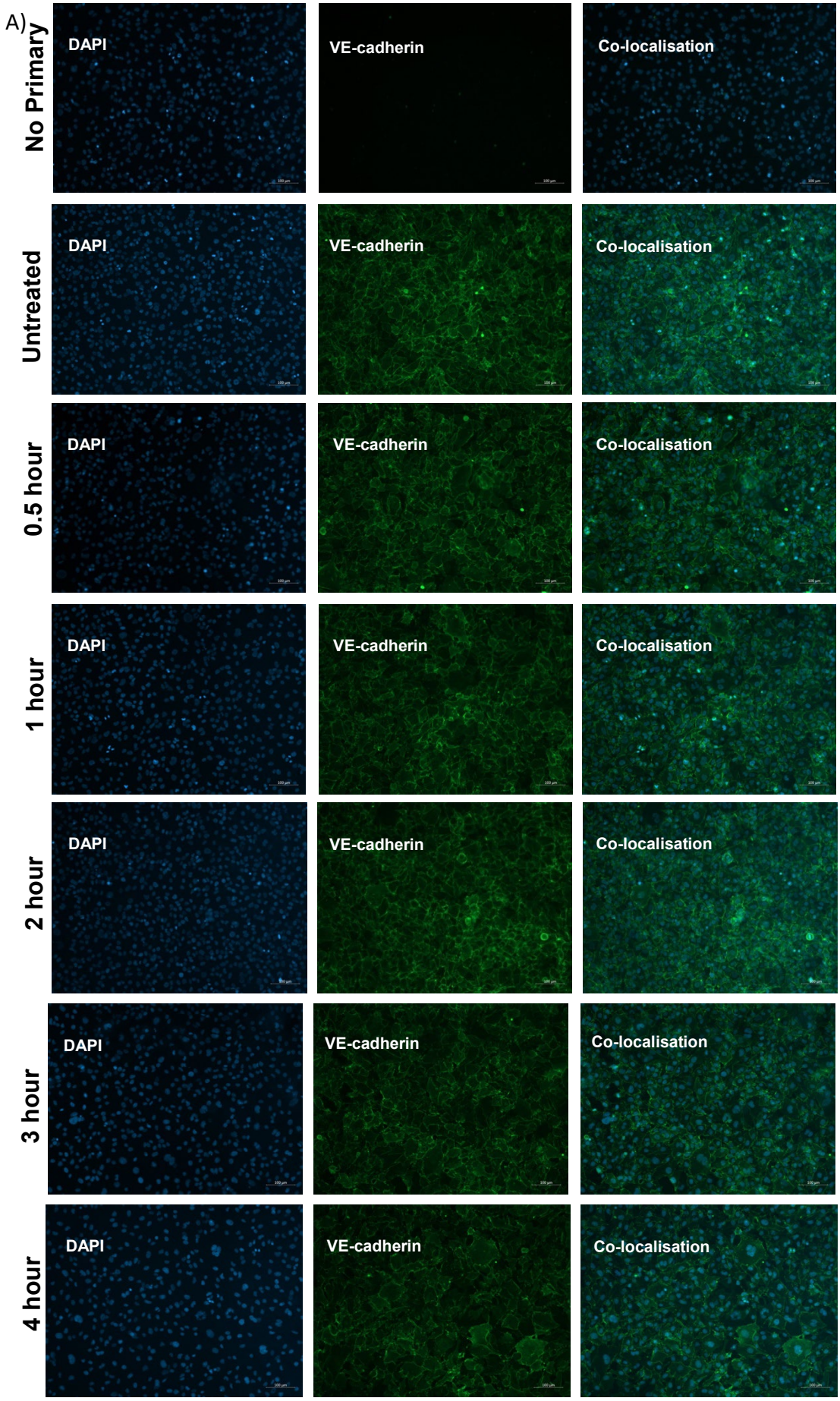
A)
No Primary
DAPI
VE-cadherin
Co-localisation
Untreated
DAPI
VE-cadherin
Co-localisation
0.5 hour
DAPI
VE-cadherin
Co-localisation
1 hour
DAPI
VE-cadherin
Co-localisation
2 hour
DAPI
VE-cadherin
Co-localisation
3 hour
DAPI
VE-cadherin
Co-localisation
4 hour
DAPI
VE-cadherin
Co-localisation

B)

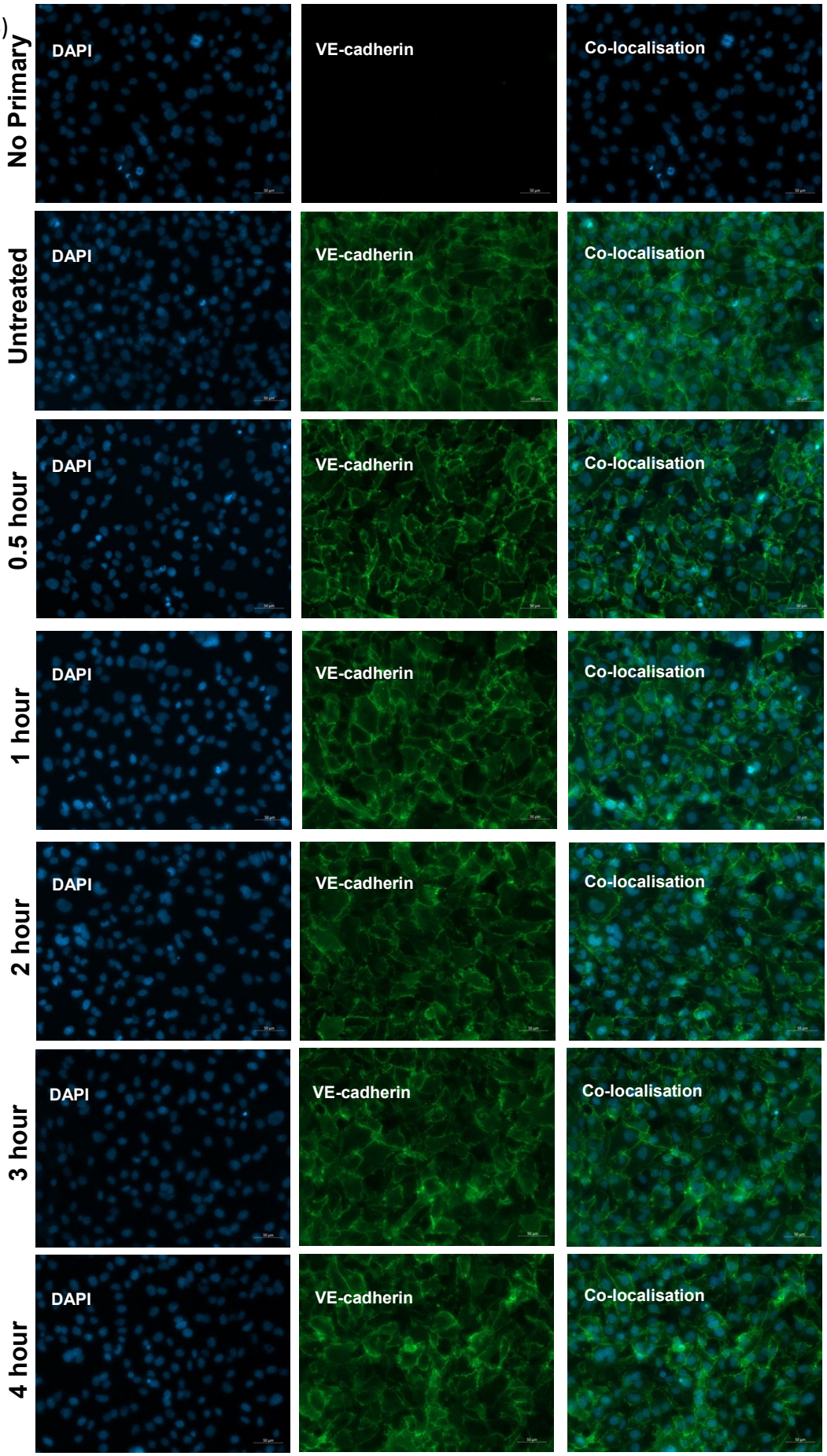
No Primary
DAPI
VE-cadherin
Co-localisation
Untreated
DAPI
VE-cadherin
Co-localisation
0.5 hour
DAPI
VE-cadherin
Co-localisation
1 hour
DAPI
VE-cadherin
Co-localisation
2 hour
DAPI
VE-cadherin
Co-localisation
3 hour
DAPI
VE-cadherin
Co-localisation
4 hour
DAPI
VE-cadherin
Co-localisation

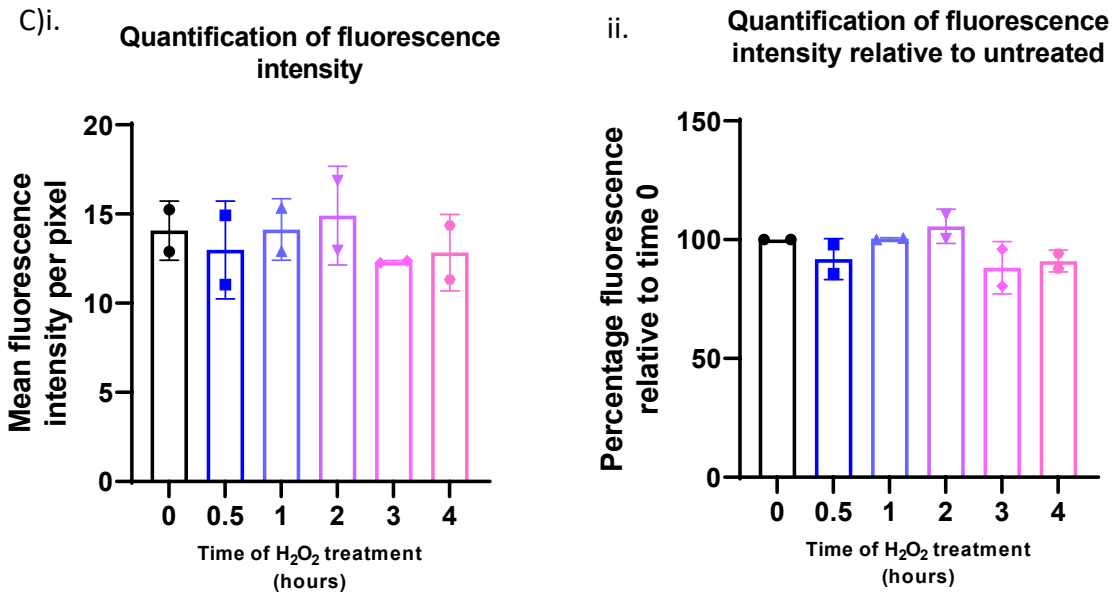

Figure 4.12. HMEC-1 VE-cadherin cell surface expression in response to H_2O_2.

Cells were treated with 100 µM H_2O_2 and immunofluorescence staining was used to determine changes to VE-cadherin localisation at the cell surface over time. **A)** Images at a 10x magnification. Scale: 100 µm. **B)** Images at a 20x magnification. Scale: 50 µm. Green=VE-cadherin. Blue=DAPI. A no primary (NP) control was included. 3 images were taken for each well. Images representative of N=2. **C)** Quantification of cell surface expression of VE-cadherin: **i)** Mean fluorescence intensity per pixel and **ii)** Mean fluorescence intensity per pixel relative to untreated. For each time point, an average mean fluorescence intensity was taken of 3 images per repeat. N=2. Mean is presented with standard deviation. Statistical significance was determined using a one-way ANOVA with multiple comparisons. *p<0.05, **p<0.01, ***p<0.001, ****p<0.0001.

A)

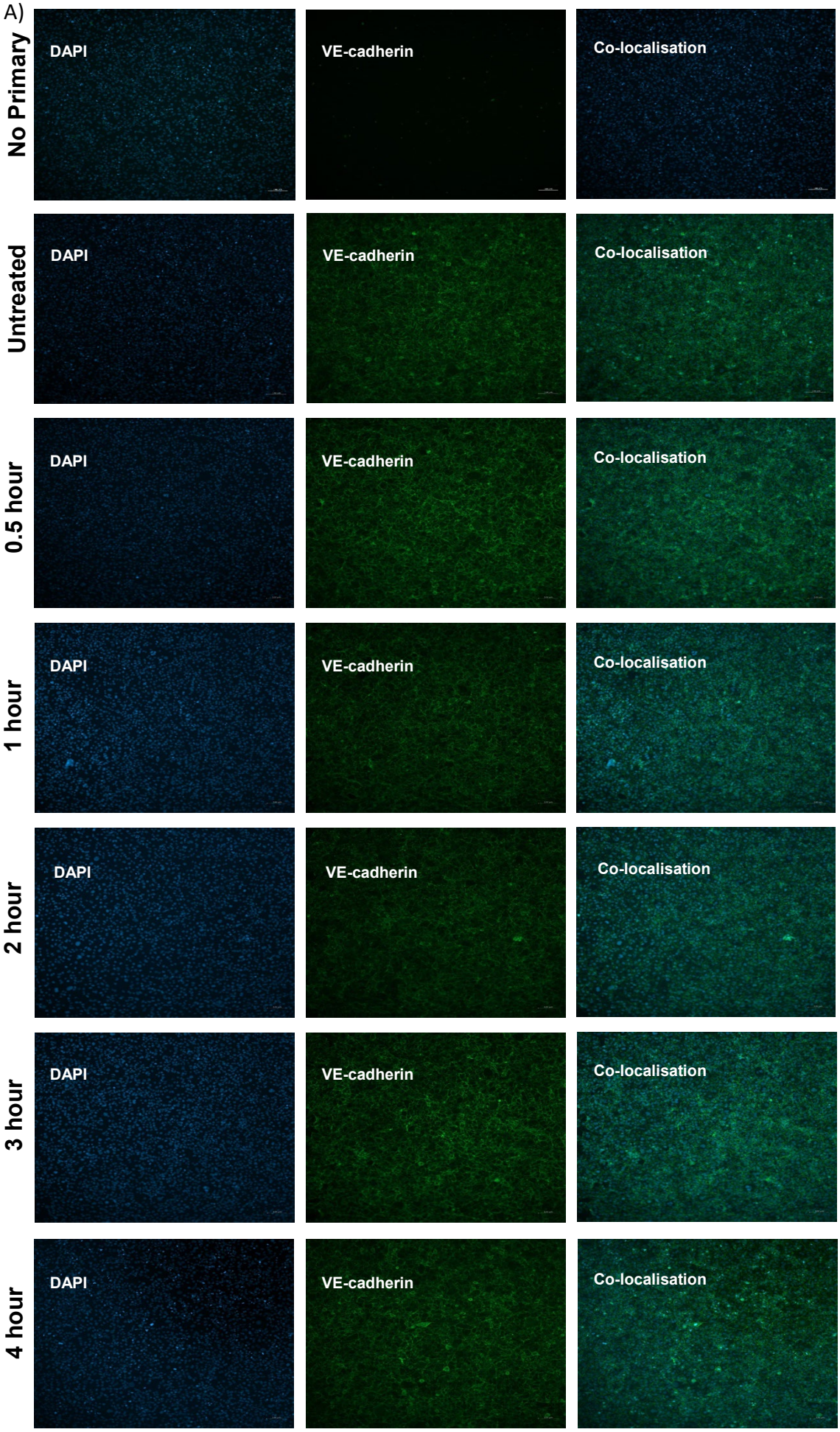
No Primary
DAPI
VE-cadherin
Co-localisation
Untreated
DAPI
VE-cadherin
Co-localisation
0.5 hour
DAPI
VE-cadherin
Co-localisation
1 hour
DAPI
VE-cadherin
Co-localisation
2 hour
DAPI
VE-cadherin
Co-localisation
3 hour
DAPI
VE-cadherin
Co-localisation
4 hour
DAPI
VE-cadherin
Co-localisation

B)

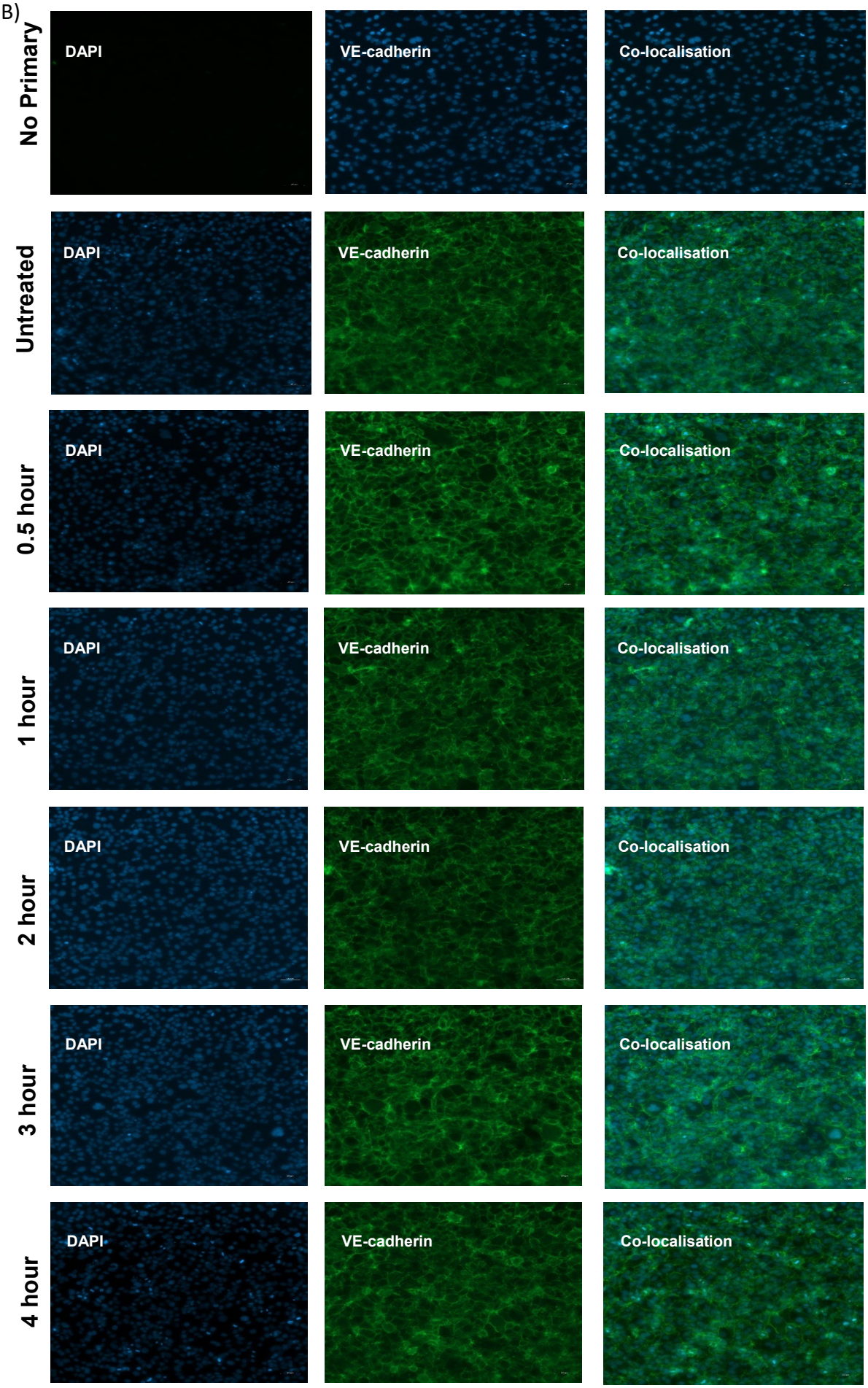
No Primary
DAPI
VE-cadherin
Co-localisation
Untreated
DAPI
VE-cadherin
Co-localisation
0.5 hour
DAPI
VE-cadherin
Co-localisation
1 hour
DAPI
VE-cadherin
Co-localisation
2 hour
DAPI
VE-cadherin
Co-localisation
3 hour
DAPI
VE-cadherin
Co-localisation
4 hour
DAPI
VE-cadherin
Co-localisation

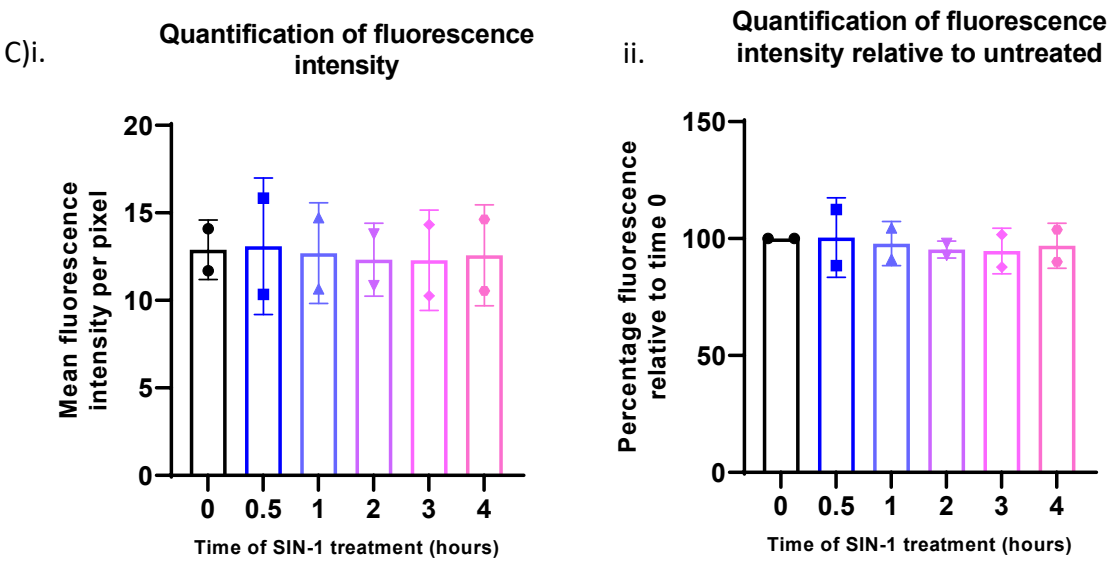

Figure 4.13. HMEC-1 VE-cadherin cell surface expression in response to SIN-1.

Cells were treated with 1 mM SIN-1 and immunofluorescence staining was used to determine changes to VE-cadherin localisation at the cell surface over time. **A)** Images at a 10x magnification. Scale: 100 µm. **B)** Images at a 20x magnification. Scale: 50 µm. Green=VE-cadherin. Blue=DAPI. A no primary (NP) control was included. 3 images were taken for each well. Images representative of N=2. **C)** Quantification of cell surface expression of VE-cadherin: **i)** Mean fluorescence intensity per pixel and **ii)** Mean fluorescence intensity per pixel relative to untreated. For each time point, an average mean fluorescence intensity was taken of 3 images per repeat. N=2. Mean is presented with standard deviation. Statistical significance was determined using a one-way ANOVA with multiple comparisons. *p<0.05, **p<0.01, ***p<0.001, ****p<0.0001.

4.3.3.2. Effect of H_2O_2 and SIN-1 on gene expression

4.3.3.2.1. Effect of H_2O_2 and SIN-1 on S1P and IRI related gene expression over time

Gene expression of *S1PR1* and IRI related genes was assessed over time in HMEC-1 in response to H_2O_2 and SIN-1. Following H_2O_2 treatment, *S1PR1* showed no significant changes over time, but did seem to show a trend of reduction over time (Figure 4.14Ai). H_2O_2 caused a time dependant increase in *VEGFA* expression, which reached significance by 3 hours (Figure 4.14Aii). *HIF1A* showed a directly opposite trend, showing a significant decrease by 3 hours (Figure 4.14Aiv). *CXCL8* showed a significant increase compared to untreated at 30 minutes, which gradually reduced over time until reaching levels that were comparable to untreated at 3 hours (Figure 4.14Aiii).

SIN-1 seemed to increase *S1PR1* initially, but expression was reduced compared to time 0 at 8 hours, albeit not significantly (Figure 4.14Bi). Much like H_2O_2, SIN-1 increased *VEGFA* expression and decreased *HIF1A* expression over time, but this was not significant (Figure 4.14Bii and iv respectively). *CXCL8* suggested an increase over time, although this did not reach significance (Figure 4.14Biii).

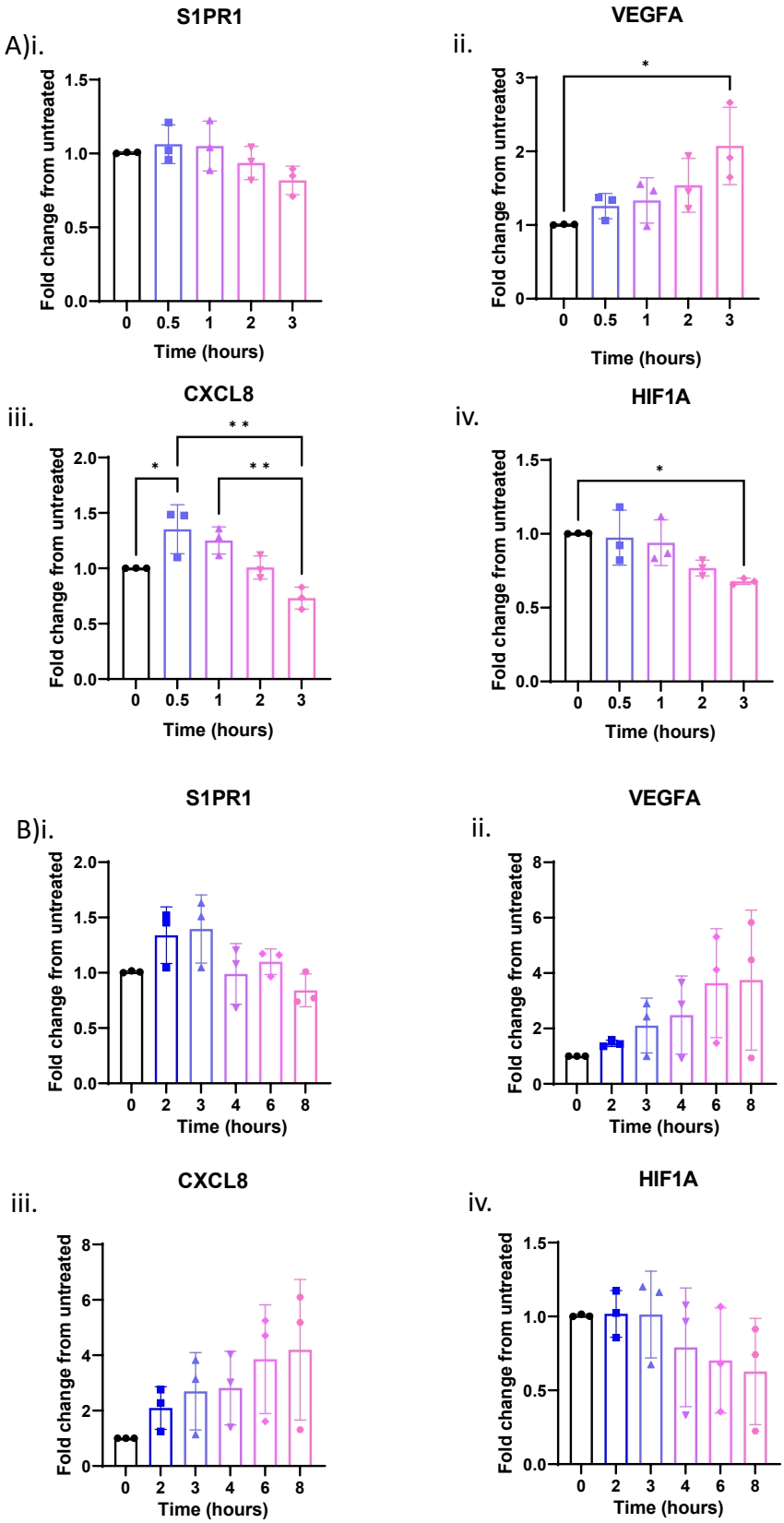

Figure 4.14. Gene expression over time in response to H_2O_2 and SIN-1 in HMEC-1.

RT-qPCR was used to quantify gene expression in response to **A)** H_2O_2 (100 µM) and **B)** SIN-1 (1mM) of **i)** *S1PR1,* **ii)** *VEGFA*, **iii)** *CXCL8* and **iv)** *HIF1A* over time. N=3. Gene expression is depicted as relative to untreated. Mean is presented with standard deviation. Statistical significance was determined using a one-way ANOVA. *p<0.05, **p<0.01, ***p<0.001, ****p<0.0001.

4.3.3.2.2. Effect of H_2O_2 and SIN-1 on S1P related genes

Following treatment with H_2O_2, *S1PR1* and *SPHK2* were significantly decreased (Figure 4.15Ai and Aiv). No significant gene expression changes were observed for *S1PR3* and *SGPL1* (Figure 4.15Aii and Aiii). SIN-1 had no significant impact on S1P related gene expression (Figure 4.15B).

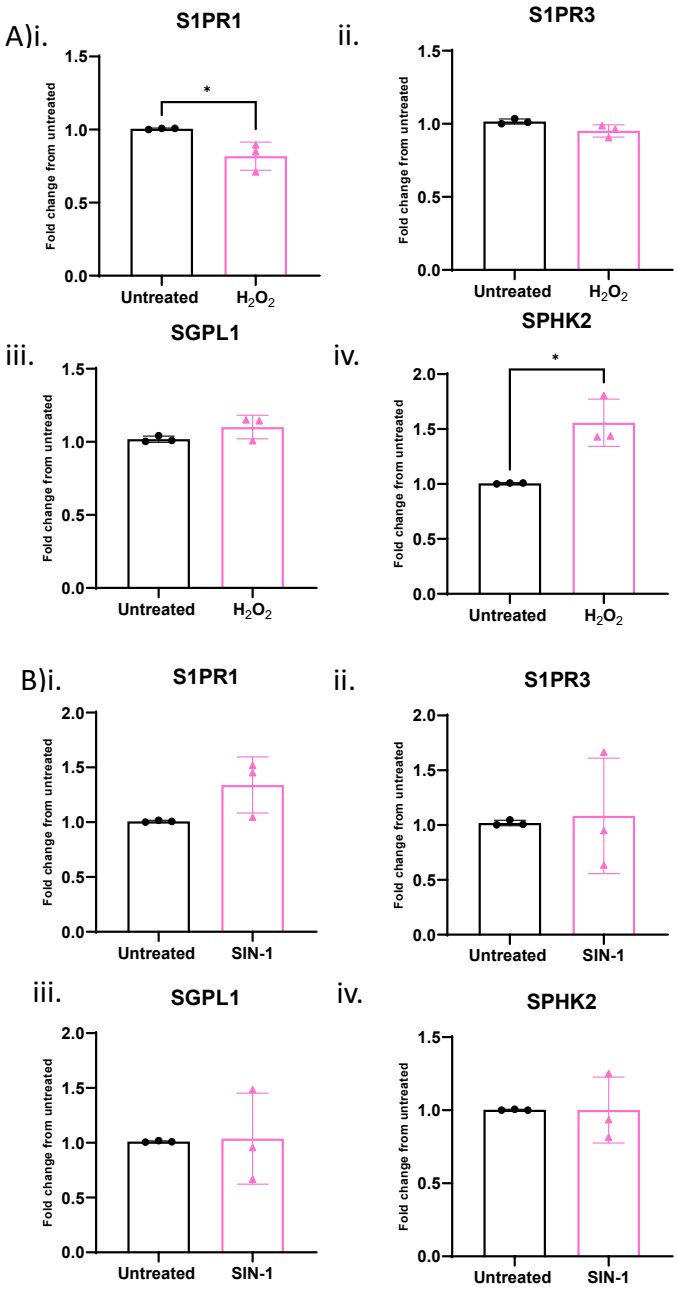

Figure 4.15. Gene expression of S1P-related genes in response to H_2O_2 and SIN-1 in HMEC-1.

RT-qPCR was used to quantify gene expression in response to **A)** H_2O_2 (100 µM) for 3 hours and **B)** SIN-1 (1mM) for 2 hours of **i)** *S1PR1*, **ii)** *S1PR3*, **iii)** *SGPL1* and **iv)** *SPHK2*. N=3. Gene expression is depicted as relative to untreated. Mean is presented with standard deviation. Statistical significance was determined using an unpaired t test. *p<0.05, **p<0.01, ***p<0.001, ****p<0.0001.

4.3.4. Effect of RNS and ROS on endothelial permeability of HPMEC and PPMEC

The primary aim of this chapter was to identify a model of IRI which would induce barrier disruption in endothelial cells. Work in cell lines had identified optimal dose and time ranges to be applied to primary cells and so we aimed to assess the effects of these on HPMEC and PPMEC permeability.

Prior to assessment of effects on endothelial permeability, HPMEC and PPMEC viability in response to H_2O_2 and SIN-1 were assessed in order to identify a physiologically relevant dose which causes the least cell death. This was to ensure that reductions in permeability were due to changes to endothelial cell and junction morphology and not cell death. In HPMEC, 200 μM H_2O_2 significantly reduced cell viability (Figure 4.16Ai), whilst the highest dose of SIN-1 (2 mM) had comparable survival to untreated cells (Figure 4.16Aii). Therefore, these doses were carried forward for permeability testing. PPMEC showed that viability following treatment with 200 μM H_2O_2 was unchanged from untreated (Figure 4.16Bi), whilst 1 and 2 mM SIN-1 caused significant cell death (Figure 4.16Bii). Therefore, 200 μM H_2O_2 and 0.5 mM SIN-1 was carried forward.

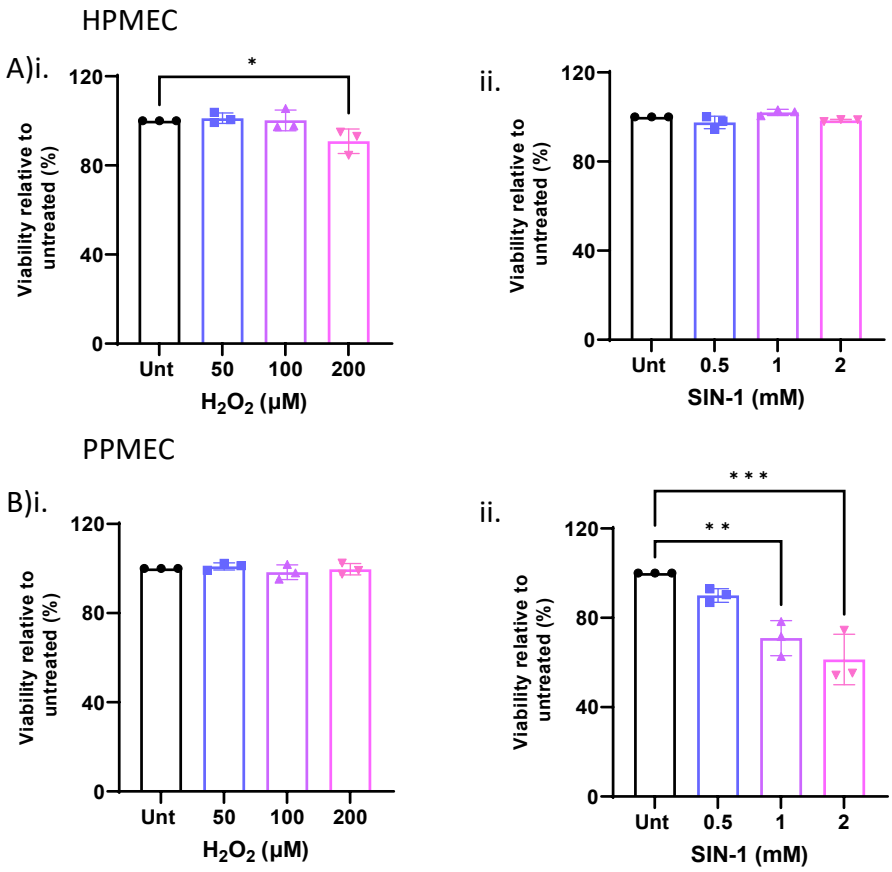

Figure 4.16. Primary endothelial cell viability in response to H_2O_2 and SIN-1.

An XTT assay was used to assess viability changes in **A)** HPMEC and **B)** PPMEC response to increasing concentrations of **i)** H_2O_2 and **ii)** SIN-1 for 3 hours. Viability is presented as a percentage relative to untreated (unt). N=3. Mean is presented with standard deviation. A two-way ANOVA with multiple comparisons was used to calculate statistical significance from untreated. *p<0.05, **p<0.01, ***p<0.001, ****p<0.0001.

Primary cells form monolayers due to contact inhibition, meaning they are good candidates for assessing permeability changes in response to treatments. Measuring TEER is a widely used technique which can be used to detect alterations to monolayer permeability, with resistance increases indicating higher monolayer integrity. HPMEC and PPMEC were grown on transwells until forming confluent monolayers, before treating with optimised concentrations of H_2O_2 and SIN-1 and measuring resistance over time. H_2O_2 did not significantly impact monolayer resistance overall in both HPMEC and PPMEC (Figure 4.17Ai and Bi respectively). However, SIN-1 significantly reduced monolayer permeability in both cell types (Figure 4.17Aii and Bii). Furthermore, multiple comparisons identified a significant decreased in resistance compared with untreated for HPMEC at 5 hours.

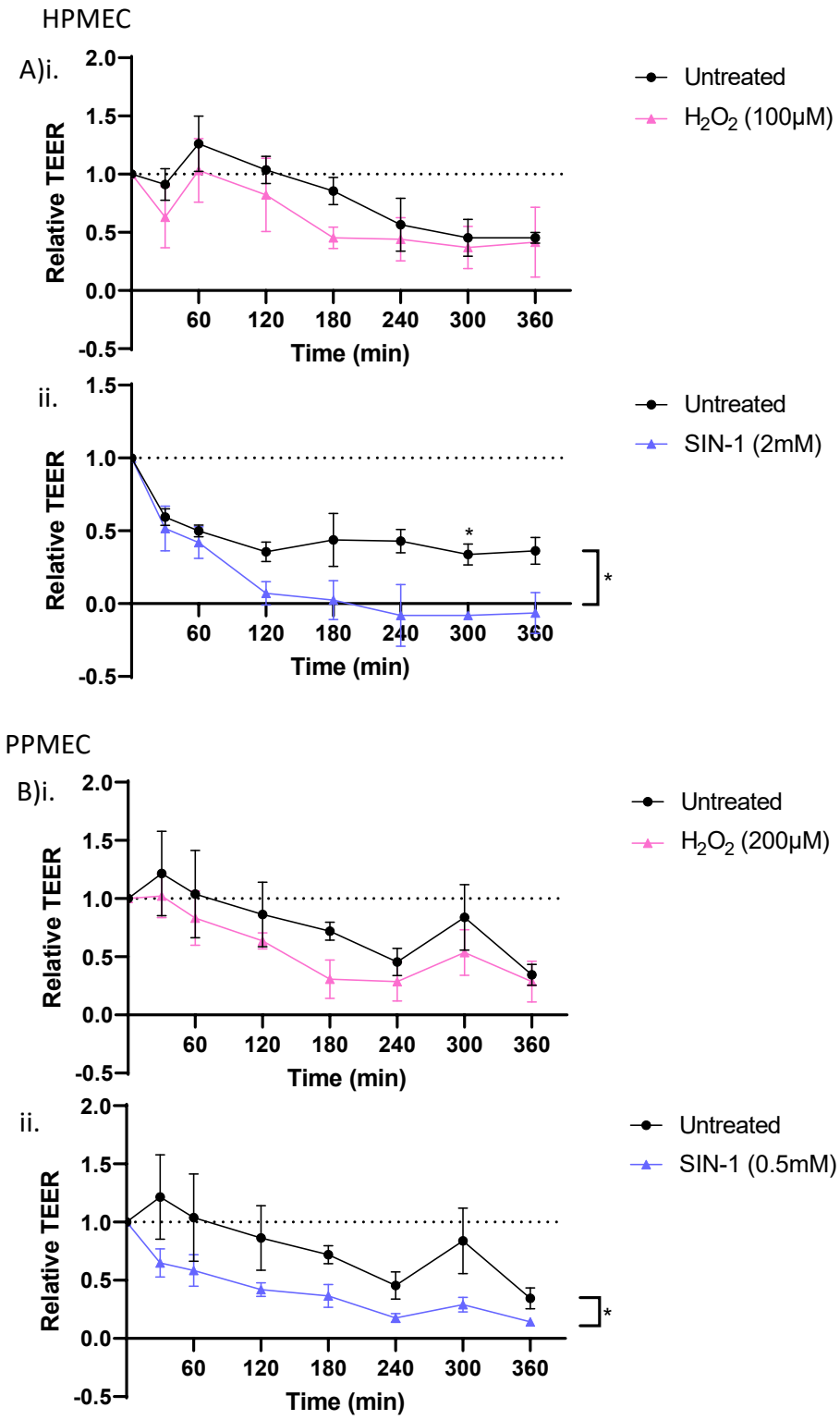

Figure 4.17. Primary endothelial monolayer permeability in response to H_2O_2 and SIN-1.

Confluent monolayers of **A)** HPMEC and **B)** PPMEC were treated with **i)** H_2O_2 and **ii)** SIN-1. Resistance was measured pre-treatment and at 0.5, 1, 2, 3, 4, 5 and 6 hours. TER was calculated by subtracting blank transwell readings and multiplying by the transwell surface area. Then values were presented as relative to pre readings. N=3. Mean is presented with standard deviation. A two-way repeated measures ANOVA with multiple comparisons was used to calculate statistical significance of treated versus untreated at every time point and also to calculate the overall statistical significance of the column effect. *p<0.05, **p<0.01, ***p<0.001, ****p<0.0001.

4.4. Discussion

Modelling aspects of IRI *in vitro* is not only useful to define the mechanisms of pathology driving the disease process, but also to use as a context in which to administer therapeutics and to assess their effectiveness in mitigating this injury. In this chapter, we aimed to explore and optimise models of IRI in an endothelial cell line, before progression to primary endothelial cells. We used hypoxia, H_2O_2 and SIN-1 treatment to assess the effects on IRI and S1P related gene expression to gain insights at the transcriptomic level. Furthermore, a dose and time of ROS/RNS treatment range was optimised via assessment of viability, ROS release, gene expression and VE-cadherin cell surface localisation, before application to primary cells to assess monolayer permeability changes.

Of the ROS produced during IRI, it is believed that H_2O_2 overproduction contributes to a large percentage of IR-mediated tissue damage (Bae *et al*., 2016), whilst peroxynitrite is one of the most reactive and potentially damaging RNS (Pacher *et al*., 2007, Radi *et al*., 1991). Thus, we sought to utilise H_2O_2 and peroxynitrite donor SIN-1 treatment for our *in vitro* IRI models. Although it was useful to look at effects of hypoxia and hypoxia/reoxygenation on gene expression, ultimately it was decided that treatment with ROS/RNS with physiological oxygen levels maintained was more reflective of lung IRI. Furthermore, as permeability increases occur very readily following treatment and can quickly return to baseline, we wanted to have the capacity to carry out shorter term time points as little as 5 minutes. This was perhaps not achievable with the hypoxic incubator model, especially taking into account the fact that O_2 dissolved in media would take time to deplete.

In normoxia, HIF-1α is hydroxylated and targeted for proteasomal degradation, whilst in hypoxia, it is stabilised, dimerises with HIF-1β and promotes expression of hypoxia response genes. It is suggested that stabilisation of HIF-1α results in a negative feedback loop, which downregulates *HIF1A* mRNA (Cavadas *et al*., 2015). Accordingly, our data showed downregulation of *HIF1A* gene expression in our IRI models. *VEGFA* is a hypoxia response gene which is trans-activated during IRI; upregulation of *VEGFA* mRNA has been established in multiple *in vivo* IRI models across various organs (Banai *et al*., 1994, Hashimoto *et al*., 1994, Tuder *et al*., 1995, Tsurui *et al*., 2005). In this study, RT-qPCR analysis identified that *VEGFA* expression increased over time following hypoxia, H_2O_2 and SIN-1 treatment. Indeed, it is well established that hypoxia time dependently increases *VEGFA* mRNA expression in multiple

different cell types *in vitro* (Shweiki *et al*., 1992) and specifically in endothelial cells (Liu *et al*., 1995, Mukhopadhyay *et al*., 1995). H_2O_2 has also been shown to induce *VEGFA* gene expression dose/time dependently in endothelial (Chua *et al*., 1998) and epithelial cells (Kuroki *et al*., 1996). The same has been shown for SIN-1 in chondrocytes (Fay *et al*., 2006) and specifically, in peroxynitrite-treated endothelial cells (Platt *et al*., 2005). Thus, we were able to validate these models via interrogation of *HIF1A* and *VEGFA* gene expression in tandem.

There is considerably less literature on the changes to endothelial cell specific S1PR gene expression and the data is often conflicting dependent on cell/organ type. Due to their role in modulating endothelial barrier integrity, gene expression of *S1PR1* and *S1PR3* was measured in response to models of IRI. Our data showed that all of our *in vitro* IRI models reduced *S1PR1* gene expression, whilst *S1PR3* was reduced only in our hypoxia and hypoxia/reperfusion models. However, it has been shown that hypoxic incubation of cardiomyocytes increased *S1PR1, S1PR2* and *S1PR3* mRNA levels *in vitro* (Yang *et al*., 2018) and *in vivo*, murine models of IRI resulted in increased *S1PR1* mRNA in the kidney and lung (Awad *et al*., 2006, Zhu *et al*., 2018) and increased *S1PR3* mRNA in the brain and kidney (Moon *et al*., 2015, Awad *et al*., 2006). In contrast, *S1PR1* mRNA was decreased following a murine stroke model (Moon *et al*., 2015).

SGPL1 encodes SPL, which irreversibly catabolises S1P in tissues (Proia and Hla, 2015), whilst SPHK2, encoded by the *SPHK2* gene, has been postulated to have a somewhat undefined role of clearing S1P from the circulation (Mehaffey *et al*., 2018). Thus, modulating these enzymes could influence S1P levels in the body and have therapeutic potential. Therefore, we sought to assess their gene expression during pathology. Whilst we showed that hypoxia and hypoxia/reoxygenation reduced *SPHK2* gene expression, treatment with H_2O_2 resulted in a significant increase. Previous studies have shown that in response to IRI, it is solely *SPHK1* mRNA that is induced, whilst SPHK2 is unchanged both *in vitro* and *in vivo* (Moon *et al*., 2015, Schwalm *et al*., 2008). Our data also showed that *SGPL1* was reduced in response to hypoxia and hypoxia/reoxygenation, whilst ROS and RNS treatments had no significant effect. Literature in part agrees with our findings; *in vitro* studies assessing the effects of hypoxia have shown reduced *SGPL1* mRNA in synoviocytes and adipocytes (Zhao *et al*., 2015, Ito *et al*., 2013), whilst an *in vivo* cardiac IRI model demonstrated unaltered expression of *SGPL1*, despite increases in lyase activity (Bandhuvula *et al*., 2011). If anything, our data suggests a

distinction between injury in the absence and presence of oxygen and its corresponding gene expression profiles of S1P related genes.

Our data also showed that *CXCL8* gene expression decreased in hypoxia, whilst H_2O_2 caused an early significant increase followed by a significant decrease over time and SIN-1 non-significantly increased gene expression over time. Meanwhile, other studies have showed that hypoxia increased *CXCL8* mRNA in HMEC-1 (D'Alessandro *et al*., 2019, Karakurum *et al*., 1994), whilst Loboda *et al* demonstrated the opposite (Loboda *et al*., 2006). Another study showed that H_2O_2 treatment had no effect on *CXCL8* mRNA in endothelial cells, whilst a significant upregulation was observed in epithelial cells, indicating the activation of different mechanisms dependent on cell type (Lakshminarayanan *et al*., 1997). To date, no other literature describes the effect of SIN-1 on *CXCL8* gene expression.

Taken together, our data indicates that our IRI models activate distinct gene expression pathways. It is suggested that not only could these mechanisms be dependent on the stimulus of signalling, but also the cell type (Lakshminarayanan *et al*., 1997). Assessment of protein expression of IRI and S1P-related mediators in response to the models would determine if this is something which was also seen following translation. It should also be taken into account that time of treatment could have influenced data as only hypoxic incubation was extended to 24 hours, whilst H_2O_2 and SIN-1 treatment was carried out for a much shorter duration.

This study also sought to optimise a model of IRI for application to permeability assessment in primary cells. Cell viability was assessed to identify a dose which would not cause significant cell death to ensure that permeability changes were instead due to morphological changes to the endothelium. As ROS-induced ROS release is typical of IRI (Zhou *et al*., 2018), we assessed intracellular ROS release in response to our models; indeed we saw significantly increased ROS in response to H_2O_2 and SIN-1. Furthermore, IRI is associated with a destabilisation and internalisation of VE-cadherin at the cell surface, which contributes to the characteristic endothelial hyper-permeability (Wang *et al*., 2022a, Wang *et al*., 2021). Accordingly, both SIN-1 and H_2O_2 have been shown to cause VE-cadherin disorganisation and loss at the cell surface (Zhang *et al*., 2005b, Ito *et al*., 2018). Whilst not significant, we did see a small increase in mean fluorescence intensity per pixel of VE-cadherin staining following H_2O_2 and SIN-1 treatment at 3 and 2 hours respectively. Perhaps assessment of the phosphorylation status of VE-cadherin would have been a more useful measure of junction instability, as numerous

studies have described VEGF-mediated VE-cadherin phosphorylation and internalisation downstream (Wessel *et al*., 2014, Wallez and Huber, 2008, Monaghan-Benson and Burridge, 2009, Murakami and Simons, 2009).

Ultimately, the main focus of this study is modulating endothelial integrity during IRI. As such, we sought to assess the effects of our ROS/RNS model on HPMEC and PPMEC monolayer permeability. During IRI, endothelial permeability is increased as a result of VEGF-α, thrombin, histamine and bradykinin-mediated mechanisms (Mehta and Malik, 2006). However, literature has also suggested that peroxynitrite influences barrier integrity by nitrating various proteins. Wu *et al* suggested a role for peroxynitrite-induced nitration of protein phosphatase type 2A, which causes its activation and the redistribution of tight junction proteins (Wu and Wilson, 2008). Similarly, Siddiqui *et al* suggested that peroxynitrite-mediated nitration of a GTPase activating protein (GAP) was responsible for increased endothelial permeability due to impairment of GAP activity and activation of RhoA (Siddiqui *et al*., 2011). Indeed, it has even been suggested that peroxynitrite is essential for H_2O_2-mediated barrier decline; blockade of NO production or peroxynitrite scavenging attenuated H_2O_2 induced hyper-permeability (Zhou *et al*., 2019). In line with this, our study showed that SIN-1, a peroxynitrite donor, significantly reduced TEER in HPMEC and PPMEC, indicating increased permeability. Due to the fact that SIN-1 had no significant effect of fluorescence intensity of VE-cadherin staining, this could suggest barrier modulation through mechanisms unrelated to VE-cadherin localisation. Either way, in this chapter we were able to identify an ideal candidate for therapeutic testing.

In this chapter, establishing a valid *in vitro* model of ischaemia and reperfusion was necessary prior to *in vitro* and *ex vivo* therapeutic testing in the context of injury. This allows the opportunity to identify appropriate S1PR agonists which may be useful in mitigating injury during porcine and human EVLP. In this chapter we identified that SIN-1 not only influenced endothelial expression of IRI and S1P-related genes, but significantly increased ROS release and increased endothelial permeability in both human and porcine pulmonary endothelium without causing significant cell death. Therefore, this was a good candidate to bring forward for *in vitro* and *ex vivo* testing.

5. The effects of S1PR1 agonist CYM5442 *in vitro* and during *ex vivo* lung perfusion

5.1. Introduction

Sphingosine-1-phosphate (S1P) is a lipid mediator which has roles in modulating endothelial integrity via signalling through S1P receptors S1PR1-3. As such, its therapeutic potential in inflammatory states such as ischaemia reperfusion injury (IRI) has been extensively studied and research has shown the protective effects of increasing circulating S1P during cardiac IRI (Bandhuvula *et al*., 2011, Morel *et al*., 2016) and S1P or S1PR agonist supplementation during liver (Lee *et al*., 2011, Ito *et al*., 2018), brain (Hasegawa *et al*., 2010) and lung IRI (Okazaki *et al*., 2007, Stone *et al*., 2015).

It has become well established that S1PR1 is crucial in conferring S1P-mediated vascular endothelial barrier protection; studies have used S1PR1 gene suppression or deletion and receptor antagonism and described increased endothelial permeability during baseline and disease states (Burg *et al*., 2018, Sammani *et al*., 2010, Tauseef *et al*., 2008), even after S1P supplementation (Garcia *et al*., 2001, Schaphorst *et al*., 2003, Tauseef *et al*., 2008). In fact, S1PR1 signalling has been shown to be vital for S1P-mediated protection during kidney IRI (Awad *et al*., 2006, Perry *et al*., 2016, Park *et al*., 2012). In contrast, S1PR2 and 3 have been shown to have opposing effects; S1PR2 contributes to barrier disruption in kidney IRI (Park *et al*., 2012), whilst S1PR3 activation has been shown to be damaging during liver (Hu *et al*., 2019) and brain IRI (Gaire *et al*., 2018). Additionally, the benefits of S1PR2 knockout and S1PR3 gene silencing has been described during acute lung injury (Sammani *et al*., 2010).

Signalling through S1PRs leads to differential small GTPase activation, which determines the effects on barrier integrity. S1PR1 causes activation of Rac, which causes cell spreading and intercellular junction stabilisation (Wójciak-Stothard *et al*., 2001), whilst S1PR 2 and 3 activates Rho, which antagonises Rac and causes cellular contraction and stress fibre formation (Li *et al*., 2015, Vouret-Craviari *et al*., 2002). GTPase activation has been shown to be dependent on circulating S1P concentrations, with high concentrations causing Rho-mediated signalling through S1PR2 and 3 and physiologically relevant concentrations causing activation of Rac via S1PR1 (Shikata *et al*., 2003).

S1P is normally present in human plasma at a concentration of 0.5-1μM (Berdyshev *et al*., 2005, Venkataraman *et al*., 2006, Hänel *et al*., 2007). S1P in excess of physiological concentrations has been shown to have detrimental effects on endothelial barrier integrity (Li *et al*., 2015, Liu *et al*., 2008) and Garcia *et al*. was the first to show that higher concentrations of S1P were associated with barrier decline (Garcia *et al*., 2001). Indeed, Li *et al* showed that excessive S1P activated S1PR2 and the RhoA/RhoA kinase pathway, causing F-actin disorganisation and disassembly of tight junction protein zonula occludens (ZO)-1 (Li *et al*., 2015). Similarly, Sammani *et al*. showed that S1P protected the pulmonary vasculature against LPS-mediated dysfunction at lower doses, whilst higher doses were associated with barrier disruption (Sammani *et al*., 2010).

Whilst the therapeutic potential of S1P and its associated analogues has been extensively studied in IRI of other organs, a smaller body of literature exists for the lung. However, Okazaki *et al* did describe attenuation of injury in a rat model of lung transplantation with reduced tissue wet to dry ratios and Evan's blue (EB) extravasation in response to S1P treatment (Okazaki *et al*., 2007). Similarly, Stone *et al* demonstrated S1PR1-mediated barrier enhancement in a murine model of lung IRI, with S1PR1 agonist treatment resulting in improved lung function, decreased vascular leak and reduced pro-inflammatory cytokine and neutrophil accumulation (Stone *et al*., 2015).

Ex vivo lung perfusion (EVLP) offers an excellent opportunity to recondition donor lungs prior to transplantation, away from donor or recipient influence. Whilst research into the application of therapeutics during EVLP has increased exponentially in the last few years, only one study to date has assessed the effects of S1P administration. Mehaffey *et al* used murine EVLP and assessed the effect of adding S1P in tandem with a sphingosine kinase 2 (SPHK2) inhibitor, which functions to reduce circulating S1P clearance. As such, the study described increased lung compliance and reduced vascular permeability to EB dye and provided some of the first evidence of the potential benefits of targeting the S1P axis during EVLP (Mehaffey *et al*., 2018).

Evidence therefore suggests that modulation of S1P signalling during EVLP could be used to recondition vascular integrity in extended criteria donor (ECD) organs and ultimately increase donor lung utilisation, which is the currently the lowest of any organ (NHS Blood and Transplant, 2022). However, administration of S1P alone could potentially lead to activation

of off target receptors and barrier disruption. In this study, S1PR1 agonist CYM5442 was chosen for testing based on its high potency compared with other S1PR1 agonists (Gonzalez-Cabrera *et al*., 2008), whilst S1PR1,3,4,5 agonist FTY720P was chosen based on the success of Fingolimod in treating multiple sclerosis in clinical trials (Khatri, 2016).

Thus, this chapter aimed to:

- Assess the effects of CYM5442 and FTY720P on endothelial permeability *in vitro* and optimise a therapeutic dose for translation.
- Progress to use in porcine and human paired lung EVLP models and assess the effects on lung permeability to EB dye, lung weight and wet to dry (W/D) ratios and lung water content.

5.2. Materials and Methods

5.2.1. XTT Cell Proliferation assay

During initial testing, viability of human pulmonary microvascular endothelial cells (HPMEC) in response to CYM5442 and FTY720P was assessed. 10,000 HPMEC were seeded onto 96-well plates in triplicates and incubated overnight. The next day, wells were washed with 100 μL PBS and cells were treated with 200 μL 10, 25, 50, 75 or 100 μM CYM5442 or 0.1, 0.25, 0.5, 0.75, 1 μM FTY720P or left untreated for 6 hours to mimic EVLP duration and then an XTT assay was carried out as described in section 2.1.6.2.

Prior to testing the effects of CYM5442 in perfusate solution rather than serum free media on endothelial permeability, porcine pulmonary microvascular endothelial cell (PPMEC) and HPMEC viability was assessed in Steen and Dulbecco's Modified Eagle Medium (DMEM) respectively. PPMEC and HPMEC were seeded at a density of 10,000 cells per well in triplicates, incubated overnight and then washed with PBS. Then PPMEC were treated with Steen or left in complete media and HPMEC were treated with modified DMEM or left in complete media for 6 hours to mimic EVLP duration. Then an XTT assay was carried out as described in section 2.1.6.2, but with complete media in place of serum free.

5.2.2. Western blot to assess ERK phosphorylation

For time course experiments, 200,000 HPMEC were seeded in duplicates onto 6-well plates and incubated overnight. Media was aspirated and wells were washed with 1 mL PBS, before serum starving in serum free media for 1 hr. Then wells were treated with 1 μM CYM5442 or FTY720P for 2, 5 or 10 min or left untreated.

For comparison of signalling in HPMEC and PPMEC, 200,000 HPMEC and PPMEC were seeded per well in duplicates onto 6-well plates and incubated overnight. Then media was removed and wells were washed with 1 mL PBS, before replacing with serum free media and serum starving for 1 hr. Then cells were treated with 1 μM CYM5442 or FTY720P for 5 min.

Following treatment, wells were washed with ice cold PBS, before carrying out the western blot workflow described in 2.5.1. Membranes were probed for P-ERK1/2, before stripping and re-probing for Pan ERK1/2 and then for α-tubulin, which was used as a house keeping. For

quantification, densitometry analysis was carried out using Image Studio™ and used to determine P-ERK/ERK ratio.

5.2.3. Phospho-ERK ELISA on cell lysates

To assess ERK phosphorylation in response to agonists in cellular lysates, an ERK 1/2 (Total/Phospho) InstantOne ELISA™ Kit was used (cat. 85-86013; Invitrogen). The kit allows simultaneous detection of both ERK 1/2 and phospho (P)-ERK 1/2 (Thr202/Tyr204, Thr185/Tyr187) on the same plate by including antibody cocktails for both.

Kit reagents were made up only immediately prior to use. Cell Lysis Mix (5X) was made up according to kit protocol by diluting Enhancer solution 10-fold with Cell Lysis Buffer (5X) and this was then diluted 5-fold with diH_2O to make Cell Lysis Mix (1X). Wash Buffer (10X) was diluted 10-fold with diH_2O to make Wash Buffer (1X). Positive control cell lysate was reconstituted with diH_2O as instructed in the protocol. The ERK 1/2 Antibody Cocktail and the P-ERK 1/2 (Thr202/Tyr204, Thr185/Tyr187) was each made by mixing equal volumes of corresponding Capture Antibody Reagent with corresponding Detection Antibody Reagent and mixing by inversion as specified in the kit protocol.

Per treatment, 14 wells of HPMEC were seeded at a density of 15,000 cells per well onto 96-well plates and allowed to incubate overnight. The next day, wells were washed with 100 μL PBS, before a 1 hr serum starvation in 100 μL serum free media. Cells were then treated with concentrations of CYM5442 ranging from 1 nM -100 μM and FTY720P ranging from 0.1 nM-10 μM or left untreated for 5 min as optimised by western blot. Following treatment, wells were washed with PBS, before adding of 25 μL Cell Lysis Mix (1X) per well and shaking at 300 RPM at room temperature for 10 minutes. The lysates for the same treatment were compiled in the same tube.

50 μL of each lysate was then added to 6 wells each of the InstantOne ELISA™ plate, with a triplicate for each antibody cocktail. 50 μL of the positive Control Cell lysate and Cell Lysis Mix (1X) as a negative control were also added. This was immediately followed by 50 μL of either the prepared ERK 1/2 Antibody Cocktail or the prepared P-ERK 1/2 (Thr202/Tyr204, Thr185/Tyr187) Antibody Cocktail before sealing and incubating at room temperature for 1 hour on a microplate shaker (300 RPM). Wells were then aspirated and washed with 200 μL per well Wash Buffer (1X) 3 times. Then 100 μL Detection reagent was added to each well and

incubated for 10-30 minutes with shaking (300 RPM) until colour was sufficient. Reaction was stopped using 100 μL Stop Solution per well and then absorbance was measured using a microplate reader set at 450 nm. Negative control readings were subtracted from values before plotting.

5.2.4. Measurement of endothelial permeability *in vitro* in response to agonist treatment

Prior to experiments, HPMEC and PPMEC were grown on transwells until forming confluent monolayers as optimised in section 4.2.5.1. Empty transwells were used as controls. Complete media was removed and transwells were washed with PBS and put into new 24-well plates. 300 μL serum free media was added to the top of each transwell, with 700 μL below and wells were serum starved for 1 hr.

5.2.4.1. Trans-endothelial electrical resistance

Resistance was measured pre-treatment immediately following serum starvation. Then cells were treated as described below.

For testing of increasing concentrations of agonists over time, PPMEC were treated with 0.2, 0.5, 1, 2, 5 or 10 μM CYM5442 or FTY720P or left untreated, whilst HPMEC were treated with 0.05, 0.1, 0.2, 0.5, 1 or 10 μM CYM5442 or FTY720P or left untreated. For agonist testing in perfusate solutions, treatment was performed with no serum starvation; PPMEC monolayers were left untreated or treated with 0.1, 0.2, 0.5, 1 or 2 μM CYM5442 in Steen solution, whilst HPMEC monolayers were left untreated or treated with 0.025, 0.05, 0.2 or 1 μM CYM5442 in modified DMEM solution. Then resistance was measured at 5, 15, 30, 60, 120, 180, 240, 300 and 360 min after treatment and trans-endothelial electrical resistance (TEER) was calculated as per 2.2.1. Then TEER was presented relative to pre-treatment values.

For agonist testing in the context of injury, duplicate wells of PPMEC were either left untreated, treated with 0.5 mM SIN-1 or treated with 1 or 2 μM CYM5442 with or without 0.5 mM SIN-1. HPMEC were either left untreated, treated with 2 mM SIN-1 or treated with 0.05 or 0.2 μM CYM5442 with or without 2 mM SIN-1. For agonist retreatment experiments, PPMEC were either left untreated, treated with 0.5 mM SIN-1 or treated with 2 μM CYM5442 with or without 0.5 mM SIN-1 in duplicates. There were also two 'retreatment' groups, which were treated with 2 μM CYM5442 with or without 0.5 mM SIN-1 initially, before undergoing

a retreatment with 2 μM CYM5442 at 3 hours. Resistance was measured at 30, 60, 120, 180, 240, 300 and 360 min after treatment and TEER was calculated as per 2.2.1. Then TEER was presented relative to pre-treatment values.

5.2.4.2. FITC-dextran permeability assay

PPMEC monolayers were either left untreated or pre-treated with 0.2 or 2 μM CYM5442 for 1 hr. Then 200 μL 0.5 mg/mL FITC dextran in phenol red and serum free endothelial cell medium (Cell Biologics; M1168PF) was added to the top of each transwell with or without 0.5 mM SIN-1. 600 μL phenol red and serum free medium was added to the bottom of each transwell with or without SIN-1. Then 50 μL were taken in duplicates at given time points and fluorescence intensity was quantified as described in 2.2.2.

5.2.5. RT-qPCR

HPMEC were seeded onto 6-well plates in duplicates at a density of 200,000 cells per well and left to incubate overnight. Then media was removed and wells were washed with 1 mL PBS, before serum starving in serum free media for 1 hr. Cells were then left untreated or treated with 0.5 ng/mL IL-1β, 2 mM SIN-1, 2 mM SIN-1 in combination with 0.2 μM CYM5442 or 0.2 μM CYM5442 alone for 6 hours. Then treatment was removed, wells washed with PBS and RNA was extracted as in 2.4.1.1 and cDNA synthesised as in 2.4.2. Then qPCR was performed as detailed in section 2.4.3 using Taqman™ gene expression assays to quantify expression of *ICAM1*. C_t values were normalised against *RPLP0* and then fold changes were calculated relative to untreated.

5.2.6. *Ex vivo* lung perfusion

5.2.6.1. Porcine lungs

Ethical approval for porcine work was obtained from NU AWERB (ID973). Female white landrace pigs weighing up to 80 kg were used from Cockle Park Farm and retrieval was carried out on-site. A porcine donation after circulatory death (DCD) model was used in this study; humane sedation and terminal anaesthesia of the donor pig was carried out by qualified farm staff prior to retrieval. For sedation, Zoletil®100 (Virbac) was injected intramuscularly before terminal anaesthesia via ear vein injection of Euthatal. Asystole was confirmed prior to operating. Retrieval of porcine lungs was carried out by a cardiothoracic surgeon. In short,

following confirmation of cardiac arrest, the trachea was cut and an endotracheal (ET) tube inserted for lung inflation with an Ambu® bag or left uninflated. Then the sternum was split using an oscillating saw and retrieval was carried out as per standard clinical lung retrieval, but with modifications for the differing anatomy of the pig lung. Lungs were flushed anterogradely with 1 L room temperature Perfadex® Plus followed by 2 L at 4 °C and then 1 L retrogradely at 4 °C, each containing 5000 U/L of heparin. Once the lungs were isolated, the trachea was clamped and lungs were stored in 2L Perfadex® Plus and triple bagged. Warm ischaemic time (WIT) and cold ischaemic time (CIT) was changed for every experiment in order to identify the optimal conditions.

5.2.6.2. Human lungs

Human donor lungs which were declined by all UK centres for clinical transplantation were accepted for research after consent from donor's next of kin was obtained. Furthermore, to be accepted for this study lungs had to have no unilateral pathology, no active untreated lower respiratory tract infection and no concerning x-ray or CT findings. Organs were obtained under Human Research Authority Research Ethics Committee approval (REC:16/NE/0230) as part of NHSBT Study 66, entitled 'Further Evaluation of *Ex vivo* Lung Perfusion to Improve Transplantation Outcomes' and were retrieved by a clinical retrieval team as per standard practice.

5.2.6.3. Split lung EVLP

In order to assess the effects of a therapeutic agent in tandem with a control group, a split lung EVLP model was used, which has been optimised by our group and is described by Pither *et al* (Pither *et al*., 2023). EVLP experiments were carried out in a controlled access laboratory within the Centre for Life Perfusion laboratory, Newcastle upon Tyne.

5.2.6.3.1. Preparation of isolated lung perfusate

For porcine EVLP, Steen solution was used as per the work of collaborators XVIVO Perfusion.

For human EVLP, a customised DMEM solution was used. Bovine serum albumin (BSA; MP Biomedical) was added to 500 mL DMEM (high glucose, sodium bicarbonate, without L-glutamine, sodium pyruvate and phenol red; Sigma) at a concentration of 5 %. The solution was mixed for approximately 15 minutes on a rocker, before filtering with a 0.45 μm pore

vacuum filter unit (Fisher Scientific). Perfusate solution was then refrigerated at 4 °C prior to use and stored for up to 1 month.

5.2.6.3.2. Priming the circuit

Two Medtronic© circuits (Medtronic) were assembled and each primed with 1.5 L Steen for porcine perfusions or DMEM solution for human perfusions, with 7500 units of heparin. Each circuit was de-aired and perfusate was circulated at a flow rate of 0.5-1 L/min. The perfusate was warmed by attaching the heater-cooler unit to the oxygenator on the circuit and setting it to 32 °C. 7 % CO_2/N_2 gas was also attached to the oxygenator.

The set-up of the circuits is depicted in Figure 5.1.

Blood gas measurements of each circuit were obtained by sampling from the reservoir and running on the RAPIDPoint® 500e blood gas analyser (Siemens). Partial pressure of CO_2 was maintained between 3-5 kPa/mmHg and pH between 7.3-7.5. Physiological oxygen was maintained using a membrane oxygenator gas flow titrated to the CO_2 concentration. The former was altered if necessary by further opening or closing of the gas regulator, whilst pH was maintained via addition of Tromethamine (THAM) to increase pH.

Figure 5.1. Human split lung EVLP set up.

Lungs were split and attached to two separate Medtronic circuits which allow simultaneous perfusion of a treated and untreated lung. Depicted is both circuits with each lung attached.

5.2.6.4. Calculation of cardiac output

5.2.6.4.1. Porcine

To calculate the required flow rates (ml/min) for each lung for porcine EVLP, 100 % cardiac output (CO) was calculated as below (van Essen *et al*., 2018). Actual body weight was used rather than ideal body weight (IBW) as for human EVLP.

$$100\%\ CO = 0.55 \times Body\ weight^{0.52}$$

$$40\%\ CO = (0.55 \times Body\ weight^{0.52}) \times 0.4$$

$$20\%\ CO = (0.55 \times Body\ weight^{0.52}) \times 0.2$$

Values were then split based on the actual percentage of each lung of total lung weight.

5.2.6.4.2. Human

Ideal body weight equation:

To calculate the donor ideal body weight (IBW) in kg, the donor height in cm was inserted into the below equations for male and female.

$$Male\ IBW\ = \big((Height\ cm - 154) \times 0.9\big) + 50$$

$$Female\ IBW\ = \big((Height\ cm - 154) \times 0.9\big) + 45.5$$

IBW was then used to calculate flow rates for each lung, as well as tidal volume and respiratory rate (breaths per min) for ventilation.

Cardiac output equations:

To calculate the required flow rates (ml/min) for each lung for human EVLP, 100 % CO was calculated as below.

$$100\%\ CO = (70ml\ \times\ IBWkg) \times Percent\ of\ total\ lung\ weight$$

$$40\%\ CO = \big((70ml\ \times\ IBWkg) \times Percent\ of\ total\ lung\ weight\big) \times 0.4$$

$$20\%\ CO = \big((70ml\ \times\ IBWkg) \times Percent\ of\ total\ lung\ weight\big) \times 0.2$$

Values were split into 45 % and 55 % for the left and right lung respectively.

5.2.6.5. Lung preparation for perfusion

The preparation procedure was carried out with the lungs resting in cold preservation solution in a metal bowl. Lungs were also left inflated and were covered with wet swabs. The left and right branches of the pulmonary artery (PA) and pulmonary vein were each cannulated (XVIVO). Then the trachea was dissected until location of the carina. The trachea was clamped just before the left bifurcation, before cutting to deflate the left lung and suctioning the airway. Then an adult ET tube was inserted and secured with a purse string stitch. Following this, the right lung was deflated and the airway suctioned. In pigs, the right upper lobe bronchus arises directly from the trachea. Therefore, the ET tube for the right lung was secured in the proximal trachea, with the orifice to the left main bronchus oversewn. Then another ET tube was inserted and secured. Figure 5.2 shows lungs following cannulation, splitting and insertion of ET tube into airway.

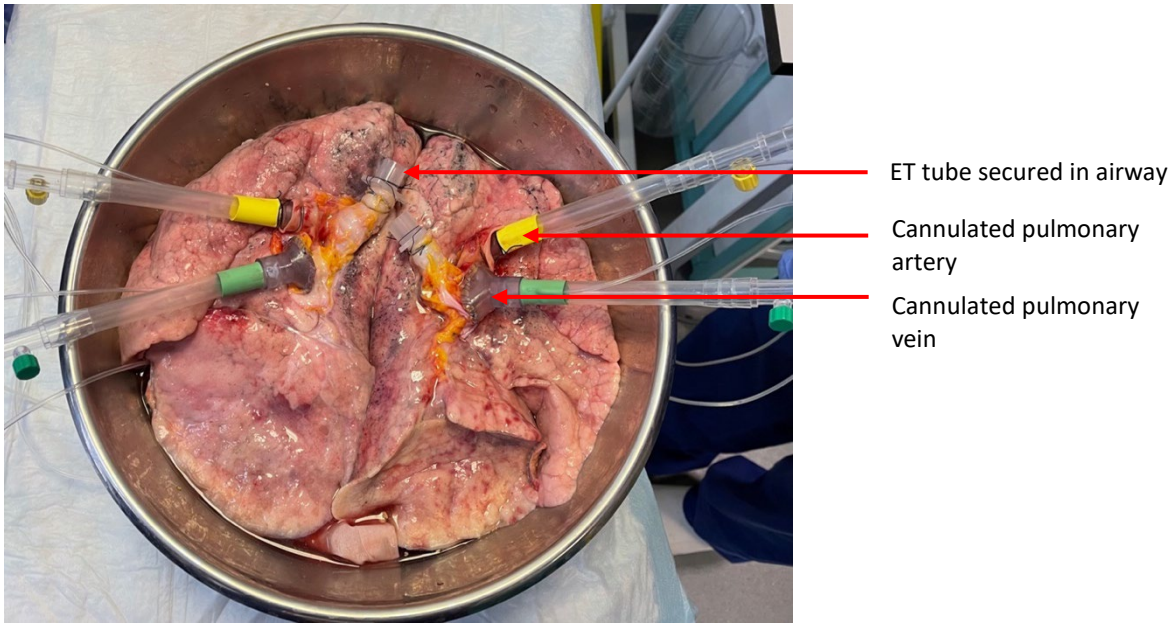

Figure 5.2. Lungs following preparation for EVLP.

Pulmonary arteries (yellow) and veins (green) were cannulated for each lung. Then the bronchus was divided after the carina and an ET tube inserted into each airway. The lungs shown are ready to attach to each circuit.

5.2.6.6. Perfusion procedure

Immediately after splitting, lungs were weighed and connected to each circuit. Initially, a flow rate of 20 % CO was used, which was calculated for each lung as described above. As soon as lungs were connected, pre-primed pressure monitoring lines were attached to PA and LA cannulas, before flushing with saline and zeroing with the 3-way tap open to air. Once zeroed, the tap was opened to the lung. For pressure monitoring, a bonded DPS Single Line Pressure Monitoring kit (Smith Medical) was used, with a GE DASH 5000 monitor (GE Healthcare).

Following attachment, the flow rate was gradually increased to 40 % CO over a period of 15 minutes. Once the lungs had reached a temperature of 32 °C, a ventilator (Drager) was attached to each lung and parameters were set to a PEEP of 5, TINSP of 1.3 and O_2 of 21. Tidal volume and respiratory rate were set depending on IBW for human EVLP or actual weight for porcine EVLP. Tidal volumes were split into 45 % and 55 % for the left and right lung respectively for human EVLP, whilst tidal volume for porcine EVLP was split for left and right lungs based on calculated percentage of total lung weight. Tidal volume and respiratory rate were slowly increased as the temperature of each lung increased but did not exceed the maximum settings described for the corresponding IBW. This process is detailed in Figure 5.3.

Lungs were perfused for 6 hours. Throughout perfusion, regular blood gas measurements were recorded and pH and CO_2 was altered as required. Haemodynamic and ventilator parameters were also recorded throughout EVLP. A stable left atrial pressure (LAP) was maintained between 1 and 5 mmHg at the designated 40 % CO flow rate for each lung.

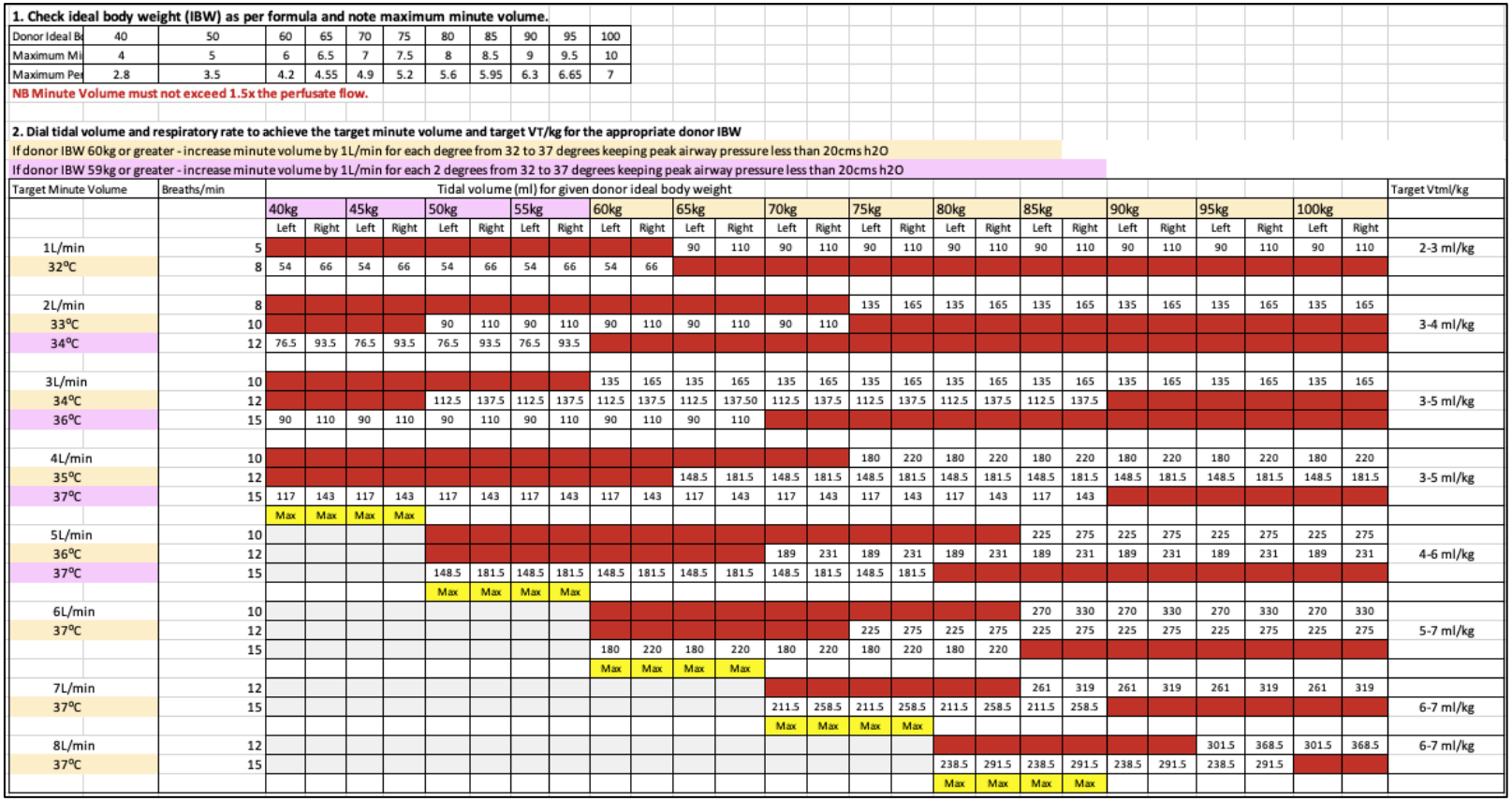

1. Check ideal body weight (IBW) as per formula and note maximum minute volume.

Donor Ideal Bo	40	50	60	65	70	75	80	85	90	95	100
Maximum Mi	4	5	6	6.5	7	7.5	8	8.5	9	9.5	10
Maximum Per	2.8	3.5	4.2	4.55	4.9	5.2	5.6	5.95	6.3	6.65	7

NB Minute Volume must not exceed 1.5x the perfusate flow.

2. Dial tidal volume and respiratory rate to achieve the target minute volume and target VT/kg for the appropriate donor IBW

If donor IBW 60kg or greater - increase minute volume by 1L/min for each degree from 32 to 37 degrees keeping peak airway pressure less than 20cms h2O

If donor IBW 59kg or greater - increase minute volume by 1L/min for each 2 degrees from 32 to 37 degrees keeping peak airway pressure less than 20cms h2O

Target Minute Volume	Breaths/min	Tidal volume (ml) for given donor ideal body weight																												Target Vtml/kg
		40kg		45kg		50kg		55kg		60kg		65kg		70kg		75kg		80kg		85kg		90kg		95kg		100kg				
		Left	Right	Left	Right	Left	Right	Left	Right	Left	Right	Left	Right	Left	Right	Left	Right	Left	Right	Left	Right	Left	Right	Left	Right	Left	Right			
1L/min	5											90	110	90	110	90	110	90	110	90	110	90	110	90	110	90	110			2-3 ml/kg
32ºC	8	54	66	54	66	54	66	54	66	54	66																			
2L/min	8															135	165	135	165	135	165	135	165	135	165	135	165			
33ºC	10					90	110	90	110	90	110	90	110	90	110															3-4 ml/kg
34ºC	12	76.5	93.5	76.5	93.5	76.5	93.5	76.5	93.5																					
3L/min	10									135	165	135	165	135	165	135	165	135	165	135	165	135	165	135	165	135	165			
34ºC	12					112.5	137.5	112.5	137.5	112.5	137.5	112.5	137.50	112.5	137.5	112.5	137.5	112.5	137.5	112.5	137.5									3-5 ml/kg
36ºC	15	90	110	90	110	90	110	90	110	90	110	90	110																	
4L/min	10															180	220	180	220	180	220	180	220	180	220	180	220			
35ºC	12											148.5	181.5	148.5	181.5	148.5	181.5	148.5	181.5	148.5	181.5	148.5	181.5	148.5	181.5	148.5	181.5			3-5 ml/kg
37ºC	15	117	143	117	143	117	143	117	143	117	143	117	143	117	143	117	143	117	143	117	143									
		Max	Max	Max	Max																									
5L/min	10																			225	275	225	275	225	275	225	275			
36ºC	12													189	231	189	231	189	231	189	231	189	231	189	231	189	231			4-6 ml/kg
37ºC	15					148.5	181.5	148.5	181.5	148.5	181.5	148.5	181.5	148.5	181.5	148.5	181.5													
						Max	Max	Max	Max																					
6L/min	10																			270	330	270	330	270	330	270	330			
37ºC	12															225	275	225	275	225	275	225	275	225	275	225	275			5-7 ml/kg
	15									180	220	180	220	180	220	180	220	180	220											
										Max	Max	Max	Max																	
7L/min	12																			261	319	261	319	261	319	261	319			
37ºC	15													211.5	258.5	211.5	258.5	211.5	258.5	211.5	258.5									6-7 ml/kg
														Max	Max	Max	Max													
8L/min	12																							301.5	368.5	301.5	368.5			6-7 ml/kg
37ºC	15																	238.5	291.5	238.5	291.5	238.5	291.5	238.5	291.5					
																		Max	Max	Max	Max									

Figure 5.3. Calculation of tidal volume and breaths per minute from donor ideal body weight.

Both the tidal volume and respiratory rate for each lung were calculated based off the ideal body weight (IBW). Settings were increased with temperature after the lungs reached 32 ºC as depicted.

5.2.6.7. Administration of CYM5442 and Evan's Blue

Lungs were randomly allocated to treatment or control groups.

Once stable ventilation at 37 °C was achieved for each lung, this was recorded as time zero. CYM5442 was reconstituted in diH_2O to a stock concentration of 1.5 mM. Then CYM5442 was added to the reservoir of the circuit allocated to the treatment group to a final concentration of 0.2 μM for the first lung pair and then subsequently, a lower dose of 0.05 μM for following lungs based on results from the first perfusion and *in vitro* optimisation. For the control, an equal volume of diH_2O was added as a vehicle. For the first lung pair that was perfused, this was also re-dosed with the same concentration of CYM5442 at 2 hours to test the effects of retreatment, whilst subsequent lungs treated with 0.05 μM were not retreated.

Evan's blue was added into each circuit at 2 hours following time zero as described by Shaver *et al* (Shaver *et al*., 2018). In short, 1.5 g EB was dissolved in 50 mL diH_2O at a w/v of 3 %. Then 25 mL of this solution was added to the reservoir of each circuit to achieve a final concentration of 0.05 %.

5.2.6.8. Sample collection and processing during EVLP

5.2.6.8.1. Perfusate

10 mL perfusate samples were collected at sequential time points over the course of EVLP. Samples were then centrifuged at 1000 g for 10 minutes in a refrigerated centrifuge to remove cells and debris. Supernatant was removed and mixed before 1 mL aliquots were taken and stored at -80 °C.

5.2.6.8.2. Biopsies

Biopsy samples were taken pre attachment, as well as at 4 hours and 6 hours (post) EVLP. Tissue was collected using a TA30 stapler (Medtronic) to prevent vessel or airway leak during perfusion. The samples collected at each time point are detailed in Table 5.1.

Tissue was either placed in RNAlater™ stabilisation solution (ThermoFisher Scientific), 10 % neutral buffered formalin (Cell Pathologies), flash frozen in liquid nitrogen or mounted in optimal cutting temperature (OCT) compound over dry ice. RNAlater samples were stored at 4 °C for 24 hours, before storage at -80 °C. Formalin fixed samples were left at room

temperature for 48 hours, before replacing formalin with PBS. Fixed tissues were then paraffin embedded, cut and mounted onto slides by the Cellular Pathology Node at the Royal Victoria Infirmary (RVI), Newcastle upon Tyne Hospitals. Flash frozen and OCT tissues were stored at -80 °C.

Tissue was also used to calculate W/D ratio at the beginning and end of perfusion. Tissue was weighed to record 'wet weight', before drying for 48 hours in an incubator at 75 °C and weighing again to record 'dry weight'. Then ratios were calculated by dividing wet by dry weight.

To calculate the amount of EB in tissue at 4 hours and 6 hours EVLP, tissue biopsies were dissected into 3 separate chunks weighing <150 mg, which were rinsed in saline and blotted dry, before weighing and recording weights. Each chunk was then placed into a tube containing 1 mL formamide and then placed into a heat block at 55 °C for 24 hours for EB extraction from tissue. Samples were then spun at 12000 RPM for 45 min, before collection of the supernatant in a new tube. 50 μL of each sample was then added to a black clear bottom 96-well plate in duplicates, as well as two wells of formamide alone as blank readings. Then both the absorbance (620 nm) and the fluorescence (Ex: 620 nm, Em: 680 nm) was measured using a TECAN Spark® plate reader. Blank readings were subtracted from each value, before dividing each by their recorded tissue weight in g. Then the average of the three samples for each lung for each time point was calculated.

Lung	Time (min)	Lobe	Biopsy samples
Right	Pre	Lower	RNA later (x5), Formalin, Flash frozen, OCT, W/D ratio
	240	Lower	Formamide (x3), RNA later (x5), Formalin, Flash frozen, OCT
	360/post	Upper, lower, middle	Formamide (x3), RNA later (x5), Formalin, Flash frozen, OCT, W/D ratio
Left	Pre	Lower	RNA later (x5), Formalin, Flash frozen, OCT, W/D ratio
	240	Lower	Formamide (x3), RNA later (x5), Formalin, Flash frozen, OCT
	360/post	Upper, lower	Formamide (x3), RNA later (x5), Formalin, Flash frozen, OCT, W/D ratio

Table 5.1. Biopsy samples taken during EVLP experiments.

5.2.6.8.3. Bronchoalveolar lavage

A baseline BAL sample was collected at time zero immediately before CYM5442 administration. Then repeat BAL were collected at 4 and 6 hours, from a different area of lung each time. For collection of BALF, a video bronchoscopy was performed before instillation of 40 mL saline. As much fluid as possible was retrieved, before spinning at 1000 g for 10 minutes in a refrigerated centrifuge. Supernatants were added to a new tube and samples were spun for a second time at 734 g for 6 minutes.

The concentration of EB in BAL samples was then quantified; 50 μL of each BAL sample in duplicates was added to a black clear bottom 96-well plate alongside a two-fold standard curve from 1000 μg/mL to 1.95 μg/mL. PBS alone was also included for blank subtraction. Plates were read at an absorbance of 620 nm on a Tecan Spark plate reader. Then blank readings were subtracted from values and a standard curve was constructed using GraphPad Prism. Sample EB concentrations were then calculated based on the standard curve and present as μg/mL.

5.2.6.9. Direct Lung Ultrasound Evaluation technique

For evaluation of lung water, a novel Direct Lung Ultrasound Evaluation (CLUE) technique, was used as per the protocol described by Ayyat *et al* (Ayyat *et al*., 2020, Ayyat *et al*., 2019). In short, a grading of 1-4 was given for specified sections of the lung and recorded in a score sheet. Then a CLUE score was calculated for each lung as below:

$$\frac{(No.of\ Grade\ 1\ images\ \times 1) + (No.of\ Grade\ 2\ images\ \times 2) + (No.of\ Grade\ 3\ images\ \times 3) + (No.of\ Grade\ 4\ images\ \times 4) + (No.of\ consolidation\ images\ \times 5)}{No.of\ images\ taken}$$

5.2.7. ELISA on perfusate samples

ELISA was used for protein quantification of CXCL8, IL-1β and IL-6 in perfusate collected during EVLP. Human Duoset® CXCL8 (DY208-05) and IL-1β (DY201) ELISA kits were used (R&D) and ELISAs performed according to manufacturer instructions as detailed in sections 2.5.2.

5.2.8. Histology

5.2.8.1. Haematoxylin and Eosin Staining

To visualise histology of porcine lungs, paraffin embedded sections were dewaxed and rehydrated, before H&E staining, dehydration and mounting as in section 2.5.3.1.1.

5.2.8.2. Immunofluorescence staining

Immunofluorescence staining was performed on biopsy samples of each lung taken pre-perfusion. Tissues were dewaxed and rehydrated and Tris-EDTA buffer was used for antigen retrieval. Then immunofluorescence staining of vascular endothelial (VE)-cadherin was carried out as per section 2.5.3.2.2. Sections were visualised using the Zeiss Axioimager and Zen Pro Software, with 3 images taken per section. Then a representative image was presented for each set of lungs for each pig.

5.3. Results

5.3.1. Initial dose range optimisation for CYM5442 and FTY720P *in vitro*

5.3.1.1. ERK phosphorylation in HPMEC

Phosphorylation of ERK1/2 was assessed in response to CYM5442 and FTY720P to confirm receptor activation and signalling and to optimise an initial dose range. As human S1PR agonists, experiments were initially carried out in human cells and then signalling was confirmed in porcine cells.

In order to optimise a time of agonist treatment prior to P-ERK ELISA, HPMEC were treated with 1 μM CYM5442 or FTY720P for 0, 2, 5 or 10 mins before running of lysates on a western blot and probing for ERK 1/2 and p-ERK 1/2. Both CYM5442 and FTY720P stimulation caused maximal phosphorylation at 5 minutes (Figure 5.4A and B).

Then a p-ERK ELISA was performed in order to identify a range of concentrations causing maximal signalling. As shown in Figure 5.4Ci, CYM5442 exponentially increased p-ERK between concentrations 1-100 μM, whilst figure 5.4Cii showed maximal increases between 0.1-1 μM, with a sharp decrease between 1 and 10 μM (presumed to be a result of cell death due to lesser dilution of chloroform vehicle). Total ERK was relatively stable for both.

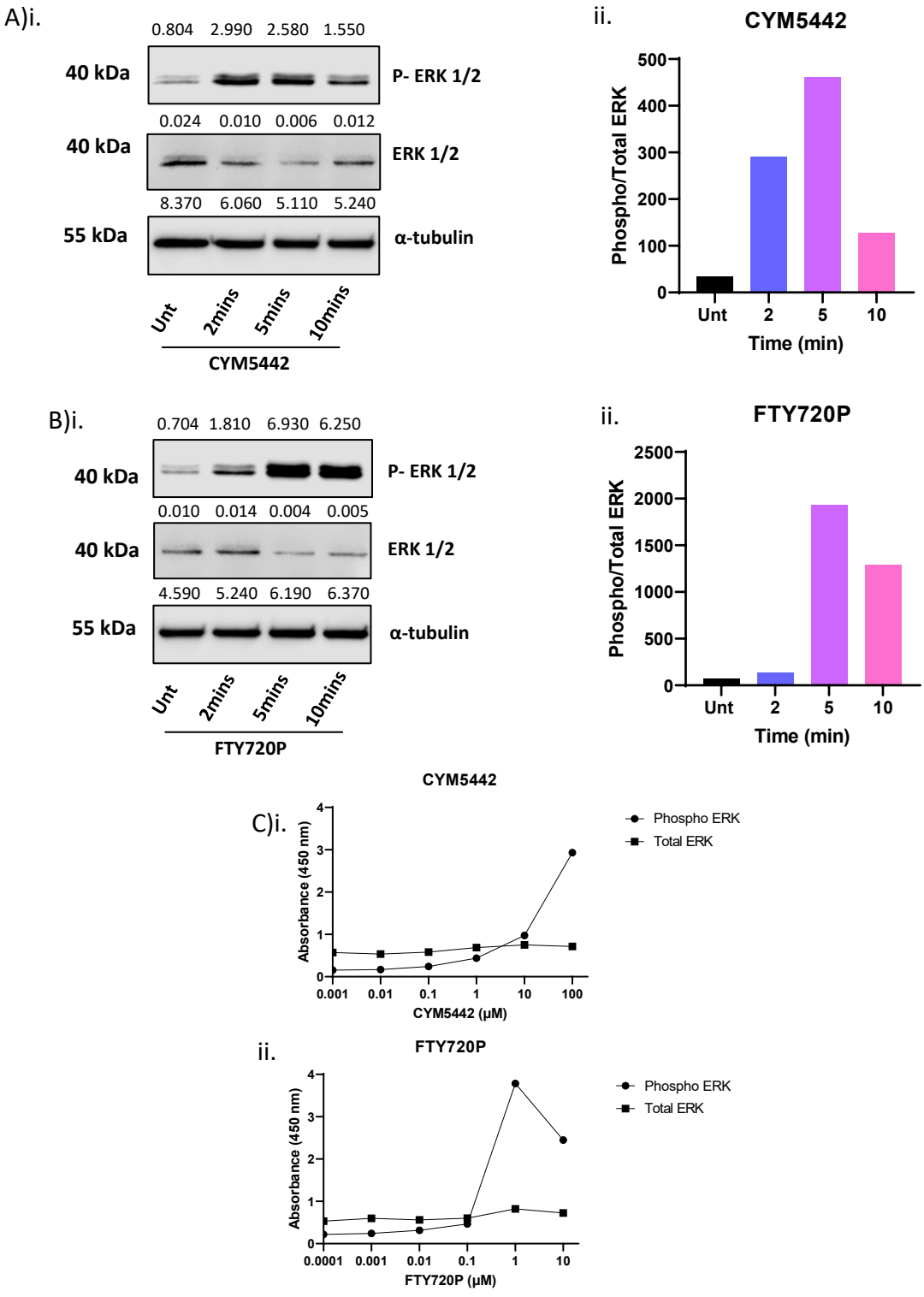

Figure 5.4. Initial dose range optimization of CYM5442 and FTY720P.

Erk phosphorylation was assessed to identify the most effective dose range. **A-B)** For western blot analysis, HPMECs were treated with **A)** 1 µM CYM5442 or **B)** 1 µM FTY720P for for 2, 5 or 10 minutes or left untreated in serum free media, before lysis and running on SDS PAGE for western blot. **i)** Membranes were probed with phospho (P)-ERK1/2 and total ERK1/2 was used as a loading control. α- tubulin was used as a housekeeping. **ii)** Band density of P-ERK is presented as a ratio of pan ERK for each treatment. N=1. **C)** P-ERK ELISA performed with lysates following treatment of HPMEC with increasing concentrations of **i)** CYM5442 and **ii)** FTY720P for 5 minutes as optimised in A-B. N=1.

As such, these doses were carried forward and HPMEC viability was assessed to determine the safety of dose ranges. Viability was maintained even at high doses of agonist treatment; CYM5442 treated cells showed a trend towards reduced viability at 75 and 100 μM, but viability was otherwise stable up to 50 μM (Figure 5.5A). FTY720P caused a significant increase in proliferation at 0.5 μM, but was otherwise comparable to untreated (Figure 5.5B).

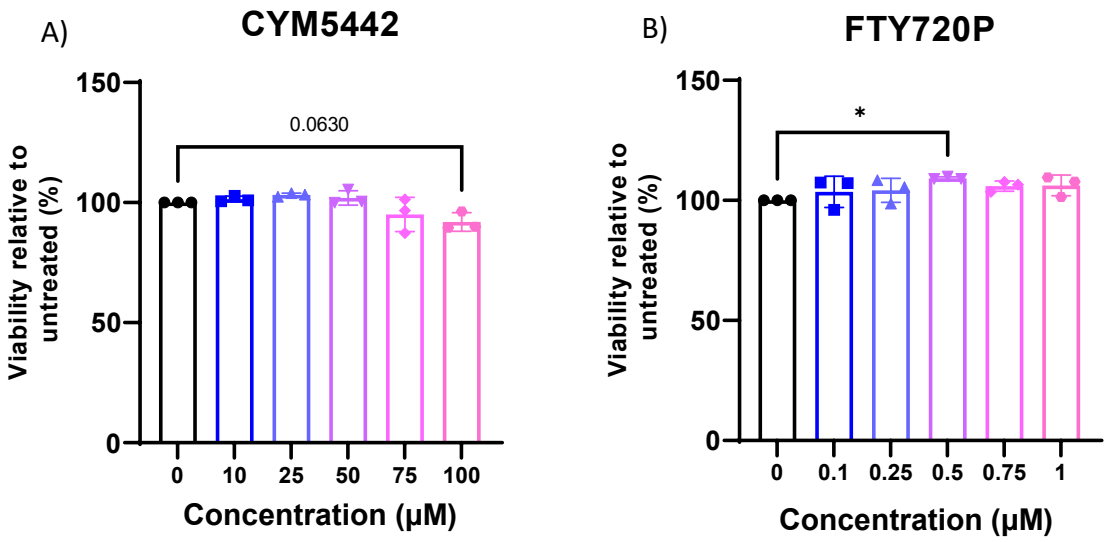

Figure 5.5. Cell viability in response to CYM5442 and FTY720P.

An XTT assay was used to assess viability changes in response to **A)** CYM5442 and **B)** FTY720P treatment over a range of concentrations. Viability is presented as a percentage relative to the untreated. N=3. Mean is presented with standard deviation. A one-way ANOVA with multiple comparisons was used to calculate statistical significance from untreated. *p<0.05, **p<0.01, ***p<0.001, ****p<0.0001.

5.3.1.3. ERK phosphorylation in PPMEC

CYM5442 and FTY720P are human S1PR agonists and human and pig S1PRs do not share 100 % homology. As we planned to test optimised S1PR agonists in PPMEC and during porcine EVLP, the ability of agonists to initiate signalling in porcine endothelial cells had to be validated. Both HPMEC and PPMEC were treated with 1 µM CYM5442 or FTY720P and western blot was performed to compare the extent of ERK phosphorylation. Following normalisation against total ERK, it was discovered that both cell types exhibited ERK phosphorylation in response to agonists albeit to different extents (Figure 5.6A-B). However, relative to untreated, PPMEC showed reduced P-ERK in response to both CYM5442 and FTY720P than HPMEC (Figure 5.6C), suggesting higher concentrations should be carried forward for testing in pig.

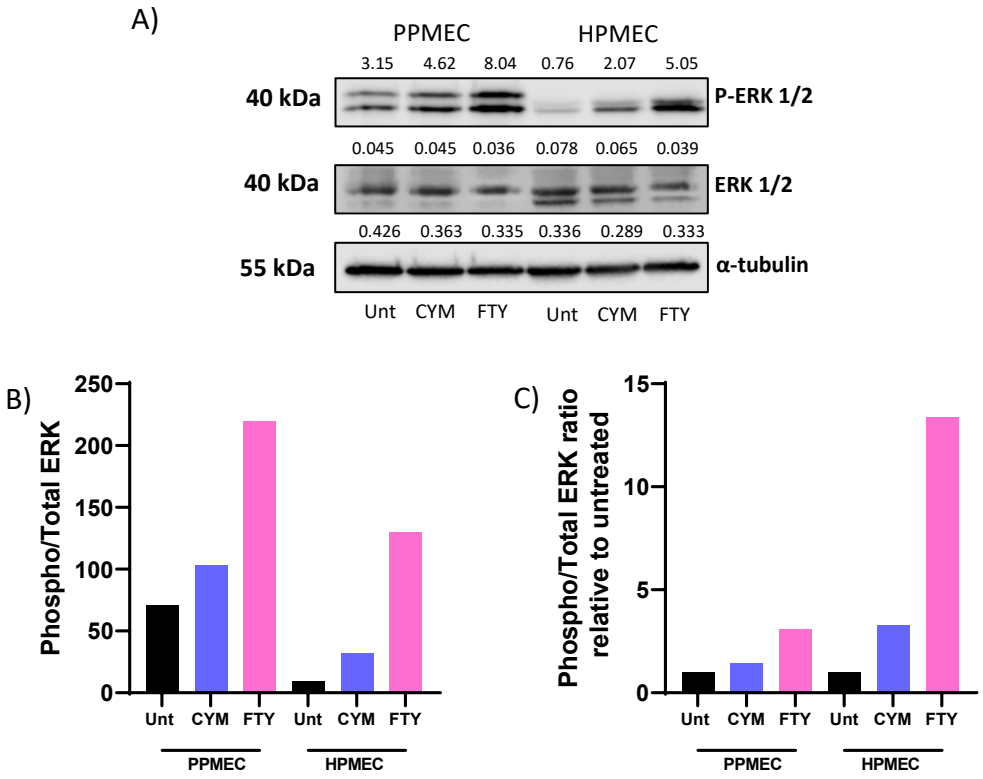

Figure 5.6. Validation of CYM5442 and FTY720P signaling in PPMEC.

For western blot analysis of phospho (P)-ERK, HPMECs were treated with 1 µM CYM5442 or 1 µM FTY720P for 5 minutes or left untreated in serum free media, before lysis and running on SDS-PAGE for western blot. **A)** Membranes were probed with P-ERK1/2 and total ERK1/2 was used as a loading control. α- tubulin was used as a housekeeping. **B)** Band density of P-ERK is presented as a ratio of pan ERK for each treatment. **C)** Band density of P-ERK presented as a ratio of pan ERK relative to untreated for each cell type. N=1.

5.3.2. *In vitro* testing of S1PR agonists in porcine endothelial cells

5.3.2.1. Trans-endothelial electrical resistance in response to CYM5442 and FTY720P at baseline

Prior to application to porcine EVLP, both CYM5442 and FTY720P were tested *in vitro* in PPMEC. Confluent monolayers of PPMEC were treated with increasing concentrations of CYM5442 or FTY720P and monolayer resistance was measured at sequential time points. Comparing each concentration at every time point showed that 2 μM CYM5442 significantly increased relative TEER compared to untreated at 60 and 360 minutes post treatment, whilst 1 μM significantly increased TEER at 240 and 360 minutes (Figure 5.7A). Figure 5.7Bi and 5.7Bii show 1 μM and 2 μM respectively compared with untreated alone, with both concentrations showing a significant increase overall.

Figure 5.8 shows that treatment with increasing concentrations of FTY720P caused a non-significant increase in PPMEC TEER up to 5 μM. 10 μM FTY720P caused a significant reduction in TEER at 5 and 6 hours. Therefore FTY720P was not carried forward.

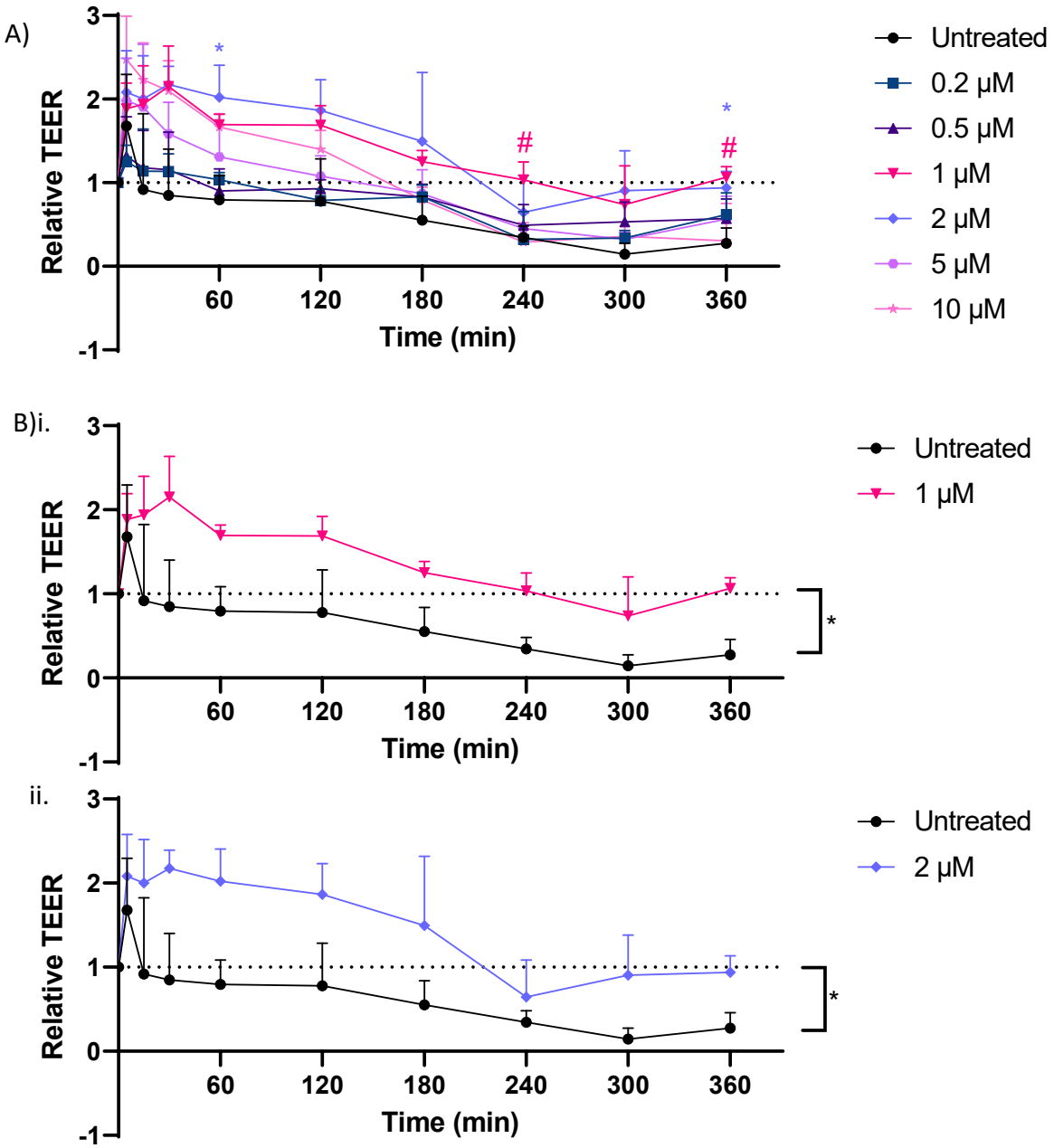

Figure 5.7. PPMEC monolayer permeability in response to increasing concentrations of CYM5442.

PPMEC were seeded onto 0.4 µm transwells and grown until a confluent monolayer was formed. Monolayers were treated with increasing concentrations of CYM5442 or left untreated. Resistance was measured pre-treatment and at 5, 15, 30 minutes and 1, 2, 3, 4, 5 and 6 hours post treatment. TEER was calculated by subtracting blank transwell readings and multiplying by the transwell surface area. Then values were presented as relative to pre readings. **A)** A time course of relative TEER in response to increasing concentrations of CYM5442. A two-way repeated measures ANOVA with multiple comparisons was used to calculate statistical significance of each concentration versus untreated at every time point. **Bi)** A time course of relative TEER in response to 1 µM CYM5442 compared with untreated alone. **Bii)** A time course of relative TEER in response to 2 µM CYM5442 compared with untreated alone. A two-way repeated measures ANOVA calculate the overall statistical significance of the column effect. N=3. Mean is presented with standard deviation. *p<0.05, **p<0.01, ***p<0.001, ****p<0.0001.

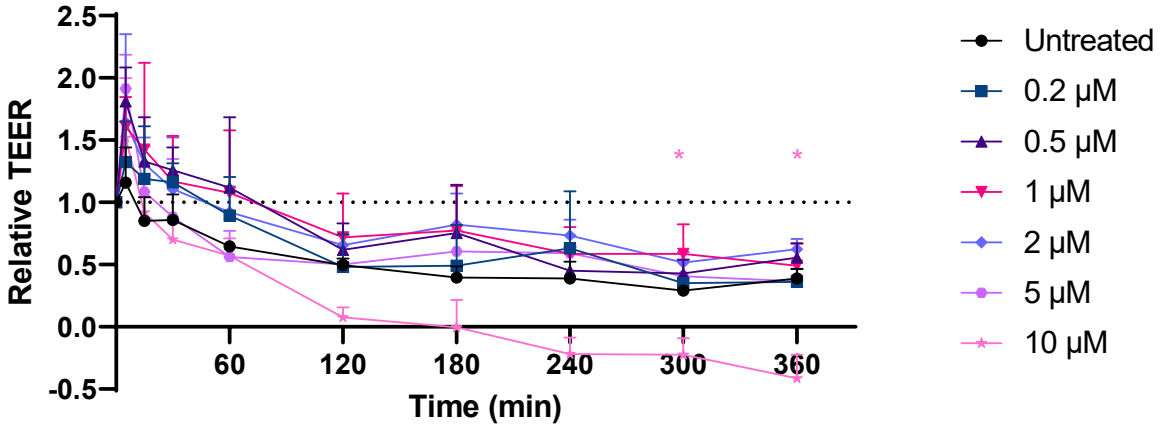

Figure 5.8. PPMEC monolayer permeability in response to increasing concentrations of FTY720P.

PPMEC were seeded onto 0.4 µm transwells and grown until a confluent monolayer was formed. Monolayers were treated with increasing concentrations of FTY720P or left untreated. Resistance was measured pre-treatment and at 5, 15, 30 minutes and 1, 2, 3, 4, 5 and 6 hours post treatment. TEER was calculated by subtracting blank transwell readings and multiplying by the transwell surface area. Then values were presented as relative to pre readings. Depicted is a time course of relative TEER in response to increasing concentrations of FTY720P. N=3. Mean is presented with standard deviation. A two-way repeated measures ANOVA with multiple comparisons was used to calculate statistical significance of each concentration versus untreated at every time point *p<0.05, **p<0.01, ***p<0.001, ****p<0.0001.

5.3.2.2. Trans-endothelial electrical resistance in response to CYM5442 during injury

Following dose optimisation of CYM5442, PPMEC were co-treated with CYM5442 and SIN-1 and resistance was measured over time to assess the effects of CYM5442 in the context of injury. Optimal SIN-1 concentration was identified in chapter 4. Compared with SIN-1 alone, co-treatment with 2 μM CYM5442 increased relative TEER, with significance at 2 and 4 hours. Co-treatment with 1 μM CYM5442 showed a significant increase at 4 hours. Although not significant at every time point, both generally had higher TEER over time than monolayers treated with SIN-1 alone and even untreated monolayers (Figure 5.9A). Figure 5.9Bi and 5.9Bii show SIN-1 co-treatment with 1 μM and 2 μM CYM5442 respectively compared with SIN-1 alone, with both concentrations showing a significant increase overall. Figure 5.9C depicts relative TEER at 30 minutes post treatment. In the absence of SIN-1, CYM5442 significantly increased TEER compared to untreated at both 1 and 2 μM, whereas only 2 μM CYM5442 significantly increased relative TEER in the presence of SIN-1.

Because measurement of monolayer resistance in response to CYM5442 and SIN-1 co-treatment seemed to reduce over time, the effects of retreating with CYM5442 at 3 hours was assessed to see if monolayer integrity could be better maintained. Figure 5.10A suggested that retreatment with CYM5442 at 3 hours potentiated its barrier enhancing effects compared to SIN-1 alone. Indeed, comparison of relative TEER at 30 min following initial treatment versus 30 min post retreatment showed that retreating with CYM5442 in the presence or absence of SIN-1 prevented the loss of CYM5442-mediated barrier enhancement over time (Figure 5.10B). In contrast, monolayers which did not undergo retreatment showed a significant loss of barrier enhancement with or without SIN-1.

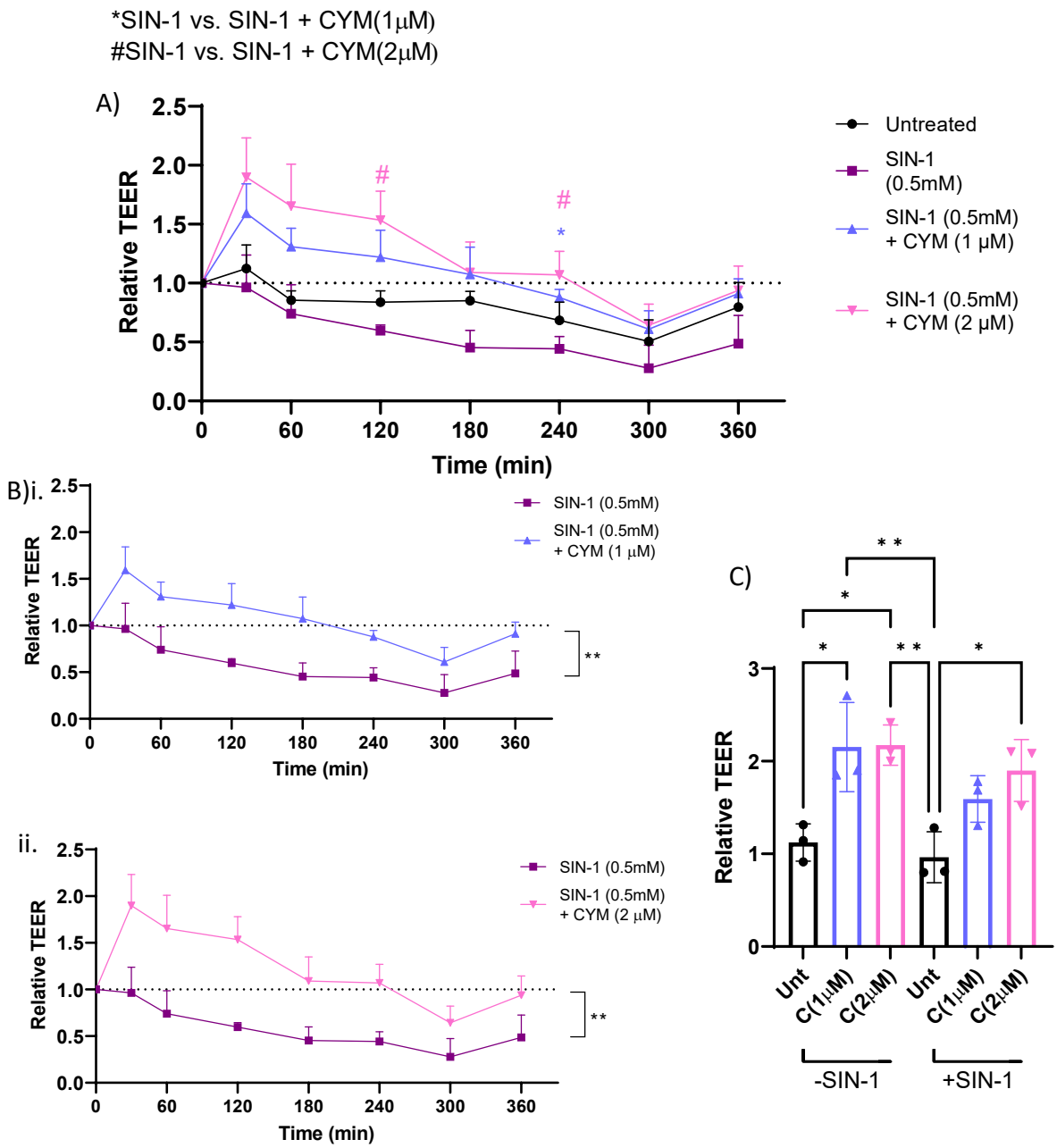

Figure 5.9. PPMEC monolayer permeability in response to CYM5442 and SIN-1 co-treatment.

PPMEC were seeded onto 0.4 µm transwells and grown until a confluent monolayer was formed. Monolayers were then treated with or without SIN-1 (0.5 mM) in combination with no treatment, CYM5442 (1 µM) or CYM5442 (2 µM). Resistance was measured pre-treatment and at 0.5, 1, 2, 3, 4, 5 and 6 hours post treatment. TEER was calculated by subtracting blank transwell readings and multiplying by the transwell surface area. Then values were presented as relative to pre readings. **A)** A time course of relative TEER in response to no treatment, SIN-1 alone or SIN-1 in combination with CYM5442. A two-way repeated measures ANOVA with multiple comparisons was used to calculate statistical significance at each time point when comparing against untreated and SIN-1 alone. **Bi)** A time course of relative TEER in response to SIN-1 + 1 µM CYM5442 compared with SIN-1 alone. **Bii)** A time course of relative TEER in response to SIN-1 + 2 µM CYM5442 compared with SIN-1 alone. A two-way repeated measures ANOVA calculate the overall statistical significance of the column effect. **C)** Comparison of TEER of all treatment groups at 30 minutes post treatment. A one-way ANOVA was used to calculate statistical significance between groups. N=3. Mean is presented with standard deviation. *p<0.05, **p<0.01, ***p<0.001, ****p<0.0001.

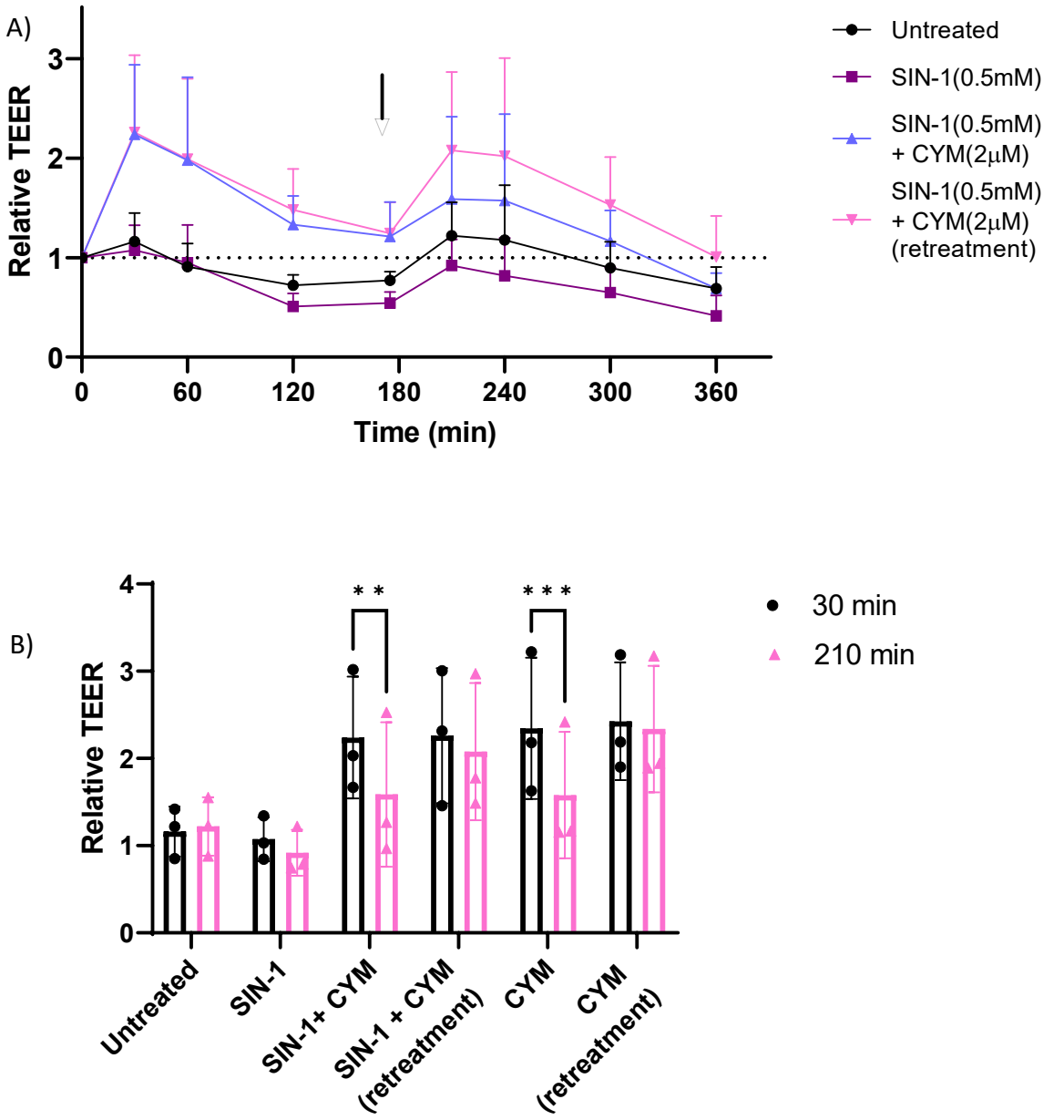

Figure 5.10. PPMEC monolayer permeability in response to CYM5442 and SIN-1 co-treatment (with CYM5442 retreatment).

PPMEC were seeded onto 0.4 µm transwells and grown until a confluent monolayer was formed. Monolayers were then treated with or without SIN-1 (0.5 mM) in combination with no treatment or CYM5442 (2 µM). Retreatment groups were retreated with CYM5442 again at 3 hours following recording of resistance at that time point. Resistance was measured pre-treatment and at 0.5, 1, 2, 3, 4, 5 and 6 hours post treatment. TEER was calculated by subtracting blank transwell readings and multiplying by the transwell surface area. Then values were presented as relative to pre readings. **A)** A time course of relative TEER in response to no treatment, SIN-1 alone or SIN-1 in combination with CYM5442 with or without retreatment. The arrow depicts retreatment. A two-way repeated measures ANOVA with multiple comparisons was used to calculate statistical significance at each time point when comparing against untreated and SIN-1 alone. **B)** Comparison of TEER of all treatment groups at 30 minutes post treatment and 30 minutes post retreatment. A two-way ANOVA with repeated measures was used to compare between 30 minutes and 210 minutes for each treatment. N=3. Mean is presented with standard deviation. *p<0.05, **p<0.01, ***p<0.001, ****p<0.0001.

5.3.2.3. FITC-dextran permeability assay in response to injury following CYM5442 pre-treatment

As well as measuring monolayer resistance, monolayer permeability to FITC-dextran was also assessed in response to SIN-1 following CYM5442 pre-treatment. The amount of FITC dextran which had travelled through the endothelial monolayer was assessed at sequential time points (Figure 5.11A). At 60 minutes post SIN-1/FITC-dextran addition, there was a trend towards a concentration dependent reduction in monolayer permeability in response to CYM5442 pre-treatment compared to untreated in the presence and absence of SIN-1 (Figure 5.11B). Overall, monolayers treated with SIN-1 also seemed to have a slightly higher permeability. Data was not significant due to variability between biological repeats. Empty transwells were used as a positive control and showed higher permeability to FITC-dextran than transwells containing cell monolayers.

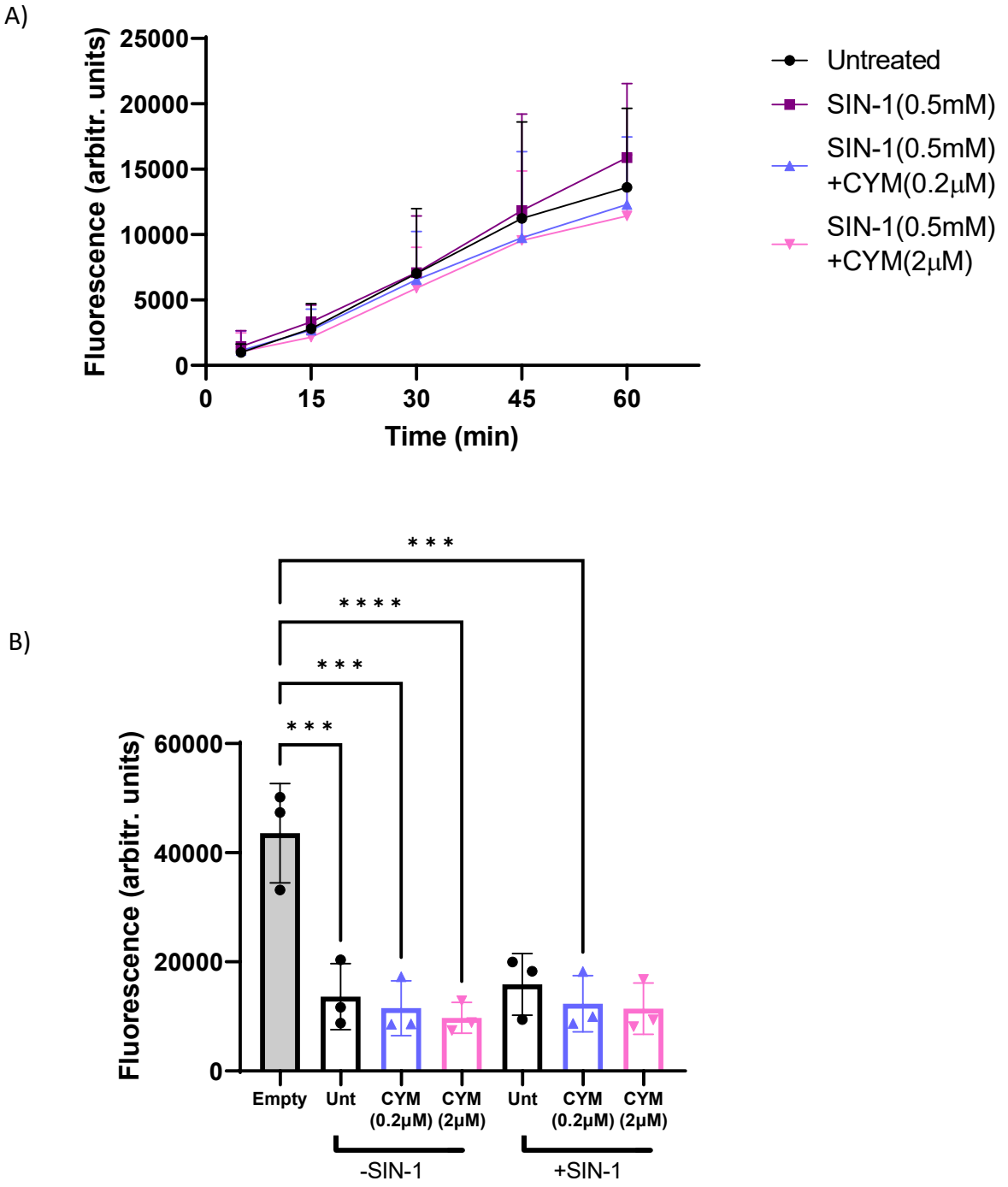

Figure 5.11. PPMEC monolayer permeability to FITC-dextran in response to SIN-1 following CYM5442 pre-treatment.

PPMEC were seeded onto 0.4 µm transwells and grown until a confluent monolayer was formed. Monolayers were then pretreated with or without CYM5442 (0.2 µM or 2 µM), before treating with or without SIN-1 (0.5 mM) in the presence of FITC-dextran. Samples were taken from below the transwell and fluorescence was quantified at 5, 15, 30, 45 and 60 minutes. **A)** A time course of fluorescence in response to no treatment, SIN-1 alone or SIN-1 following pre-treatment with in CYM5442. A two-way repeated measures ANOVA with multiple comparisons was used to calculate statistical significance at every time point. **B)** Comparison of fluorescence of all treatment groups at 60 minutes post treatment. A one-way ANOVA was used to calculate statistical significance between groups. N=3. Mean is presented with standard deviation. *p<0.05, **p<0.01, ***p<0.001, ****p<0.0001.

Thus far, TEER in response to agonists had only been tested in a serum free system; to more accurately replicate treatment during EVLP, the effects of CYM5442 on monolayer resistance were tested in perfusate solution, Steen. Firstly, PPMEC viability in Steen solution was examined, showing no significant difference (Figure 5.12A). Then changes to PPMEC monolayer resistance was examined. All concentrations showed a significant increase in relative TEER at 15 mins post-treatment (Figure 5.12B). 0.1 and 0.2 μM seemed to facilitate and maintain the greatest increases in TEER compared with untreated, with significance at 60, 120 and 300 mins post treatment for 0.1 μM and significance at 120, 240 and 300 mins for 0.2 μM.

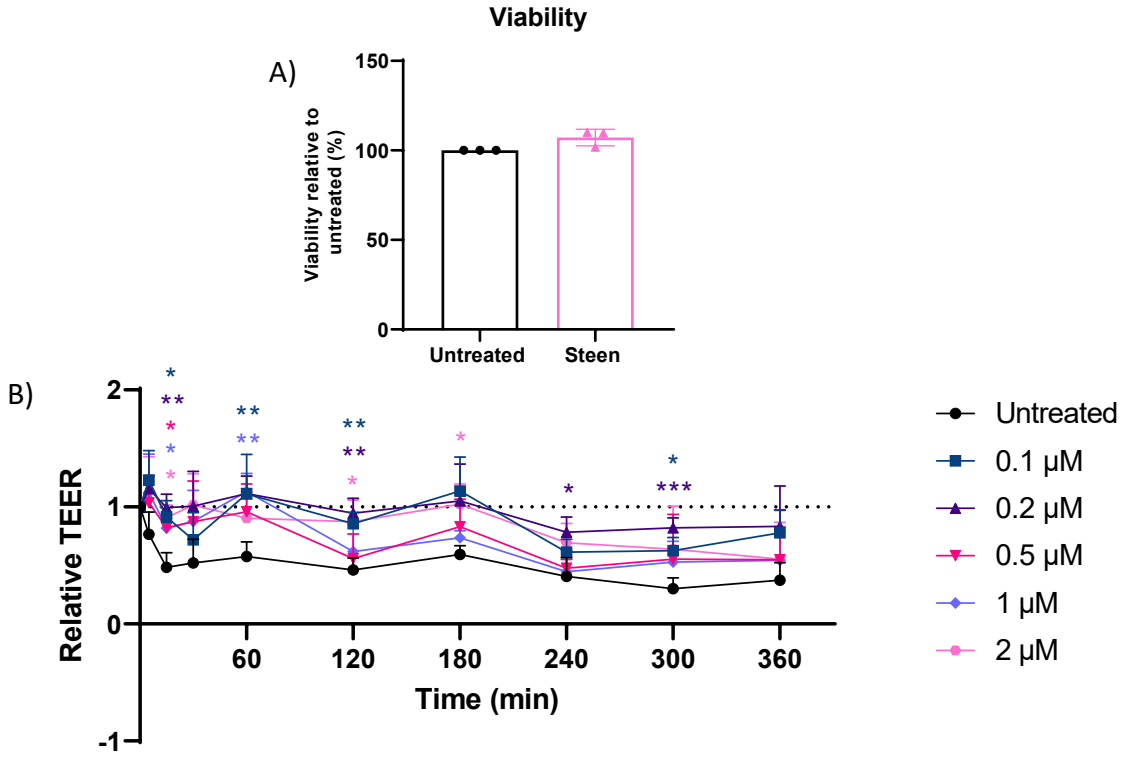

Figure 5.12. PPMEC monolayer permeability in response to increasing concentrations of CYM5442 in Steen solution.

A) PPMEC were incubated with complete media (untreated) or Steen solution for 6 hours and viability was assessed using an XTT assay. An unpaired t-test was used to determine statistical significance. **B)** A time course of relative TEER in response to increasing concentrations of CYM5442 in Steen solution. PPMEC were seeded onto 0.4 μm transwells and grown until a confluent monolayer was formed. Monolayers were treated with increasing concentrations of CYM5442 or left untreated in perfusate Steen solution. Resistance was measured pre-treatment and at 5, 15, 30 minutes and 1, 2, 3, 4, 5 and 6 hours post treatment. TEER was calculated by subtracting blank transwell readings and multiplying by the transwell surface area. Then values were presented as relative to pre readings. A two-way repeated measures ANOVA with multiple comparisons was used to calculate statistical significance of each concentration versus untreated at every time point. N=3. Mean is presented with standard deviation. *p<0.05, **p<0.01, ***p<0.001, ****p<0.0001.

5.3.3. Porcine EVLP

Prior to EVLP, we sought to optimise a porcine DCD lung model and Table 5.2 describes the inflation states and warm and cold ischaemic times used for each set of pig lungs during retrieval. For PIG001, the lung was not inflated during the WIT, whilst PIG002 and PIG003 lungs were inflated in order to reduce injury. WIT was shortened for PIG002 and 3 and the CIT was made considerable shorter for PIG003. However, despite lung inflation and reducing ischaemic times, lungs displayed instant and overwhelming fluid accumulation in the bronchus shortly after connection to the EVLP circuit, indicating complete loss of endothelial integrity.

Pig ID	Pig weight (kg)	Inflation during WIT (Y/N)	WIT (mins)	CIT (hours)
PIG001	65.5	N	25	19
PIG002	76.5	Y	15	20
PIG003	75	Y	15	8

Table 5.2. Porcine lung retrieval information.

Pathology was explored using samples taken pre-perfusion to assess lung quality and determine why perfusions were unsuccessful. Histology of lungs should show open air spaces with thin, single cell thick alveolar walls. However, Figure 5.13 showed interstitial thickening, consolidation and trapped red cells evident in all three lung pairs, despite reducing WIT, CIT and inflating.

To assess endothelial integrity of porcine lungs, immunofluorescence staining of VE-cadherin was carried out on tissue sections from biopsies pre-EVLP. Vessel VE-cadherin staining was then visualised. For PIG001, VE-cadherin staining was faint, with brightness increasing as optimisation progressed to PIG002 and PIG003, with PIG003 displaying the brightest staining. Particularly for PIG002, VE-cadherin staining of the vessel lumen appears disrupted and non-continuous. The no-primary showed no staining for VE-cadherin (Figure 5.14). Despite VE-cadherin staining appearing to increase in intensity with optimisation, lungs were ultimately still too damaged to perfuse.

As desired perfusion times were not possible, porcine EVLP was abandoned in favour of a human model.

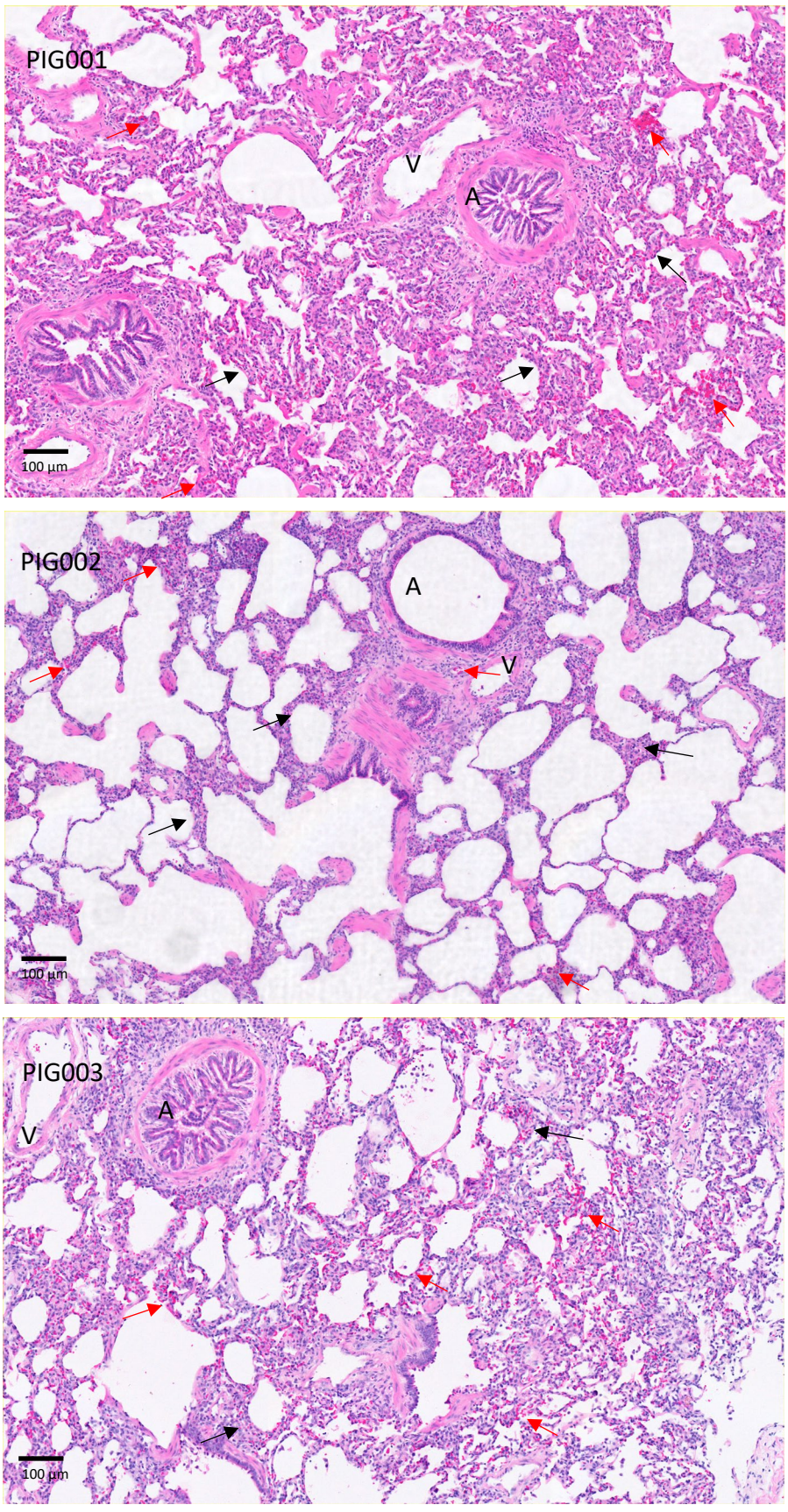

Figure 5.13. H&E staining of lung histology for optimization of porcine lung retrieval.

Tissue biopsies were collected pre-perfusion, sectioned and stained with haematoxylin and eosin. A representative image is shown for each pair of lungs. Red arrows depict trapped red blood cells. Black arrows depict examples of alveolar thickening and consolidation. A=Airway, V=Vessel. Scale: 100 µm

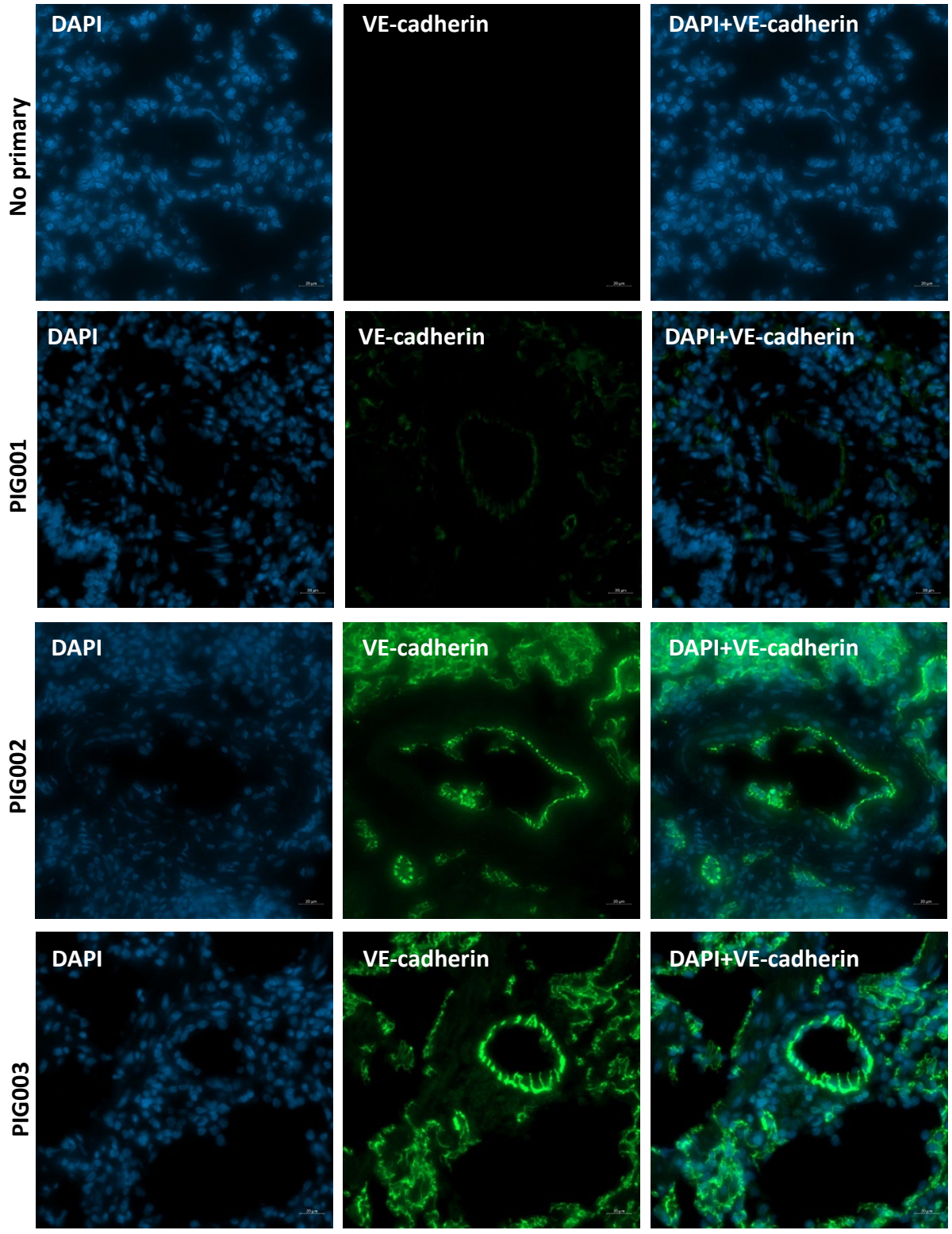

Figure 5.14. VE-cadherin vessel staining for optimisation of porcine lung retrieval.

Tissue biopsies were collected pre-perfusion, sectioned and stained for VE-cadherin. Each image shows vessel staining of VE-cadherin. A representative image is shown for each pair of lungs. Images are at 40x magnification. Scale: 20 μm.

5.3.4. *In vitro* testing of S1PR agonists in human endothelial cells

5.3.4.1. Trans-endothelial electrical resistance in response to CYM5442 and FTY720P at baseline

Prior to application to human EVLP, CYM5442 and FTY720P were tested *in vitro* in HPMEC. Confluent monolayers of HPMEC were treated with increasing concentrations of CYM5442 or FTY720P and monolayer resistance was measured at sequential time points. At 5 mins post-treatment, only 0.2 μM treated monolayers showed an increase in relative TEER which was almost significant, although appeared to maintain a higher TEER than untreated across all time points. Although not significant, monolayers treated with 0.05, 0.1 and 0.5 μM also seemed to exhibit a higher TEER than untreated monolayers at time points up to 3 hours. 10 μM seemed to reduce resistance compared to untreated from 15 minutes onwards (Figure 5.15A). When comparing TEER overall between 0.2 μM and untreated alone, 0.2 μM treated monolayers showed a trend towards higher TEER values, with the difference almost being significant (Figure 5.15B).

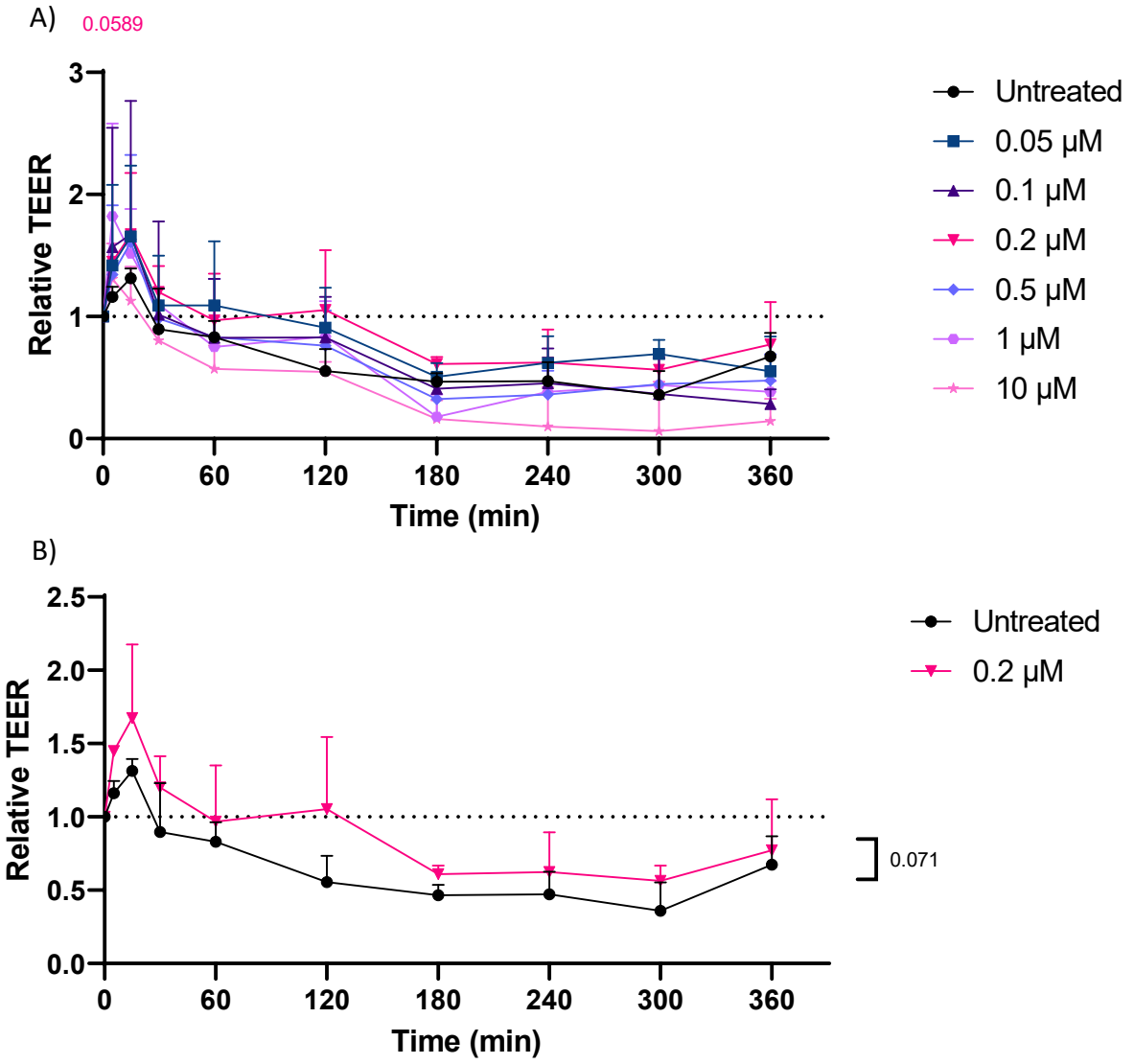

Figure 5.15. HPMEC monolayer permeability in response to increasing concentrations of CYM5442.

HPMEC were seeded onto 0.4 µm transwells and grown until a confluent monolayer was formed. Monolayers were treated with increasing concentrations of CYM5442 or left untreated. Resistance was measured pre-treatment and at 5, 15, 30 minutes and 1, 2, 3, 4, 5 and 6 hours post treatment. TEER was calculated by subtracting blank transwell readings and multiplying by the transwell surface area. Then values were presented as relative to pre readings. **A)** A time course of relative TEER in response to increasing concentrations of CYM5442. A two-way repeated measures ANOVA with multiple comparisons was used to calculate statistical significance of each concentration versus untreated at every time point. **B)** A time course of relative TEER in response to 0.2 µM CYM5442 compared with untreated alone. A two-way repeated measures ANOVA calculate the overall statistical significance of the column effect. N=3. Mean is presented with standard deviation. *p<0.05, **p<0.01, ***p<0.001, ****p<0.0001.

HPMEC monolayers were also treated with increasing concentrations of FTY720P, with a concentration of 0.05 µM significantly increasing TEER at 5 mins post-treatment compared with untreated. In contrast, 1 µM seemed to cause barrier disruption and significantly reduced TEER at 4 hours compared to untreated (Figure 5.16A). Comparison of 0.2 µM and untreated alone using a two-way ANOVA showed that treatment resulted in no significant change in monolayer TEER overall (Figure 5.16B). Therefore, only CYM5442 was carried forward for further testing.

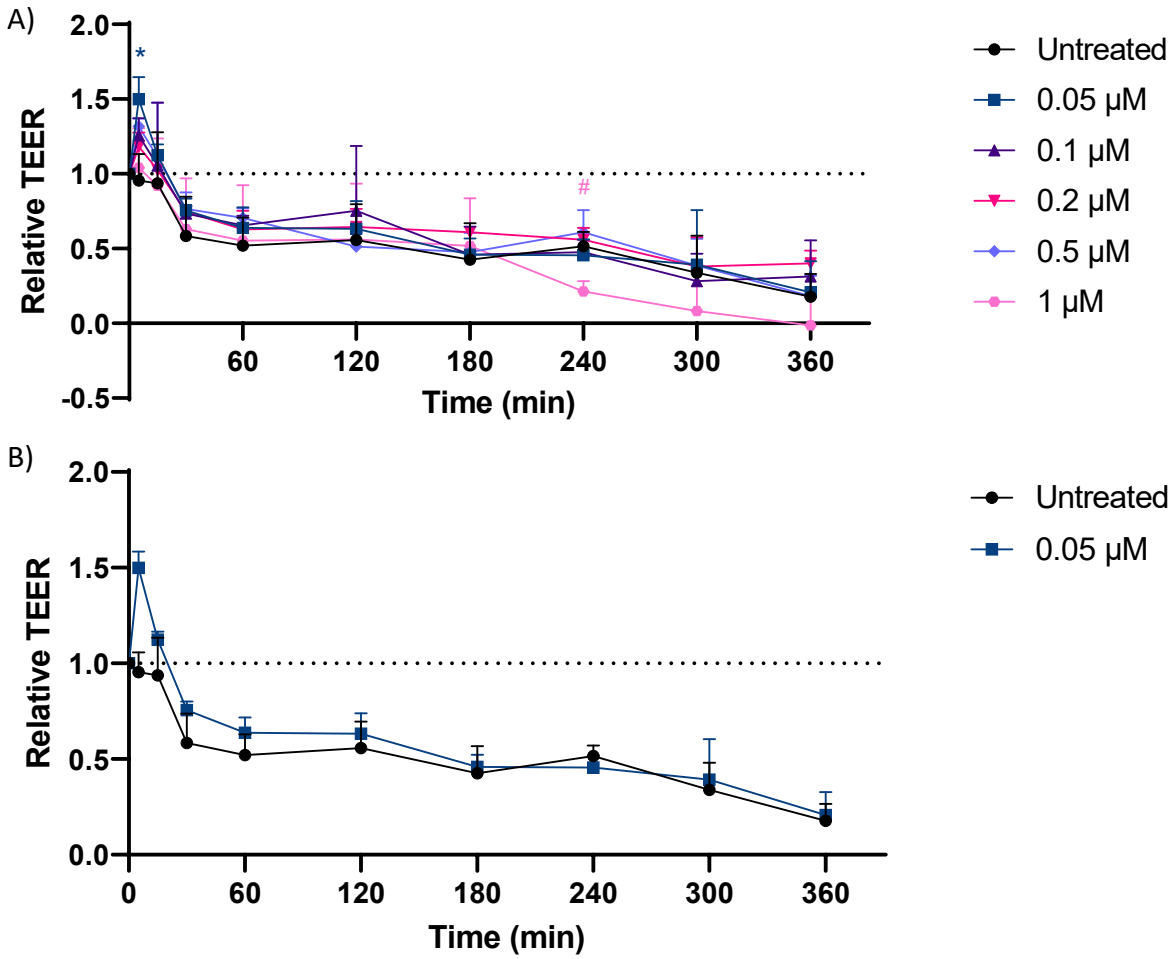

Figure 5.16. HPMEC monolayer permeability in response to increasing concentrations of FTY720P.

HPMEC were seeded onto 0.4 µm transwells and grown until a confluent monolayer was formed. Monolayers were treated with increasing concentrations of FTY720P or left untreated. Resistance was measured pre-treatment and at 5, 15, 30 minutes and 1, 2, 3, 4, 5 and 6 hours post treatment. TEER was calculated by subtracting blank transwell readings and multiplying by the transwell surface area. Then values were presented as relative to pre readings. **A)** A time course of relative TEER in response to increasing concentrations of FTY720P. A two-way repeated measures ANOVA with multiple comparisons was used to calculate statistical significance of each concentration versus untreated at every time point. **B)** A time course of relative TEER in response to 0.05 µM CYM5442 compared with untreated alone. A two-way repeated measures ANOVA calculate the overall statistical significance of the column effect. N=3. Mean is presented with standard deviation. *p<0.05, **p<0.01, ***p<0.001, ****p<0.0001.

5.3.4.2. Trans-endothelial electrical resistance in response to CYM5442 during injury

In order to test optimised doses of CYM5442 in the context of injury, HPMEC monolayers were co-treated with a previously optimised concentration of SIN-1 and CYM5442. Compared to SIN-1 alone, co-treatment with 0.2 μM CYM5442 seemed to increase relative TEER across all time points, nearly reaching significance at 30 minutes. In fact, co-treating with 0.2 μM CYM5442 in the presence of SIN-1 increased TEER to levels which seemed to even exceed untreated monolayers up until 3 hours, albeit non-significantly (Figure 5.17A). Figure 5.17Bi and 5.17Bii show SIN-1 co-treatment with 0.05 μM and 0.2 μM CYM5442 respectively compared with SIN-1 alone, with 0.2 μM CYM5442 co-treatment showing a significant increase overall. Figure 5.17C depicts relative TEER specifically at 30 minutes post-treatment. Although not significant, CYM5442 generally increased relative TEER dose dependently compared to untreated, both in the presence and absence of SIN-1.

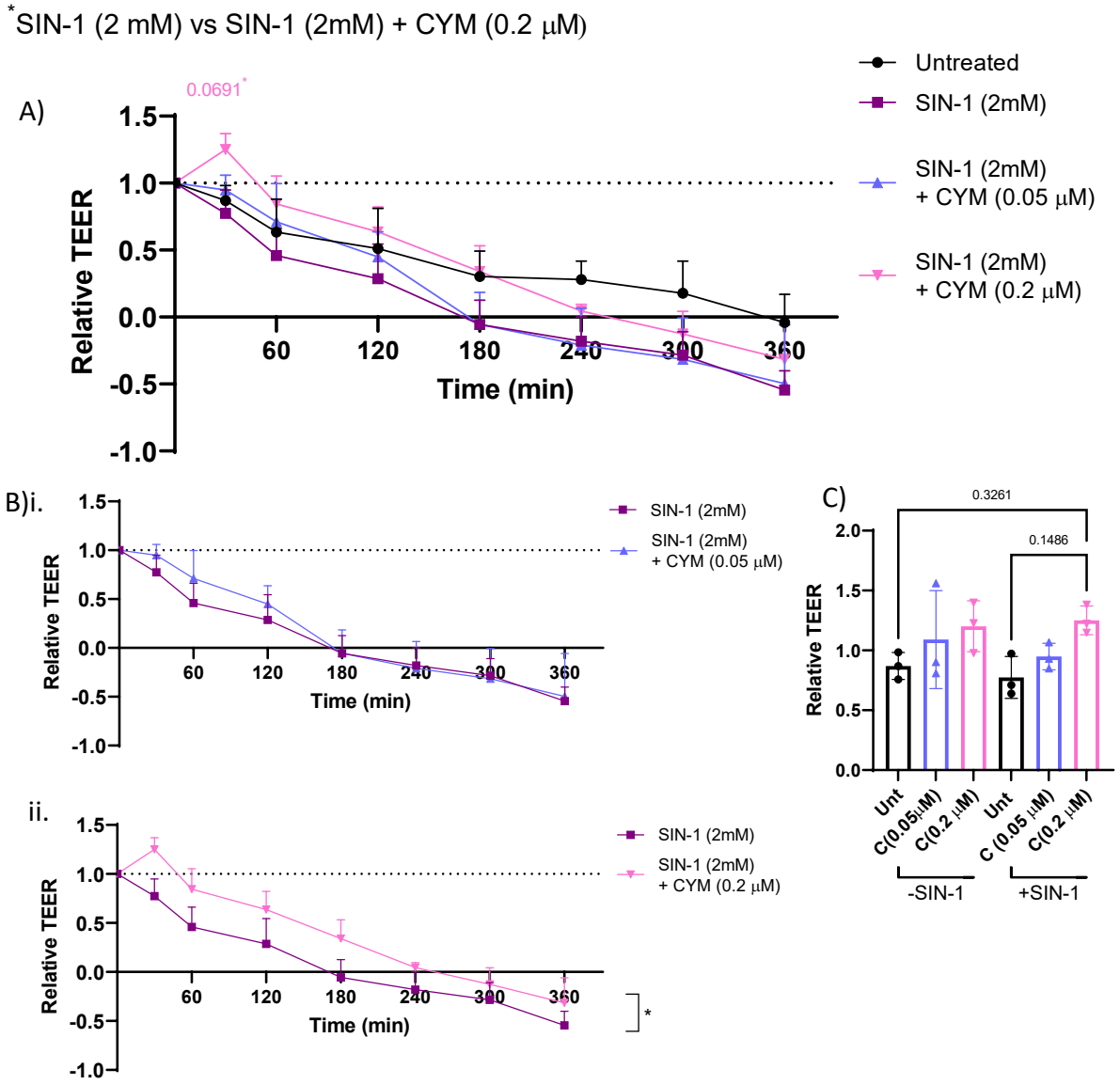

Figure 5.17. HPMEC monolayer permeability in response to CYM5442 and SIN-1 co-treatment.

HPMEC were seeded onto 0.4 µm transwells and grown until a confluent monolayer was formed. Monolayers were then treated with or without SIN-1 (2 mM) in combination with no treatment, CYM5442 (0.05 µM) or CYM5442 (0.2 µM). Resistance was measured pre-treatment and at 0.5, 1, 2, 3, 4, 5 and 6 hours post treatment. TEER was calculated by subtracting blank transwell readings and multiplying by the transwell surface area. Then values were presented as relative to pre readings. **A)** A time course of relative TEER in response to no treatment, SIN-1 alone or SIN-1 in combination with CYM5442. A two-way repeated measures ANOVA with multiple comparisons was used to calculate statistical significance at each time point when comparing against untreated and SIN-1 alone. **Bi)** A time course of relative TEER in response to SIN-1 + 0.05 µM CYM5442 compared with SIN-1 alone. **Bii)** A time course of relative TEER in response to SIN-1 + 0.2 µM CYM5442 compared with SIN-1 alone. A two-way repeated measures ANOVA calculate the overall statistical significance of the column effect. **C)** Comparison of TEER of all treatment groups at 30 minutes post treatment. A one-way ANOVA was used to calculate statistical significance between groups. N=3. Mean is presented with standard deviation. *p<0.05, **p<0.01, ***p<0.001, ****p<0.0001.

As the optimised perfusate solution for our human EVLP protocol, changes to monolayer resistance in response to CYM5442 were tested in modified DMEM. Firstly, HPMEC viability was assessed, with cells showing a small decrease in viability in response to a 6 hr incubation in DMEM compared with complete media (Figure 5.18A). Whilst testing of increasing concentrations of CYM5442 in serum free media identified 0.2 μM as the optimal therapeutic concentration, 0.05 μM CYM5442 caused the greatest increases in TEER in DMEM (Figure 5.18B). In fact, 0.05 μM CYM5442 significantly increased TEER compared with untreated at 5, 120 and 180 mins and appeared generally higher than untreated at all time points up to 240 mins. In contrast, the highest concentration of 1 μM CYM5442 significantly reduced monolayer resistance at 360 mins compared to untreated. 0.025 μM also caused a significant reduction, but this appeared very minor.

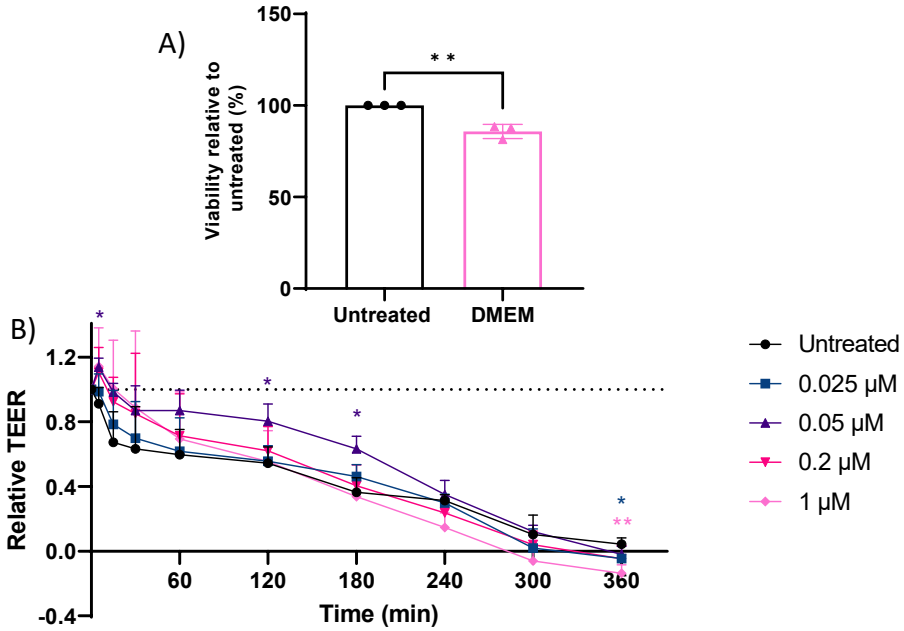

Figure 5.18. HPMEC monolayer permeability in response to increasing concentrations of CYM5442 in DMEM perfusate solution.

A) HPMEC were incubated with complete media (untreated) or DMEM for 6 hours and viability was assessed using an XTT assay. An unpaired t-test was used to determine statistical significance. **B)** A time course of relative TEER in response to increasing concentrations of CYM5442 in DMEM perfusate solution. PPMEC were seeded onto 0.4 μm transwells and grown until a confluent monolayer was formed. Monolayers were treated with increasing concentrations of CYM5442 or left untreated in perfusate Steen solution. Resistance was measured pre-treatment and at 5, 15, 30 minutes and 1, 2, 3, 4, 5 and 6 hours post treatment. TEER was calculated by subtracting blank transwell readings and multiplying by the transwell surface area. Then values were presented as relative to pre readings. A two-way repeated measures ANOVA with multiple comparisons was used to calculate statistical significance of each concentration versus untreated at every time point. N=3. Mean is presented with standard deviation. *p<0.05, **p<0.01, ***p<0.001, ****p<0.0001.

5.3.4.4. *ICAM1* expression in response to CYM5442

To assess the effect of CYM5442 on endothelial activation, *ICAM1* gene expression was assessed in response to no treatment, SIN-1, SIN-1 and CYM5442 co-treatment and CYM5442 alone in Figure 5.19. Positive control IL-1β caused significant upregulation of *ICAM1* gene expression compared to all other treatment groups. There was no significant change in gene expression in any of the treatment groups compared to untreated, although SIN-1 and CYM5442 co-treatment showed a trend towards lower gene expression that SIN-1 alone treated groups. CYM5442 alone also seemed to cause a minor increase in *ICAM1* gene expression compared with untreated.

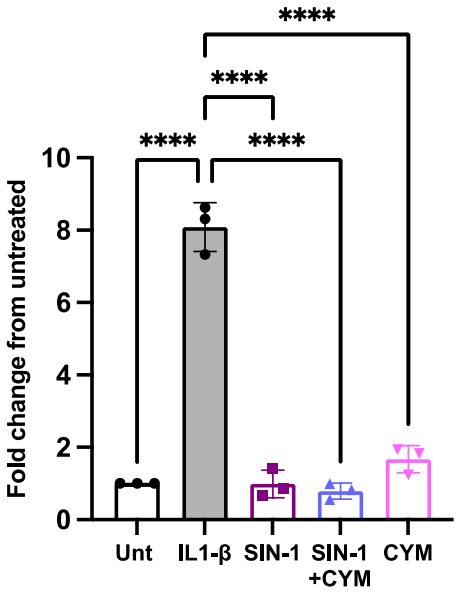

Figure 5.19. HPMEC gene expression of *ICAM1* in response to CYM5442 during injury.

RT-qPCR was used to quantify gene expression in response to 2 mM SIN-1 alone, 2 mM SIN-1 in combination with 0.2 µM CYM5442, 0.2 µM CYM5442 alone or 0.5 ng/mL IL-1β as a positive control. N=3. Gene expression is depicted as relative to untreated. Mean is presented with standard deviation. Statistical significance was determined using a one-way ANOVA. *p<0.05, **p<0.01, ***p<0.001, ****p<0.0001.

5.3.5. Assessment of CYM5442 during human EVLP

5.3.5.1. Donor and perfusion information

Lungs used for this study were declined for clinical lung transplantation on the basis of poor function, past medical history or lack of suitable recipients. 5 pairs of donor lungs were accepted as part of the study; donor age ranged from 21-46 years and all lungs were unintentionally obtained from male donors. 4 lungs were retrieved following DBD and one from DCD. All donors had a smoking history. Donor 1, 3 and 5 had clear chest x-rays, but donor 3 lungs had slight left lung consolidation upon inspection. Donor 2 and 4 had consolidation reported on a chest X-ray, but donor 4 lung consolidation was not visible upon inspection. Donor information is shown in Table 5.3.

Lungs from donor 2 and donor 5 were unable to be perfused due to extensive oedema formation upon attachment to the circuit in both lungs for donor 2 and the right lung in donor 5. This was believed to be due to a history of asthma and technical problems during retrieval respectively.

In vitro data suggested that 0.2 μM CYM5442 was the optimal dose in rescuing HPMEC from SIN-1-mediated barrier disruption, with protective effects lost over time. Therefore, donor 1 lung was split and treated with vehicle or 0.2 μM CYM5442 with a retreatment at 2 hours EVLP. Perfusion was terminated at 4 hours when it was clear that the treated lung was significantly worse than untreated. Following analysis of results, dosing was changed to a single dose of 0.05 μM CYM5442, which was shown to be the optimal dose when testing TEER in DMEM. Thus, donor 3 and 4 lungs were split and treated with either 0.05 μM CYM5442 or vehicle and successfully perfused for 6 hours. Despite randomisation, treatment groups were always the right lung. EVLP information is described in Table 5.4.

Donor	Age (yrs)	Sex (M/F)	Bodyweight (kg)	Height (cm)	Donation type	Smoker (Y/N)	Reason for decline	Consolidation, infection or secretions	Cause of death	Relevant medical history
1	32	M	88	179	DBD	Y	No suitable recipient	Chest x-ray clear, Infection (treated), minimal non-purulent secretions	Hypoxic brain damage	Asthma
2	34	M	90	177	DBD	Y	Function and past medical history	Chest x ray - left lower lobe consolidation, infection (treated), thick and clear non-purulent secretions	Hypoxic brain damage	Asthma
3	21	M	60	179	DBD	Y	No suitable recipient	Chest x-ray clear except minor lung contusions on right upper lobe, infection unknown, dirty and purulent secretions	Hypoxic brain damage	No
4	35	M	110	183	DBD	Y	Function	Chest x-ray – left lung consolidation, but not visible upon inspection, infection unknown, no secretions	Intracranial haemorrhage	No
5	46	M	90	186	DCD	Y	Past medical history	Chest x-ray clear, No consolidation, infection (treated), minimal non-purulent secretions	Intracranial haemorrhage	Alpha-1 antitrypsin deficiency

Table 5.3. Donor information for human lungs used in this study.

Donor		Vehicle or CYM5442	WIT (min)	CIT (min)	EVLP duration (hours)	Lung weight pre (g)	Lung weight post (g)
1	Right	CYM5442 (0.2 μM + retreatment))	-	787	4	561	979.5
	Left	Vehicle	-	793	4	452.5	698
2	Right	N/A	-	725	N/A	380	N/A
	Left	N/A	-	713	N/A	409	N/A
3	Right	CYM5442 (single dose 0.05 μM)	-	627	6	478	1007.5
	Left	Vehicle	-	640	6	640	1216
4	Right	CYM5442 (single dose 0.05 μM)	-	667	6	562	1262.5
	Left	Vehicle	-	682	6	470.5	1299.5
5	Right	N/A	22	933	N/A	542	N/A
	Left	N/A	22	923	N/A	540.5	N/A

Table 5.4. Perfusion information for human lungs used in this study.

5.3.5.2. Dose optimisation - administration of 0.2 μM CYM5442 with retreatment during EVLP

As the first donor lung, lungs from donor 1 were used for optimisation and were treated with a high dose of CYM5442 (0.2 μM) with retreatment for assessment of efficacy and safety.

5.3.5.2.1. Physiological parameters

As controlled parameters, flow rate and left atrial pressure (LAP) were relatively constant throughout EVLP. LAP was generally kept between 1-5 throughout EVLP except at 40 min for the untreated and 210 min for the CYM5442 treated lung (Figure 5.20A).

Figure 5.20B. showed physiological parameters that were recorded during EVLP. Pulmonary artery pressure (PAP) and compliance did not differ between groups. Generally, despite a sharp decline in compliance between 0 min and 20 min, compliance of the untreated lung

seemed to be on its way up during EVLP, with the drug lung showing the opposite. PVR seemed to reduce over time for both groups, but there seemed to be no difference between treated and untreated when taking into account the starting point for each lung. Peak airway pressure seemed to slightly reduce over time of perfusion for both groups, with no difference between the two. At the end of perfusion, peak airway pressure of the CYM5442 treated lung seemed to be starting to increase, whilst untreated seemed to be starting to decrease.

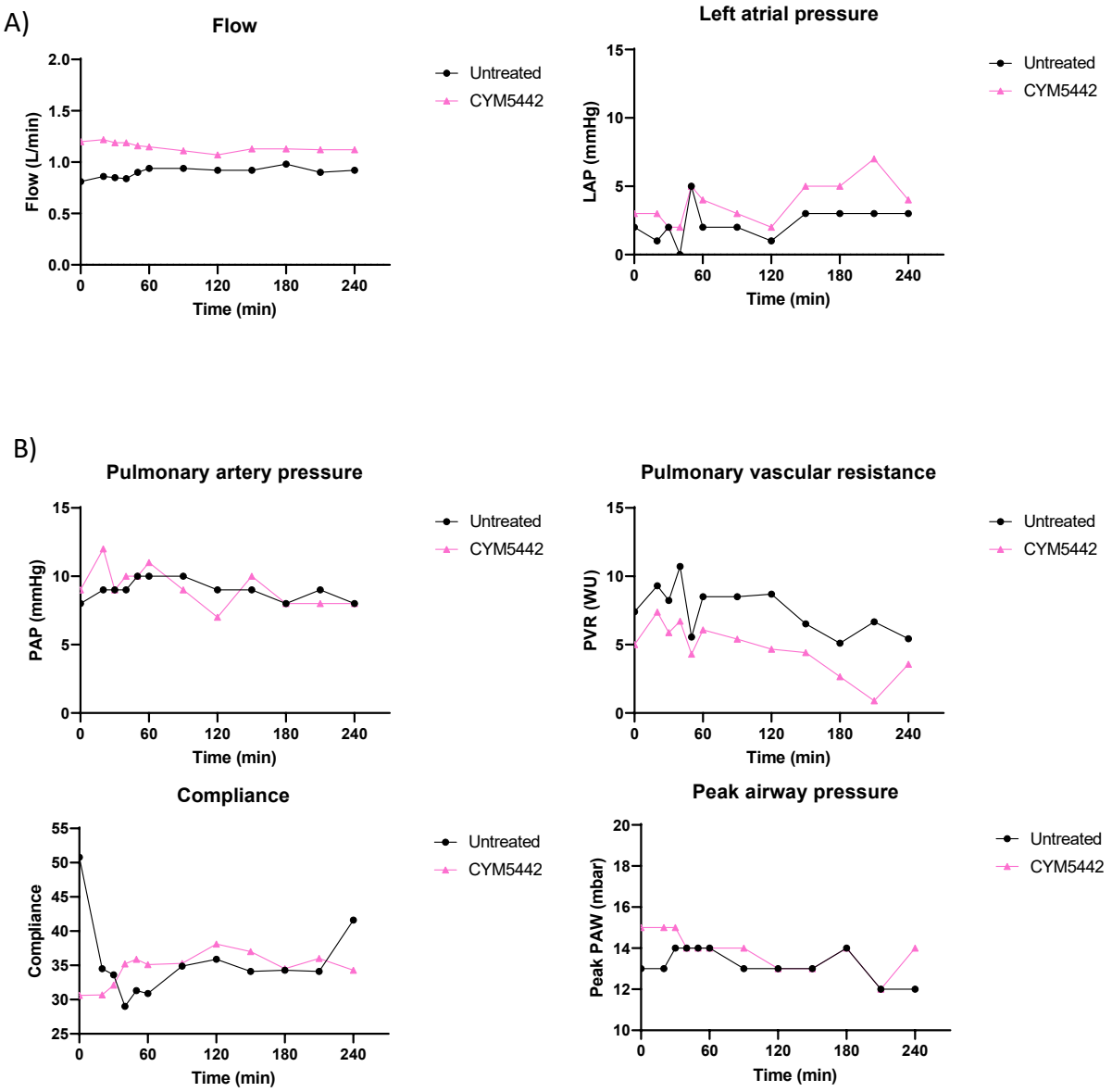

Figure 5.20. Physiological parameters recorded during EVLP of lungs treated with 0.2 µM CYM5442 with retreatment or vehicle.

Parameters were recorded at 0, 20, 30, 40, 50, 60, 120, 180 and 240 minutes following stable ventilation and first drug/vehicle administration. **A)** Controlled parameters flow and left atrial pressure (LAP) during perfusion. **B)** Pulmonary artery pressure (PAP), pulmonary vascular resistance (PVR), compliance and peak airway pressure during perfusion. N=1.

Figure 5.21A showed that despite controlling for pH with addition of THAM, the CYM5442-treated lung in particular showed an uncontrolled decline in pH compared to untreated, suggesting increased acidosis. The partial pressure of carbon dioxide (PCO_2) was kept relatively stable for both lungs within the intended limit of 1-5 kPa (Figure 5.21B). There was no difference between the partial pressure of oxygen (PO_2) between groups (Figure 5.21C).

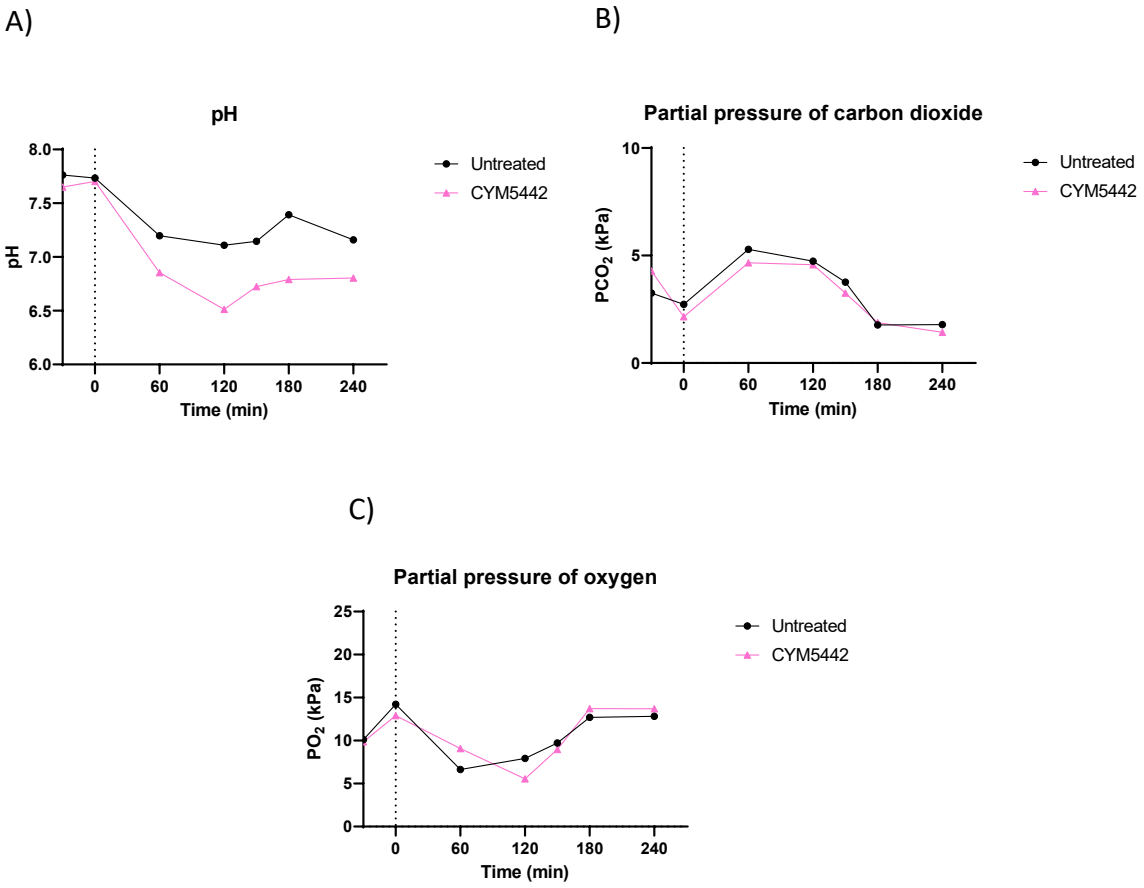

Figure 5.21. Blood gases recorded during EVLP of lungs treated with 0.2 µM CYM5442 with retreatment or vehicle.

Blood gases were recorded pre lung attachment and at 0, 60, 120, 180 and 240 minutes following stable ventilation and first drug/vehicle administration. Controlled parameters **A)** pH, **B)** partial pressure of carbon dioxide (PCO_2) and **C)** partial pressure of oxygen (PO_2) during perfusion. N=1.

5.3.5.2.3. Oedema formation and permeability to Evan's Blue

To assess the effects of CYM5442 on endothelial permeability and subsequent oedema formation, weight gain and permeability to EB was assessed during perfusion.

Literature has suggested that at higher doses, CYM5442 can cause functional antagonism of S1PR1 (Kim *et al*., 2018), which would ultimately lead to barrier disruption. Indeed, both absolute and percentage weight gain were greater for the lung treated/retreated with 0.2 μM CYM5442 indicating increased oedema formation (Figure 5.22A and B respectively). Treated lungs also had a higher concentration of EB in BAL (Figure 5.23A), as well as a trend towards increased absorbance and fluorescence intensity in tissue (Figure 5.23B). This indicated increased endothelial permeability to EB in response to our administered dose of 0.2 μM CYM5442 with retreatment.

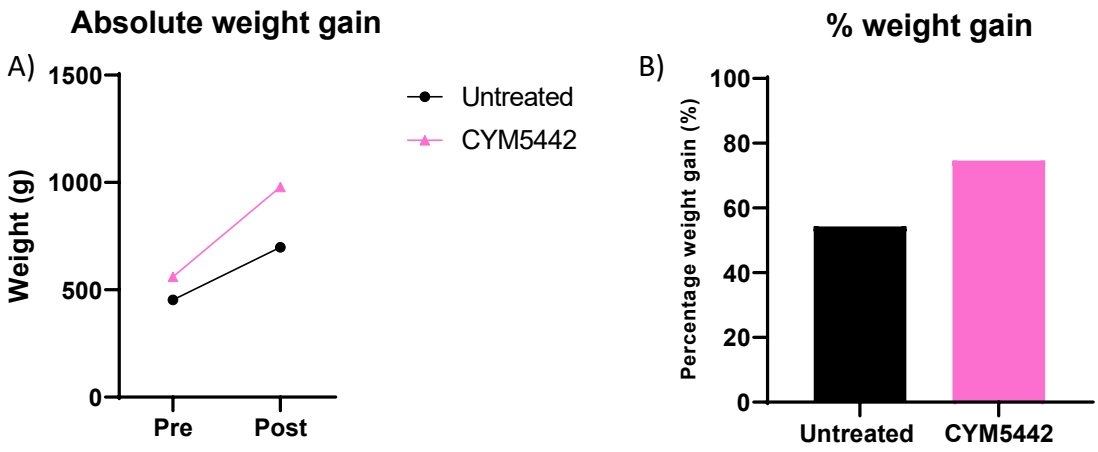

Figure 5.22. Weight gain following EVLP of lungs treated with 0.2 μM CYM5442 with retreatment or vehicle.

Lung weight was measured for each lung pre and post perfusion. **A)** Absolute weight pre and after 240 min perfusion. **B)** Percentage weight gain after 240 min perfusion. N=1.

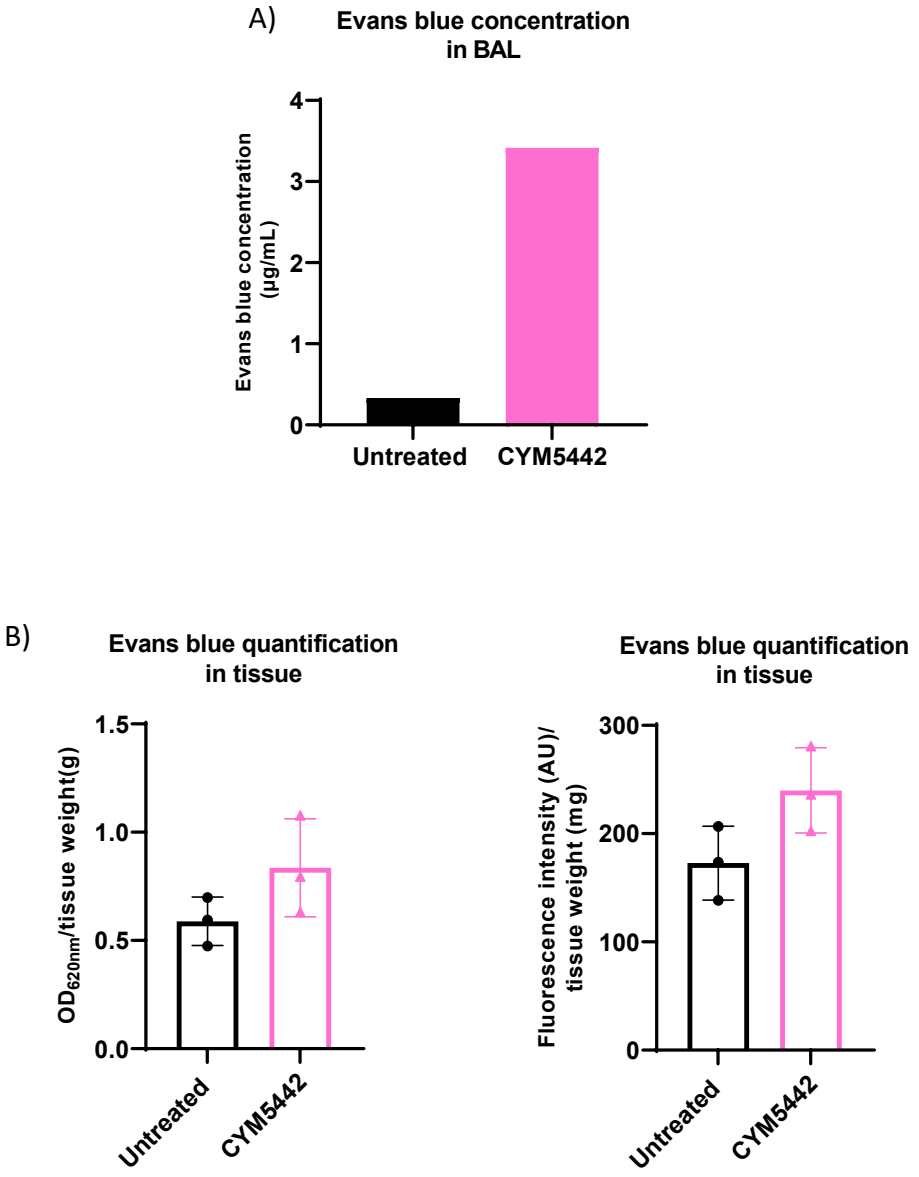

Figure 5.23. Evan's blue quantification in BAL and tissue of lungs treated with 0.2 µM CYM5442 with retreatment or vehicle during EVLP.

Evan's blue (EB) dye was administered to each circuit at 2 hours following first drug/vehicle administration and stable ventilation. Then bronchoalveolar lavage (BAL) was performed and triplicate tissue samples collected from the lower lobe at 4 hours perfusion. EB was then quantified in samples. **A)** EB concentration in BAL. **B)** EB quantification in tissue using both absorbance and fluorescence. Depicted are triplicate samples of the lower lobe and not biological replicates. Mean is presented with standard deviation. N=1.

5.3.5.3. Administration of 0.05 μM CYM5442 during EVLP

Data from the first optimisation experiment suggested that our treatment was too high and achieved functional antagonism of S1PR1. Thus, for further experiments, a lower dose of 0.05 μM was used without retreatment and carried forward as the optimal working dose.

5.3.5.3.1. Physiological Parameters

Functional parameters were relatively unchanged between untreated and CYM5442 treated lungs. Flow and left atrial pressure were stable throughout perfusion as controlled variables (Figure 5.24A). Figure 5.24B showed that there was no difference between PAP or PVR between groups and both seemed to be relatively stable throughout perfusion. Although compliance started at a similar level for both groups, it seemed to be slightly higher for CYM5442-treated lungs throughout, although this was not significant. Regardless of treatment, compliance for both groups seemed to improve over time up until around 3 hours, after which there was a decline in compliance, which seemed more profound in the untreated group. Peak airway pressure was relatively similar between groups until around 4 hours EVLP, where there was a sharper increase over time for the untreated group compared to CYM5442-treated lungs. In general, peak airway pressure decreased over time until around 3 hours EVLP, after which both groups showed an increase.

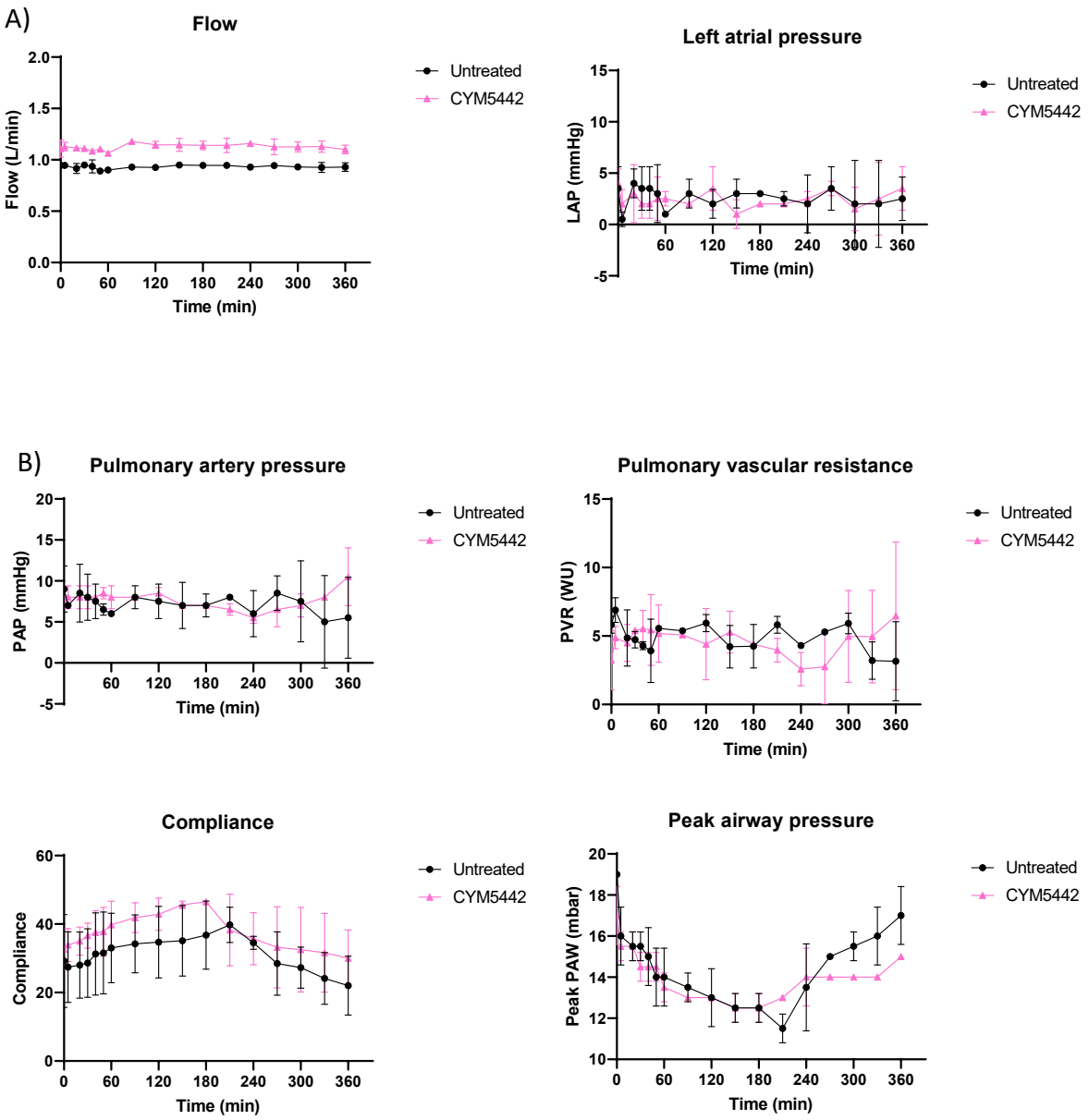

Figure 5.24. Physiological parameters recorded during EVLP of lungs treated with 0.05 µM CYM5442 or vehicle.

Parameters were recorded at 0, 20, 30, 40, 50, 60, 120, 180, 240, 300 and 360 minutes following stable ventilation and drug/vehicle administration. **A)** Controlled parameters flow and left atrial pressure (LAP) during perfusion. **B)** Pulmonary artery pressure (PAP), pulmonary vascular resistance (PVR), compliance and peak airway pressure during perfusion. N=2. A two-way repeated measures ANOVA was used to calculate statistical significance. Mean is presented with standard deviation.

Figure 5.25 showed that controlled parameters pH, PCO_2 and PO_2 were relatively stable with no significant difference between groups.

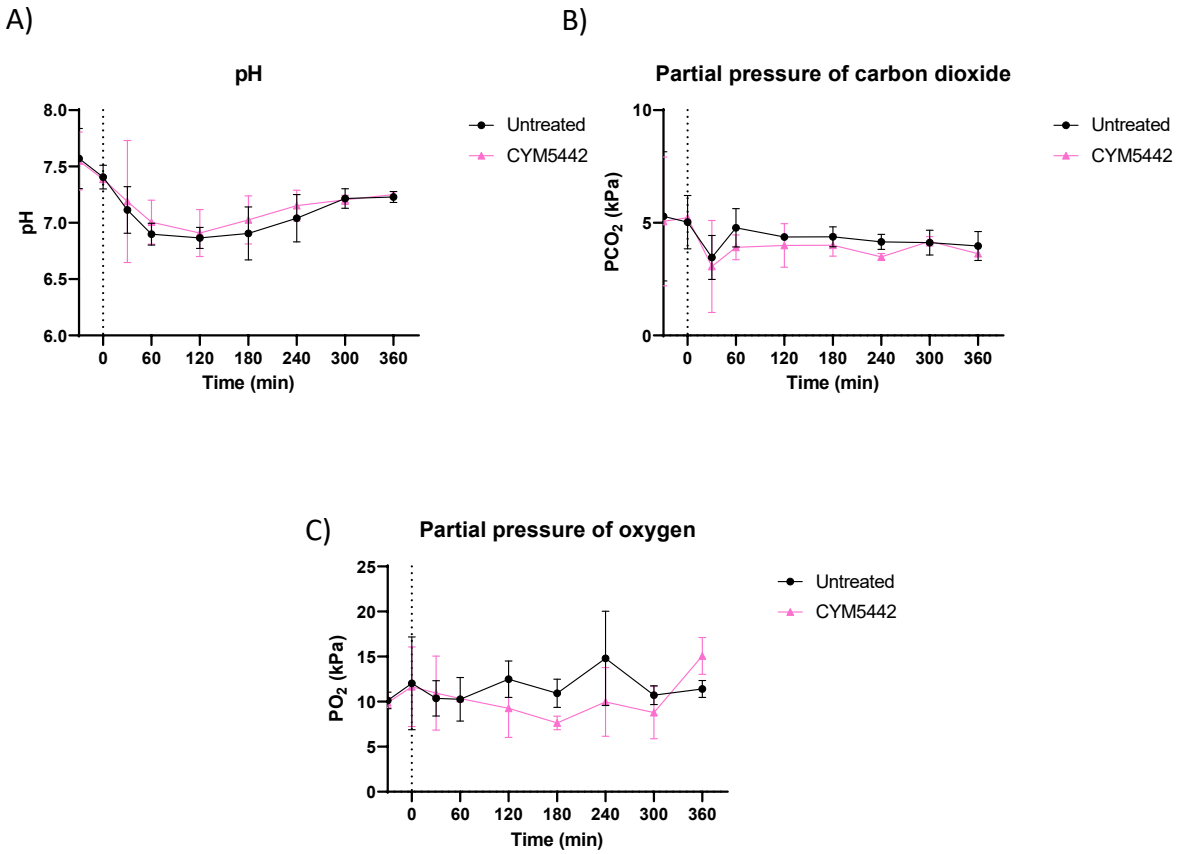

Figure 5.25. Blood gases recorded during EVLP of lungs treated with 0.05 µM CYM5442 or vehicle.

Blood gases were recorded pre lung attachment and at 0, 60, 120, 180, 240, 300 and 360 minutes following stable ventilation and drug/vehicle administration. Controlled parameters **A)** pH, **B)** partial pressure of carbon dioxide (PCO_2) and **C)** partial pressure of oxygen (PO_2) during perfusion. N=2. A two-way repeated measures ANOVA was used to calculate statistical significance. Mean is presented with standard deviation.

5.3.5.3.3. Oedema formation and permeability to Evan's blue

Although both absolute weight gain and percentage weight gain post-EVLP were slightly higher in the untreated group, there was no significant difference (Figure 5.26A). However, the wet/dry ratio of CYM5442 treated lungs was significantly lower than untreated lungs post-EVLP, despite seeming to start slightly higher (Figure 5.26B). A lower CLUE score for CYM5442-treated lungs indicated reduced lung water, although this did not reach significance (Figure 5.26C). Overall, data suggested that lungs treated with 0.05 μM CYM5442 showed reduced oedema formation during perfusion.

EB was quantified in BAL at 4 and 6 hours perfusion. A two-way repeated measures ANOVA showed that the CYM5442 group had significantly lower EB BAL concentration overall. Multiple comparisons at each time point showed a reduced BAL EB in the CYM5442 group compared to untreated at both 4 and 6 hours, which was almost significant at 6 hours (Figure 5.27A). Quantification of EB in tissue at 4 and 6 hours perfusion also showed a trend towards reduced absorbance and fluorescence at both time points in the treated group (Figure 5.27B). Figure 5.27C depicts a pair of lungs at the end of perfusion, with the untreated group appearing darker blue than the CYM5442-treated group. Overall, data suggested that lungs treated with 0.05 μM CYM5442 showed reduced endothelial permeability to EB dye during perfusion.

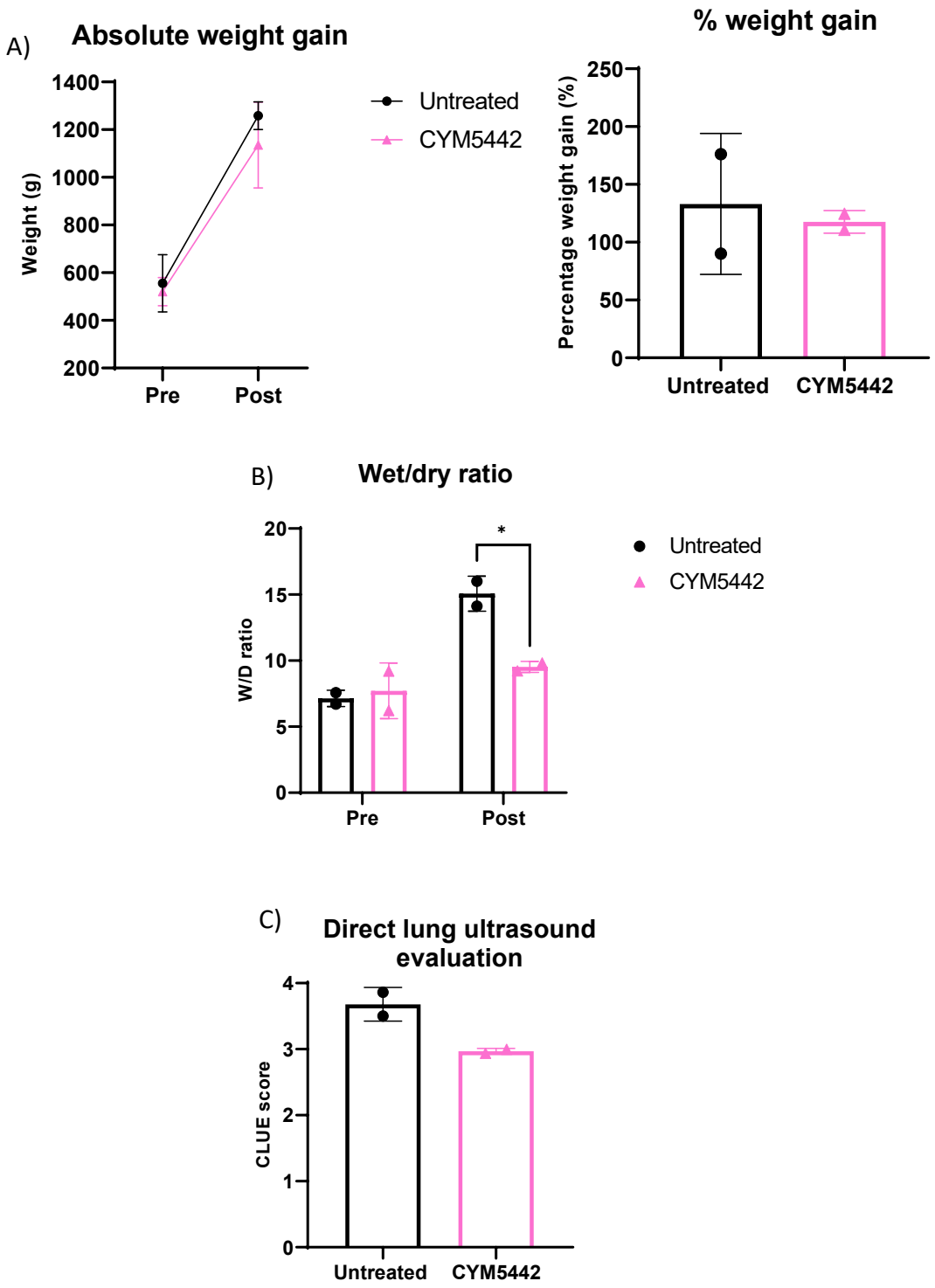

Figure 5.26. Oedema formation during EVLP of lungs treated with 0.05 µM CYM5442 or vehicle.

A) Lung weight was measured for each lung pre and post perfusion. Depicted is absolute weight pre and after 360 min perfusion and percentage weight gain after 360 min perfusion. A paired t test was used to calculate statistical significance. **B)** Tissue samples were obtained from the lower lobe pre perfusion and after perfusion for 6 hours. Wet weight was recorded before drying of tissues and measuring dry weight. Then the ratio of wet/dry weight was calculated. Depicted is the W/D ratio pre and post perfusion. A two-way repeated measures ANOVA with multiple comparisons was used to determine statistical significance between treatment groups at each time point. **C)** Depicted is a direct lung ultrasound evaluation (CLUE) score determined following perfusion for 360 min. A paired t-test was used to determine statistical significance. N=2. Mean is presented with standard deviation.

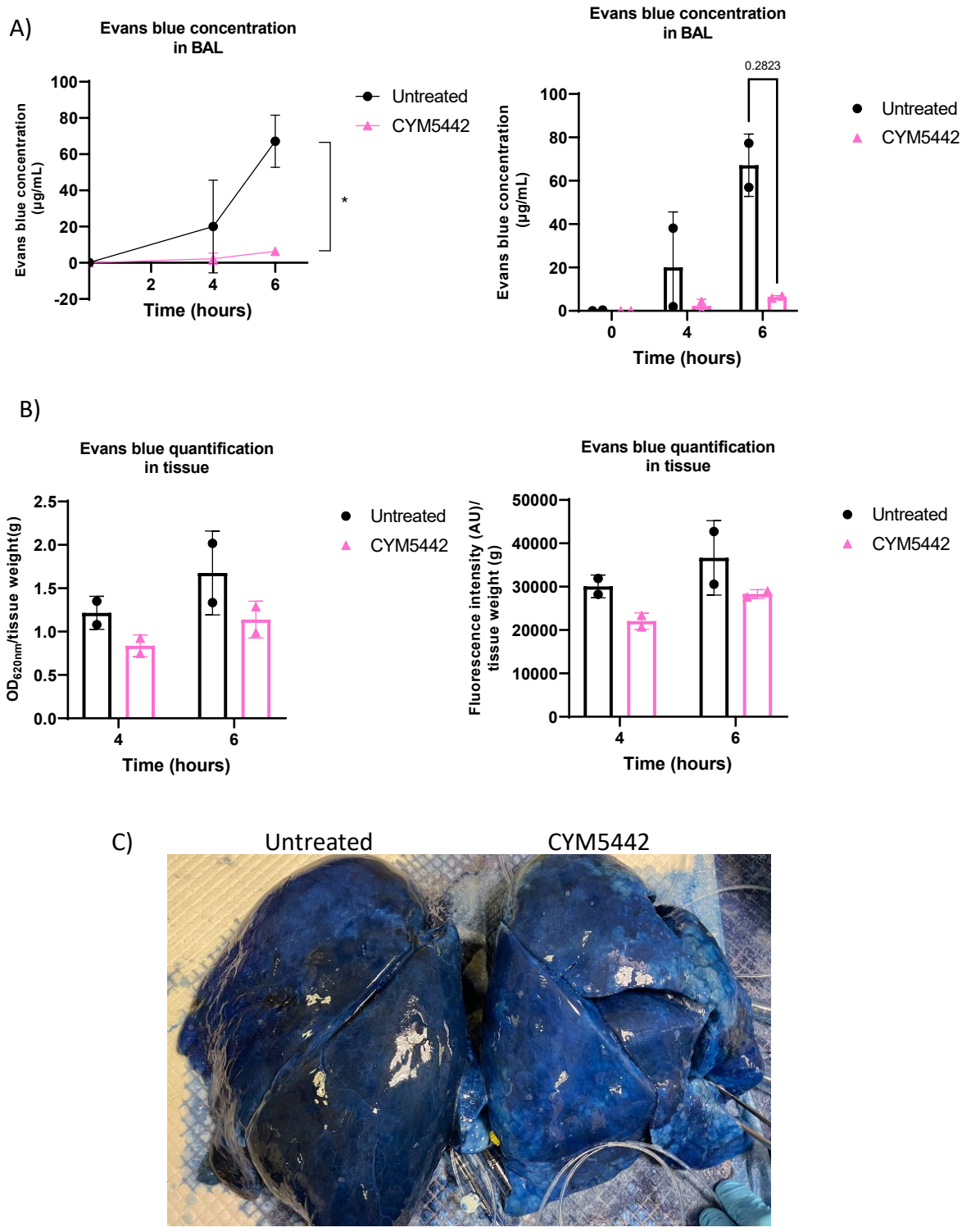

Figure 5.27. Evan's blue quantification in BAL and tissue of lungs treated with 0.05 µM CYM5442 or vehicle during EVLP.

Evan's blue (EB) dye was administered to each circuit at 2 hours following first drug/vehicle administration and stable ventilation. Then bronchoalveolar lavage (BAL) was performed and triplicate tissue samples collected from the lower lobe at 4 and 6 hours perfusion. EB was then quantified in samples. **A)** EB concentration in BAL. **B)** EB quantification in tissue using both absorbance and fluorescence. The average of each lower lobe triplicate is depicted for each lung. A two-way repeated measures ANOVA with multiple comparisons was used to determine statistical significance between treatment groups at each time point. Mean is presented with standard deviation. **C)** A representative image of lungs post perfusion showing untreated versus CYM5442 (0.05 µM) treated lung. N=2.

Levels of IL-1β in perfusate have been shown to be predictive of post-transplant outcome (Andreasson *et al*., 2017) and CXCL8 is released during IRI by alveolar macrophages, endothelial cells and alveolar type II epithelial cells (den Hengst *et al*., 2010, Laubach and Sharma, 2016). Thus, quantification of IL-1β and CXCL8 in sequential perfusate samples was carried out using ELISA. Levels of both cytokines increased over time in perfusate. For IL-1β, perfusate from untreated lungs had higher levels at every time point, with both groups starting at similar levels at time zero (Figure 5.28A). For CXCL8 the untreated group demonstrated increased perfusate levels at all time points except 180 and 300 min, when levels were comparable (Figure 5.28B). Starting levels were similar for both groups. What was notable is the variation between donors; donor 3 seemed to have higher levels of both IL-1β and CXCL8 compared to donor 4.

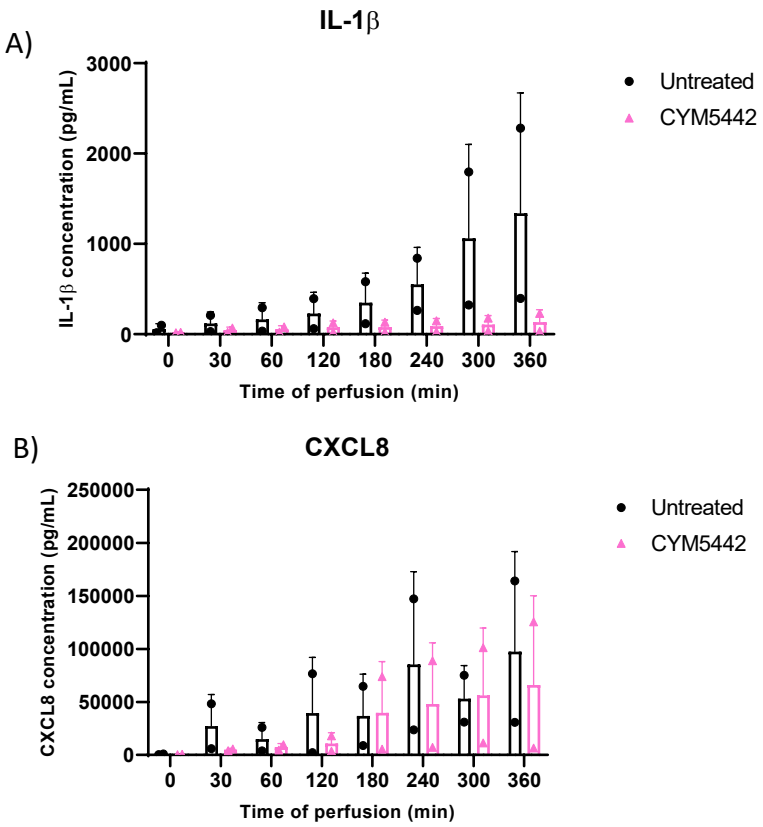

Figure 5.28. Cytokine release into perfusate during EVLP of lungs treated with 0.05 µM CYM5442 or vehicle.

Perfusate samples were taken at 0, 30, 60, 120, 180, 240, 300 and 360 min after stable ventilation and drug/ vehicle administration and protein levels in perfusate were measured using ELISA and compared. **A)** IL-1β and **B)** CXCL8 levels in perfusate measured in pg/mL over time during perfusion. A two-way repeated measures ANOVA with multiple comparisons was used to determine statistical significance between treatment groups at each time point. Mean is presented with standard deviation. N=2.

5.4. Discussion

S1P mediates endothelial barrier protection during pathology via S1PR1 signalling and has therapeutic potential to reduce vascular permeability of donor lungs during EVLP. In this chapter, we aimed to assess the effects of S1PR agonists on endothelial permeability *in vitro* in both human and porcine endothelial cells. Subsequently, we aimed to apply an optimised dose to porcine and human EVLP. PPMEC and HPMEC monolayer TEER was assessed in response to S1PR1 agonist CYM5442 and S1PR1,3,4,5 agonist FTY720P at baseline, as well as CYM5442 and SIN-1 co-treatment to determine efficacy during injury. CYM5442-mediated permeability changes were then measured during EVLP by assessment of endothelial permeability to EB dye and oedema formation.

Whilst the therapeutic potential of S1P has been well established (Zhang *et al*., 2010, Sammani *et al*., 2010, Schaphorst *et al*., 2003, Garcia *et al*., 2001, Tauseef *et al*., 2008), S1P also has the capacity to cause RhoA/RhoA kinase mediated barrier disruption through activation of S1PR2 and 3 (Li *et al*., 2015, Sammani *et al*., 2010). Due to the promiscuous nature of S1P signalling, we sought to specifically target S1PR1, reducing the chances of off target or undesirable effects. Indeed, the importance of S1PR1 in facilitating the barrier enhancing effects of S1P has been established in multiple disease models (Tauseef *et al*., 2008, Sammani *et al*., 2010, Burg *et al*., 2018, Lee *et al*., 2009). CYM5442 is a potent S1PR1 agonist, whilst FTY720P is an agonist for S1PR1, 3,4 and 5; testing the two concurrently allowed us to compare the effects of more targeted therapeutic modulation versus a less selective approach.

It was first established in 1995 that S1PR activation causes ERK phosphorylation downstream through coupling with g-protein $G_{\alpha i}$ (Goodemote *et al*., 1995). Thus, our initial optimisation experiments sought to confirm that CYM5442 and FTY720P phosphorylated ERK in HPMEC; indeed, we showed maximal stimulation after 5 mins with western blot and also showed an exponential increase in p-ERK between a dose range of 0.01-100 μM and 0.001-1 μM for CYM5442 and FTY720P respectively with a p-ERK ELISA. Unlike FTY720 (Hawksworth *et al*., 2012), CYM5442 has thus far never been tested in a pig model. As porcine and human S1PR1 only share approximately 95 % protein sequence homology (Altschul *et al*., 1997), signalling had to be confirmed in PPMEC. Data did suggest that both agonists signalled less potently through porcine receptors and so higher doses would be required for therapeutic modulation.

Measurement of TEER of PPMEC and HPMEC monolayers identified the superiority of targeted S1PR1 signalling as opposed to signalling with FTY720P, which had limited effects on monolayer permeability *in vitro* and was not carried forward as therapeutically efficacious. A handful of studies exist that pharmacologically target the S1P/S1PR axis in the lung (Okazaki *et al*., 2007, Peng *et al*., 2004, McVerry *et al*., 2004, Liu *et al*., 2008, Müller *et al*., 2011) and currently, very few have tested the effects of targeting S1PR1 specifically. However, Sammani *et al* showed that intravenous administration of S1PR1 agonist SEW-2871 reduced LPS-induced lung oedema dose dependently up to 0.3 mg/kg (Sammani *et al*., 2010). Stone *et al* showed similar findings in a rat model of transplantation in response to S1PR1 agonist VPC01091. Furthermore, literature on the effects of CYM5442 on permeability are scarce. However, Burg *et al* did demonstrate barrier-protective effects *in vitro*; 0.05-0.2 μM induced an increase in HUVEC resistance at baseline and 0.2 μM CYM5442 reversed PMN-induced reductions in resistance (Burg *et al*., 2018). Accordingly, our data showed that the same dose reversed SIN-1 mediated barrier disruption in HPMEC *in vitro*. Similarly, CYM5442 increased monolayer resistance in PPMEC at baseline and during injury, albeit at higher doses. Retreatment experiments also prevented significant loss of monolayer integrity over time.

EVLP offers a targeted and isolated approach to reconditioning donor lungs prior to transplantation and literature in the last few years has focused on exploring the efficacy of a wide range of therapeutics administered during EVLP. There remain a small number that focus on specifically targeting endothelial permeability, despite many papers measuring it as a primary outcome. Currently, only one paper has explored the potential benefits of modulating the S1P axis during EVLP using a murine model (Mehaffey *et al*., 2018). Therefore, we sought to evaluate the effects of CYM5442 administration during porcine and human EVLP.

Unfortunately, we were unable to successfully optimise a porcine DCD model which yielded perfusable lungs. Studies using a porcine DCD model prior to perfusion tended to have shorter CITs (0-4 hours) than we were able to replicate within this study (Mulloy *et al*., 2012, Kalka *et al*., 2020, Beller *et al*., 2020), although there also exists studies with longer periods of cold storage (Olbertz *et al*., 2020, Olbertz *et al*., 2019). There is a consensus, however, on the importance of lung inflation in reducing the severity of IRI (Pak *et al*., 2017). Despite lung inflation and reducing CIT to as short as feasibly possible for the capacity of our perfusion team, success was limited. However, we did show an improvement in endothelial integrity over time. Although we were unable to optimise a porcine DCD EVLP model, we were able to

test therapeutic potential using our human split lung platform, which is more clinically relevant. Our split lung model also enables therapeutic testing concurrently with a paired control group.

Both FTY720P and CYM5442 have the capacity to act as functional antagonists of S1PR1 by causing receptor internalisation (Kim *et al*., 2018, Cheng *et al*., 2015). 0.2 μM CYM5442 was shown to be the optimal dose in our *in vitro* serum free system and data suggested the need for a retreatment at 2 hours due to loss of barrier stabilisation over time. However, application to EVLP caused barrier disruption, as evident by increased EB concentration in BAL and tissue and increased weight gain. This suggested functional antagonism of S1PR1 and that CYM5442 concentration should be reduced. We concluded that the differences in optimal dosing were due to the presence of serum in perfusate DMEM, which had been absent during our *in vitro* testing. Serum contains S1P, meaning that addition of too high doses of CYM5442 could exceed physiological relevance, causing S1PR1 internalisation and facilitating serum S1P interaction with barrier disrupting S1PR2 and 3. This highlights the challenges of moving from *in vitro* to *ex vivo* or *in vivo* and reinforces the importance of a model that is physiologically relevant.

Indeed, treating HPMEC with increasing concentrations of CYM5442 in modified DMEM identified 0.05 μM as the optimal dose, with concentration as low as 1 μM causing barrier disruption. Administration of this lower dose during EVLP significantly reduced lung W/D ratio at the end of EVLP and EB concentration in BAL. There was also a trend towards reduced EB in tissue at 4 and 6 hours EVLP and reduced lung water as determined by the CLUE score. This indicates that CYM5442 was able to reduce endothelial permeability of donor lungs and is the first study to demonstrate the potential of S1PR1 agonism during EVLP. Similar to our findings, Zhao *et al* showed that intra-tracheal delivery of CYM5442 reduced W/D ratio in an *in vivo* virus-mediated acute lung injury model in mice (Zhao *et al*., 2019). In contrast, systemic CYM5442 administration had no effect on lung endothelial permeability to EB in a murine model of immune complex-induced vascular injury (Burg *et al*., 2018). This perhaps highlights the importance of administration techniques and favours the targeted modulation of specific organs that *ex vivo* perfusion allows.

As well as its effects on endothelial permeability, CYM5442 has also been shown to reduce *ICAM1* gene expression in pulmonary endothelial cells in the context of viral infection (Jiang

et al., 2017). *In vitro* and *in vivo* studies have suggested that this is through inhibition of NFκB, a transcription factor which initiates expression of pro-inflammatory cytokines (Zhao *et al*., 2019, Jiang *et al*., 2017). As such, Zhao *et al* showed that CYM5442 suppressed the immune response following viral infection in a mouse model of acute lung injury (Zhao *et al*., 2019). Accordingly, whilst we showed no significant change in *ICAM1* gene expression during injury *in vitro*, we did show reduced perfusate CXCL8 and IL-1β compared to untreated during EVLP in support of existing literature.

Clinically, lungs are perfused for around 4 hours to allow assessment as per the Toronto protocol (Cypel *et al*., 2011, Machuca and Cypel, 2014, Slama *et al*., 2017, Valenza *et al*., 2014). Our study showed that during EVLP, compliance and peak airway pressure improved up to around 3 hours, before declining for both lungs irrespective of treatment. This may suggest that for reconditioning of lungs with our model, 3 hours perfusion is the optimal time course required for perfusion.

Ayyat *et al* developed a novel direct lung ultrasound evaluation (CLUE) technique and demonstrated its superiority in evaluating donor lungs compared with other techniques used clinically during EVLP, such as dynamic compliance, PVR and peak airway pressure (Ayyat *et al*., 2019, Ayyat *et al*., 2020). This current study uses the CLUE technique and shows alignment of data with research techniques not used clinically such as permeability to EB and W/D ratio. This helps to reinforce the usefulness of CLUE in research, especially as, unlike these techniques, CLUE is non-invasive and clinically feasible.

In conclusion, our data suggests that CYM5442 reduces endothelial permeability and inflammatory processes compared to untreated during our human split lung perfusion model. This study is the first to confirm the therapeutic potential of targeting S1PR1 during EVLP and show reduced oedema formation as a result. Whilst our data undoubtedly demonstrates the capacity of CYM5442 administration to limit oedema formation during assessment, more study would be needed to determine its usefulness in actually reconditioning un-transplantable organs. For example, to determine whether organs are better off following perfusion with CYM5442 than organs not perfused at all.

6. Discussion, limitations and future directions

6.1. General discussion

Lung transplantation is the only viable treatment option for patients with end stage lung diseases. Despite advances in immunosuppression and surgical technique, lung transplantation remains a limited treatment option due to the scarcity of donor lungs and low utilisation rates (NHS Blood and Transplant, 2022). IRI acquired during the transplantation process can also lead to primary graft dysfunction and effect recipient outcomes (Chen-Yoshikawa, 2021). EVLP has the potential to address these issues. Firstly, through allowing objective evaluation of organs, EVLP could allow identification of ECD organs with good function, reducing discard. Secondly, EVLP offers an isolated platform to which therapeutics can be administered in order to recondition ECD organs with poor function. The latter has become the focus of a large volume of studies which have focused on targeting the lung injury acquired during ischaemia and reperfusion.

Reperfusion of organs with EVLP is associated with pro-inflammatory cytokine accumulation and significant oedema formation over longer periods. As a result, we hypothesised that formulation of a modified Steen solution which contained anti-inflammatory salicylic acid (SA) and retinoic acid (RA) could limit inflammation and lung function decline during EVLP.

Professor Stig Steen and colleagues were instrumental in driving the success and clinical adoption of EVLP through development of Steen solution. Steen allows maintenance of organ viability during EVLP for up to 12 hours (Cypel *et al*., 2008, Cypel *et al*., 2009) and is used as the standard of care today. However, studies have shown that inflammatory processes are triggered during perfusion and increase exponentially with time (Andreasson *et al*., 2017, Kakishita *et al*., 2010), with longer EVLP durations causing lung injury (Erasmus *et al*., 2006, Brandes *et al*., 2002). This is a significant obstacle to longer term evaluation and extended therapies. Thus, chapter 3 sought to examine the potential of a novel perfusate "Modified Steen" in reducing the inflammatory profile of porcine lungs during perfusion. The formulation of modified Steen included the addition of SA and RA, both of which have been shown to interfere with NFκB signalling (Kopp and Ghosh, 1994, Yin *et al*., 1998, Bayón *et al*., 1999, Rafa *et al*., 2017). As such, chapter 3 identified significant negative enrichment of inflammatory pathways such as TNF-α signalling via NFκB in lungs perfused with modified Steen compared

to lungs perfused with Steen. We also identified a reduction in inflammatory *IL6* and *TNFAIP3* gene expression with qPCR and showed that protein levels of IL-6 and TNF-α in perfusate were not significantly different from Fresh in modified Steen. This indicates ablation of inflammatory accumulation during EVLP.

We also showed that this led to improvements in functional parameters such as PVR and maintenance of higher flow rates in agreement with other studies (Kosaka *et al*., 2022, van Zanden *et al*., 2021). This could indicate reduced oedema formation, predict better outcomes post-transplant (Spratt *et al*., 2018, Okamoto *et al*., 2016) and increased likelihood of functionality, as well as allow more physiologically relevant evaluation.

The purpose of chapter 3 was also to gain insight into the inflammatory processes driving IRI so that we may better understand the pathology. Using GSEA, we were able to define the pathways most positively enriched during static storage followed by EVLP, with TNF-α signalling via NFκB the most significant, in agreement with Ferdinand *et al* (Ferdinand *et al*., 2022). IPA also identified the most activated pathways were TNFR1 and TNFR2 signalling. Indeed it has been argued that TNF-α is one of the key initiators of the inflammatory cascade during IRI, alongside NFκB (Krishnadasan *et al*., 2003, Eppinger *et al*., 1997, Naidu *et al*., 2004), which our data agreed with. Our findings not only reinforced the need for therapeutic intervention during EVLP, but also helped to identify a potential target. Indeed, other studies have had success in specifically targeting NFκB during EVLP (Francioli *et al*., 2017, Weathington *et al*., 2018).

As previously mentioned, as well as a platform for objective lung assessment, research in more recent years has focused on administration of therapeutics during EVLP to repair marginal organs. S1PR1 has been shown to facilitate endothelial cell spreading and intercellular junction stabilisation during IRI (Wójciak-Stothard *et al*., 2001). Therefore, we hypothesised that administration of S1PR1 agonist CYM5442 during EVLP could be used to recondition lungs prior to transplantation by improving endothelial barrier integrity.

As such, during chapter 4 we aimed to optimise a model of IRI *in vitro* that would allow therapeutic testing in the context of injury, ahead of application to EVLP. Due to the non-anoxic nature of lung IRI, we chose to administer treatments with physiological oxygen maintained. Because of their key roles in IR-mediated tissue damage, H_2O_2 and peroxynitrite donor SIN-1 were used to model oxidative and nitrosative stress respectively (Bae *et al*., 2016,

Pacher *et al*., 2007, Radi *et al*., 1991). In line with existing literature, we showed negative feedback induced downregulation of *HIF1A* gene expression, in combination with an upregulation of *VEGFA* gene expression following treatment (Cavadas *et al*., 2015, Chua *et al*., 1998, Platt *et al*., 2005). *S1PR1* downregulation was also demonstrated in response to treatment, although this remains somewhat controversial in the literature (Yang *et al*., 2018, Zhu *et al*., 2018, Awad *et al*., 2006, Moon *et al*., 2015). Either way, it did help to identify S1PR1 as an important therapeutic target during IRI. SIN-1 and H_2O_2 also caused significant intracellular ROS release as would be seen during IRI (Zhou *et al*., 2018).

As we sought to modulate endothelial permeability within this study, our primary interest was whether our treatments could reduce primary cell monolayer TEER so that we could attempt to reverse this pharmacologically. Whilst H_2O_2 had no significant effect in human and porcine primary endothelium, SIN-1 significantly reduced monolayer permeability at a dose which did not negatively impact endothelial viability. Similarly, other studies have described peroxynitrite-mediated endothelial barrier disruption through nitration of regulatory proteins which ultimately cause intercellular junction destabilisation (Wu and Wilson, 2008, Siddiqui *et al*., 2011). As such, SIN-1 was carried forward as an ideal candidate for therapeutic testing in the context of injury.

CYM5442 is a potent S1PR1 agonist and has been shown to inhibit NFκB signalling (Zhao *et al*., 2019, Jiang *et al*., 2017), inhibit macrophage recruitment (Cheng *et al*., 2015) and of most relevance to this current study, reduce endothelial permeability during inflammatory conditions (Burg *et al*., 2018, Zhao *et al*., 2019). Although previous studies have identified the importance of S1PR1 in limiting disease-mediated endothelial barrier disruption (Tauseef *et al*., 2008, Sammani *et al*., 2010, Lee *et al*., 2009, Burg *et al*., 2018) and showed efficacy of pharmacological targeting of S1PR1 (Sammani *et al*., 2010, Stone *et al*., 2015), there currently exists no studies which have targeted S1PR1 during EVLP.

Although Mehaffey *et al* showed benefits from co-administration of S1P and an SPHK2 inhibitor during EVLP, there was no significant difference in endothelial permeability achieved with S1P alone (Mehaffey *et al*., 2018). Thus, due to the promiscuous nature of S1P signalling and the lack of current literature, we sought to specifically target S1PR1 during EVLP. We used a human split lung model, which allowed use to test a particular concentration of CYM5442 in

tandem with an untreated control lung. We used lungs declined for transplantation and aimed to assess whether we could improve endothelial integrity.

Although the time scale of this project only allowed us to reach N=2 for testing of therapeutic dose 0.05 μM CYM5442, we showed a significant reduction in tissue W/D ratio post EVLP and EB concentrations in BAL compared to the untreated lung. We also showed a trend towards a reduced CLUE score and reduced EB quantification in tissue post-EVLP. This demonstrated the capacity of CYM5442 treatment to reduce endothelial permeability and oedema formation during EVLP. Our *in vitro* work also showed the efficacy of CYM5442 in increasing barrier integrity at baseline and during injury in HPMEC, in corroboration with doses used by Burg *et al* in HUVEC (Burg *et al*., 2018). In agreement with the suggestion that CYM5442 reduces NFκB signalling (Zhao *et al*., 2019, Jiang *et al*., 2017), we also found a reduction in CXCL8 and IL-1β release into perfusate during EVLP for treated lungs, suggesting a dual mechanism for CYM5442-mediated protection from IRI.

We also, albeit unintentionally, demonstrated the functional antagonism capabilities of CYM5442 at higher doses, which has been shown by a limited number of studies (Kim *et al*., 2018, Cheng *et al*., 2015). We showed barrier disruption during EVLP via increased permeability to EB and increased weight gain at the end of EVLP. *In vitro*, we found that treatment with CYM5442 in DMEM caused barrier disruption at doses as low as 1 μM. Accordingly, Burg *et al* found that administration of CYM5442 at 10 mg/kg yielded a plasma concentration of around 1 μM and caused significant EB leakage *in vivo* (Burg *et al*., 2018). Thus, we were able to demonstrate the potential of CYM5442 in limiting endothelial permeability during EVLP, but also emphasise the limited therapeutic window of the drug.

We also found that lung compliance and peak airway pressure improved during the course of EVLP, but only up to around 3 hours. This perhaps has implications for the time frame of reconditioning and suggests that with our model, only short periods of EVLP are feasible for reconditioning. However, this also draws focus back to the need for new perfusion technologies and novel perfusates like modified Steen, in order to facilitate longer and more stable perfusions during which the lung does not worsen over time.

Our findings could have significant impact on directing research in the future and also in addressing gaps which currently exist. Few studies have defined the biological processes occurring during lung IRI using RNA-sequencing. In this study, we identified the genes and

pathways associated with IRI using biopsy samples from a large animal model. In agreement with Ferdinand *et al*, we found that the most significantly enriched pathway after EVLP was TNF-α signalling via NFκB (Ferdinand *et al*., 2022). Thus, as well as confirming existing findings in the literature, we provide a good basis for therapeutic targeting which could be explored in the future. Furthermore, literature on S1P and associated agonists in the lung is less extensive than other organs (Stone *et al*., 2015, Sammani *et al*., 2010); thus this current study helps to address this. In agreement with Mehaffey *et al*. we have demonstrated the benefits of targeting the S1P axis during EVLP (Mehaffey *et al*., 2018), but are the first to show the success of a more targeted approach. Furthermore, only two studies have assessed the effects of CYM5442 on endothelial permeability (Zhao *et al*., 2019, Burg *et al*., 2018). We add to this existing literature by corroborating their findings, but add novelty by assessing the agonist in an *ex vivo* context. Thus we identify a potential therapeutic to ameliorate endothelial hyper-permeability during IRI, which could incite further research in the future.

In conclusion, although a very preliminary study with a small number of biological repeats, we demonstrate the feasibility of modulating endothelial integrity during EVLP. We demonstrate that CYM5442 can be used to reduce endothelial permeability *in vitro* and are the first study to demonstrate this during EVLP. Thus, S1PR1 agonism could be used to increase endothelial integrity of marginal lungs prior to transplantation, expanding the donor pool. It could also be used to limit subsequent IRI, reducing the chances of PGD in the recipient.

6.2. Limitations of the study

In chapter 3, we performed RNA-sequencing on tissue biopsies which had already been collected as part of an ongoing study by XVIVO to test modified Steen. As part of their workflow, pre-EVLP samples are not collected prior to perfusing lungs so as not to interfere with established protocols. Therefore, rather than having a pre-perfusion sample for every lung pair, we opted to use one Fresh control group as our no intervention control group. One main limitation with this is that it does not account for the heterogeneity between lung sets.

Another limitation with our baseline control group is that we elected to take these samples during retrieval. This meant that comparison with post-EVLP samples allowed us to gain insight into the mechanisms occurring through the entire transplantation process ie. cold static storage and then reperfusion. However, having matched pre-perfusion samples taken

after cold storage would have allowed us to underpin the processes which occur with EVLP/reperfusion specifically.

Our *in vitro* testing was limited by the simplification of the system; growing a single endothelial cell type on transwells is not fully representative of the heterogeneous cell population that would be present in a vessel. We also used a static system, whereas growing cells under flow and subjecting them to stop of flow would have arguably been the best method of modelling lung ischaemia (Zhang *et al*., 2005a, Zhang *et al*., 2008, Wei *et al*., 1999, Chatterjee *et al*., 2006). Furthermore, most of our testing was done in either low serum or serum free media, which impacted our results compared to testing in perfusate solutions containing serum. This calls into question the physiological relevance of testing in a serum free system. Furthermore, for initial optimisation of our IRI models, we used HMEC-1, which are an endothelial cell line and not fully representative of lung endothelium. This is why we used primary endothelial cells for permeability experiments as HMEC-1 do not have the capacity to form a monolayer due to their lack of contact inhibition. In addition, our IRI models are hugely simplified compared to the multifaceted and complex process of IRI, particularly in the lung.

A significant limitation of this current study was the small sample size for our human EVLPs; we were only able to test our therapeutic dose of 0.5 μM CYM5442 in two pairs of donor lungs. We originally planned to randomise two right and two left lungs to receive treatment, achieving N=4. However, due to not being able to perfuse lungs from donor 2 and donor 5, we were unable to achieve this within the time frame of the study. Thus, we ended up treating the right lung for both repeats, which does not account for physiological difference between the two.

Ultimately, the biggest limitation of this study was the lack of capacity to carry out a transplantation model due to the use of human lungs. Whilst this is something which would be possible with a large animal model, we were unable to optimise a porcine DCD retrieval model. This would have allowed us to assess the effects of pre-treating lungs with CYM5442 during EVLP prior to transplantation. Based off our current data, there is no way to know whether lungs perfused with CYM5442 would perform better following transplant than lungs which underwent no EVLP at all. This limits our ability to draw conclusions about CYM5442 as a therapeutic to recondition marginal organs, even though we did see an improvement

compared to lungs which underwent EVLP without CYM5442. A transplant model with a cold static storage control group would help address these questions.

6.3. Future directions

In order to complete this preliminary study, we aim to complete 2 more lung perfusions, with the drug administered to the left lung. This will allow us to truly validate the therapeutic potential of CYM5442 during EVLP, whilst accounting for physiological differences between left and right lungs.

Because of extensive sample collection before, during and after EVLP, there are various things that could be explored to validate the potential of CYM5442 and better identify its mechanisms of action. Firstly, RNA-sequencing could be carried out on tissue samples to see if CYM5442 mediated transcriptomic changes; of particular interest would be S1P-related genes or genes which are regulated via NFκB. Whilst our ELISA data was informative, it would be useful to use a more robust and high throughput method to explore pro-inflammatory cytokine concentration in perfusate. For example, mesoscale discovery (MSD) assays would allow us to quantify many different biomarkers at once.

S1PR1 signalling has been shown to increase the stabilisation and localisation of VE cadherin at intercellular junctions (Wójciak-Stothard *et al*., 2001). Thus it would be interesting to explore this via IF staining, especially as we have already optimised the antibody for use in this current study. Furthermore, the glycocalyx has been shown to be important in maintaining endothelial integrity and is shed during injury (Abassi *et al*., 2020). Thus, it would be useful to stain for proteoglycans such as syndecan or glycosaminoglycans like hyaluronic acid and heparan sulfate to determine whether CYM5442 had any protective effects on the glycocalyx.

Our split lung perfusion model has become well established and offers the opportunity to assess other therapeutics aside from CYM5442. For example Mr Nicholas Chilvers is currently exploring the therapeutic potential of extracellular vesicles (EVs) isolated from human amniotic epithelial cells (HAECs). HAECs are believed to have immunomodulatory properties via paracrine action and it is believed that their protective effects are mediated through EV release. Therefore, there are plans to test these isolated EVs using our optimised split lung EVLP model to assess their capacity to limit IRI.

7. References

ABASSI, Z., ARMALY, Z. & HEYMAN, S. N. 2020. Glycocalyx Degradation in Ischemia-Reperfusion Injury. *The American Journal of Pathology,* 190**,** 752-767.

ADADA, M., CANALS, D., HANNUN, Y. A. & OBEID, L. M. 2013. Sphingosine-1-phosphate receptor 2. *Febs j,* 280**,** 6354-66.

ADRIAN, K., SKOGBY, M., GATZINSKY, V., FRIBERG, L.-G. & MELLGREN, K. 2006. Procedure-induced Inflammation and Endothelial Cell Activation in an Artificially Ventilated and Circulated Porcine Double-Lung Model. *Artificial Organs,* 30**,** 922-928.

AEBERHARD, E. E., HENDERSON, S. A., ARABOLOS, N. S., GRISCAVAGE, J. M., CASTRO, F. E., BARRETT, C. T. & IGNARRO, L. J. 1995. Nonsteroidal anti-inflammatory drugs inhibit expression of the inducible nitric oxide synthase gene. *Biochem Biophys Res Commun,* 208**,** 1053-9.

AL-MEHDI, A. B., ISCHIROPOULOS, H. & FISHER, A. B. 1996. Endothelial cell oxidant generation during K(+)-induced membrane depolarization. *J Cell Physiol,* 166**,** 274-80.

AL-MEHDI, A. B., SHUMAN, H. & FISHER, A. B. 1997a. Intracellular generation of reactive oxygen species during nonhypoxic lung ischemia. *Am J Physiol,* 272**,** L294-300.

AL-MEHDI, A. B., SHUMAN, H. & FISHER, A. B. 1997b. Oxidant generation with K(+)-induced depolarization in the isolated perfused lung. *Free Radic Biol Med,* 23**,** 47-56.

AL-MEHDI, A. B., ZHAO, G., DODIA, C., TOZAWA, K., COSTA, K., MUZYKANTOV, V., ROSS, C., BLECHA, F., DINAUER, M. & FISHER, A. B. 1998. Endothelial NADPH oxidase as the source of oxidants in lungs exposed to ischemia or high K+. *Circ Res,* 83**,** 730-7.

AL-MEHDI, A. B., ZHAO, G., TOZAWA, K. & FISHER, A. B. 2000. Depolarization-associated iron release with abrupt reduction in pulmonary endothelial shear stress in situ. *Antioxid Redox Signal,* 2**,** 335-45.

ALKADHIM, M., ZOCCALI, C., ABBASIFARD, S., AVILA, M. J., PATEL, A. S., SATTAROV, K., WALTER, C. M. & BAAJ, A. A. 2015. The surgical vascular anatomy of the minimally invasive lateral lumbar interbody approach: a cadaveric and radiographic analysis. *Eur Spine J,* 24 Suppl 7**,** 906-11.

ALLINGHAM, M. J., VAN BUUL, J. D. & BURRIDGE, K. 2007. ICAM-1-mediated, Src- and Pyk2-dependent vascular endothelial cadherin tyrosine phosphorylation is required for leukocyte transendothelial migration. *J Immunol,* 179**,** 4053-64.

ALLPORT, J. R., MULLER, W. A. & LUSCINSKAS, F. W. 2000. Monocytes induce reversible focal changes in vascular endothelial cadherin complex during transendothelial migration under flow. *J Cell Biol,* 148**,** 203-16.

ALTSCHUL, S. F., MADDEN, T. L., SCHÄFFER, A. A., ZHANG, J., ZHANG, Z., MILLER, W. & LIPMAN, D. J. 1997. Gapped BLAST and PSI-BLAST: a new generation of protein database search programs. *Nucleic Acids Res,* 25**,** 3389-402.

ANAYA-PRADO, R., TOLEDO-PEREYRA, L. H., LENTSCH, A. B. & WARD, P. A. 2002. Ischemia/reperfusion injury. *J Surg Res,* 105**,** 248-58.

ANDREASSON, A. S. I., BORTHWICK, L. A., GILLESPIE, C., JIWA, K., SCOTT, J., HENDERSON, P., MAYES, J., ROMANO, R., ROMAN, M., ALI, S., FILDES, J. E., MARCZIN, N., DARK, J. H. & FISHER, A. J. 2017.

The role of interleukin-1β as a predictive biomarker and potential therapeutic target during clinical ex vivo lung perfusion. *J Heart Lung Transplant,* 36**,** 985-995.

ANTONETTI, D. A., BARBER, A. J., KHIN, S., LIETH, E., TARBELL, J. M. & GARDNER, T. W. 1998. Vascular permeability in experimental diabetes is associated with reduced endothelial occludin content: vascular endothelial growth factor decreases occludin in retinal endothelial cells. Penn State Retina Research Group. *Diabetes,* 47**,** 1953-1959.

ARNI, S., MAEYASHIKI, T., LATSHANG, T., OPITZ, I. & INCI, I. 2021. Ex Vivo Lung Perfusion with K(ATP) Channel Modulators Antagonize Ischemia Reperfusion Injury. *Cells,* 10.

ASHKI, N., CHAN, A. M., QIN, Y., WANG, W., KIYOHARA, M., LIN, L., BRAUN, J., WADEHRA, M. & GORDON, L. K. 2014. Peroxynitrite upregulates angiogenic factors VEGF-A, BFGF, and HIF-1α in human corneal limbal epithelial cells. *Invest Ophthalmol Vis Sci,* 55**,** 1637-46.

AWAD, A. S., YE, H., HUANG, L., LI, L., FOSS, F. W., JR., MACDONALD, T. L., LYNCH, K. R. & OKUSA, M. D. 2006. Selective sphingosine 1-phosphate 1 receptor activation reduces ischemia-reperfusion injury in mouse kidney. *Am J Physiol Renal Physiol,* 290**,** F1516-24.

AYYAT, K. S., OKAMOTO, T., NIIKAWA, H., ITODA, Y., DUGAR, S., LATIFI, S. Q., LEBOVITZ, D. J., MOGHEKAR, A. & MCCURRY, K. R. 2019. DireCt Lung Ultrasound Evaluation (CLUE): A novel technique for monitoring extravascular lung water in donor lungs. *The Journal of Heart and Lung Transplantation,* 38**,** 757-766.

AYYAT, K. S., OKAMOTO, T., NIIKAWA, H., SAKANOUE, I., DUGAR, S., LATIFI, S. Q., LEBOVITZ, D. J., MOGHEKAR, A. & MCCURRY, K. R. 2020. A CLUE for better assessment of donor lungs: Novel technique in clinical ex vivo lung perfusion. *The Journal of Heart and Lung Transplantation,* 39**,** 1220-1227.

BAE, S., PARK, M., KANG, C., DILMEN, S., KANG, T. H., KANG, D. G., KE, Q., LEE, S. U., LEE, D. & KANG, P. M. 2016. Hydrogen Peroxide-Responsive Nanoparticle Reduces Myocardial Ischemia/Reperfusion Injury. *J Am Heart Assoc,* 5.

BALDA, M. S., WHITNEY, J. A., FLORES, C., GONZÁLEZ, S., CEREIJIDO, M. & MATTER, K. 1996. Functional dissociation of paracellular permeability and transepithelial electrical resistance and disruption of the apical-basolateral intramembrane diffusion barrier by expression of a mutant tight junction membrane protein. *J Cell Biol,* 134**,** 1031-49.

BANAI, S., SHWEIKI, D., PINSON, A., CHANDRA, M., LAZAROVICI, G. & KESHET, E. 1994. Upregulation of vascular endothelial growth factor expression induced by myocardial ischaemia: implications for coronary angiogenesis. *Cardiovasc Res,* 28**,** 1176-9.

BANDHUVULA, P., HONBO, N., WANG, G. Y., JIN, Z. Q., FYRST, H., ZHANG, M., BOROWSKY, A. D., DILLARD, L., KARLINER, J. S. & SABA, J. D. 2011. S1P lyase: a novel therapeutic target for ischemia-reperfusion injury of the heart. *Am J Physiol Heart Circ Physiol,* 300**,** H1753-61.

BAYÓN, Y., ALONSO, A. & SÁNCHEZ CRESPO, M. 1999. 4-trifluoromethyl derivatives of salicylate, triflusal and its main metabolite 2-hydroxy-4-trifluoromethylbenzoic acid, are potent inhibitors of nuclear factor kappaB activation. *Br J Pharmacol,* 126**,** 1359-66.

BAZZONI, G. & DEJANA, E. 2004. Endothelial Cell-to-Cell Junctions: Molecular Organization and Role in Vascular Homeostasis. *Physiological Reviews,* 84**,** 869-901.

BELLER, J. P., BYLER, M. R., MONEY, D. T., CHANCELLOR, W. Z., ZHANG, A., ZHAO, Y., STOLER, M. H., NARAHARI, A. K., SHANNON, A., MEHAFFEY, J. H., TRIBBLE, C. G., LAUBACH, V. E., KRON, I. L. &

ROESER, M. E. 2020. Reduced-flow ex vivo lung perfusion to rehabilitate lungs donated after circulatory death. *J Heart Lung Transplant,* 39**,** 74-82.

BENEDETTI, E. L. & EMMELOT, P. 1965. Electron microscopic observations on negatively stained plasma membranes isolated from rat liver. *J Cell Biol,* 26**,** 299-305.

BERDYSHEV, E. V., GORSHKOVA, I. A., GARCIA, J. G., NATARAJAN, V. & HUBBARD, W. C. 2005. Quantitative analysis of sphingoid base-1-phosphates as bisacetylated derivatives by liquid chromatography-tandem mass spectrometry. *Anal Biochem,* 339**,** 129-36.

BLAHO, V. A. & HLA, T. 2014. An update on the biology of sphingosine 1-phosphate receptors. *J Lipid Res,* 55**,** 1596-608.

BONILLA, I. M., SRIDHAR, A., NISHIJIMA, Y., GYÖRKE, S., CARDOUNEL, A. J. & CARNES, C. A. 2013. Differential Effects of the Peroxynitrite Donor, SIN-1, on Atrial and Ventricular Myocyte Electrophysiology. *Journal of Cardiovascular Pharmacology,* 61**,** 401-407.

BORUTAITE, V., JEKABSONE, A., MORKUNIENE, R. & BROWN, G. C. 2003. Inhibition of mitochondrial permeability transition prevents mitochondrial dysfunction, cytochrome c release and apoptosis induced by heart ischemia. *J Mol Cell Cardiol,* 35**,** 357-66.

BOTHA, P., TRIVEDI, D., WEIR, C. J., SEARL, C. P., CORRIS, P. A., DARK, J. H. & SCHUELER, S. V. 2006. Extended donor criteria in lung transplantation: impact on organ allocation. *J Thorac Cardiovasc Surg,* 131**,** 1154-60.

BRANDES, H., ALBES, J. M., CONZELMANN, A., WEHRMANN, M. & ZIEMER, G. 2002. Comparison of pulsatile and nonpulsatile perfusion of the lung in an extracorporeal large animal model. *Eur Surg Res,* 34**,** 321-9.

BRINCKERHOFF, C. E., COFFEY, J. W. & SULLIVAN, A. C. 1983. Inflammation and Collagenase Production in Rats with Adjuvant Arthritis Reduced with 13-cis-Retinoic Acid. *Science,* 221**,** 756-758.

BRINGOLD, U., GHAFOURIFAR, P. & RICHTER, C. 2000. Peroxynitrite formed by mitochondrial NO synthase promotes mitochondrial Ca2+ release. *Free Radic Biol Med,* 29**,** 343-8.

BROOKES, P. S., YOON, Y., ROBOTHAM, J. L., ANDERS, M. W. & SHEU, S. S. 2004. Calcium, ATP, and ROS: a mitochondrial love-hate triangle. *Am J Physiol Cell Physiol,* 287**,** C817-33.

BRYAN, A. M. & DEL POETA, M. 2018. Sphingosine-1-phosphate receptors and innate immunity. *Cell Microbiol,* 20**,** e12836.

BURG, N., SWENDEMAN, S., WORGALL, S., HLA, T. & SALMON, J. E. 2018. Sphingosine 1-Phosphate Receptor 1 Signaling Maintains Endothelial Cell Barrier Function and Protects Against Immune Complex-Induced Vascular Injury. *Arthritis Rheumatol,* 70**,** 1879-1889.

CAMERER, E., REGARD, J. B., CORNELISSEN, I., SRINIVASAN, Y., DUONG, D. N., PALMER, D., PHAM, T. H., WONG, J. S., PAPPU, R. & COUGHLIN, S. R. 2009. Sphingosine-1-phosphate in the plasma compartment regulates basal and inflammation-induced vascular leak in mice. *J Clin Invest,* 119**,** 1871-9.

CARBONE, F., BONAVENTURA, A. & MONTECUCCO, F. 2019. Neutrophil-Related Oxidants Drive Heart and Brain Remodeling After Ischemia/Reperfusion Injury. *Front Physiol,* 10**,** 1587.

CAVADAS, M. A. S., MESNIERES, M., CRIFO, B., MANRESA, M. C., SELFRIDGE, A. C., SCHOLZ, C. C., CUMMINS, E. P., CHEONG, A. & TAYLOR, C. T. 2015. REST mediates resolution of HIF-dependent gene expression in prolonged hypoxia. *Scientific Reports,* 5**,** 17851.

CERUTTI, C. & RIDLEY, A. J. 2017. Endothelial cell-cell adhesion and signaling. *Exp Cell Res,* 358**,** 31-38.

CHADJICHRISTOS, C. E., SCHECKENBACH, K. E., VEEN, T. A. V., SARIEDDINE, M. Z. R., WIT, C. D., YANG, Z., ROTH, I., BACCHETTA, M., VISWAMBHARAN, H. & FOGLIA, B. 2010. Endothelial-specific deletion of connexin40 promotes atherosclerosis by increasing CD73-dependent leukocyte adhesion. *Circulation***,** 123-131.

CHAMBERS, D. C., CHERIKH, W. S., HARHAY, M. O., HAYES, D., JR., HSICH, E., KHUSH, K. K., MEISER, B., POTENA, L., ROSSANO, J. W., TOLL, A. E., SINGH, T. P., SADAVARTE, A., ZUCKERMANN, A. & STEHLIK, J. 2019. The International Thoracic Organ Transplant Registry of the International Society for Heart and Lung Transplantation: Thirty-sixth adult lung and heart-lung transplantation Report-2019; Focus theme: Donor and recipient size match. *J Heart Lung Transplant,* 38**,** 1042-1055.

CHATTERJEE, S., BROWNING, E. A., HONG, N., DEBOLT, K., SOROKINA, E. M., LIU, W., BIRNBAUM, M. J. & FISHER, A. B. 2012. Membrane depolarization is the trigger for PI3K/Akt activation and leads to the generation of ROS. *Am J Physiol Heart Circ Physiol,* 302**,** H105-14.

CHATTERJEE, S. & FISHER, A. B. 2004. ROS to the rescue. *American Journal of Physiology-Lung Cellular and Molecular Physiology,* 287**,** L704-L705.

CHATTERJEE, S. & FISHER, A. B. 2014. Mechanotransduction: forces, sensors, and redox signaling. *Antioxid Redox Signal,* 20**,** 868-71.

CHATTERJEE, S., LEVITAN, I., WEI, Z. & FISHER, A. B. 2006. KATP channels are an important component of the shear-sensing mechanism in the pulmonary microvasculature. *Microcirculation,* 13**,** 633-44.

CHATTERJEE, S., NIEMAN, G. F., CHRISTIE, J. D. & FISHER, A. B. 2014. Shear stress-related mechanosignaling with lung ischemia: lessons from basic research can inform lung transplantation. *American journal of physiology. Lung cellular and molecular physiology,* 307**,** L668-L680.

CHEN, Q., MOGHADDAS, S., HOPPEL, C. L. & LESNEFSKY, E. J. 2008. Ischemic defects in the electron transport chain increase the production of reactive oxygen species from isolated rat heart mitochondria. *Am J Physiol Cell Physiol,* 294**,** C460-6.

CHEN-YOSHIKAWA, T. F. 2021. Ischemia-Reperfusion Injury in Lung Transplantation. *Cells,* 10.

CHENG, Q., MA, S., LIN, D., MEI, Y., GONG, H., LEI, L., CHEN, Y., ZHAO, Y., HU, B., WU, Y., YU, X., ZHAO, L. & LIU, H. 2015. The S1P1 receptor-selective agonist CYM-5442 reduces the severity of acute GVHD by inhibiting macrophage recruitment. *Cell Mol Immunol,* 12**,** 681-91.

CHRISTENSEN, P. M., LIU, C. H., SWENDEMAN, S. L., OBINATA, H., QVORTRUP, K., NIELSEN, L. B., HLA, T., DI LORENZO, A. & CHRISTOFFERSEN, C. 2016. Impaired endothelial barrier function in apolipoprotein M-deficient mice is dependent on sphingosine-1-phosphate receptor 1. *Faseb j,* 30**,** 2351-9.

CHRISTIE, I. G., CHAN, E. G., RYAN, J. P., HARANO, T., MORRELL, M., LUKETICH, J. D. & SANCHEZ, P. G. 2021. National Trends in Extended Criteria Donor Utilization and Outcomes for Lung Transplantation. *Ann Thorac Surg,* 111**,** 421-426.

CHUA, C. C., HAMDY, R. C. & CHUA, B. H. 1998. Upregulation of vascular endothelial growth factor by H2O2 in rat heart endothelial cells. *Free Radic Biol Med,* 25**,** 891-7.

CHUN, J., HLA, T., LYNCH, K. R., SPIEGEL, S. & MOOLENAAR, W. H. 2010. International Union of Basic and Clinical Pharmacology. LXXVIII. Lysophospholipid receptor nomenclature. *Pharmacol Rev,* 62**,** 579-87.

COMI, G., HARTUNG, H. P., BAKSHI, R., WILLIAMS, I. M. & WIENDL, H. 2017. Benefit-Risk Profile of Sphingosine-1-Phosphate Receptor Modulators in Relapsing and Secondary Progressive Multiple Sclerosis. *Drugs,* 77**,** 1755-1768.

COOPER, D., STOKES, K. Y., TAILOR, A. & GRANGER, D. N. 2002. Oxidative stress promotes blood cell-endothelial cell interactions in the microcirculation. *Cardiovasc Toxicol,* 2**,** 165-80.

CORADA, M., MARIOTTI, M., THURSTON, G., SMITH, K., KUNKEL, R., BROCKHAUS, M., LAMPUGNANI, M. G., MARTIN-PADURA, I., STOPPACCIARO, A., RUCO, L., MCDONALD, D. M., WARD, P. A. & DEJANA, E. 1999. Vascular endothelial-cadherin is an important determinant of microvascular integrity in vivo. *Proc Natl Acad Sci U S A,* 96**,** 9815-20.

COSGUN, T., ISKENDER, I., YAMADA, Y., ARNI, S., LIPISKI, M., VAN TILBURG, K., WEDER, W. & INCI, I. 2017. Ex vivo administration of trimetazidine improves post-transplant lung function in pig model. *Eur J Cardiothorac Surg,* 52**,** 171-177.

CYPEL, M., RUBACHA, M., YEUNG, J., HIRAYAMA, S., TORBICKI, K., MADONIK, M., FISCHER, S., HWANG, D., PIERRE, A., WADDELL, T. K., DE PERROT, M., LIU, M. & KESHAVJEE, S. 2009. Normothermic ex vivo perfusion prevents lung injury compared to extended cold preservation for transplantation. *Am J Transplant,* 9**,** 2262-9.

CYPEL, M., YEUNG, J. C., HIRAYAMA, S., RUBACHA, M., FISCHER, S., ANRAKU, M., SATO, M., HARWOOD, S., PIERRE, A., WADDELL, T. K., DE PERROT, M., LIU, M. & KESHAVJEE, S. 2008. Technique for Prolonged Normothermic Ex Vivo Lung Perfusion. *The Journal of Heart and Lung Transplantation,* 27**,** 1319-1325.

CYPEL, M., YEUNG, J. C., LIU, M., ANRAKU, M., CHEN, F., KAROLAK, W., SATO, M., LARATTA, J., AZAD, S., MADONIK, M., CHOW, C.-W., CHAPARRO, C., HUTCHEON, M., SINGER, L. G., SLUTSKY, A. S., YASUFUKU, K., DE PERROT, M., PIERRE, A. F., WADDELL, T. K. & KESHAVJEE, S. 2011. Normothermic Ex Vivo Lung Perfusion in Clinical Lung Transplantation. *New England Journal of Medicine,* 364**,** 1431-1440.

D'ALESSANDRO, S., MAGNAVACCA, A., PEREGO, F., FUMAGALLI, M., SANGIOVANNI, E., PRATO, M., DELL'AGLI, M. & BASILICO, N. 2019. Effect of Hypoxia on Gene Expression in Cell Populations Involved in Wound Healing. *BioMed Research International,* 2019**,** 2626374.

DAS, T., CHEN, Z., HENDRIKS, R. W. & KOOL, M. 2018. A20/Tumor Necrosis Factor α-Induced Protein 3 in Immune Cells Controls Development of Autoinflammation and Autoimmunity: Lessons from Mouse Models. *Front Immunol,* 9**,** 104.

DE PERROT, M., LIU, M., WADDELL, T. K. & KESHAVJEE, S. 2003. Ischemia–Reperfusion–induced Lung Injury. *American Journal of Respiratory and Critical Care Medicine,* 167**,** 490-511.

DEN HENGST, W. A., GIELIS, J. F., LIN, J. Y., VAN SCHIL, P. E., DE WINDT, L. J. & MOENS, A. L. 2010. Lung ischemia-reperfusion injury: a molecular and clinical view on a complex pathophysiological process. *American Journal of Physiology-Heart and Circulatory Physiology,* 299**,** H1283-H1299.

DRAGOMIR, E., MANDUTEANU, I., VOINEA, M., COSTACHE, G., MANEA, A. & SIMIONESCU, M. 2004. Aspirin rectifies calcium homeostasis, decreases reactive oxygen species, and increases NO production in high glucose-exposed human endothelial cells. *J Diabetes Complications,* 18**,** 289-99.

DU, J., ZENG, C., LI, Q., CHEN, B., LIU, H., HUANG, X. & HUANG, Q. 2012. LPS and TNF-α induce expression of sphingosine-1-phosphate receptor-2 in human microvascular endothelial cells. *Pathology - Research and Practice,* 208**,** 82-88.

DUDEK, S. M. & GARCIA, J. G. N. 2001. Cytoskeletal regulation of pulmonary vascular permeability. *Journal of Applied Physiology,* 91**,** 1487-1500.

DUDEK, S. M., JACOBSON, J. R., CHIANG, E. T., BIRUKOV, K. G., WANG, P., ZHAN, X. & GARCIA, J. G. 2004. Pulmonary endothelial cell barrier enhancement by sphingosine 1-phosphate: roles for cortactin and myosin light chain kinase. *J Biol Chem,* 279**,** 24692-700.

DUILIO, C., AMBROSIO, G., KUPPUSAMY, P., DIPAULA, A., BECKER, L. C. & ZWEIER, J. L. 2001. Neutrophils are primary source of O2 radicals during reperfusion after prolonged myocardial ischemia. *Am J Physiol Heart Circ Physiol,* 280**,** H2649-57.

ECKENHOFF, R. G., DODIA, C., TAN, Z. & FISHER, A. B. 1992. Oxygen-dependent reperfusion injury in the isolated rat lung. *J Appl Physiol (1985),* 72**,** 1454-60.

EHRSAM, J. P., CHEN, J., RODRIGUEZ CETINA BIEFER, H., OPITZ, I., ARNI, S. & INCI, I. 2022. Ex Vivo Lung Perfusion with β-Nicotinamide Adenine Dinucleotide (NAD(+)) Improves Ischemic Lung Function. *Antioxidants (Basel),* 11.

ELICEIRI, B. P., PAUL, R., SCHWARTZBERG, P. L., HOOD, J. D., LENG, J. & CHERESH, D. A. 1999. Selective requirement for Src kinases during VEGF-induced angiogenesis and vascular permeability. *Mol Cell,* 4**,** 915-24.

EPPINGER, M. J., DEEB, G. M., BOLLING, S. F. & WARD, P. A. 1997. Mediators of ischemia-reperfusion injury of rat lung. *Am J Pathol,* 150**,** 1773-84.

ERASMUS, M. E., FERNHOUT, M. H., ELSTRODT, J. M. & RAKHORST, G. 2006. Normothermic ex vivo lung perfusion of non-heart-beating donor lungs in pigs: from pretransplant function analysis towards a 6-h machine preservation. *Transpl Int,* 19**,** 589-93.

EREN, E., BLACK, S. M., READER, B. F., BEAL, E., CUDDINGTON, C., BELCHER, D. A., PALMER, A. F. & WHITSON, B. A. 2023. Novel Polymerized Human Serum Albumin For Ex Vivo Lung Perfusion. *Asaio j*.

ESSELTINE, J. L. & LAIRD, D. W. 2016. Next-Generation Connexin and Pannexin Cell Biology. *Trends Cell Biol,* 26**,** 944-955.

FAN, X., LIU, L., SHI, Y., GUO, F., HE, X., ZHAO, X., ZHONG, D. & LI, G. 2021. Recent advances of the function of sphingosine 1-phosphate (S1P) receptor S1P3. *Journal of Cellular Physiology,* 236**,** 1564-1578.

FARQUHAR, M. G. & PALADE, G. E. 1963. Junctional complexes in various epithelia. *J Cell Biol,* 17**,** 375-412.

FAY, J., VAROGA, D., WRUCK, C. J., KURZ, B., GOLDRING, M. B. & PUFE, T. 2006. Reactive oxygen species induce expression of vascular endothelial growth factor in chondrocytes and human articular cartilage explants. *Arthritis Research & Therapy,* 8**,** R189.

FERDINAND, J. R., MORRISON, M. I., ANDREASSON, A., CHARLTON, C., CHHATWAL, A. K., SCOTT, W. E., 3RD, BORTHWICK, L. A., CLATWORTHY, M. R. & FISHER, A. J. 2022. Transcriptional analysis identifies potential novel biomarkers associated with successful ex-vivo perfusion of human donor lungs. *Clin Transplant,* 36**,** e14570.

FERRARI, R. S. & ANDRADE, C. F. 2015. Oxidative Stress and Lung Ischemia-Reperfusion Injury. *Oxid Med Cell Longev,* 2015**,** 590987.

FISHER, A., ANDREASSON, A., CHRYSOS, A., LALLY, J., MAMASOULA, C., EXLEY, C., WILKINSON, J., QIAN, J., WATSON, G., LEWINGTON, O., CHADWICK, T., MCCOLL, E., PEARCE, M., MANN, K., MCMEEKIN, N., VALE, L., TSUI, S., YONAN, N., SIMON, A., MARCZIN, N., MASCARO, J. & DARK, J. 2016. An observational study of Donor Ex Vivo Lung Perfusion in UK lung transplantation: DEVELOP-UK. *Health Technol Assess,* 20**,** 1-276.

FORGIE, K. A., FIALKA, N., FREED, D. H. & NAGENDRAN, J. 2021. Lung Transplantation, Pulmonary Endothelial Inflammation, and Ex-Situ Lung Perfusion: A Review. *Cells,* 10.

FÖRSTERMANN, U. & MÜNZEL, T. 2006. Endothelial nitric oxide synthase in vascular disease: from marvel to menace. *Circulation,* 113**,** 1708-14.

FRANCIOLI, C., WANG, X., PARAPANOV, R., ABDELNOUR, E., LUGRIN, J., GRONCHI, F., PERENTES, J., ECKERT, P., RIS, H. B., PIQUILLOUD, L., KRUEGER, T. & LIAUDET, L. 2017. Pyrrolidine dithiocarbamate administered during ex-vivo lung perfusion promotes rehabilitation of injured donor rat lungs obtained after prolonged warm ischemia. *PLoS One,* 12**,** e0173916.

FUMARULO, R., CONESE, M., RICCARDI, S., GIORDANO, D., MONTEMURRO, P., COLUCCI, M. & SEMERARO, N. 1991. Retinoids inhibit the respiratory burst and degranulation of stimulated human polymorphonuclear leukocytes. *Agents Actions,* 34**,** 339-44.

GAENGEL, K., NIAUDET, C., HAGIKURA, K., LAVIÑA, B., MUHL, L., HOFMANN, JENNIFER J., EBARASI, L., NYSTRÖM, S., RYMO, S., CHEN, LONG L., PANG, M.-F., JIN, Y., RASCHPERGER, E., ROSWALL, P., SCHULTE, D., BENEDITO, R., LARSSON, J., HELLSTRÖM, M., FUXE, J., UHLÉN, P., ADAMS, R., JAKOBSSON, L., MAJUMDAR, A., VESTWEBER, D., UV, A. & BETSHOLTZ, C. 2012. The Sphingosine-1-Phosphate Receptor S1PR1 Restricts Sprouting Angiogenesis by Regulating the Interplay between VE-Cadherin and VEGFR2. *Developmental Cell,* 23**,** 587-599.

GAIRE, B. P., SONG, M. R. & CHOI, J. W. 2018. Sphingosine 1-phosphate receptor subtype 3 (S1P(3)) contributes to brain injury after transient focal cerebral ischemia via modulating microglial activation and their M1 polarization. *J Neuroinflammation,* 15**,** 284.

GANE, J. & STOCKLEY, R. 2012. Mechanisms of neutrophil transmigration across the vascular endothelium in COPD. *Thorax,* 67**,** 553.

GARCIA, J. G., LIU, F., VERIN, A. D., BIRUKOVA, A., DECHERT, M. A., GERTHOFFER, W. T., BAMBERG, J. R. & ENGLISH, D. 2001. Sphingosine 1-phosphate promotes endothelial cell barrier integrity by Edg-dependent cytoskeletal rearrangement. *J Clin Invest,* 108**,** 689-701.

GBD CHRONIC RESPIRATORY DISEASE COLLABORATORS 2020. Prevalence and attributable health burden of chronic respiratory diseases, 1990-2017: a systematic analysis for the Global Burden of Disease Study 2017. *Lancet Respir Med,* 8**,** 585-596.

GHAFOURIFAR, P., SCHENK, U., KLEIN, S. D. & RICHTER, C. 1999. Mitochondrial nitric-oxide synthase stimulation causes cytochrome c release from isolated mitochondria. Evidence for intramitochondrial peroxynitrite formation. *J Biol Chem,* 274**,** 31185-8.

GIELIS, J. F., LIN, J. Y., WINGLER, K., VAN SCHIL, P. E., SCHMIDT, H. H. & MOENS, A. L. 2011. Pathogenetic role of eNOS uncoupling in cardiopulmonary disorders. *Free Radic Biol Med,* 50**,** 765-76.

GONZALEZ-CABRERA, P. J., JO, E., SANNA, M. G., BROWN, S., LEAF, N., MARSOLAIS, D., SCHAEFFER, M. T., CHAPMAN, J., CAMERON, M., GUERRERO, M., ROBERTS, E. & ROSEN, H. 2008. Full pharmacological efficacy of a novel S1P1 agonist that does not require S1P-like headgroup interactions. *Mol Pharmacol,* 74**,** 1308-18.

GOODEMOTE, K. A., MATTIE, M. E., BERGER, A. & SPIEGEL, S. 1995. Involvement of a pertussis toxin-sensitive G protein in the mitogenic signaling pathways of sphingosine 1-phosphate. *J Biol Chem,* 270**,** 10272-7.

GOTSCH, U., BORGES, E., BOSSE, R., BÖGGEMEYER, E., SIMON, M., MOSSMANN, H. & VESTWEBER, D. 1997. VE-cadherin antibody accelerates neutrophil recruitment in vivo. *J Cell Sci,* 110 (Pt 5)**,** 583-8.

GRIFFITHS, C., SCOTT, W. E., ALI, S. & FISHER, A. J. 2020. Maximising organs for donation: the potential for ex-situ normothermic machine perfusion. *Qjm*.

HAAM, S., LEE, J. G., PAIK, H. C., PARK, M. S. & LIM, B. J. 2018. Hydrogen gas inhalation during ex vivo lung perfusion of donor lungs recovered after cardiac death. *J Heart Lung Transplant,* 37**,** 1271-1278.

HAAM, S., NODA, K., PHILIPS, B. J., HARANO, T., SANCHEZ, P. G. & SHIGEMURA, N. 2020. Cyclosporin A Administration During Ex Vivo Lung Perfusion Preserves Lung Grafts in Rat Transplant Model. *Transplantation,* 104.

HALLIWELL, B. & GUTTERIDGE, J. M. 1990. Role of free radicals and catalytic metal ions in human disease: an overview. *Methods Enzymol,* 186**,** 1-85.

HÄNEL, P., ANDRÉANI, P. & GRÄLER, M. H. 2007. Erythrocytes store and release sphingosine 1-phosphate in blood. *Faseb j,* 21**,** 1202-9.

HARHAJ, N. S., FELINSKI, E. A., WOLPERT, E. B., SUNDSTROM, J. M., GARDNER, T. W. & ANTONETTI, D. A. 2006. VEGF activation of protein kinase C stimulates occludin phosphorylation and contributes to endothelial permeability. *Invest Ophthalmol Vis Sci,* 47**,** 5106-15.

HARTWIG, M. G., KLAPPER, J. A., POOLA, N., BANGA, A., SANCHEZ, P. G., MURALA, J. S. & POTENZIANO, J. L. 2022. A Randomized, Multicenter, Blinded Pilot Study Assessing the Effects of Gaseous Nitric Oxide in an Ex Vivo System of Human Lungs. *Pulm Ther***,** 1-13.

HASEGAWA, Y., SUZUKI, H., SOZEN, T., ROLLAND, W. & ZHANG, J. H. 2010. Activation of sphingosine 1-phosphate receptor-1 by FTY720 is neuroprotective after ischemic stroke in rats. *Stroke,* 41**,** 368-74.

HASHIMOTO, E., OGITA, T., NAKAOKA, T., MATSUOKA, R., TAKAO, A. & KIRA, Y. 1994. Rapid induction of vascular endothelial growth factor expression by transient ischemia in rat heart. *Am J Physiol,* 267**,** H1948-54.

HAWKSWORTH, J. S., GRAYBILL, J. C., BROWN, T. S., WALLACE, S. M., DAVIS, T. A., TADAKI, D. K. & ELSTER, E. A. 2012. Lymphocyte modulation with FTY720 improves hemorrhagic shock survival in swine. *PLoS One,* 7**,** e34224.

HELLENTHAL, K. E. M., BRABENEC, L. & WAGNER, N. M. 2022. Regulation and Dysregulation of Endothelial Permeability during Systemic Inflammation. *Cells,* 11.

HENDRIX, M. J., SEFTOR, E. A., MELTZER, P. S., GARDNER, L. M., HESS, A. R., KIRSCHMANN, D. A., SCHATTEMAN, G. C. & SEFTOR, R. E. 2001. Expression and functional significance of VE-cadherin in aggressive human melanoma cells: role in vasculogenic mimicry. *Proc Natl Acad Sci U S A,* 98**,** 8018-23.

HEO, J. Y. & IM, D. S. 2019. Pro-Inflammatory Role of S1P(3) in Macrophages. *Biomol Ther (Seoul),* 27**,** 373-380.

HERNÁNDEZ-RESÉNDIZ, S., MUÑOZ-VEGA, M., CONTRERAS, W. E., CRESPO-AVILAN, G. E., RODRIGUEZ-MONTESINOS, J., ARIAS-CARRIÓN, O., PÉREZ-MÉNDEZ, O., BOISVERT, W. A., PREISSNER, K. T. & CABRERA-FUENTES, H. A. 2018. Responses of Endothelial Cells Towards Ischemic Conditioning Following Acute Myocardial Infarction. *Cond Med,* 1**,** 247-258.

HIJIYA, K., CHEN-YOSHIKAWA, T. F., KONDO, T., MOTOYAMA, H., OHSUMI, A., NAKAJIMA, D., SAKAMOTO, J., OHATA, K., TAKAHASHI, M., TANAKA, S., MIYAMOTO, E., AOYAMA, A. & DATE, H. 2017. Bronchodilator Inhalation During Ex Vivo Lung Perfusion Improves Posttransplant Graft Function After Warm Ischemia. *The Annals of Thoracic Surgery,* 103**,** 447-453.

HILLYARD, R., ANDERSON, J. & RAJ, J. U. 1991. Effect of edema on segmental vascular resistance in isolated perfused rat lungs. *Lung,* 169**,** 97-108.

HOGG, N., DARLEY-USMAR, V. M., WILSON, M. T. & MONCADA, S. 1992. Production of hydroxyl radicals from the simultaneous generation of superoxide and nitric oxide. *Biochem J,* 281 (Pt 2)**,** 419-24.

HU, Y., YANG, C., SHEN, G., YANG, S., CHENG, X., CHENG, F., RAO, J. & WANG, X. 2019. Hyperglycemia-Triggered Sphingosine-1-Phosphate and Sphingosine-1-Phosphate Receptor 3 Signaling Worsens Liver Ischemia/Reperfusion Injury by Regulating M1/M2 Polarization. *Liver Transpl,* 25**,** 1074-1090.

IGARASHI, J., MIYOSHI, M., HASHIMOTO, T., KUBOTA, Y. & KOSAKA, H. 2007. Hydrogen peroxide induces S1P1 receptors and sensitizes vascular endothelial cells to sphingosine 1-phosphate, a platelet-derived lipid mediator. *Am J Physiol Cell Physiol,* 292**,** C740-8.

ISKENDER, I., CYPEL, M., MARTINU, T., CHEN, M., SAKAMOTO, J., KIM, H., YU, K., LIN, H., GUAN, Z., HASHIMOTO, K., WADDELL, T. K., LIU, M. & KESHAVJEE, S. 2018. Effects of Warm Versus Cold Ischemic Donor Lung Preservation on the Underlying Mechanisms of Injuries During Ischemia and Reperfusion. *Transplantation,* 102.

ITO, S., IWAKI, S., KOIKE, K., YUDA, Y., NAGASAKI, A., OHKAWA, R., YATOMI, Y., FURUMOTO, T., TSUTSUI, H., SOBEL, B. E. & FUJII, S. 2013. Increased plasma sphingosine-1-phosphate in obese individuals and its capacity to increase the expression of plasminogen activator inhibitor-1 in adipocytes. *Coron Artery Dis,* 24**,** 642-50.

ITO, T., KURIYAMA, N., KATO, H., MATSUDA, A., MIZUNO, S., USUI, M., SAKURAI, H. & ISAJI, S. 2018. Sinusoidal protection by sphingosine-1-phosphate receptor 1 agonist in liver ischemia-reperfusion injury. *Journal of Surgical Research,* 222**,** 139-152.

JIANG, H., SHEN, S. M., YIN, J., ZHANG, P. P. & SHI, Y. 2017. Sphingosine 1-phosphate receptor 1 (S1PR1) agonist CYM5442 inhibits expression of intracellular adhesion molecule 1 (ICAM1) in endothelial cells infected with influenza A viruses. *PLoS One,* 12**,** e0175188.

JIN, F., HAGEMANN, N., SUN, L., WU, J., DOEPPNER, T. R., DAI, Y. & HERMANN, D. M. 2018. High-density lipoprotein (HDL) promotes angiogenesis via S1P3-dependent VEGFR2 activation. *Angiogenesis,* 21**,** 381-394.

JOBS, A., SCHMIDT, K., SCHMIDT, V. J., LÜBKEMEIER, I., VEEN, T. A. B. V., KURTZ, A., WILLECKE, K. & WIT, C. D. 2012. Defective Cx40 maintains Cx37 expression but intact Cx40 is crucial for conducted dilations irrespective of hypertension. *Hypertension***,** 1422-1429.

JOHNSON, E. R. & MATTHAY, M. A. 2010. Acute lung injury: epidemiology, pathogenesis, and treatment. *J Aerosol Med Pulm Drug Deliv,* 23**,** 243-52.

JUNG, B., OBINATA, H., GALVANI, S., MENDELSON, K., DING, B. S., SKOURA, A., KINZEL, B., BRINKMANN, V., RAFII, S., EVANS, T. & HLA, T. 2012. Flow-regulated endothelial S1P receptor-1 signaling sustains vascular development. *Dev Cell,* 23**,** 600-10.

KAKISHITA, T., OTO, T., HORI, S., MIYOSHI, K., OTANI, S., YAMAMOTO, S., WAKI, N., YOSHIDA, O., OKAZAKI, M., YAMANE, M., TOYOOKA, S., SANO, Y. & MIYOSHI, S. 2010. Suppression of Inflammatory Cytokines During Ex Vivo Lung Perfusion With an Adsorbent Membrane. *The Annals of Thoracic Surgery,* 89**,** 1773-1779.

KALKA, K., KELDENICH, Z., CARSTENS, H., HILKEN, G., OLBERTZ, C., PIZANIS, N., KAMLER, M., REINER, G. & KOCH, A. 2020. Porcine slaughterhouse lungs for ex vivo lung perfusion - a pilot project. *Am J Transl Res,* 12**,** 6455-6463.

KALOGERIS, T., BAO, Y. & KORTHUIS, R. J. 2014. Mitochondrial reactive oxygen species: a double edged sword in ischemia/reperfusion vs preconditioning. *Redox Biol,* 2**,** 702-14.

KANDASAMY, K., ESCUE, R., MANNA, J., ADEBIYI, A. & PARTHASARATHI, K. 2015. Changes in endothelial connexin 43 expression inversely correlate with microvessel permeability and VE-cadherin expression in endotoxin-challenged lungs. *American Journal of Physiology-Lung Cellular and Molecular Physiology,* 309**,** L584-L592.

KANEDA, H., WADDELL, T. K., LIU, M. & KESHAVJEE, S. 2005. Dynamic changes in cytokine gene expression during cold ischemia predicts outcome after lung transplantation in humans. *The Journal of Heart and Lung Transplantation,* 24**,** S79.

KARAKURUM, M., SHREENIWAS, R., CHEN, J., PINSKY, D., YAN, S. D., ANDERSON, M., SUNOUCHI, K., MAJOR, J., HAMILTON, T., KUWABARA, K., ROT, A., NOWYGROD, R. & STERN, D. 1994. Hypoxic induction of interleukin-8 gene expression in human endothelial cells. *J Clin Invest,* 93**,** 1564-70.

KENNEDY, T. P., RAO, N. V., HOPKINS, C., PENNINGTON, L., TOLLEY, E. & HOIDAL, J. R. 1989. Role of reactive oxygen species in reperfusion injury of the rabbit lung. *The Journal of clinical investigation,* 83**,** 1326-1335.

KEPKA-LENHART, D., CHEN, L.-C. & MORRIS JR., S. M. 1996. Novel actions of aspirin and sodium salicylate: discordant effects on nitric oxide synthesis and induction of nitric oxide synthase mRNA in a murine macrophage cell line. *Journal of Leukocyte Biology,* 59**,** 840-846.

KHATRI, B. O. 2016. Fingolimod in the treatment of relapsing-remitting multiple sclerosis: long-term experience and an update on the clinical evidence. *Ther Adv Neurol Disord,* 9**,** 130-47.

KIM, J.-L., READER, B. F., DUMOND, C., LEE, Y., MOKADAM, N. A., BLACK, S. M. & WHITSON, B. A. 2021. Pegylated-Catalase Is Protective in Lung Ischemic Injury and Oxidative Stress. *The Annals of Thoracic Surgery,* 111**,** 1019-1027.

KIM, S., BIELAWSKI, J., YANG, H., KONG, Y., ZHOU, B. & LI, J. 2018. Functional antagonism of sphingosine-1-phosphate receptor 1 prevents cuprizone-induced demyelination. *Glia,* 66**,** 654-669.

KIMURA, A., OHMORI, T., KASHIWAKURA, Y., OHKAWA, R., MADOIWA, S., MIMURO, J., SHIMAZAKI, K., HOSHINO, Y., YATOMI, Y. & SAKATA, Y. 2008. Antagonism of sphingosine 1-phosphate receptor-2 enhances migration of neural progenitor cells toward an area of brain. *Stroke,* 39**,** 3411-7.

KINOSHITA, K., YOO, B. S., NOZAKI, Y., SUGIYAMA, M., IKOMA, S., OHNO, M., FUNAUCHI, M. & KANAMARU, A. 2003. Retinoic acid reduces autoimmune renal injury and increases survival in NZB/W F1 mice. *J Immunol,* 170**,** 5793-8.

KNAPP, M., BARANOWSKI, M., CZARNOWSKI, D., LISOWSKA, A., ZABIELSKI, P., GÓRSKI, J. & MUSIAŁ, W. 2009. Plasma sphingosine-1-phosphate concentration is reduced in patients with myocardial infarction. *Med Sci Monit,* 15**,** Cr490-3.

KOPP, E. & GHOSH, S. 1994. Inhibition of NF-kappa B by sodium salicylate and aspirin. *Science,* 265**,** 956-9.

KOSAKA, R., SAKOTA, D., SAKANOUE, I., NIIKAWA, H., OHUCHI, K., ARAI, H., MCCURRY, K. R. & OKAMOTO, T. 2022. Real-time Lung Weight Measurement During Cellular Ex Vivo Lung Perfusion: An Early Predictor of Transplant Suitability. *Transplantation*.

KOTO, T., TAKUBO, K., ISHIDA, S., SHINODA, H., INOUE, M., TSUBOTA, K., OKADA, Y. & IKEDA, E. 2007. Hypoxia disrupts the barrier function of neural blood vessels through changes in the expression of claudin-5 in endothelial cells. *Am J Pathol,* 170**,** 1389-97.

KRISHNADASAN, B., NAIDU, B. V., BYRNE, K., FRAGA, C., VERRIER, E. D. & MULLIGAN, M. S. 2003. The role of proinflammatory cytokines in lung ischemia-reperfusion injury. *J Thorac Cardiovasc Surg,* 125**,** 261-72.

KRUTSINGER, D., REED, R. M., BLEVINS, A., PURI, V., DE OLIVEIRA, N. C., ZYCH, B., BOLUKBAS, S., VAN RAEMDONCK, D., SNELL, G. I. & EBERLEIN, M. 2015. Lung transplantation from donation after cardiocirculatory death: a systematic review and meta-analysis. *J Heart Lung Transplant,* 34**,** 675-84.

KSIĄŻEK, M., CHACIŃSKA, M., CHABOWSKI, A. & BARANOWSKI, M. 2015. Sources, metabolism, and regulation of circulating sphingosine-1-phosphate. *J Lipid Res,* 56**,** 1271-81.

KUROKI, M., VOEST, E. E., AMANO, S., BEEREPOOT, L. V., TAKASHIMA, S., TOLENTINO, M., KIM, R. Y., ROHAN, R. M., COLBY, K. A., YEO, K. T. & ADAMIS, A. P. 1996. Reactive oxygen intermediates increase vascular endothelial growth factor expression in vitro and in vivo. *J Clin Invest,* 98**,** 1667-75.

LAKSHMINARAYANAN, V., BENO, D. W. A., COSTA, R. H. & ROEBUCK, K. A. 1997. Differential Regulation of Interleukin-8 and Intercellular Adhesion Molecule-1 by H2O2 and Tumor Necrosis Factor-α in Endothelial and Epithelial Cells*. *Journal of Biological Chemistry,* 272**,** 32910-32918.

LAUBACH, V. E. & SHARMA, A. K. 2016. Mechanisms of lung ischemia-reperfusion injury. *Curr Opin Organ Transplant,* 21**,** 246-52.

LEE, D. B. N., JAMGOTCHIAN, N., ALLEN, S. G., ABELES, M. B. & WARD, H. J. 2008. A lipid-protein hybrid model for tight junction. *American Journal of Physiology-Renal Physiology,* 295**,** F1601-F1612.

LEE, J. F., GORDON, S., ESTRADA, R., WANG, L., SIOW, D. L., WATTENBERG, B. W., LOMINADZE, D. & LEE, M. J. 2009. Balance of S1P1 and S1P2 signaling regulates peripheral microvascular permeability in rat cremaster muscle vasculature. *Am J Physiol Heart Circ Physiol,* 296**,** H33-42.

LEE, J. F., ZENG, Q., OZAKI, H., WANG, L., HAND, A. R., HLA, T., WANG, E. & LEE, M. J. 2006. Dual roles of tight junction-associated protein, zonula occludens-1, in sphingosine 1-phosphate-mediated endothelial chemotaxis and barrier integrity. *J Biol Chem,* 281**,** 29190-200.

LEE, M. J., THANGADA, S., CLAFFEY, K. P., ANCELLIN, N., LIU, C. H., KLUK, M., VOLPI, M., SHA'AFI, R. I. & HLA, T. 1999. Vascular endothelial cell adherens junction assembly and morphogenesis induced by sphingosine-1-phosphate. *Cell,* 99**,** 301-12.

LEE, M. J., VAN BROCKLYN, J. R., THANGADA, S., LIU, C. H., HAND, A. R., MENZELEEV, R., SPIEGEL, S. & HLA, T. 1998. Sphingosine-1-phosphate as a ligand for the G protein-coupled receptor EDG-1. *Science,* 279**,** 1552-5.

LEE, S. Y., KIM, D. H., SUNG, S. A., KIM, M. G., CHO, W. Y., KIM, H. K. & JO, S. K. 2011. Sphingosine-1-phosphate reduces hepatic ischaemia/reperfusion-induced acute kidney injury through attenuation of endothelial injury in mice. *Nephrology (Carlton),* 16**,** 163-73.

LEVITT, D. G. & LEVITT, M. D. 2016. Human serum albumin homeostasis: a new look at the roles of synthesis, catabolism, renal and gastrointestinal excretion, and the clinical value of serum albumin measurements. *Int J Gen Med,* 9**,** 229-55.

LI, C., KONG, Y., WANG, H., WANG, S., YU, H., LIU, X., YANG, L., JIANG, X., LI, L. & LI, L. 2009. Homing of bone marrow mesenchymal stem cells mediated by sphingosine 1-phosphate contributes to liver fibrosis. *Journal of Hepatology,* 50**,** 1174-1183.

LI, Q., CHEN, B., ZENG, C., FAN, A., YUAN, Y., GUO, X., HUANG, X. & HUANG, Q. 2015. Differential activation of receptors and signal pathways upon stimulation by different doses of sphingosine-1-phosphate in endothelial cells. *Experimental Physiology,* 100**,** 95-107.

LIN, H., CHEN, M., TIAN, F., TIKKANEN, J., DING, L., ANDREW CHEUNG, H. Y., NAKAJIMA, D., WANG, Z., MARISCAL, A., HWANG, D., CYPEL, M., KESHAVJEE, S. & LIU, M. 2018. Anti-trypsin improves function of porcine donor lungs during ex-vivo lung perfusion. *The Journal of Heart and Lung Transplantation,* 37**,** 656-666.

LIU, F., VERIN, A. D., WANG, P., DAY, R., WERSTO, R. P., CHREST, F. J., ENGLISH, D. K. & GARCIA, J. G. 2001. Differential regulation of sphingosine-1-phosphate- and VEGF-induced endothelial cell chemotaxis. Involvement of G(ialpha2)-linked Rho kinase activity. *Am J Respir Cell Mol Biol,* 24**,** 711-9.

LIU, H. B., CUI, N. Q., WANG, Q., LI, D. H. & XUE, X. P. 2008. Sphingosine-1-phosphate and its analogue FTY720 diminish acute pulmonary injury in rats with acute necrotizing pancreatitis. *Pancreas,* 36**,** e10-5.

LIU, W., LAN, T., XIE, X., HUANG, K., PENG, J., HUANG, J., SHEN, X., LIU, P. & HUANG, H. 2012. S1P2 receptor mediates sphingosine-1-phosphate-induced fibronectin expression via MAPK signaling pathway in mesangial cells under high glucose condition. *Exp Cell Res,* 318**,** 936-43.

LIU, Y., COX, S. R., MORITA, T. & KOUREMBANAS, S. 1995. Hypoxia regulates vascular endothelial growth factor gene expression in endothelial cells. Identification of a 5' enhancer. *Circ Res,* 77**,** 638-43.

LIU, Y., WADA, R., YAMASHITA, T., MI, Y., DENG, C. X., HOBSON, J. P., ROSENFELDT, H. M., NAVA, V. E., CHAE, S. S., LEE, M. J., LIU, C. H., HLA, T., SPIEGEL, S. & PROIA, R. L. 2000. Edg-1, the G protein-coupled receptor for sphingosine-1-phosphate, is essential for vascular maturation. *J Clin Invest,* 106**,** 951-61.

LIU, Y., ZHAO, J., LU, M., WANG, H. & TANG, F. 2020. Retinoic acid attenuates cardiac injury induced by hyperglycemia in pre- and post-delivery mice. *Can J Physiol Pharmacol,* 98**,** 6-14.

LOBODA, A., JAZWA, A., JOZKOWICZ, A., MOLEMA, G. & DULAK, J. 2006. Angiogenic transcriptome of human microvascular endothelial cells: Effect of hypoxia, modulation by atorvastatin. *Vascul Pharmacol,* 44**,** 206-14.

LONATI, C., BASSANI, G. A., BRAMBILLA, D., LEONARDI, P., CARLIN, A., FAVERSANI, A., GATTI, S. & VALENZA, F. 2018. Influence of ex vivo perfusion on the biomolecular profile of rat lungs. *The FASEB Journal,* 32**,** 5532-5549.

LONATI, C., BASSANI, G. A., BRAMBILLA, D., LEONARDI, P., CARLIN, A., MAGGIONI, M., ZANELLA, A., DONDOSSOLA, D., FONSATO, V., GRANGE, C., CAMUSSI, G. & GATTI, S. 2019. Mesenchymal stem cell–derived extracellular vesicles improve the molecular phenotype of isolated rat lungs during ischemia/reperfusion injury. *The Journal of Heart and Lung Transplantation,* 38**,** 1306-1316.

LONATI, C., BATTISTIN, M., DONDOSSOLA, D. E., BASSANI, G. A., BRAMBILLA, D., MERIGHI, R., LEONARDI, P., CARLIN, A., MERONI, M., ZANELLA, A., CATANIA, A. & GATTI, S. 2021. NDP-MSH treatment recovers marginal lungs during ex vivo lung perfusion (EVLP). *Peptides,* 141**,** 170552.

LOOR, G., WARNECKE, G., VILLAVICENCIO, M. A., SMITH, M. A., KUKREJA, J., ARDEHALI, A., HARTWIG, M., DANESHMAND, M. A., HERTZ, M. I., HUDDLESTON, S., HAVERICH, A., MADSEN, J. C. & VAN RAEMDONCK, D. 2019. Portable normothermic ex-vivo lung perfusion, ventilation, and functional assessment with the Organ Care System on donor lung use for transplantation from extended-criteria donors (EXPAND): a single-arm, pivotal trial. *Lancet Respir Med,* 7**,** 975-984.

LYNCH, M. J., GRUM, C. M., GALLAGHER, K. P., BOLLING, S. F., DEEB, G. M. & MORGANROTH, M. L. 1988. Xanthine oxidase inhibition attenuates ischemic-reperfusion lung injury. *Journal of Surgical Research,* 44**,** 538-544.

MACHUCA, T. N. & CYPEL, M. 2014. Ex vivo lung perfusion. *J Thorac Dis,* 6**,** 1054-62.

MACHUCA, T. N., CYPEL, M., BONATO, R., YEUNG, J. C., CHUN, Y. M., JUVET, S., GUAN, Z., HWANG, D. M., CHEN, M., SAITO, T., HARMANTAS, C., DAVIDSON, B. L., WADDELL, T. K., LIU, M. & KESHAVJEE, S. 2017. Safety and Efficacy of Ex Vivo Donor Lung Adenoviral IL-10 Gene Therapy in a Large Animal Lung Transplant Survival Model. *Hum Gene Ther,* 28**,** 757-765.

MACHUCA, T. N., CYPEL, M., YEUNG, J. C., BONATO, R., ZAMEL, R., CHEN, M., AZAD, S., HSIN, M. K., SAITO, T., GUAN, Z., WADDELL, T. K., LIU, M. & KESHAVJEE, S. 2015. Protein Expression Profiling Predicts Graft Performance in Clinical Ex Vivo Lung Perfusion. *Annals of Surgery,* 261.

MAGRUDER, J. T., GRIMM, J. C., CRAWFORD, T. C., JOHNSTON, L., SANTHANAM, L., STEPHENS, R. S., BERKOWITZ, D. E., SHAH, A. S., BUSH, E. L., DAMARLA, M., DAMICO, R. L., HASSOUN, P. M. & KIM, B. S. 2018. Imatinib Is Protective Against Ischemia-Reperfusion Injury in an Ex Vivo Rabbit Model of Lung Injury. *Ann Thorac Surg,* 105**,** 950-956.

MANEVICH, Y., AL-MEHDI, A., MUZYKANTOV, V. & FISHER, A. B. 2001. Oxidative burst and NO generation as initial response to ischemia in flow-adapted endothelial cells. *American Journal of Physiology-Heart and Circulatory Physiology,* 280**,** H2126-H2135.

MARTENS, A., BOADA, M., VANAUDENAERDE, B. M., VERLEDEN, S. E., VOS, R., VERLEDEN, G. M., VERBEKEN, E. K., VAN RAEMDONCK, D., SCHOLS, D., CLAES, S. & NEYRINCK, A. P. 2016. Steroids can reduce warm ischemic reperfusion injury in a porcine donation after circulatory death model with ex vivo lung perfusion evaluation. *Transpl Int,* 29**,** 1237-1246.

MARTENS, A., ORDIES, S., VANAUDENAERDE, B. M., VERLEDEN, S. E., VOS, R., VAN RAEMDONCK, D. E., VERLEDEN, G. M., ROOBROUCK, V. D., CLAES, S., SCHOLS, D., VERBEKEN, E., VERFAILLIE, C. M. & NEYRINCK, A. P. 2017. Immunoregulatory effects of multipotent adult progenitor cells in a porcine ex vivo lung perfusion model. *Stem Cell Research & Therapy,* 8**,** 159.

MCVERRY, B. J., PENG, X., HASSOUN, P. M., SAMMANI, S., SIMON, B. A. & GARCIA, J. G. 2004. Sphingosine 1-phosphate reduces vascular leak in murine and canine models of acute lung injury. *Am J Respir Crit Care Med,* 170**,** 987-93.

MEENS, M. J., ALONSO, F., GAL, L. L., KWAK, B. R. & HAEFLIGER, J. A. 2015. Endothelial connexin37 and connexin40 participate in basal but not agonist-induced NO release. *Cell Communication and Signaling***,** 34.

MEHAFFEY, J. H., CHARLES, E. J., NARAHARI, A. K., SCHUBERT, S., LAUBACH, V. E., TEMAN, N. R., LYNCH, K. R., KRON, I. L. & SHARMA, A. K. 2018. Increasing circulating sphingosine-1-phosphate attenuates lung injury during ex vivo lung perfusion. *J Thorac Cardiovasc Surg,* 156**,** 910-917.

MEHTA, D. & MALIK, A. B. 2006. Signaling Mechanisms Regulating Endothelial Permeability. *Physiological Reviews,* 86**,** 279-367.

MONAGHAN-BENSON, E. & BURRIDGE, K. 2009. The regulation of vascular endothelial growth factor-induced microvascular permeability requires Rac and reactive oxygen species. *J Biol Chem,* 284**,** 25602-11.

MOON, E., HAN, J. E., JEON, S., RYU, J. H., CHOI, J. W. & CHUN, J. 2015. Exogenous S1P Exposure Potentiates Ischemic Stroke Damage That Is Reduced Possibly by Inhibiting S1P Receptor Signaling. *Mediators Inflamm,* 2015**,** 492659.

MOREL, S., CHRISTOFFERSEN, C., AXELSEN, L. N., MONTECUCCO, F., ROCHEMONT, V., FRIAS, M. A., MACH, F., JAMES, R. W., NAUS, C. C., CHANSON, M., LAMPE, P. D., NIELSEN, M. S., NIELSEN, L. B. & KWAK, B. R. 2016. Sphingosine-1-phosphate reduces ischaemia-reperfusion injury by phosphorylating the gap junction protein Connexin43. *Cardiovasc Res,* 109**,** 385-96.

MORENO, P., ALVAREZ, A., SANTOS, F., VAQUERO, J. M., BAAMONDE, C., REDEL, J., CEREZO, F., ALGAR, F. J. & SALVATIERRA, A. 2014. Extended recipients but not extended donors are associated with poor outcomes following lung transplantation†. *European Journal of Cardio-Thoracic Surgery,* 45**,** 1040-1047.

MUKHOPADHYAY, D., TSIOKAS, L., ZHOU, X. M., FOSTER, D., BRUGGE, J. S. & SUKHATME, V. P. 1995. Hypoxic induction of human vascular endothelial growth factor expression through c-Src activation. *Nature,* 375**,** 577-81.

MÜLLER, H. C., HOCKE, A. C., HELLWIG, K., GUTBIER, B., PETERS, H., SCHÖNROCK, S. M., TSCHERNIG, T., SCHMIEDL, A., HIPPENSTIEL, S., N'GUESSAN, P. D., ROSSEAU, S., SUTTORP, N. & WITZENRATH, M. 2011. The Sphingosine-1 Phosphate receptor agonist FTY720 dose dependently affected endothelial integrity in vitro and aggravated ventilator-induced lung injury in mice. *Pulm Pharmacol Ther,* 24**,** 377-85.

MULLIGAN, M. J., SANCHEZ, P. G., EVANS, C. F., WANG, Y., KON, Z. N., RAJAGOPAL, K., IACONO, A. T., GAMMIE, J. S., GRIFFITH, B. P. & PHAM, S. M. 2016. The use of extended criteria donors

decreases one-year survival in high-risk lung recipients: A review of the United Network of Organ Sharing Database. *J Thorac Cardiovasc Surg,* 152**,** 891-898.e2.

MULLOY, D. P., STONE, M. L., CROSBY, I. K., LAPAR, D. J., SHARMA, A. K., WEBB, D. V., LAU, C. L., LAUBACH, V. E. & KRON, I. L. 2012. Ex vivo rehabilitation of non-heart-beating donor lungs in preclinical porcine model: delayed perfusion results in superior lung function. *J Thorac Cardiovasc Surg,* 144**,** 1208-15.

MURAKAMI, M. & SIMONS, M. 2009. Regulation of vascular integrity. *J Mol Med (Berl),* 87**,** 571-82.

MUTHUSAMY, A., LIN, C. M., SHANMUGAM, S., LINDNER, H. M., ABCOUWER, S. F. & ANTONETTI, D. A. 2014. Ischemia-reperfusion injury induces occludin phosphorylation/ubiquitination and retinal vascular permeability in a VEGFR-2-dependent manner. *J Cereb Blood Flow Metab,* 34**,** 522-31.

NAGASAWA, K., CHIBA, H., FUJITA, H., KOJIMA, T., SAITO, T., ENDO, T. & SAWADA, N. 2006. Possible involvement of gap junctions in the barrier function of tight junctions of brain and lung endothelial cells. *J Cell Physiol,* 208**,** 123-32.

NAIDU, B. V., WOOLLEY, S. M., FARIVAR, A. S., THOMAS, R., FRAGA, C. H., GOSS, C. H. & MULLIGAN, M. S. 2004. Early tumor necrosis factor-alpha release from the pulmonary macrophage in lung ischemia-reperfusion injury. *J Thorac Cardiovasc Surg,* 127**,** 1502-8.

NAKAJIMA, D., WATANABE, Y., OHSUMI, A., PIPKIN, M., CHEN, M., MORDANT, P., KANOU, T., SAITO, T., LAM, R., COUTINHO, R., CALDARONE, L., JUVET, S., MARTINU, T., IYER, R. K., DAVIES, J. E., HWANG, D. M., WADDELL, T. K., CYPEL, M., LIU, M. & KESHAVJEE, S. 2019. Mesenchymal stromal cell therapy during ex vivo lung perfusion ameliorates ischemia-reperfusion injury in lung transplantation. *J Heart Lung Transplant,* 38**,** 1214-1223.

NASIR, B. S., LANDRY, C., MENAOUAR, A., GERMAIN, J.-F., DER SARKISSIAN, S., STEVENS, L.-M., ACEROS, H., CAILHIER, J.-F., LEDUC, C., LIBERMAN, M., NOISEUX, N. & FERRARO, P. 2020. HSP90 Inhibitor Improves Lung Protection in Porcine Model of Donation After Circulatory Arrest. *The Annals of Thoracic Surgery,* 110**,** 1861-1868.

NG, H. Y., LEE, K. A., KUO, C. N. & SHEN, Y. F. 2018. Bioprinting of artificial blood vessels. *Int J Bioprint,* 4**,** 140.

NHS BLOOD AND TRANSPLANT. 2022. *Annual activity report* [Online]. Available: https://www.odt.nhs.uk/statistics-and-reports/organ-specific-reports/ [Accessed 2023].

NOEL, J., WANG, H., HONG, N., TAO, J. Q., YU, K., SOROKINA, E. M., DEBOLT, K., HEAYN, M., RIZZO, V., DELISSER, H., FISHER, A. B. & CHATTERJEE, S. 2013. PECAM-1 and caveolae form the mechanosensing complex necessary for NOX2 activation and angiogenic signaling with stopped flow in pulmonary endothelium. *Am J Physiol Lung Cell Mol Physiol,* 305**,** L805-18.

NOZAKI, Y., YAMAGATA, T., SUGIYAMA, M., IKOMA, S., KINOSHITA, K. & FUNAUCHI, M. 2006. Anti-inflammatory effect of all-trans-retinoic acid in inflammatory arthritis. *Clinical Immunology,* 119**,** 272-279.

OBINATA, H. & HLA, T. 2019. Sphingosine 1-phosphate and inflammation. *International Immunology,* 31**,** 617-625.

OJO, A. O., HEINRICHS, D., EMOND, J. C., MCGOWAN, J. J., GUIDINGER, M. K., DELMONICO, F. L. & METZGER, R. A. 2004. Organ donation and utilization in the USA. *American Journal of Transplantation,* 4**,** 27-37.

OKAMOTO, H., TAKUWA, N., GONDA, K., OKAZAKI, H., CHANG, K., YATOMI, Y., SHIGEMATSU, H. & TAKUWA, Y. 1998. EDG1 Is a Functional Sphingosine-1-phosphate Receptor That Is Linked via a G_{i/o} to Multiple Signaling Pathways, Including Phospholipase C Activation, Ca²⁺Mobilization, Ras-Mitogen-activated Protein Kinase Activation, and Adenylate Cyclase Inhibition *. *Journal of Biological Chemistry,* 273**,** 27104-27110.

OKAMOTO, T. & SUZUKI, K. 2017. The Role of Gap Junction-Mediated Endothelial Cell-Cell Interaction in the Crosstalk between Inflammation and Blood Coagulation. *Int J Mol Sci,* 18.

OKAMOTO, T., WHEELER, D., LIU, Q., QUINTINI, C., HATA, J. S. & MCCURRY, K. R. 2016. Correlation between PaO2/FiO2 and airway and vascular parameters in the assessment of cellular ex vivo lung perfusion system. *The Journal of Heart and Lung Transplantation,* 35**,** 1330-1336.

OKAZAKI, M., KREISEL, F., RICHARDSON, S. B., KREISEL, D., KRUPNICK, A. S., PATTERSON, G. A. & GELMAN, A. E. 2007. Sphingosine 1-phosphate inhibits ischemia reperfusion injury following experimental lung transplantation. *Am J Transplant,* 7**,** 751-8.

OLBERTZ, C., PIZANIS, N., BÄUMKER, H., BECKER, S., AIGNER, C., RAUEN, U., NOLTE, I., KAMLER, M. & KOCH, A. 2019. Effects of immediate versus delayed ex-vivo lung perfusion in a porcine cardiac arrest donation model. *The International Journal of Artificial Organs,* 42**,** 362-369.

OLBERTZ, C., PIZANIS, N., BÄUMKER, H., KALKA, K., AIGNER, C., RAUEN, U., NOLTE, I., KAMLER, M. & KOCH, A. 2020. Use of modified Custodiol-N as perfusion solution in ex vivo lung perfusion. *Am J Transl Res,* 12**,** 153-161.

ORENS, J. B., BOEHLER, A., DE PERROT, M., ESTENNE, M., GLANVILLE, A. R., KESHAVJEE, S., KOTLOFF, R., MORTON, J., STUDER, S. M., VAN RAEMDONCK, D., WADDEL, T. & SNELL, G. I. 2003. A review of lung transplant donor acceptability criteria. *J Heart Lung Transplant,* 22**,** 1183-200.

ORFANOS, C. E. & BAUER, R. 1983. Evidence for anti-inflammatory activities of oral synthetic retinoids: experimental findings and clinical experience. *Br J Dermatol,* 109 Suppl 25**,** 55-60.

OVECHKIN, A. V., LOMINADZE, D., SEDORIS, K. C., ROBINSON, T. W., TYAGI, S. C. & ROBERTS, A. M. 2007. Lung ischemia-reperfusion injury: implications of oxidative stress and platelet-arteriolar wall interactions. *Arch Physiol Biochem,* 113**,** 1-12.

PACHER, P., BECKMAN, J. S. & LIAUDET, L. 2007. Nitric oxide and peroxynitrite in health and disease. *Physiol Rev,* 87**,** 315-424.

PAK, O., SYDYKOV, A., KOSANOVIC, D., SCHERMULY, R. T., DIETRICH, A., SCHRÖDER, K., BRANDES, R. P., GUDERMANN, T., SOMMER, N. & WEISSMANN, N. 2017. Lung Ischaemia–Reperfusion Injury: The Role of Reactive Oxygen Species. *In:* WANG, Y.-X. (ed.) *Pulmonary Vasculature Redox Signaling in Health and Disease.* Cham: Springer International Publishing.

PAN, X., YANG, J., FU, S. & ZHAO, H. 2018. Application of ex vivo lung perfusion (EVLP) in lung transplantation. *Journal of thoracic disease,* 10**,** 4637-4642.

PAPPU, R., SCHWAB, S. R., CORNELISSEN, I., PEREIRA, J. P., REGARD, J. B., XU, Y., CAMERER, E., ZHENG, Y.-W., HUANG, Y., CYSTER, J. G. & COUGHLIN, S. R. 2007. Promotion of Lymphocyte Egress into Blood and Lymph by Distinct Sources of Sphingosine-1-Phosphate. *Science,* 316**,** 295-298.

PARK, S. W., KIM, M., BROWN, K. M., D'AGATI, V. D. & LEE, H. T. 2012. Inhibition of sphingosine 1-phosphate receptor 2 protects against renal ischemia-reperfusion injury. *J Am Soc Nephrol,* 23**,** 266-80.

PASTEN, C., LOZANO, M., ROCCO, J., CARRIÓN, F., ALVARADO, C., LIBERONA, J., MICHEA, L. & IRARRÁZABAL, C. E. 2021. Aminoguanidine Prevents the Oxidative Stress, Inhibiting Elements of Inflammation, Endothelial Activation, Mesenchymal Markers, and Confers a Renoprotective Effect in Renal Ischemia and Reperfusion Injury. *Antioxidants (Basel),* 10.

PATTERSON, G. A., COOPER, J. D., DARK, J. H. & JONES, M. T. 1988. Experimental and clinical double lung transplantation. *J Thorac Cardiovasc Surg,* 95**,** 70-4.

PENG, X., HASSOUN, P. M., SAMMANI, S., MCVERRY, B. J., BURNE, M. J., RABB, H., PEARSE, D., TUDER, R. M. & GARCIA, J. G. 2004. Protective effects of sphingosine 1-phosphate in murine endotoxin-induced inflammatory lung injury. *Am J Respir Crit Care Med,* 169**,** 1245-51.

PERRY, H. M., HUANG, L., YE, H., LIU, C., SUNG, S. J., LYNCH, K. R., ROSIN, D. L., BAJWA, A. & OKUSA, M. D. 2016. Endothelial Sphingosine 1-Phosphate Receptor-1 Mediates Protection and Recovery from Acute Kidney Injury. *J Am Soc Nephrol,* 27**,** 3383-3393.

PIKE, M. M., LUO, C. S., CLARK, M. D., KIRK, K. A., KITAKAZE, M., MADDEN, M. C., CRAGOE, E. J., JR. & POHOST, G. M. 1993. NMR measurements of Na+ and cellular energy in ischemic rat heart: role of Na(+)-H+ exchange. *Am J Physiol,* 265**,** H2017-26.

PISAM, M. & RIPOCHE, P. 1976. Redistribution of surface macromolecules in dissociated epithelial cells. *J Cell Biol,* 71**,** 907-20.

PITHER, T., WANG, L., BATES, L., MORRISON, M., CHARLTON, C., GRIFFITHS, C., MACDONALD, J., BIGLEY, V., MAVRIDOU, M., BARSBY, J., BORTHWICK, L., DARK, J., SCOTT, W., 3RD, ALI, S. & FISHER, A. J. 2023. Modeling the Effects of IL-1β-mediated Inflammation During Ex Vivo Lung Perfusion Using a Split Human Donor Model. *Transplantation*.

PLATT, D. H., BARTOLI, M., EL-REMESSY, A. B., AL-SHABRAWEY, M., LEMTALSI, T., FULTON, D. & CALDWELL, R. B. 2005. Peroxynitrite increases VEGF expression in vascular endothelial cells via STAT3. *Free Radic Biol Med,* 39**,** 1353-61.

PORTEOUS, M. K., DIAMOND, J. M. & CHRISTIE, J. D. 2015. Primary graft dysfunction: lessons learned about the first 72 h after lung transplantation. *Curr Opin Organ Transplant,* 20**,** 506-14.

POTTER, M. D., BARBERO, S. & CHERESH, D. A. 2005. Tyrosine Phosphorylation of VE-cadherin Prevents Binding of p120- and β-Catenin and Maintains the Cellular Mesenchymal State*. *Journal of Biological Chemistry,* 280**,** 31906-31912.

PROIA, R. L. & HLA, T. 2015. Emerging biology of sphingosine-1-phosphate: its role in pathogenesis and therapy. *J Clin Invest,* 125**,** 1379-87.

RADI, R., BECKMAN, J. S., BUSH, K. M. & FREEMAN, B. A. 1991. Peroxynitrite oxidation of sulfhydryls. The cytotoxic potential of superoxide and nitric oxide. *J Biol Chem,* 266**,** 4244-50.

RAFA, H., BENKHELIFA, S., AITYOUNES, S., SAOULA, H., BELHADEF, S., BELKHELFA, M., BOUKERCHA, A., TOUMI, R., SOUFLI, I., MORALÈS, O., DE LAUNOIT, Y., MAHFOUF, H., NAKMOUCHE, M. H., DELHEM, N. & TOUIL-BOUKOFFA, C. 2017. All-Trans Retinoic Acid Modulates TLR4/NF-κB Signaling Pathway Targeting TNF-α and Nitric Oxide Synthase 2 Expression in Colonic Mucosa during Ulcerative Colitis and Colitis Associated Cancer. *Mediators of Inflammation,* 2017**,** 7353252.

RANDJELOVIC, P., VELJKOVIC, S., STOJILJKOVIC, N., JANKOVIC-VELICKOVIC, L., SOKOLOVIC, D., STOILJKOVIC, M. & ILIC, I. 2012. Salicylic acid attenuates gentamicin-induced nephrotoxicity in rats. *ScientificWorldJournal,* 2012**,** 390613.

RANSY, C., VAZ, C., LOMBÈS, A. & BOUILLAUD, F. 2020. Use of H(2)O(2) to Cause Oxidative Stress, the Catalase Issue. *Int J Mol Sci,* 21.

REGARD, J. B., SATO, I. T. & COUGHLIN, S. R. 2008. Anatomical profiling of G protein-coupled receptor expression. *Cell,* 135**,** 561-71.

RODRIGUES, S. F. & GRANGER, D. N. 2010. Role of blood cells in ischaemia–reperfusion induced endothelial barrier failure. *Cardiovascular Research,* 87**,** 291-299.

ROVIEZZO, F., BRANCALEONE, V., DE GRUTTOLA, L., VELLECCO, V., BUCCI, M., D'AGOSTINO, B., COOPER, D., SORRENTINO, R., PERRETTI, M. & CIRINO, G. 2011. Sphingosine-1-phosphate modulates vascular permeability and cell recruitment in acute inflammation in vivo. *J Pharmacol Exp Ther,* 337**,** 830-7.

RUIZ, M., FREJ, C., HOLMÉR, A., GUO, L. J., TRAN, S. & DAHLBÄCK, B. 2017. High-Density Lipoprotein–Associated Apolipoprotein M Limits Endothelial Inflammation by Delivering Sphingosine-1-Phosphate to the Sphingosine-1-Phosphate Receptor 1. *Arteriosclerosis, Thrombosis, and Vascular Biology,* 37**,** 118-129.

RYU, Y. S., LEE, J. H., SEOK, J. H., HONG, J. H., LEE, Y. S., LIM, J. H., KIM, Y. M. & HUR, G. M. 2000. Acetaminophen inhibits iNOS gene expression in RAW 264.7 macrophages: differential regulation of NF-kappaB by acetaminophen and salicylates. *Biochem Biophys Res Commun,* 272**,** 758-64.

SÁEZ, J. C., BERTHOUD, V. M., BRAÑES, M. C., MARTÍNEZ, A. D. & BEYER, E. C. 2003. Plasma Membrane Channels Formed by Connexins: Their Regulation and Functions. *Physiological Reviews,* 83**,** 1359-1400.

SAGONE, A. L., JR. & HUSNEY, R. M. 1987. Oxidation of salicylates by stimulated granulocytes: evidence that these drugs act as free radical scavengers in biological systems. *J Immunol,* 138**,** 2177-83.

SAMMANI, S., MORENO-VINASCO, L., MIRZAPOIAZOVA, T., SINGLETON, P. A., CHIANG, E. T., EVENOSKI, C. L., WANG, T., MATHEW, B., HUSAIN, A., MOITRA, J., SUN, X., NUNEZ, L., JACOBSON, J. R., DUDEK, S. M., NATARAJAN, V. & GARCIA, J. G. 2010. Differential effects of sphingosine 1-phosphate receptors on airway and vascular barrier function in the murine lung. *Am J Respir Cell Mol Biol,* 43**,** 394-402.

SANCHEZ, P. G., CHAN, E. G., DAVIS, R. D., HARTWIG, M., MACHUCA, T., WHITSON, B., DANESHMAND, M., OVIDIO, F. D., DCUNHA, J., WEYANT, M., JESSEN, M., BERMUDEZ, C., MULLIGAN, M., WOZNIAK, T., LYNCH, W., NEMEH, H., CALDEIRA, C., SONG, T., KREISEL, D., CAMP, P., RAMZY, D., GRIFFITH, B. & CANTU, E. 2022. Normothermic Ex Vivo Lung Perfusion (Novel) as an Assessment of Extended Criteria Donor Lungs: A Prospective Multi-Center Clinical Trial. *The Journal of Heart and Lung Transplantation,* 41**,** S40-S41.

SANCHEZ, T., SKOURA, A., WU, M. T., CASSERLY, B., HARRINGTON, E. O. & HLA, T. 2007. Induction of vascular permeability by the sphingosine-1-phosphate receptor-2 (S1P2R) and its downstream effectors ROCK and PTEN. *Arterioscler Thromb Vasc Biol,* 27**,** 1312-8.

SÁNCHEZ-CÁMARA, S., ASENSIO-LÓPEZ, M. C., ROYO-VILLANOVA, M., SOLER, F., JARA-RUBIO, R., GARRIDO-PEÑALVER, J. F., PINAR, E., HERNÁNDEZ-VICENTE, Á., HURTADO, J. A., LAX, A. & PASCUAL-FIGAL, D. A. 2022. Critical warm ischemia time point for cardiac donation after circulatory death. *American Journal of Transplantation,* 22**,** 1321-1328.

SANTIAGO, E., CONTRERAS, C., GARCÍA-SACRISTÁN, A., SÁNCHEZ, A., RIVERA, L., CLIMENT, B. & PRIETO, D. 2013. Signaling pathways involved in the H2O2-induced vasoconstriction of rat coronary arteries. *Free Radic Biol Med,* 60**,** 136-46.

SAYAH, D. M., MALLAVIA, B., LIU, F., ORTIZ-MUÑOZ, G., CAUDRILLIER, A., DERHOVANESSIAN, A., ROSS, D. J., LYNCH, J. P., 3RD, SAGGAR, R., ARDEHALI, A., WARE, L. B., CHRISTIE, J. D., BELPERIO, J. A. & LOONEY, M. R. 2015. Neutrophil extracellular traps are pathogenic in primary graft dysfunction after lung transplantation. *Am J Respir Crit Care Med,* 191**,** 455-63.

SCHAPHORST, K. L., CHIANG, E., JACOBS, K. N., ZAIMAN, A., NATARAJAN, V., WIGLEY, F. & GARCIA, J. G. 2003. Role of sphingosine-1 phosphate in the enhancement of endothelial barrier integrity by platelet-released products. *Am J Physiol Lung Cell Mol Physiol,* 285**,** L258-67.

SCHMIDT, V. J., WÖLFLE, S. E., BOETTCHER, M. & WIT, C. D. 2008. Gap junctions synchronize vascular tone within the microcirculation. *Pharmacological Reports***,** 68-74.

SCHWAB, S. R., PEREIRA, J. P., MATLOUBIAN, M., XU, Y., HUANG, Y. & CYSTER, J. G. 2005. Lymphocyte sequestration through S1P lyase inhibition and disruption of S1P gradients. *Science,* 309**,** 1735-9.

SCHWALM, S., DÖLL, F., RÖMER, I., BUBNOVA, S., PFEILSCHIFTER, J. & HUWILER, A. 2008. Sphingosine kinase-1 is a hypoxia-regulated gene that stimulates migration of human endothelial cells. *Biochemical and Biophysical Research Communications,* 368**,** 1020-1025.

SCOTTI, L., DI PIETRO, M., PASCUALI, N., IRUSTA, G., ZÚÑIGA, I. D., GOMEZ PEÑA, M., POMILIO, C., SARAVIA, F., TESONE, M., ABRAMOVICH, D. & PARBORELL, F. 2016. Sphingosine-1-phosphate restores endothelial barrier integrity in ovarian hyperstimulation syndrome. *Mol Hum Reprod,* 22**,** 852-866.

SHAVER, C. M., WICKERSHAM, N., MCNEIL, J. B., NAGATA, H., MILLER, A., LANDSTREET, S. R., KUCK, J. L., DIAMOND, J. M., LEDERER, D. J., KAWUT, S. M., PALMER, S. M., WILLE, K. M., WEINACKER, A., LAMA, V. N., CRESPO, M. M., ORENS, J. B., SHAH, P. D., HAGE, C. A., CANTU, E., 3RD, PORTEOUS, M. K., DHILLON, G., MCDYER, J., BASTARACHE, J. A., CHRISTIE, J. D. & WARE, L. B. 2018. Cell-free hemoglobin promotes primary graft dysfunction through oxidative lung endothelial injury. *JCI Insight,* 3.

SHIKATA, Y., BIRUKOV, K. G. & GARCIA, J. G. 2003. S1P induces FA remodeling in human pulmonary endothelial cells: role of Rac, GIT1, FAK, and paxillin. *J Appl Physiol (1985),* 94**,** 1193-203.

SHWEIKI, D., ITIN, A., SOFFER, D. & KESHET, E. 1992. Vascular endothelial growth factor induced by hypoxia may mediate hypoxia-initiated angiogenesis. *Nature,* 359**,** 843-5.

SIDDIKUZZAMAN & GRACE, V. M. 2013. Antioxidant potential of all-trans retinoic acid (ATRA) and enhanced activity of liposome encapsulated ATRA against inflammation and tumor-directed angiogenesis. *Immunopharmacol Immunotoxicol,* 35**,** 164-73.

SIDDIQUI, M. R., KOMAROVA, Y. A., VOGEL, S. M., GAO, X., BONINI, M. G., RAJASINGH, J., ZHAO, Y. Y., BROVKOVYCH, V. & MALIK, A. B. 2011. Caveolin-1-eNOS signaling promotes p190RhoGAP-A nitration and endothelial permeability. *J Cell Biol,* 193**,** 841-50.

SIMON, A. M. & GOODENOUGH, D. A. 1998. Diverse functions of vertebrate gap junctions. *Trends in Cell Biology,* 8**,** 477-483.

SLAMA, A., SCHILLAB, L., BARTA, M., BENEDEK, A., MITTERBAUER, A., HOETZENECKER, K., TAGHAVI, S., LANG, G., MATILLA, J., ANKERSMIT, H., HAGER, H., ROTH, G., KLEPETKO, W. & AIGNER, C. 2017.

Standard donor lung procurement with normothermic ex vivo lung perfusion: A prospective randomized clinical trial. *J Heart Lung Transplant,* 36**,** 744-753.

SMITS, J. M., VAN DER BIJ, W., VAN RAEMDONCK, D., DE VRIES, E., RAHMEL, A., LAUFER, G., DE PAUW, M. & MEISER, B. 2011. Defining an extended criteria donor lung: an empirical approach based on the Eurotransplant experience1. *Transplant International,* 24**,** 393-400.

SONG, C., AL-MEHDI, A. B. & FISHER, A. B. 2001. An immediate endothelial cell signaling response to lung ischemia. *Am J Physiol Lung Cell Mol Physiol,* 281**,** L993-1000.

SPIEGEL, S., MACZIS, M. A., MACEYKA, M. & MILSTIEN, S. 2019. New insights into functions of the sphingosine-1-phosphate transporter SPNS2. *Journal of Lipid Research,* 60**,** 484-489.

SPRATT, J. R., MATTISON, L. M., IAIZZO, P. A., MEYER, C., BROWN, R. Z., ILES, T., PANOSKALTSIS-MORTARI, A. & LOOR, G. 2018. Lung transplant after prolonged ex vivo lung perfusion: predictors of allograft function in swine. *Transplant International,* 31**,** 1405-1417.

STEEN, S., INGEMANSSON, R., ERIKSSON, L., PIERRE, L., ALGOTSSON, L., WIERUP, P., LIAO, Q., EYJOLFSSON, A., GUSTAFSSON, R. & SJOBERG, T. 2007. First human transplantation of a nonacceptable donor lung after reconditioning ex vivo. *Ann Thorac Surg,* 83**,** 2191-4.

STEEN, S., KIMBLAD, P. O., SJÖBERG, T., LINDBERG, L., INGEMANSSON, R. & MASSA, G. 1994. Safe lung preservation for twenty-four hours with Perfadex. *Ann Thorac Surg,* 57**,** 450-7.

STEEN, S., SJÖBERG, T., PIERRE, L., LIAO, Q., ERIKSSON, L. & ALGOTSSON, L. 2001. Transplantation of lungs from a non-heart-beating donor. *Lancet,* 357**,** 825-9.

STONE, M. L., SHARMA, A. K., ZHAO, Y., CHARLES, E. J., HUERTER, M. E., JOHNSTON, W. F., KRON, I. L., LYNCH, K. R. & LAUBACH, V. E. 2015. Sphingosine-1-phosphate receptor 1 agonism attenuates lung ischemia-reperfusion injury. *Am J Physiol Lung Cell Mol Physiol,* 308**,** L1245-52.

STONE, M. L., ZHAO, Y., ROBERT SMITH, J., WEISS, M. L., KRON, I. L., LAUBACH, V. E. & SHARMA, A. K. 2017. Mesenchymal stromal cell-derived extracellular vesicles attenuate lung ischemia-reperfusion injury and enhance reconditioning of donor lungs after circulatory death. *Respir Res,* 18**,** 212.

STONEY, P. N., FRAGOSO, Y. D., SAEED, R. B., ASHTON, A., GOODMAN, T., SIMONS, C., GOMAA, M. S., SEMENTILLI, A., SEMENTILLI, L., ROSS, A. W., MORGAN, P. J. & MCCAFFERY, P. J. 2016. Expression of the retinoic acid catabolic enzyme CYP26B1 in the human brain to maintain signaling homeostasis. *Brain Struct Funct,* 221**,** 3315-26.

SUH, J. W., LEE, J. G., PARK, M. S., KIM, S. Y., JEONG, S. J. & PAIK, H. C. 2020. Impact of extended-criteria donor lungs according to preoperative recipient status and age in lung transplantation. *Korean J Transplant,* 34**,** 185-192.

SUN, X., SINGLETON, P. A., LETSIOU, E., ZHAO, J., BELVITCH, P., SAMMANI, S., CHIANG, E. T., MORENO-VINASCO, L., WADE, M. S., ZHOU, T., LIU, B., PARASTATIDIS, I., THOMSON, L., ISCHIROPOULOS, H., NATARAJAN, V., JACOBSON, J. R., MACHADO, R. F., DUDEK, S. M. & GARCIA, J. G. 2012. Sphingosine-1-phosphate receptor-3 is a novel biomarker in acute lung injury. *Am J Respir Cell Mol Biol,* 47**,** 628-36.

TAKASHIMA, S., SUGIMOTO, N., TAKUWA, N., OKAMOTO, Y., YOSHIOKA, K., TAKAMURA, M., TAKATA, S., KANEKO, S. & TAKUWA, Y. 2008. G12/13 and Gq mediate S1P2-induced inhibition of Rac and migration in vascular smooth muscle in a manner dependent on Rho but not Rho kinase. *Cardiovasc Res,* 79**,** 689-97.

TAN, Y. B., PASTUKH, V. M., GORODNYA, O. M., MULEKAR, M. S., SIMMONS, J. D., MACHUCA, T. N., BEAVER, T. M., WILSON, G. L. & GILLESPIE, M. N. 2020. Enhanced Mitochondrial DNA Repair Resuscitates Transplantable Lungs Donated After Circulatory Death. *J Surg Res,* 245**,** 273-280.

TAUSEEF, M., KINI, V., KNEZEVIC, N., BRANNAN, M., RAMCHANDARAN, R., FYRST, H., SABA, J., VOGEL, S. M., MALIK, A. B. & MEHTA, D. 2008. Activation of sphingosine kinase-1 reverses the increase in lung vascular permeability through sphingosine-1-phosphate receptor signaling in endothelial cells. *Circ Res,* 103**,** 1164-72.

TAVERNE, Y. J. H. J., BOGERS, A. J. J. C., DUNCKER, D. J. & MERKUS, D. 2013. Reactive Oxygen Species and the Cardiovascular System. *Oxidative Medicine and Cellular Longevity,* 2013**,** 862423.

TERMEER, C. C., WEISS, J. M., SCHÖPF, E., VANSCHEIDT, W. & SIMON, J. C. 1998. The low molecular weight Dextran 40 inhibits the adhesion of T lymphocytes to endothelial cells. *Clin Exp Immunol,* 114**,** 422-6.

THOMPSON, S., MARTÍNEZ-BURGO, B., SEPURU, K. M., RAJARATHNAM, K., KIRBY, J. A., SHEERIN, N. S. & ALI, S. 2017. Regulation of Chemokine Function: The Roles of GAG-Binding and Post-Translational Nitration. *Int J Mol Sci,* 18.

TONKS, N. K. 2006. Protein tyrosine phosphatases: from genes, to function, to disease. *Nature Reviews Molecular Cell Biology,* 7**,** 833-846.

TORONTO LUNG TRANSPLANT GROUP 1986. Unilateral lung transplantation for pulmonary fibrosis. *N Engl J Med,* 314**,** 1140-5.

TOZAWA, K., AL-MEHDI, A. B., MUZYKANTOV, V. & FISHER, A. B. 1999. In situ imaging of intracellular calcium with ischemia in lung subpleural microvascular endothelial cells. *Antioxid Redox Signal,* 1**,** 145-54.

TSUKITA, S., FURUSE, M. & ITOH, M. 2001. Multifunctional strands in tight junctions. *Nature Reviews Molecular Cell Biology,* 2**,** 285-293.

TSURUI, Y., SHO, M., KUZUMOTO, Y., HAMADA, K., AKASHI, S., KASHIZUKA, H., IKEDA, N., NOMI, T., MIZUNO, T., KANEHIRO, H. & NAKAJIMA, Y. 2005. Dual role of vascular endothelial growth factor in hepatic ischemia-reperfusion injury. *Transplantation,* 79**,** 1110-5.

TUDER, R. M., FLOOK, B. E. & VOELKEL, N. F. 1995. Increased gene expression for VEGF and the VEGF receptors KDR/Flk and Flt in lungs exposed to acute or to chronic hypoxia. Modulation of gene expression by nitric oxide. *J Clin Invest,* 95**,** 1798-807.

TZIMA, E., IRANI-TEHRANI, M., KIOSSES, W. B., DEJANA, E., SCHULTZ, D. A., ENGELHARDT, B., CAO, G., DELISSER, H. & SCHWARTZ, M. A. 2005. A mechanosensory complex that mediates the endothelial cell response to fluid shear stress. *Nature,* 437**,** 426-31.

VALENZA, F., ROSSO, L., COPPOLA, S., FROIO, S., PALLESCHI, A., TOSI, D., MENDOGNI, P., SALICE, V., RUGGERI, G. M., FUMAGALLI, J., VILLA, A., NOSOTTI, M., SANTAMBROGIO, L. & GATTINONI, L. 2014. Ex vivo lung perfusion to improve donor lung function and increase the number of organs available for transplantation. *Transpl Int,* 27**,** 553-61.

VAN ESSEN, G. J., TE LINTEL HEKKERT, M., SOROP, O., HEINONEN, I., VAN DER VELDEN, J., MERKUS, D. & DUNCKER, D. J. 2018. Cardiovascular Function of Modern Pigs Does not Comply with Allometric Scaling Laws. *Scientific Reports,* 8**,** 792.

VAN RAEMDONCK, D., KESHAVJEE, S., LEVVEY, B., CHERIKH, W. S., SNELL, G., ERASMUS, M., SIMON, A., GLANVILLE, A. R., CLARK, S., D'OVIDIO, F., CATARINO, P., MCCURRY, K., HERTZ, M. I., VENKATESWARAN, R., HOPKINS, P., INCI, I., WALIA, R., KREISEL, D., MASCARO, J., DILLING, D. F., CAMP, P., MASON, D., MUSK, M., BURCH, M., FISHER, A., YUSEN, R. D., STEHLIK, J. & CYPEL, M. 2019. Donation after circulatory death in lung transplantation—five-year follow-up from ISHLT Registry. *The Journal of Heart and Lung Transplantation,* 38**,** 1235-1245.

VAN ZANDEN, J. E., LEUVENINK, H. G. D., VERSCHUUREN, E. A. M., VELDHUIS, Z. J., OTTENS, P. J., ERASMUS, M. E. & HOTTENROTT, M. C. 2021. Ex Vivo Perfusion With Methylprednisolone Attenuates Brain Death-induced Lung Injury in Rats. *Transplant Direct,* 7**,** e682.

VENKATARAMAN, K., THANGADA, S., MICHAUD, J., OO, M. L., AI, Y., LEE, Y. M., WU, M., PARIKH, N. S., KHAN, F., PROIA, R. L. & HLA, T. 2006. Extracellular export of sphingosine kinase-1a contributes to the vascular S1P gradient. *Biochem J,* 397**,** 461-71.

VERMEIREN, G. L. J., CLAEYS, M. J., VAN BOCKSTAELE, D., GROBBEN, B., SLEGERS, H., BOSSAERT, L. & JORENS, P. G. 2000. Reperfusion injury after focal myocardial ischaemia: polymorphonuclear leukocyte activation and its clinical implications. *Resuscitation,* 45**,** 35-61.

VESTWEBER, D., WESSEL, F. & NOTTEBAUM, A. F. 2014. Similarities and differences in the regulation of leukocyte extravasation and vascular permeability. *Semin Immunopathol,* 36**,** 177-92.

VÉZINA, A., CHARFI, C., ZGHEIB, A. & ANNABI, B. 2018. Cerebrovascular Angiogenic Reprogramming upon LRP1 Repression: Impact on Sphingosine-1-Phosphate-Mediated Signaling in Brain Endothelial Cell Chemotactism. *Molecular Neurobiology,* 55**,** 3551-3563.

VOURET-CRAVIARI, V., BOURCIER, C., BOULTER, E. & VAN OBBERGHEN-SCHILLING, E. 2002. Distinct signals via Rho GTPases and Src drive shape changes by thrombin and sphingosine-1-phosphate in endothelial cells. *J Cell Sci,* 115**,** 2475-84.

WALLEZ, Y., CAND, F., CRUZALEGUI, F., WERNSTEDT, C., SOUCHELNYTSKYI, S., VILGRAIN, I. & HUBER, P. 2007. Src kinase phosphorylates vascular endothelial-cadherin in response to vascular endothelial growth factor: identification of tyrosine 685 as the unique target site. *Oncogene,* 26**,** 1067-1077.

WALLEZ, Y. & HUBER, P. 2008. Endothelial adherens and tight junctions in vascular homeostasis, inflammation and angiogenesis. *Biochimica et Biophysica Acta (BBA) - Biomembranes,* 1778**,** 794-809.

WANG, L., GE, C. & ZHANG, X. 2022a. Sufentanil ameliorates oxygen-glucose deprivation/reoxygenation-induced endothelial barrier dysfunction in HCMECs via the PI3K/Akt signaling pathway. *Exp Ther Med,* 24**,** 437.

WANG, T., LIU, C., PAN, L. H., LIU, Z., LI, C. L., LIN, J. Y., HE, Y., XIAO, J. Y., WU, S., QIN, Y., LI, Z. & LIN, F. 2020a. Inhibition of p38 MAPK Mitigates Lung Ischemia Reperfusion Injury by Reducing Blood-Air Barrier Hyperpermeability. *Front Pharmacol,* 11**,** 569251.

WANG, W., QIAN, J., ZHU, M., WANG, Y. & PAN, Y. 2022b. Normothermic ex vivo lung perfusion outperforms conventional cold preservation in a deceased rat lung. *Annals of Translational Medicine,* 10**,** 99.

WANG, Z., HIGASHIKAWA, K., YASUI, H., KUGE, Y., OHNO, Y., KIHARA, A., MIDORI, Y. A., HOUKIN, K. & KAWABORI, M. 2020b. FTY720 Protects Against Ischemia-Reperfusion Injury by Preventing the Redistribution of Tight Junction Proteins and Decreases Inflammation in the Subacute Phase in an Experimental Stroke Model. *Transl Stroke Res,* 11**,** 1103-1116.

WANG, Z. Y., LIN, J. Y., FENG, Y. R., LIU, D. S., ZHAO, X. Z., LI, T., LI, S. Y., SUN, J. C., LI, S. F., JIA, W. Y. & JING, H. R. 2021. Recombinant angiopoietin-like protein 4 attenuates intestinal barrier structure and function injury after ischemia/reperfusion. *World J Gastroenterol,* 27**,** 5404-5423.

WARD, A., BROGDEN, R. N., HEEL, R. C., SPEIGHT, T. M. & AVERY, G. S. 1983. Etretinate. *Drugs,* 26**,** 9-43.

WARNECKE, G., VAN RAEMDONCK, D., SMITH, M. A., MASSARD, G., KUKREJA, J., REA, F., LOOR, G., DE ROBERTIS, F., NAGENDRAN, J., DHITAL, K. K., MORADIELLOS DÍEZ, F. J., KNOSALLA, C., BERMUDEZ, C. A., TSUI, S., MCCURRY, K., WANG, I. W., DEUSE, T., LESÈCHE, G., THOMAS, P., TUDORACHE, I., KÜHN, C., AVSAR, M., WIEGMANN, B., SOMMER, W., NEYRINCK, A., SCHIAVON, M., CALABRESE, F., SANTELMO, N., OLLAND, A., FALCOZ, P. E., SIMON, A. R., VARELA, A., MADSEN, J. C., HERTZ, M., HAVERICH, A. & ARDEHALI, A. 2018. Normothermic ex-vivo preservation with the portable Organ Care System Lung device for bilateral lung transplantation (INSPIRE): a randomised, open-label, non-inferiority, phase 3 study. *Lancet Respir Med,* 6**,** 357-367.

WEATHINGTON, N. M., ÁLVAREZ, D., SEMBRAT, J., RADDER, J., CÁRDENES, N., NODA, K., GONG, Q., WONG, H., KOLLS, J., D'CUNHA, J., MALLAMPALLI, R. K., CHEN, B. B. & ROJAS, M. 2018. Ex vivo lung perfusion as a human platform for preclinical small molecule testing. *JCI Insight,* 3.

WEBSTER, K. A. 2012. Mitochondrial membrane permeabilization and cell death during myocardial infarction: roles of calcium and reactive oxygen species. *Future Cardiol,* 8**,** 863-84.

WEI, Z., COSTA, K., AL-MEHDI, A. B., DODIA, C., MUZYKANTOV, V. & FISHER, A. B. 1999. Simulated Ischemia in Flow-Adapted Endothelial Cells Leads to Generation of Reactive Oxygen Species and Cell Signaling. *Circulation Research,* 85**,** 682-689.

WEI, Z., MANEVICH, Y., AL-MEHDI, A. B., CHATTERJEE, S. & FISHER, A. B. 2004. Ca2+ flux through voltage-gated channels with flow cessation in pulmonary microvascular endothelial cells. *Microcirculation,* 11**,** 517-26.

WEIS, S., CUI, J., BARNES, L. & CHERESH, D. 2004. Endothelial barrier disruption by VEGF-mediated Src activity potentiates tumor cell extravasation and metastasis. *J Cell Biol,* 167**,** 223-9.

WESSEL, F., WINDERLICH, M., HOLM, M., FRYE, M., RIVERA-GALDOS, R., VOCKEL, M., LINNEPE, R., IPE, U., STADTMANN, A., ZARBOCK, A., NOTTEBAUM, A. F. & VESTWEBER, D. 2014. Leukocyte extravasation and vascular permeability are each controlled in vivo by different tyrosine residues of VE-cadherin. *Nat Immunol,* 15**,** 223-30.

WHALEN, D. A., JR., HAMILTON, D. G., GANOTE, C. E. & JENNINGS, R. B. 1974. Effect of a transient period of ischemia on myocardial cells. I. Effects on cell volume regulation. *Am J Pathol,* 74**,** 381-97.

WHITSON, B. A., MULIER, K., LI, H., ZHOU, X., CAI, C., BLACK, S. M., TAN, T., MA, J. & BEILMAN, G. J. 2021. MG53 as a Novel Therapeutic Protein to Treat Acute Lung Injury. *Mil Med,* 186**,** 339-345.

WILSON, S. J. & KEENAN, A. K. 2003. Role of hemin in the modulation of H2O2-mediated endothelial cell injury. *Vascul Pharmacol,* 40**,** 109-18.

WIT, C. D., ROOS, F., BOLZ, S. S., KIRCHHOFF, S., KRÜGER, O., WILLECKE, K. & POHL, U. 2000. Impaired conduction of vasodilation along arterioles in connexin40-deficient mice. *Circulation Research***,** 649-655.

WÓJCIAK-STOTHARD, B., POTEMPA, S., EICHHOLTZ, T. & RIDLEY, A. J. 2001. Rho and Rac but not Cdc42 regulate endothelial cell permeability. *J Cell Sci,* 114**,** 1343-55.

WU, F. & WILSON, J. X. 2008. Peroxynitrite-dependent activation of protein phosphatase type 2A mediates microvascular endothelial barrier dysfunction. *Cardiovascular Research,* 81**,** 38-45.

WU, M. Y., YIANG, G. T., LIAO, W. T., TSAI, A. P., CHENG, Y. L., CHENG, P. W., LI, C. Y. & LI, C. J. 2018. Current Mechanistic Concepts in Ischemia and Reperfusion Injury. *Cell Physiol Biochem,* 46**,** 1650-1667.

XIE, Q. W., KASHIWABARA, Y. & NATHAN, C. 1994. Role of transcription factor NF-kappa B/Rel in induction of nitric oxide synthase. *J Biol Chem,* 269**,** 4705-8.

YAMADA, Y., ISKENDER, I., ARNI, S., HILLINGER, S., COSGUN, T., YU, K., JUNGRAITHMAYR, W., CESAROVIC, N., WEDER, W. & INCI, I. 2017. Ex vivo treatment with inhaled N-acetylcysteine in porcine lung transplantation. *J Surg Res,* 218**,** 341-347.

YAMANASHI, K., OHSUMI, A., ODA, H., TANAKA, S., YAMADA, Y., NAKAJIMA, D. & DATE, H. 2022. Reduction of donor mononuclear phagocytes with clodronate-liposome during ex vivo lung perfusion attenuates ischemia-reperfusion injury. *The Journal of Thoracic and Cardiovascular Surgery*.

YANG, Q., HE, G. W., UNDERWOOD, M. J. & YU, C. M. 2016. Cellular and molecular mechanisms of endothelial ischemia/reperfusion injury: perspectives and implications for postischemic myocardial protection. *Am J Transl Res,* 8**,** 765-77.

YANG, T., ZHANG, X., MA, C. & CHEN, Y. 2018. TGF-β/Smad3 pathway enhances the cardio-protection of S1R/SIPR1 in in vitro ischemia-reperfusion myocardial cell model. *Exp Ther Med,* 16**,** 178-184.

YIN, M. J., YAMAMOTO, Y. & GAYNOR, R. B. 1998. The anti-inflammatory agents aspirin and salicylate inhibit the activity of I(kappa)B kinase-beta. *Nature,* 396**,** 77-80.

ZHANG, G., XU, S., QIAN, Y. & HE, P. 2010. Sphingosine-1-phosphate prevents permeability increases via activation of endothelial sphingosine-1-phosphate receptor 1 in rat venules. *Am J Physiol Heart Circ Physiol,* 299**,** H1494-504.

ZHANG, Q., CHATTERJEE, S., WEI, Z., LIU, W. D. & FISHER, A. B. 2008. Rac and PI3 kinase mediate endothelial cell-reactive oxygen species generation during normoxic lung ischemia. *Antioxid Redox Signal,* 10**,** 679-89.

ZHANG, Q., MATSUZAKI, I., CHATTERJEE, S. & FISHER, A. B. 2005a. Activation of endothelial NADPH oxidase during normoxic lung ischemia is KATP channel dependent. *Am J Physiol Lung Cell Mol Physiol,* 289**,** L954-61.

ZHANG, Y., ZHAO, S., GU, Y., LEWIS, D. F., ALEXANDER, J. S. & WANG, Y. 2005b. Effects of peroxynitrite and superoxide radicals on endothelial monolayer permeability: potential role of peroxynitrite in preeclampsia. *J Soc Gynecol Investig,* 12**,** 586-92.

ZHAO, C., MORENO-NIEVES, U., DI BATTISTA, J. A., FERNANDES, M. J., TOUAIBIA, M. & BOURGOIN, S. G. 2015. Chemical Hypoxia Brings to Light Altered Autocrine Sphingosine-1-Phosphate Signalling in Rheumatoid Arthritis Synovial Fibroblasts. *Mediators Inflamm,* 2015**,** 436525.

ZHAO, G., AL-MEHDI, A. B. & FISHER, A. B. 1997. Anoxia-reoxygenation versus ischemia in isolated rat lungs. *Am J Physiol,* 273**,** L1112-7.

ZHAO, J., ZHU, M., JIANG, H., SHEN, S., SU, X. & SHI, Y. 2019. Combination of sphingosine-1-phosphate receptor 1 (S1PR1) agonist and antiviral drug: a potential therapy against pathogenic influenza virus. *Sci Rep,* 9**,** 5272.

ZHOU, T., PRATHER, E. R., GARRISON, D. E. & ZUO, L. 2018. Interplay between ROS and Antioxidants during Ischemia-Reperfusion Injuries in Cardiac and Skeletal Muscle. *Int J Mol Sci,* 19.

ZHOU, X., QIAN, Y., YUAN, D., FENG, Q. & HE, P. 2019. H(2) O(2) -induced microvessel barrier dysfunction: the interplay between reactive oxygen species, nitric oxide, and peroxynitrite. *Physiol Rep,* 7.

ZHU, Q., ZHOU, W. Q., WAN, L., JIN, Z. Y., ZHANG, X. H. & LIN, L. N. 2018. [The Expression of Sphingosine-1-phosphate and Sphingosine-1-phosphate Receptor 1 in Mouse Model of Pulmonary Ischemia-Reperfusion Injury]. *Sichuan Da Xue Xue Bao Yi Xue Ban,* 49**,** 891-894.

8. Publications, presentations and awards

8.1. Publications

Published: **Gilmour J**, Griffiths C, Pither T, Scott WE 3rd, Fisher AJ. Normothermic machine perfusion of donor-lungs ex-vivo: promoting clinical adoption. Curr Opin Organ Transplant. 2020 Jun;25(3):285-292

Accepted: Wilkins GC, **Gilmour J**, Giannoudaki E, Kirby JA, Sheerin NS, Ali S. Underpinning the therapeutic mechanisms of sphingosine-1-phosphate receptor agonism during ischaemia-reperfusion injury.

In progress**: Gilmour J**, Fisher AJ, Sigvardsson A, Ali S. A modified perfusate solution for ex vivo lung perfusion improves organ function and reduces tissue inflammation.

8.2. Awards

Wellcome Trust Translational Partnership Early Translational Funding (2022)

DiMen Flexible funding – Advanced R with Tidyverse course, Babraham Institute (2021)

8.3. Conferences

British society of Immunology (December 2020) – Poster presentation

British transplant society annual congress (March 2023) – Poster presentation

Immunology North East AGM and Research Symposium (June 2023) – Poster presentation (1st place poster prize)